Using Chemical Ionisation Mass Spectrometry to Measure Oceanic Emissions of Trace Gases

Ieuan Joseff Roberts

Doctor of Philosophy

University of York

Chemistry

January 2023

Acknowledgements

I want to thank my supervisors Lucy Carpenter and Marvin Shaw for helping and guiding me for the past 5 and 4 years respectfully. Working in the Carpenter group has been an amazing opportunity for me, and it will be sad to move on, though I am very grateful for all those that have helped me during my time here.

I'd like to thank Liselotte, Rosie, Lucy B, Lewis, Katherine, David, Adam, Matthew, Martyn, Steve and Stu for all their help during the project. From teaching me techniques, to helping me perform measurements from home during COVID lockdown the help I have received has made this PhD a possibility and without any of them I would not be anywhere near to finishing as I am now.

I would also like to thank my flatmate Becca for tolerating my late nights and all nighters to finish the writing of the thesis and for allowing me to be anti-social to finish on time.

I would like to thank my family for their unwavering support through the course of my PhD and during the illness in the middle of it.

I want to thank my boyfriend Matthew for being there for me through the worst and most stressful times of this PhD and for giving me the drive to go forward and complete the degree. I love you, thank you so much for all you've done for me.

I would also like to thank NERC and my CASE partner Anatune ltd. for funding my PhD.

Abstract

In this thesis the capability of chemical ionisation mass spectrometry (CIMS) to measure emissions of trace gases.

Rate constants of several oxygenated volatile organic compounds (OVOCs) and benzene are reported for H_3O^+, NO^+ and O_2^+ reagent ions in nitrogen carrier gas, using a permeation tube calibration source. Higher fragmentation was observed due to changes to the lens voltages of the instrument to tune for higher sensitivity, altering the reagent ion energies. The impact of increasing flow tube temperature and voltage on the sensitivity and ionisation of benzene, butanone and butanal was shown under dry and humid conditions. It is demonstrated that a higher flow tube temperature reduces the water adduct formation, simplifying compound concentration determination.

The iodide dependence of the production of methyl iodide is debateable under natural conditions as studies that report this dependence (Y. Chen et al., 2020; Moore and Zafiriou, 1994) use iodide levels toward the top of the natural range. Iodide dependent reactions were measured in only two samples, PYSML1 and PFSML3. Further work is required to ascertain the cause of this reaction, though it is known that it is restricted the SML and only currently occurs in estuarine Plymouth samples.

PTR-ToF-MS is used to measure emissions from seawater samples exposed to both light and ozone. Significant emissions (37.7 – 40.3 TgC yr^{-1}) of VOCs were measured from photolysis of the seawater surface. These were higher than those reported in literature but could potentially be explained through the sample composition being unrepresentative of average global composition. Future work is required to confirm this magnitude of VOCs to the marine atmosphere and to provide more complete quantification and identification of the species produced. This would allow for better modelling of SOA formation, OH reactivity and concentration of VOCs in the marine atmosphere that are all often underestimated in models.

Contents

List of Tables

List of Figures

Author's Declaration

I declare that this thesis is a presentation of original work and I am the sole author. This work has not previously been presented for an award at this, or any other, University. All sources are acknowledged as References. The contents of the second chapter have largely been published in a paper (https://doi.org/10.1016/j.ijms.2022.116892) in the International Journal of Mass Spectrometry. This is also acknowledged at the beginning of the chapter.

1. Introduction

Air-sea gas exchange is an important process that controls the atmospheric composition of a large range of compounds, from the sequestration of high concentration compounds like carbon dioxide (Heinze et al., 2015) to the emission of methane (Weber et al., 2019), volatile organic compounds (VOCs) (Read et al., 2012; Sinha et al., 2007) and halogenated compounds (Carpenter et al., 2013; Küpper et al., 2018). VOCs have a wide range of impacts on both the environment and human health. VOCs can influence the atmospheric balance of the hydroxyl radical (OH) (Wang et al., 2019) which will have subsequent effects on the lifetime of atmospheric gases like methane (Saunois et al., 2020), increasing their radiative forcing. VOCs can also undergo physical or chemical processing when emitted into the atmosphere to form secondary organic aerosols (SOAs) or oxidants like ozone (O_3) (Hu et al., 2013; J. Li et al., 2019; Schneider et al., 2019). Halogenated compounds in the atmosphere, like methyl iodide (CH_3I), largely impact the atmosphere through the production of halogen radicals (Saiz-Lopez and Glasow, 2012). Methyl iodide, once emitted, will react to form atmospheric iodine radicals (see ***Section 1.2*** for details) which can react to destroy tropospheric ozone (Carpenter et al., 1999; Davis et al., 1996) or, through the formation of iodine monoxide (IO), impacts the NO_x and HO_x balance thus reducing the oxidative capacity of the atmosphere (McFiggans et al., 2000).

The focus of this thesis is on the sea-air exchange of methyl iodide and VOCs. Models of global oceanic methyl iodide emissions (Bell et al., 2002; Ordóñez et al., 2012) do not include any iodide dependence in their calculations but some studies suggest that methyl iodide production may be iodide dependent (Y. Chen et al., 2020; Moore and Zafiriou, 1994) (see ***Section 1.3.4*** *for details).* It is important to ascertain whether this iodide dependence does occur under natural conditions (i.e. natural iodide levels) to be able to incorporate this into models. The iodide dependence was investigated using measurements of methyl iodide emissions from various water samples across a range of added iodide concentrations. A missing source of tropospheric organic aerosols has been predicted in a range of models (Gantt et al., 2009; Heald et al., 2006, 2005; Roelofs, 2008; Spracklen et al., 2008) which could be partially attributed to marine VOC emissions (Meskhidze and Nenes, 2006; Yu and Li, 2021). OH reactivity is also underestimated in the remote atmosphere (Mao et al., 2009) which they linked to unidentified VOC sources producing formaldehyde and Travis et. al. (2020) estimated 340 TgC yr^{-1} of $>C_4$ alkanes was required to account for the missing OH reactivity, which was much greater than their estimated VOC source of only 28.3 TgC

yr^{-1}. Novak and Bertram (2020) suggested that there is a "significant uncertainty in the scaling of laboratory studies of interfacial VOC production to the ambient atmosphere". In this study the Vocus PTR-Tof-MS was assessed as a method of measuring a complex suite of VOC emissions, providing both assignments and individual emissions measurements for a large range of compounds.

The rest of this chapter provides a brief introduction to the mechanism of air-sea exchange and the importance, and measurement, of methyl iodide and VOC emissions from the ocean. Chapter 2 describes the calibration of the selected ion flow tube-mass spectrometer (SIFT-MS) for measuring OVOC compounds which was done to test the capability of the instrument to measure OVOCs under both dry and humid conditions. In Chapter 3 the iodide dependence of methyl iodide emissions was tested on real water samples using a Vocus PTR-ToF-MS. In Chapter 4 the Vocus PTR-ToF-MS was used to measure the emissions of a large suite of VOC compounds from a Bermuda seawater sample under zero ozone and ambient ozone mixing ratios in dark and ambient light conditions. Chapter 5 provides conclusions to the previous chapters and the thesis.

1.1 Mechanisms of Air-sea Gas Exchange

1.1.1 Diffusive Sea-air Gas Exchange

The air-sea exchange of trace gases is often calculated using the concentration difference between the atmosphere and ocean and its transfer velocity, which is sometimes referred to as diffusive sea-air gas exchange. A common model used for the ocean surface is the 'surface film' model in which two films, one on the air side and another on the ocean side, that control the exchange of momentum, heat and gases (Liss and Slater, 1974). The air-sea exchange of heat and momentum tend are limited by atmospheric transport (Liss and Slater, 1974). In this model the mass flux, F, in mol m^{-2} s^{-1} of a species across the air-sea interface can be expressed by ***Eq. 1.1*** and ***Eq. 1.2*** (Carpenter et al., 2012).

$$F = k_t \left(C_w - \frac{C_g}{H} \right) \quad (Eq. 1.1)$$

$$\frac{1}{k_t} = \frac{1}{k_w} + \frac{1}{H k_a} \quad (Eq. 1.2)$$

where C_w and C_g are the concentrations of the species being measured in the ocean and atmosphere, in mol, respectively, H is the gas-over-liquid form of the Henry's law

constant and k_t, k_w and k_a are the total, liquid and air mass transfer coefficients in m s^{-1}. The inverse of these, calculated in ***Eq. 1.2*** represent the total, liquid and air side resistances to transfer. For water soluble molecules the mass transfer in dominated by resistance in the air ($k_t \sim Hk_a$) whereas for partially soluble molecules the mass transfer is dominated by water resistance ($k_t \sim k_w$) (Carpenter et al., 2012).

The water side gas transfer coefficient (k_w) can be derived from the wind speed, solubility of the gas, molecular diffusivity of the gas and the kinematic viscosity of seawater (Liss and Merlivat, 1986; Nightingale et al., 2000; Wanninkhof, 1992). Estimates of k_w derived from the temperature, wind speed and salinity are able to account for 50 – 80 % of its variability (Ho et al., 2011).

1.1.2 Effects of the SML on Air-sea Gas Exchange

The sea surface microlayer (SML) is a thin layer of 1 – 1000 µm that is ubiquitous across the global ocean and that is chemically, physically and biologically distinct from the underlying water (Hunter, 1980). The surface microlayer is enriched in inorganic components and dissolved organic matter (DOM), consisting of amino acids, proteins, fatty acids, carbohydrates, carbonyls, carboxylic acids and aromatics, compared to the underlying water (ULW) (Liss and Duce, 1997; Stubbins et al., 2008).

Surface-active materials, or surfactants, are compounds with a polar head and non-polar tail. Measurements in the Atlantic by Sabbaghzadeh et. al. (2017) imply that surfactant enrichment in the SML, relative to the ULW, is ubiquitous in the open ocean up to wind speeds of at least 13 m s^{-1}. Surfactants at the ocean-atmosphere interface are able to suppress gas exchange through the formation of a physico-chemical barrier or through modifying the turbulent energy transfer, microscale wave breaking and through damping of small capillary waves (Frew et al., 1990; Garbe et al., 2014; McKenna and McGillis, 2004; Pereira et al., 2016; Tsai, 1998, 1996). Hydrophobic surfactants tend to form monolayers of around 2 – 3 nm thick (Hühnerfuss, 2006) which act as a physical barrier to exchange (Frew, 1997; Springer and Pigford, 1970) or through providing an additional liquid layer that provides resistance to gas transfer (Liss and Martinelli, 1978).

The suppression of emissions caused by hydrophilic surfactants is believed to be the major contribution of total surfactant concentration on gas transfer (Carpenter and Nightingale, 2015). For hydrophilic surfactants, gas transfer is thought to be lessened through hydrodynamic effects (Liss and Slinn, 1983), largely through soluble

surfactants altering the resistance of the surface to changes in surface area. This leads to a reduction in turbulence length near the surface, reduction of velocity scales, reduction in wave growth and an increase in wave energy dissipation (Frew, 1997; Hühnerfuss et al., 1983). Even at low open ocean surface film pressures the impacts of these hydrodynamic effects are thought to be sufficient enough to still reduce the gas transfer rates (Frew, 1997; Frew et al., 2006). In natural environments, the composition of the surfactant fraction is often complex and so the impact of surfactants on gas exchange is difficult to quantify due to the interactions of both soluble and insoluble surfactants (Engel et al., 2017)

1.2 Atmospheric Impacts of Methyl Iodide

Methyl iodide (CH_3I), also called iodomethane, is an iodinated halocarbon that is thought to be a major source of atmospheric iodine (Klick and Abrahamsson, 1992; Schall et al., 1997; Sherwen et al., 2016). Methyl iodide has been shown to account for roughly half of the global volatile organic iodine source of iodine, with the majority of the remaining iodine source from organic iodine being the dihalomethanes (Jones et al., 2010). Once in the atmosphere CH_3I can photolyse rapidly, producing atmospheric iodine atoms (Saiz-Lopez and Glasow, 2012).

The major impact of methyl iodide in the atmosphere is as a source of atmospheric iodine atoms. The production of iodine from the heterogenous reaction of ozone with iodide leads to the destruction of tropospheric ozone through further reaction with atmospheric iodine atoms as shown in ***(Eq. 1.3 – Eq. 1.7)*** (Carpenter et al., 1999; Davis et al., 1996)

$$2(I + O_3 \rightarrow IO + O_2) \quad (Eq. 1.3)$$
$$IO + IO \rightarrow 2I + O_2 \quad (Eq. 1.4)$$
$$\overline{2O_3 \rightarrow 3O_2}$$

$$I + O_3 \rightarrow IO + O_2 \quad (Eq. 1.5)$$
$$IO + HO_2 \rightarrow HOI + O_2 \quad (Eq. 1.6)$$
$$HOI + hv \rightarrow I + OH \quad (Eq. 1.7)$$
$$\overline{O_3 + HO_2 \rightarrow 2O_2 + OH}$$

The removal of tropospheric ozone is a net positive for both human and plant health and is a positive for the climate. Tropospheric ozone has been shown to have adverse respiratory impacts and causes inflammation of the airways, contributing to increased asthma, emphysema, chronic bronchitis and premature death (Zhang et al., 2019).

Present day crop yield losses due to tropospheric ozone exposure are estimated to range from 2.6 – 7.2 % for maize, rice, soybeans and wheat with the losses likely to increase in the future as greater ozone concentrations are observed (Tai et al., 2021). Current radiative forcing from tropospheric ozone is estimated between 0.27 – 0.51 W m^{-2} (Skeie et al., 2020)

The formation of IO ***(Eq. 1.3)*** will impact the atmospheric NO_x and HO_x balance reducing the oxidative capacity of the atmosphere. In high enough concentrations IO can shift the NO_x balance to preference NO_2 through oxidation of NO ***(Eq. 1.8)*** (McFiggans et al., 2000; Saiz-Lopez et al., 2008).

$$IO + NO \rightarrow I + NO_2 \quad (Eq. 1.8)$$

IO will also lower the mixing ratio of HO_2 through reactions ***(Eq. 1.6)*** and ***(Eq. 1.7)*** (Chameides and Davis, 1980; McFiggans et al., 2000). The impact of iodine on this reaction is greater than that for bromine, which would react in the form of BrO, as the reaction between IO and HO_2 (Eq. 3.6) is faster than BrO and HO_2 and HOI photolyses faster than HOBr (Sander et al., 2006). This is important as HO_2 is a reservoir species for OH radicals and so their removal through reaction with IO has impacts on the oxidative capacity of the atmosphere (Sherwen et al., 2016).

1.3 Studies of Methyl Iodide Emissions

1.3.1 Measurements of Aqueous Methyl Iodide

Methyl iodide has routinely been measured in water samples from the remote open ocean to coastal waters and estuaries (Carpenter et al., 2000; Chuck et al., 2005; Fogelqvist and Tanhua, 1995; Happell and Wallace, 1996; Hepach et al., 2016; Kurihara et al., 2010; Li et al., 2021; Y. Li et al., 2019; Liu et al., 2021; Lovelock, 1975; Manley et al., 1992; Moore and Groszko, 1999; Ooki et al., 2010; Rasmussen et al., 1982; Reifenhäuser and Heumann, 1992; Richter and Wallace, 2004; Schall et al., 1997; Schall and Heumann, 1993; Singh et al., 1983; Tanzer and Heumann, 1992; Tessier et al., 2002; Yuan et al., 2019). The reported concentrations of sub-surface methyl iodide concentrations range from <0.01 – 35.4 pmol L^{-1}, with the lowest, trace, levels reported in the open ocean (both Atlantic and Antarctic) (Schall et al., 1997) and the highest peak levels, 35.4 $pmol^{-1}$, measured in upwelling regions on the Peruvian coast (Hepach et al., 2016). No known measurements of methyl iodide directly within the SML have been performed. Open ocean methyl iodide

concentrations tend to be slightly lower on average than coastal concentrations. The average open ocean and coastal concentrations of the above studies are 4.3 ± 1.6 pmol L^{-1} and 5.3 ± 3.9 pmol L^{-1} respectively (Carpenter et al., 2000; Chuck et al., 2005; Fogelqvist and Tanhua, 1995; Happell and Wallace, 1996; Hepach et al., 2016; Kurihara et al., 2010; Li et al., 2021; Y. Li et al., 2019; Liu et al., 2021; Lovelock, 1975; Manley et al., 1992; Moore and Groszko, 1999; Ooki et al., 2010; Rasmussen et al., 1982; Reifenhäuser and Heumann, 1992; Richter and Wallace, 2004; Schall et al., 1997; Schall and Heumann, 1993; Singh et al., 1983; Tanzer and Heumann, 1992; Tessier et al., 2002; Yuan et al., 2019). The range measured in coastal regions, 0.8 – 6.89 pmol L^{-1}, is smaller than the <0.01-18.68 pmol L^{-1} range measured in oceanic waters. Richter and Wallace (2004) measured particularly high methyl iodide levels in the eastern tropics and Liu et. al. (2021) found that methyl iodide concentrations decreased with increasing latitude. Hepach et. al. (2016) found methyl iodide concentrations to be particularly high in upwelling regions on the Peruvian coast. The reasons for these features will be discussed further in ***Section 1.3.3.***

1.3.2 Measurements of Atmospheric Methyl Iodide

Methyl iodide is ubiquitously present in small amounts in the marine atmosphere (Lovelock et al., 1973). A range of studies (Chuck et al., 2005; Happell and Wallace, 1996; Hepach et al., 2016; Kuyper et al., 2019; Li et al., 2021; Y. Li et al., 2019; Liu et al., 2021; Lovelock et al., 1973; Moore and Groszko, 1999; Ooki et al., 2010; Rasmussen et al., 1982; Reifenhäuser and Heumann, 1992; Richter and Wallace, 2004; Schall and Heumann, 1993; Singh et al., 1983, p. 198; Yuan et al., 2019; Zheng et al., 2019; Zou et al., 2022) have reported methyl iodide levels over the open ocean, coastal and estuarine atmospheres. Like in the aqueous phase, methyl iodide mixing ratios over the open ocean tend to be lower than over coastal waters at 1.6 ± 3.4 pptv compared to 3.4 ± 2.2 pptv. The ranges in values are not dissimilar with the maximum values in coastal waters, 22 pptv (Rasmussen et al., 1982), and oceanic waters, 32.6 pptv (Richter, 2004), being an order of magnitude higher than their average value. Higher methyl iodide mixing ratios have been associated with higher dissolved organic carbon (DOC) (Liu et al., 2021) and elevated biomass productivity (Rasmussen et al., 1982).

1.3.3 Sources of Methyl Iodide

The sources of oceanic methyl iodide are varied and of uncertain proportions. Higher methyl iodide concentrations in coastal regions and in regions of elevated primary productivity indicate the high likelihood of a biogenic source. In a study on the Peruvian coast, including a high productivity upwelling region, methyl iodide was found to correlate fairly strongly with diatom abundance (r_s = 0.73) (Hepach et al., 2016). Production of methyl iodide has been demonstrated in laboratory studies from multiple biological sources, such as macroalgae (Giese et al., 1999; Küpper et al., 2018; Manley and Dastoor, 1988; Nightingale et al., 1995), marine phytoplankton (Manley and de la Cuesta, 1997; Moore et al., 1996; Murphy et al., 2000; Toda and Itoh, 2011) and marine bacteria (Amachi et al., 2001; Fujimori et al., 2012; Fuse et al., 2003; Smythe-Wright et al., 2006). Estimated emissions are 0.01 – 0.57 Gg yr^{-1} from macroalgae (Giese et al., 1999; Manley and Dastoor, 1988; Nightingale et al., 1995), 0.09 – 5.3 Gg yr^{-1} from phytoplankton (Brownell et al., 2010; Manley and de la Cuesta, 1997; Smythe-Wright et al., 2006) and 0.00 – 0.01 Gg yr^{-1} from bacteria (Amachi et al., 2001). These values are insignificant compared to the estimated oceanic emissions of methyl iodide which range from 50.0 – 610 Gg yr^{-1} (Bell et al., 2002; Butler et al., 2007; Campos et al., 1996; Jones et al., 2010; Liss and Slater, 1974; Moore and Groszko, 1999; Rasmussen et al., 1982; Singh et al., 1983; Smythe-Wright et al., 2006; Stemmler et al., 2014; Ziska et al., 2013) with a mean value of 257 ± 37.9 Gg yr^{-1}. There must be a large additional source to account for the clear difference between biological emissions and measured/modelled emissions.

An abiotic photochemical source of methyl iodide was first observed by Moore and Zafirou (1994) when they irradiated filtered seawater samples. The most likely pathway in natural, non-contaminated, waters is the radical recombination of iodine atoms and methyl radicals ***(Eq. 1.9)***.

$$CH_3^{\cdot} + I^{\cdot} \rightarrow CH_3I \quad (Eq. 1.9)$$

Moore and Zafirou (1994) performed calculations to estimate the required concentrations of methyl and iodide radicals to be 0.2 – 0.8 pM at the ocean surface to provide accumulation rates of 1 – 10 pM m^{-3} hr^{-1} of methyl iodide. According to Kieber and Blough (1990) the photolysis of acetone in the absence of an H atom donor, like methanol, can be a source of methyl radicals. The reaction of dimethyl sulfoxide with hydroxyl radicals, or other strong oxidants, is also a source of methyl

radicals, with a rate constant of k_{OH} = 6.6 x10^{9} M^{-1} s^{-1} (Gan, 2005). A slower reaction also occurs between methane and hydroxyl radicals at k_{OH} = 1.20 x10^{8} M^{-1} s^{-1} (Gan, 2005). Photolysis, or chemical reactions, of other constituents of the DOC pool with labile methyl groups are likely the major source of methyl groups in seawater. Iodine radicals can be formed through the light driven reaction of iodide with hydroxyl radicals (Mopper and Zhou, 1990; Zafiriou, 1974a), the reduction of iodate by photosensitized DOC (Saunders et al., 2012) and possibly also photoexcited DOC (De Laurentiis et al., 2012; Jammoul et al., 2009; Parker and Mitch, 2016) and chlorophyll (Reeser et al., 2009).

Happell and Wallace (1996) attributed low/negative saturation anomalies of methyl iodide at high latitudes with low light levels. Richter and Wallace (2004) performed incubation experiments where samples, both untreated and poisoned, were exposed to light. The results showed that there was a negligible difference between the untreated, 0.72 ± 0.48 nmol m^{-3} d^{-1}, and poisoned, 0.72 ± 0.24 nmol m^{-3} d^{-1}, CH_3I production in the dark. However, there was an increase in production when exposed to light for both the untreated, 4.08 ± 1.44 nmol m^{-3} d^{-1}, and poisoned, 5.04 ± 2.40 nmol m^{-3} d^{-1}, samples. This suggests that the photochemical mechanism for methyl iodide production is very important and likely largely independent of direct biological influence due to little difference between the untreated and poisoned samples. It is possible that the determining factor in the photochemical mechanism is the concentration of DOC which will provide the methyl radical shown in ***Eq. 1.9***.

1.3.4 Sinks of Methyl Iodide

The major sinks of aqueous methyl iodide are atmospheric emission and nucleophilic substitution reactions with chloride anions, with a methyl iodide half-life of 19.7 days at 292 K and 58.4 days at 284 K (Zafiriou, 1975). These two sinks are roughly equal on average, at 230 for the atmospheric emission sink and 263 Gg yr^{-1} for the chloride reaction sink respectively, though may vary due to locational conditions like temperature and windspeed (Bell et al., 2002). In areas of low surface methyl iodide concentration a negative saturation anomaly can occur as observed by Happell and Wallace (Happell and Wallace, 1996), reintroducing methyl iodide to the aqueous phase. The model runs of Stemmler et. al. (2014) showed that regions of the ocean can act as both a source and sink of methyl iodide, with a common sink feature occurring in the high latitudes of the North Atlantic Ocean in wintertime. This reduction in production likely occurs due to the lower solar irradiation of higher

northern hemisphere latitudes during winter which reduces the photochemical production of methyl iodide. Photolysis of aqueous methyl iodide is not a major sink of methyl iodide (Zika et al., 1984).

The major sink of atmospheric methyl iodide is photolysis, the carbon-iodine bond in methyl is readily broken by UV radiation ***(Eq. 1.10)*** with a absorption maximum at 260 nm (Roehl et al., 1997).

$$CH_3I + hv \rightarrow CH_3 + I \quad (Eq. 1.10)$$

The marine atmospheric boundary layer lifetime of methyl iodide in the atmosphere due to photolysis is estimated as between 4-8 days (Montzka et al., 2011; Yvon-Lewis and Butler, 2002; Zafiriou, 1974b). At higher latitudes the lower levels of UV light lead to a longer lifetime of up to 2 weeks (Blake et al., 1999). Bell et. al. (2002) estimated the photolysis sink to be 304 Gg yr^{-1}. Oceanic uptake was found to be only a minor sink (Yvon-Lewis and Butler, 2002). The loss rate due to photolysis is an order of magnitude higher than loss due to reaction with hydroxyl radicals and two orders of magnitude higher than that due to chlorine atoms (Cotter et al., 2003).

1.3.5 Questions in Methyl Iodide Research

Methyl iodide emissions have been reported to be iodide dependent (Y. Chen et al., 2020; Moore and Zafiriou, 1994). Moore and Zafiriou measured coastal and open ocean water at natural iodide levels and when spiked by 2.3 µM but measured no values in between. Similarly, Chen et. al. spiked artificial seawater with 2 mg L^{-1} of humic acid and potassium iodide ranging from 420 nM to 4.23 mM. Both of these studies (Y. Chen et al., 2020; Moore and Zafiriou, 1994) measured iodide dependence of methyl iodide production outside of the natural range of iodide which has been measured as 28 – 140 nM (Chance et al., 2014). This means that there is no direct evidence of methyl iodide emissions being iodide dependent under natural conditions expected in the ocean. Models (Bell et al., 2002; Ordóñez et al., 2012) of methyl iodide emissions currently do not account for any iodide dependence of methyl iodide production.

1.4 Atmospheric Impacts of VOCs

Volatile organic compounds (VOCs), which oxygenated volatile organic compounds (OVOCs) are a subcategory of, are ubiquitous in the ocean and marine atmosphere (Davie-Martin et al., 2020; Wohl et al., 2020; Yu and Li, 2021). VOCs have been

shown to be produced in the marine environment through biological activity (Halsey et al., 2017), heterogeneous chemistry at the ocean surface (e.g. O_3) (Novak and Bertram, 2020) and photochemistry at the ocean surface (Zhou and Mopper, 1997). As VOCs are a broad category of compounds a select few compounds have been picked out for more detailed discussion.

VOCs in the atmosphere can react with hydroxyl radicals (OH), nitrate radicals (NO_3) or ozone (O_3) to be oxidised into OVOCs which are often more soluble or have a lower vapour pressure which leads to greater partition to the aerosol phase (Yu and Li, 2021). Marine aerosols can be formed through direct emission from the surface, sea spray aerosol (Chen et al., 2020), or from the chemical processing of gases, like OVOCs, and particles to form secondary organic aerosols (Hu et al., 2013). Sea salt aerosol can contain large fractions of organic matter due to organic content in the sea surface microlayer during formation and its chemical processing post formation (Cravigan et al., 2020; Bertram et al., 2018). Marine aerosols resulting from biological activity have been estimated to account for over half of the variability in Southern Ocean cloud droplet number concentrations (McCoy et al., 2015). Organic aerosols are one of the more uncertain components of the radiative balance of Earth (Stocker et al., 2013). The uncertainties are associated with both the SOA formation and the OVOC sources.

While sea spray aerosol is the major source of cloud condensation nuclei (CCN) (McCoy et al., 2015) Liu and Matsui (2022) determined that SOA formation contributes greater than 50 % of CCN concentrations in low background aerosol environments in the remote open ocean. Marine VOC emissions can play a role in controlling CCN size through condensing onto ultrafine particles (Burkart et al., 2017; Croft et al., 2021, 2019; Yu and Li, 2021). DMS is the largest VOC source of CCN in the remote marine boundary layer, with other important compounds being alkanes, alkenes, aromatics, terpenoids, amines, halogenated organics and OVOCs (Prank et al., 2022).

The impacts of some select VOCs are described in ***Sections 1.4.1 – 1.4.4.***

1.4.1 Atmospheric Impacts of Dimethyl Sulfide (DMS)

DMS in the atmosphere has a 1-2 day lifetime with respect to oxidation (Fung et al., 2022) by hydroxide (OH) or nitrate (NO_3) to produce sulfur dioxide (SO_2) and methyl sulfonic acid (MSA) (Boucher et al., 2003; Breider et al., 2010). H_2SO_4 can then produce new particles and CCN, particularly in the free troposphere (Charlson et al.,

1987; Clarke et al., 1998; Kulmala et al., 2000; Veres et al., 2020; von Glasow and Crutzen, 2004). These CCN can then be transported from the free troposphere back into the MBL which explains a significant fraction of the measured CCN (Kazil et al., 2006; Merikanto et al., 2009; Pierce and Adams, 2006; Spracklen et al., 2007). SO_2 can further oxidise to form sulfate (SO_4) which, alongside MSA, can impact aerosol size distribution and cloud microphysics when in the particle phase (Kaufman and Tanré, 1994). Woodhouse et. al (2013) showed that a 10 % increase in DMS flux would result in a 1 % global increase in CCN. DMS is produced through the cleavage of a metabolite found in a range of phytoplankton and macroalgae, dimethylsulfoniopropionate (DMSP) as well as bacterial degradation of DMSP (Novak and Bertram, 2020; Zeng et al., 2016). DMS has also been found be produced directly by phytoplankton (Dani and Loreto, 2017).

1.4.2 Atmospheric Impacts of Alkyl Nitrates

Alkyl nitrates make up a significant portion of NO_y mixing ratios in the remote marine boundary layer at 3 – 8 ppt (Neu et al., 2008). In the Western Pacific this can lead to a 250 % increase in NO_x abundance and a 20 % increase in the O_3 mixing ratio (Neu et al., 2008). Hydrolysis of alkyl nitrates can form nitrate aerosol through the production of NO_x that can further react to from nitrate (HNO_3) which can then partition into the aerosol phase (Rindelaub et al., 2015). Fisher et. al. (2018) found that alkyl nitrates account for 20 – 60 % of the reactive nitrogen in the Southern Ocean marine boundary layer and dominates the NO_x emissions.

Alkyl nitrates can be produced in surface seawater through the reactions of nitric oxide (NO) with peroxy radicals (Dahl and Saltzman, 2008). Peroxy radicals can be formed from the photolysis of chromophoric dissolved organic matter (CDOM) followed by reaction with dissolved oxygen ***(Eq. 1.11)*** (Kieber and Blough, 1990).

$$CDOM \xrightarrow{hv,O_2} ROO^{\cdot} \quad (Eq.1.11)$$

The produced peroxy radical then reacts with NO, which can be formed in seawater by the photolysis of nitrite (Zafiriou and McFarland, 1981; Zafiriou and True, 1979), to produce either alkyl nitrates or nitrogen dioxide ***(Eq. 1.12)*** (Dahl et al., 2003).

$$ROO + NO \rightarrow ROONO \rightarrow RONO_2 \ or \ RO + NO_2 \quad (Eq.1.12)$$

1.4.3 Atmospheric Impacts of Acetone

Acetone does not contribute much to SOA formation directly but its oxidation by OH can form methylgloxal, which itself is an important SOA precursor (Ge et al., 2017). Photolysis of acetone can increase the levels of HO_x (McKeen et al., 1997; Neumaier et al., 2014), with the acetone contribution to HO_x production peaking at 24 – 27 % in the subtropical upper troposphere and lower stratosphere (S. Wang et al., 2020). Acetone has been observed to be produced through both biological sources (Halsey et al., 2017; Schlundt et al., 2017), photochemical degradation of organic matter (Kieber et al., 1990; Zhou and Mopper, 1997; Zhu and Kieber, 2018) and heterogeneous oxidation of dissolved organic matter (DOM) (Ciuraru et al., 2015a; Zhou et al., 2014), though the photochemical and heterogeneous production account for between 48 - 100 % of the production rate (Dixon et al., 2013).

1.4.4 Atmospheric Impacts of Isoprene

Isoprene has a very fast reaction rate constant with OH of $1.00 \pm 0.15 \times 10^{-10}$ cm^3 $molecule^{-1}$ s^{-1} (Guenther et al., 2006). Under polluted atmospheric conditions isoprene can account for 20 % of the OH consumption (Lewis et al., 2001) and a study by Liakakou et. al. (2007) found that daytime isoprene concentrations reduced OH radicals by up to 26 % and hydroperoxyl (HO_2) radicals by 13 % while increasing peroxy radical concentration by a factor of four. Isoprene is also a minor contributor to particle formation (Claeys et al., 2004) with Arnold et. al. (2009) finding that oceanic isoprene contributed 0.01 – 1.4 % of observed organic carbon aerosol at remote marine sites in both Northern and Southern hemispheres. Isoprene has been observed in laboratory monoculture studies of marine phytoplankton with production rates dependent on the speciation, solar irradiation, temperature and nutrient loading (Booge et al., 2016; Dani and Loreto, 2017; Exton et al., 2013; Moore et al., 1994; Shaw et al., 2010).

1.5 Studies of VOC Emissions

Emissions of DMS vary due to local concentration, wind speed and water temperature (Carpenter et al., 2012). DMS emissions are estimated globally between 14.7 – 21.1 Tg C yr^{-1} (Galí et al., 2018; Kloster et al., 2006; Lana et al., 2011). Measurements of alkyl nitrates in the atmosphere have reported mixing ratios in the range of 25 – 80 pptv in the tropics and Antarctic (Blake et al., 1999; Fischer et al., 2002; Jones et al., 1999). Estimates of the marine flux of acetone into the atmosphere range from -2 to

-7.5 Tg yr^{-1} with a net sink in the northern and southern extra-tropics and net production in the tropics (Fischer et al., 2012; S. Wang et al., 2020; Yang et al., 2014).

Isoprene emissions parametrized by oceanic concentrations (bottom up) are estimated at 0.1 Tg C yr^{-1} and emissions from remote sensing (top down) are estimated at 12 Tg C yr^{-1} (Broadgate et al., 1997; Matsunaga et al., 2002). Further studies have shown marine fluxes of isoprene of 0.1 – 11.6 Tg C yr^{-1} (Arnold et al., 2009; Booge et al., 2016; Conte et al., 2020; Gantt et al., 2009; Hu et al., 2013; Luo and Yu, 2010; Palmer and Shaw, 2005; Sinha et al., 2007). Monoterpene emissions range from 0.01 (bottom up) to 29.5 (top down) Tg C yr^{-1} (Luo and Yu, 2010). During a fall 2013 campaign in the North Atlantic (Kim et al., 2017) mean sea-to-air fluxes were scaled up to global fluxes leading to 0.57 Tg C yr^{-1} for isoprene and 0.60 Tg C yr^{-1} for monoterpenes.

Lewis et. al. (2005) found that under maritime conditions at Mace Head, Ireland, OVOCs including methanol, acetaldehyde and acetone together contributed up to 80 % of the estimated OH radical sink. Read et. al. (2012) found that, compared to the no OVOC case, the inclusion of these OVOCs led to an approximately 40 % reduction in the modelled OH radical concentration in the Eastern Tropical Atlantic.

Mungall et. al. (2017) used on-line high-resolution time-of-flight mass spectrometry with acetate ionisation, a technique particularly useful for measuring organic acids. Observations in the summertime Arctic detected up to 4 ppbv of formic acid, 10 pptv of isocyanic acid and several other compounds that they identified as oxo-acids. A series of oxo-acids from C_4 - C_{11} was detected but not quantified. They also calculated an Ocean Factor (OF) as a function of the unassigned mass of OVOCs detected by the instrument. The OF factor was highest in the absence of long range transport, when DOC was abundant and when the solar radiation was greatest. This combined strongly suggests a surface microlayer source for the bulk of the OF species through either photochemistry or heterogeneous chemistry (e.g., O_3).

Schneider et. al. (2019) specifically measured the C_1 – C_{10} carbonyl compounds from *T. pseudonana* phytoplankton cultures in SML samples collected using a glass microscope slide and squeegee. Samples were measured under standard air and under 30 ppb O_3 and compared using the value in the culture growth media as a blank. The measurements after exposure to O_3 showed a statistically significant

increase in the emissions of C1 (formaldehyde), C5 and C7 – C10 carbonyl compounds and a statistically significant reduction in the emission of C2 (acetaldehyde) compared to measurements under standard air. Schneider et. al. (2019) rationalised this reduction in acetaldehyde as being due to emissions previously detected in PTR-MS measurements of the growth media, likely due to organic contaminants (Kameyama et al., 2011). However, they detect 76 ppb of acetaldehyde in their SML sample headspace without O_3 compared to only 25 ppb in the L1 growth media headspace, suggesting that production of acetaldehyde is occurring in the SML sample itself.

Zhou et. al. (2014) measured the products of ozonolysis of linoleic acid, a fatty acid commonly used as an SML mimic using PTR-MS. They found four major products; n-hexanal, 3-nonenal, malondialdehyde and glyoxal. Of the four products, hexanal was the major product at 75 – 79 % of the gas phase aldehyde yield under conditions of 85 – 150 ppbv O_3. Only slight variations in the aldehyde distribution were observed under increased O_3 mixing ratios or variability in the moles of linoleic acid consumed. The formation of malondialdehyde and glyoxal is a result of further ozonolysis of 3-nonenal.

Ciuraru et. al. (2015b) measured OVOC emissions from the photolysis of a real SML sample spiked with 30 mg L^{-1} of humic acid to mimic the presence of DOM in the subsurface water. From real SML samples they measured 9 - 10 pptv each of the C_5 – C_8 unsaturated carboxylic acids, 30 – 100 pptv each of the C_6 – C_9 alkanes, 10 – 50 pptv each of C_6 – C_9 alkenes, 20 – 40 pptv each of the C_6 – C_8 dienes and 10 pptv of benzene. They also measured emissions from the photolysis of nonanoic acid, another SML mimic. They found similar compounds being emitted, but more of the lower molecular weight compounds like butenoic acid and pentene were measured and other at lower concentrations were able to be detected.

Bruggeman et. al. (2017) performed measurements of VOC emissions from biofilms and autoclaved water by photochemical processing. They found that the flux from the photolysis of an autoclaved dead cell sample was 3-6 times greater than the next greatest flux which was achieved from the photolysis of a 6 day live biofilm. The ketene emissions increased from 0.100 μmol m^{-2} d^{-1} in the photolysis of the 6 day biofilm sample to 0.301 μmol m^{-2} d^{-1} in the photolysis of the autoclaved sample, a three-fold increase. A similar pattern was seen for acetaldehyde which was emited 1.38 μmol m^{-2} d^{-1} from photolysis of the 6 day biofilm sample compared to 4.64 μmol m^{-2} d^{-1} from the photolysis of the autoclaved sample, an over three-fold increase.

These large emissions show that photolysis of living organic matter can sometimes act to suppress the maximum possible flux that can be achieved on cell death of the species. Bruggeman et. al. (2017) suggest that the production of VOCs generally attributed to high biological activity may be due to a mixture of biological activity and abiotic photochemistry of both live and dead cells in surface waters.

1.5.1 Questions in VOC Emissions Research

Model runs by Mao et. al. (2009) routinely underpredict the OH reactivity in the atmosphere. During the INTEX-B campaign over the Pacific Ocean the median measured OH reactivity was 4.0 ± 1.0 s^{-1} which is higher than the steady state assumption of OH reactivity (3.3 ± 0.8 s^{-1}) and that calculated from the total measurements of OH reactants (1.6 ± 0.4 s^{-1}). A suggestion given for this was that the model is missing OH sinks that Mao et. al. assumed to be highly reactive VOCs that could oxidise to form formaldehyde. Travis et. al. (2020) determined that 340 TgC yr^{-1} of $>C_4$ alkanes were needed to account for the missing OH reactivity, much larger than their model predicted total VOC source of 28.3 TgC yr^{-1}. Donahue and Prinn (1990) also modelled that a range of 1 $x10^{10}$ – $2x10^{11}$ molecules cm^{-2} s^{-1} air-sea flux of non-methane hydrocarbons were required to model the atmospheric OH concentration in the remote marine boundary layer. These studies (Donahue and Prinn, 1990; Mao et al., 2009; Travis et al., 2020) all suggest a large missing VOC component as a cause for the underprediction of the OH reactivity in the marine atmosphere. Thames et. al. (2020) found that the missing OH reactivity correlated with formaldehyde, DMS, butanal and sea-surface temperature which suggested potentially VOC compounds were associated within the unknown reactivity. It is possible that some lower concentration VOCs that are not currently investigated could provide some of this unknown OH reactivity which is why measurements of the maximum range of VOCs possible is of importance.

Modelling studies of the marine atmosphere have suggested that there is a missing source of organic aerosols (Heald et al., 2006, 2005; Roelofs, 2008; Spracklen et al., 2008). Some studies (Gantt et al., 2009; Meskhidze and Nenes, 2006; Roelofs, 2008) have suggested that isoprene can account for the part of the missing source but they cannot account for the entirety of the missing source. Models give a wide range of values for the ocean contribution to the organic fraction of marine aerosol of between 8 and 40 TgC yr^{-1} (Spracklen et al., 2008; Thames et al., 2020). It is possible that

some of this missing source could be made up from a range of oxidation products of VOC emissions that not currently be modelled specifically.

A review of the literature by Novak and Bertram (2020) has suggested that a significant uncertainty remains in the scaling of laboratory observation of VOC production to ambient atmosphere conditions. This provides a clear area of research to identify and quantify the emissions of VOCs under ambient conditions in laboratory studies and confirm these measurements in field studies to allow for greater accuracy in modelling to address the underprediction of organic aerosols and OH reactivity in the marine atmosphere.

2. Selected Ion Flow Tube – Mass Spectrometry (SIFT-MS) Study of H_3O^+, NO^+ and O_2^+ with a Range of Oxygenated Volatile Organic Carbons (OVOCs)

Derived from paper published in the International Journal of Mass Spectrometry
https://doi.org/10.1016/j.ijms.2022.116892

2.1 Introduction

In this chapter the selected ion flow tube-mass spectrometer (SIFT-MS) was calibrated for a range of oxygenated volatile organic compounds (OVOCs) to assess the capability of CIMS to measure OVOCs under both dry and wet conditions. Some measurements of compounds for a few weeks at the beginning of the covid lockdown were co-measured, with Marvin Shaw, Stephen Andrews and Stuart Young operating the permeation oven in the lab while I operated the instrument remotely from home.

2.1.1 Introduction to SIFT-MS

SIFT-MS is a soft chemical ionisation mass spectrometry method that can quickly switch between reagent ions to allow analyses of a wide range of potential target compounds and high selectivity for compound discrimination (Smith and Španěl, 2005). It enables real time detection and quantification of complex mixtures such as ambient air that would be much more challenging using conventional electron ionisation mass spectrometry due to its higher energy causing greater fragmentation, leading to more complex and potentially unreadable spectra. Several studies have reported field measurements of atmospheric VOCs by SIFT-MS. Prince et. al. (2010) measured toluene, 1,3-butadiene, benzene, ethanol and ethene in ambient air in suburban Christchurch, New Zealand, finding mixing ratios from high ppt to low ppb levels, and were able to suggest common sources of certain compounds due to the consistent real time sampling. Wagner et. al. (2021) measured a suite of VOCs from a mobile van on a road circuit through York, UK, allowing for highly resolved temporal and spatial measurements and identifying hotspots of specific compounds. Hien et. al. (2022) measured 22 VOCs in Hanoi, Vietnam, in March 2019 demonstrating that the VOC mix was dominated by OVOCs (43 %) and alkanes (14%). These studies (Hien et al., 2022; Prince et al., 2010; Wagner et al., 2021) illustrate the utility of a real time system like SIFT-MS for performing atmospheric measurements.

In SIFT-MS, a microwave ion-source fed by humid air is used to generate a mixture of positive ions (Španěl et al., 2017). These include the primary reagent ions H_3O^+, NO^+ and O_2^+ which are individually selected by an upstream quadrupole **(Figure 2.1)** to produce a stream of specific reagent ions. These ions are injected into an inert carrier gas (helium or nitrogen) through a Venturi orifice. The reagent ion stream travels through a heated flow tube for a set distance before being introduced to the sample flow which is injected into the flow tube perpendicular to the reagent ion flow.

Reactions occur through the remainder of the flow tube (which can be of various geometries, here it bends 90 degrees). Note that reactions effectively stop at the end of the flow tube due to the pressure drop into either the ion guide (if present) or the downstream quadrupole The downstream quadrupole can be set to either scan through an *m/z* range or transmit specific *m/z* ions which correspond to the product ions of the analyte. These individual *m/z* ions are then detected by a particle multiplier and pulse counting system. A simplified schematic of the instrument is shown in ***Figure 2.1***. The instrument has been described in detail by Prince et. al. (2010).

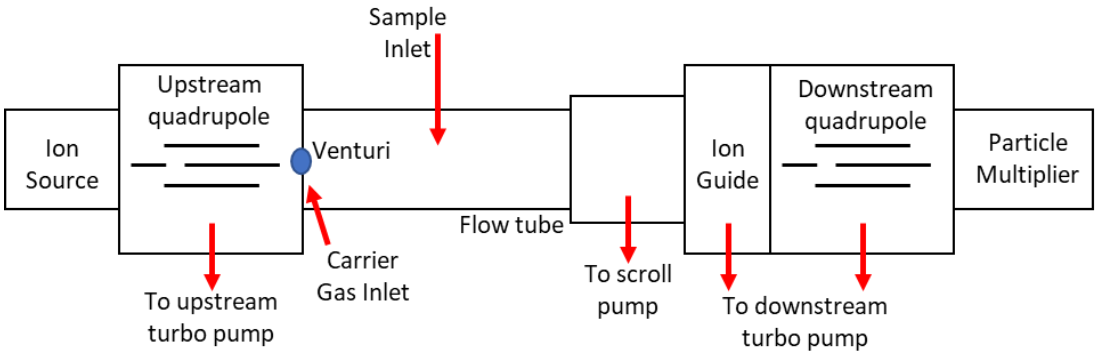

Figure 2.1 – *A basic schematic of the Voice200ultra model of the SIFT-MS instrument produced by Syft Technologies Ltd. Note the flow tube has a 90 degree curve not shown in this schematic.*

2.1.2 SIFT-MS Studies of Benzene and OVOCs

Ionisation rate constants of a range of compounds reacting with different reagent ions have been measured using SIFT-MS. Many of these studies were performed by Smith and Španěl (1997) in the late 90s and are still used. Smith and Španěl (1997) utilised the fact that proton transfer, when exothermic, generally proceeds at or very close to the collision limited rate constant, k_C. This allowed them to use the calculated k_C as a proxy for the H_3O^+ rate constant. Experimental NO^+ and O_2^+ rate constants were typically derived by introducing a known concentration of the target analyte into a plastic bag, sampling this into the instrument and then observing the decay curves of all three reagent ions simultaneously as a function of flow rate. The gradients of the NO^+ and O_2^+ reagent ions were then used to calculate the rate constants relative to the H_3O^+ rate constant. These experiments were performed on pre-commercial research instruments.

Recent work by Španěl et. al. (2017) utilised the vapour headspace of a bottle mixture of alcohols in water to measure the impacts of humidity on the product ion formation of the system. This was performed on a Profile 3 SIFT-MS (Profile 3, Instrument Science Limited, Crewe, UK) using helium as a carrier gas at a temperature of 27 °C

and a pressure of 1 Torr. This temperature is much lower than the factory pre-set tube temperature in the Voice200*ultra* (Voice200*ultra*, Syft Technologies, Christchurch, NZ) instrument produced by Syft Technologies of 120 °C. The Španěl et. al. (2017) study did not attempt to measure rate constants and was only focused on determining the impact of humidity on the product ions of the reaction. The study found major impacts from humidity at this low flow tube temperature, with methanol and propanol exhibiting double clustering, forming $MH^+(H_2O)_2$ ions, where M represents the alcohol. At an absolute sample humidity of 3.5 % the double clustering ion accounted for 50 % of the methanol and 40 % of the propanol total ion counts, with the singular water cluster accounting for 30 % of the methanol and 10 % of the propanol total ion counts. This means that the dry product ion count for methanol was only 20 % at 3.5 % sample humidity.

It is important to note that most rate constant data have been measured using helium as the carrier gas. As global helium supplies become increasingly scarce, more users will start moving towards nitrogen as a cheap and renewable alternative carrier gas. The depleting supply of helium is compounded by leaks and fires that have caused recent unplanned shutdowns of helium processing plants (Bettenhausen and Jansen, 2022; Kramer, 2022). The recent war in Ukraine has also increased concern regarding the supply of helium from Russia (Bettenhausen and Jansen, 2022; Kramer, 2022). This presents problems for some applications of SIFT-MS as the library of compounds measured in nitrogen is much smaller. One issue with nitrogen as a carrier gas compared to helium is that the energy in the system is higher, particularly when energetic collisions are encouraged by voltage gradients during injection or extraction, meaning that the H_3O^+ ions can collide with N_2 molecules to form fragment ions like $H_2O^{+\bullet}$ and OH^+ which can potentially alter the ion chemistry in the instrument (Smith et al., 2020). Also, at a pressure of 0.5 mbar and room temperature, the N_2 carrier gas readily forms adducts such as $H_3O^+N_2$ which is a catalyst to water clustering (Smith et al., 2020). The formation of water clusters can be mitigated by increasing the temperature of the carrier gas (Ghislain et al., 2019). Nitrogen also has a higher efficiency for collisional cooling than helium (Cates and Bowers, 1980), which means adduct product ions are favoured in nitrogen compared to helium. The importance of developing the database for measurements in N_2 carrier gas was recently emphasized by Smith et. al. (2020).

In this work, the rate constants, product ions and branching ratios of the reaction of SIFT-MS reagent ions with a range of OVOCs were measured with nitrogen as the carrier gas. The measurement of benzene was used as a standard to evaluate the accuracy of the data as benzene is a well characterised compound in SIFT-MS. To minimize water clustering, the measurements in this study are made at a flow tube temperature of 140 ^{o}C, much higher than the 27 ^{o}C temperatures of previous studies (Smith et al., 2003; Španěl et al., 2002; Španěl et al., 1997, 1995; Španěl and Smith, 1997; Španěl and Smith, 1998), and 20 ^{o}C higher than the standard operating temperature of the Voice200*ultra*.

2.2 Methodology and Experimental Work

2.2.1 Calibration and Permeation Tube Methodology

Permeation tubes are commonly used to deliver stable concentrations of compounds for calibration (Mitchell, 2000; Saltzman et al., 1971). Permeation tubes are useful for calibration of trace gases as many exist in the liquid phase under standard conditions. In this work, permeation tubes were made from ¼" PTFE tubing with an internal diameter of 5.8 mm (wall thickness of 0.275 mm) with either brass or stainless-steel Swagelok fittings as caps. An 8 cm length of tubing was used, when including the Swagelok fittings this gave an approximately 5 cm permeation window.

All chemicals were obtained from Sigma-Aldrich, except for butanal which was purchased from Merck, and had the following purities: benzene (≥99 %), butanal (99 %), 2-butenal (≥99.5 %), 2-butanone (≥99.9 %), hexanal (98 %), 2-hexenal (98 %), 2-octanone (98 %), 2-pentanone (≥98 %), 1-propanol (99.7 %) and nonanal (99 %). These compounds were chosen as they have been identified as potentially significant atmospheric emissions from the surface of seawater (Schlundt et al., 2017; Vichi et al., 2021; N. Wang et al., 2020; Yang et al., 2014; Zhou et al., 2014).

A certified gas standard (National Physics Laboratory, NPL) containing a mixture of 14 gases was also used for verification of some measurements; methanol (1.03 ± 0.10 ppm), ethanol (0.99 ± 0.05 ppm), acetonitrile (1.02 ± 0.03 ppm), acetone (1.01 ± 0.05 ppm), isoprene (1.01 ± 0.05 ppm), butenone (1.03 ± 0.05 ppm), 2-butanone (1.01 ± 0.05 ppm), benzene (1.03 ± 0.03 ppm), toluene (1.04 ± 0.03 ppm), m-xylene (1.02 ± 0.05 ppm), 1,2,4-trimethylbenzene (1.02 ± 0.03 ppm), 1,3-butadiene (1.04 ± 0.03 ppm), n-octane (1.02 ± 0.05 ppm), n-nonane (1.01 ± 0.10 ppm), n-decane (1.01 ± 0.10 ppm) and n-dodecane (1.00 ± 0.05 ppm).

Figure 2.2 shows the experimental setup that was used for all SIFT-MS experiments. The permeation oven temperatures were individually controlled by temperature controllers (6100+, West Control Solutions, Gurnee, IL, USA). The nitrogen gas was generated by a Nitrogen Generator (Infinity NM32L, Peak Scienific, Inchinnan, UK). When measuring from the calibration gas cylinder (NPL) the cylinder was attached at the same T-junction that the permeation oven outlet attaches to during normal measurement. The permeation oven was unattached during these calibration cylinder measurements.

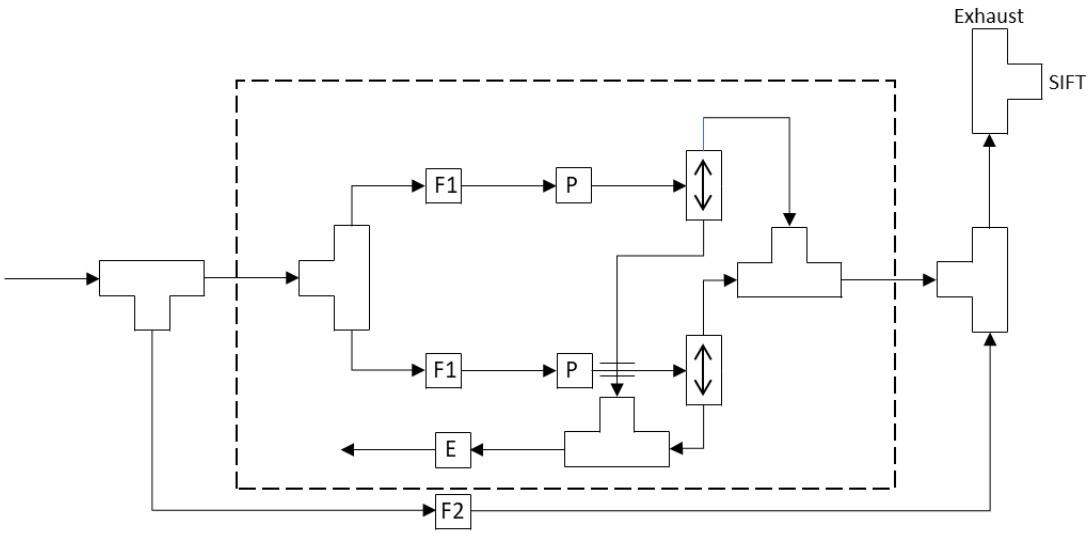

Figure 2.2 – *The permeation tube calibration system. F1 are 100 sccm mass flow controllers (FC-280SA, Tylan, and 1179A, MKS Instruments, Andover, MA, USA), F2 is a 0-10 slpm (standard litres per minute) mass flow controller (10-SLPM-D, Alicat Scientific, Tucson, AZ, USA) which controls diluent flow, P are permeation ovens, E is an exhaust filter and the dashed box shows the permeation oven casing.*

For humid scans, the flow setup had to be modified to allow the diluent to flow through a dew-point generator (DG3, Michell Instruments, Ely, UK). This was placed in between the mass flow controller F2 and the t-piece seen in ***Figure 2.2***. This allowed a flow with a relative humidity of up to 100 % to be generated, which was then diluted by the introduction of the permeation flow. The flow rates through F2 and the humidity generator were variable, between 0.05 and 1.00 sccm (standard cubic centimetres), allowing for the humidity to be altered. Humid scans were performed identically to a full mass scan, only with a humid diluent flow rather than a dry diluent flow. The scans were performed over a range of diluent flows.

Each permeation tube was weighed approximately every fortnight over a period of at least six months, with each weighing repeated 3 times to ensure a stable value. The permeation rate of each compound was calculated as the ratio of the gradient of the mass loss over time divided by the molecular mass of the given compound. This was then converted directly into a concentration by choosing a standard exposure time

and the mixing ratio calculated by dividing this concentration by the moles of carrier gas passed through the permeation oven in the given exposure time.

2.2.2 SIFT-MS Operating Conditions

The Voice200*ultra* was operated with two major changes from the standard operating conditions. Firstly, the flow tube temperature was 20 °C higher than operationally recommended by the manufacturer and over 100 °C higher than the flow tube temperature used in older literature by Smith and Španěl. This was done to reduce water clustering during high humidity measurements.

Secondly, the lens voltages in the SIFT-MS in this study have been tuned to improve the sensitivity of the instrument. These same lens voltages were used by Wagner et. al. (2021) in their study. The major change from the lens voltages adopted for atmospheric measurements in this study, compared to those of a standard Voice200*ultra*, is an increase of the upstream FT voltage from 25 V to 50 V. The lens voltages were increased in order to increase transmission of ions through the flow tube. However, this change, and other minor changes to other lenses, affects the ion energetics of the instrument.

Experiments were performed at a range of flow tube temperatures (38 °C, 120 °C and 140 °C) and flow tube voltages (25 V and 50 V) under both dry and humid conditions to ascertain the impacts on both sensitivity and product ion chemistry. Due to the curve of the flow tube in the Voice200*ultra*, the flow tube voltage could not be reduced to 0 V as used in other SIFT-MS instruments as a small flow tube voltage is required to guide the reagent and product ions through the flow tube.

The SIFT-MS responses to benzene, butanal and butanone over the six combinations of flow tube temperatures and voltages were tested. All experiments were performed with a nitrogen carrier gas flow rate of 172 ± 4 sccm with a sample inlet flow rate of 25 sccm. This meant the sample flow was always 14-15 % of the total flow through the instrument. For the production of reagent ions it was found that, under dry conditions, the increase of temperature gradually reduced the overall H_3O^+ reagent ion count by reducing the $H_3O^+.H_2O$ ion count with no large impact on the reagent ion counts for NO^+ or O_2^+. The increase in voltage caused an increase in the proportion of the H_3O^+ reagent ion in the H_3O^+ channel without reducing the overall reagent ion count but did reduce the reagent ion count in the NO^+ channel by 15 % and in the O_2^+ channel by 10 %.

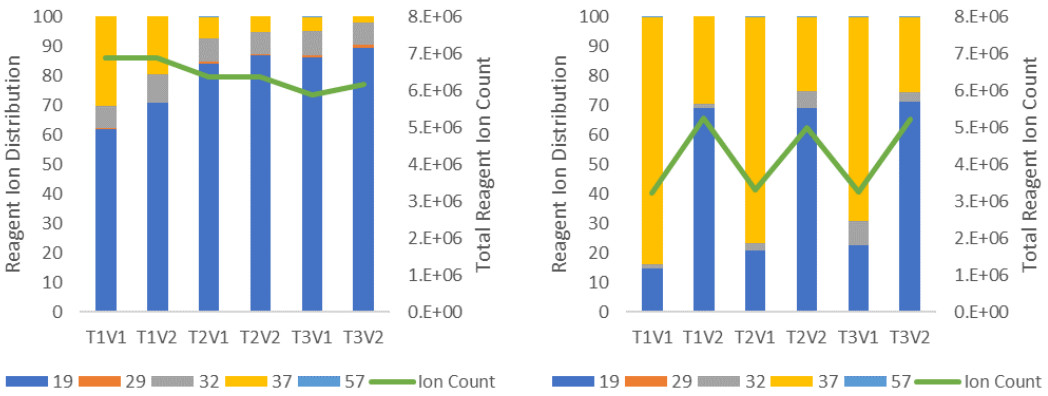

Figure 2.3 – *H_3O^+ reagent ion counts and distribution under dry (left) and humid conditions (right). The temperatures and voltages are denoted by the column labels, where T1 = 38 °C, T2 = 120 °C, T3 = 140 °C, V1 = 25 V and V2 = 50 V. The identities of the ions are 19 = H_3O^+, 29 = N_2H^+, 32 = O_2^+, 37 = $H_3O^+.H_2O$ and 57 = $H_3O^+.(H_2O)_2$.*

Under humid conditions (sample flow of roughly 100 % relative humidity) the increase in temperature had little impact on the total ion count in the H_3O^+ and NO^+ channel and increased the ion count of the O_2^+ channel. The increase in temperature slightly increased the proportion of H_3O^+ to $H_3O^+.H_2O$ in the H_3O^+ channel ***(Figure 2.3)*** and the proportion of the O_2^+ reagent ion in the O_2^+ channel ***(Figure 2.5)***. Increasing the temperature did introduce slight fragmentation in the NO+ channel ***(Figure 2.4)***, but no more than under dry conditions. Increasing the flow tube voltage caused a large increase in the H_3O^+ channel ion count, both increasing the total and percentage of the H_3O^+ reagent ion in the H_3O^+ channel as shown in ***Figure 2.3***. The increased voltage also caused a slight reduction in the NO^+ ion count and a large increase in the O_2^+ reagent ion count in the O_2^+ channel, associated with an increase of H_3O^+ reagent ion in the O_2^+ channel.

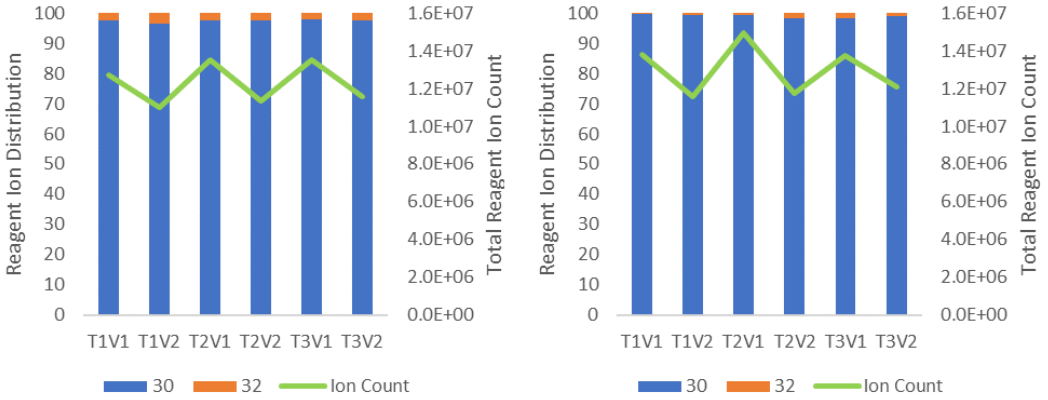

Figure 2.4 – *NO^+ reagent ion counts and distribution under dry (left) and humid conditions (right). The temperatures and voltages are denoted by the column labels, where T1 = 38 °C, T2 = 120 °C, T3 = 140 °C, V1 = 25 V and V2 = 50 V. The identities of the ions are 30 = NO^+ and 32 = O_2^+.*

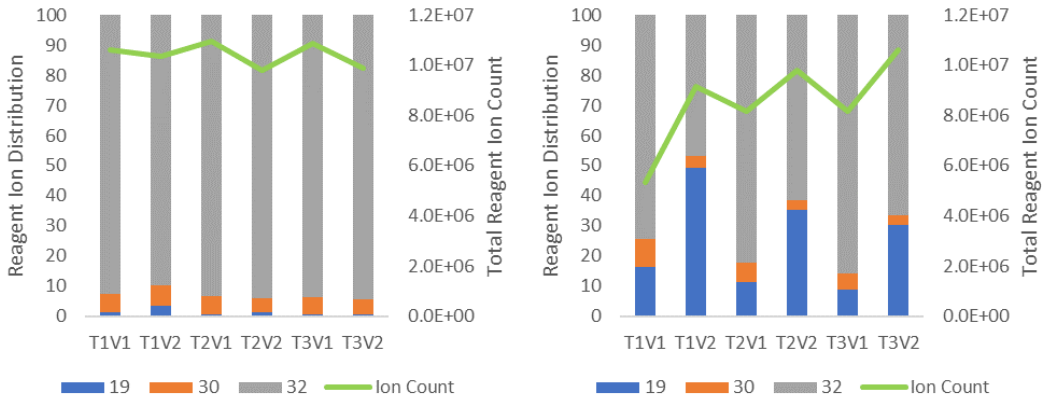

Figure 2.5 – *O_2^+ reagent ion counts and distribution under dry (left) and humid conditions (right). The temperatures and voltages are denoted by the column labels, where T1 = 38 °C, T2 = 120 °C, T3 = 140 °C, V1 = 25 V and V2 = 50 V. The identities of the ions are 19 = H_3O^+, 30 = NO^+ and 32 = O_2^+.*

Under dry conditions the increase in temperature caused a consistent decrease in sensitivity. The increase of the flow tube voltage in dry conditions caused little change in the sensitivity of benzene ***(Figure 2.6)*** and butanal ***(Figure 2.7)*** but a large decrease in the sensitivity of butanone ***(Figure 2.8)***, attributed to a large drop in the NO^+ sensitivity. This is likely due to increased energy being unfavourable to adduct formation reactions, the major product ion of ketones with NO^+. Under humid conditions, increasing the temperature decreased the sensitivity of benzene ***(Figure 2.6)*** but led to an increase in sensitivity of both butanal ***(Figure 2.7)*** and butanone ***(Figure 2.8)***. Increasing the voltage caused no real change in the sensitivity of benzene but increased the sensitivity of butanal and again decreased the sensitivity of butanone. The decreased butanone sensitivity is again driven by a loss of NO^+ sensitivity but, like with the butanal, is accompanied by an increased H_3O^+ sensitivity.

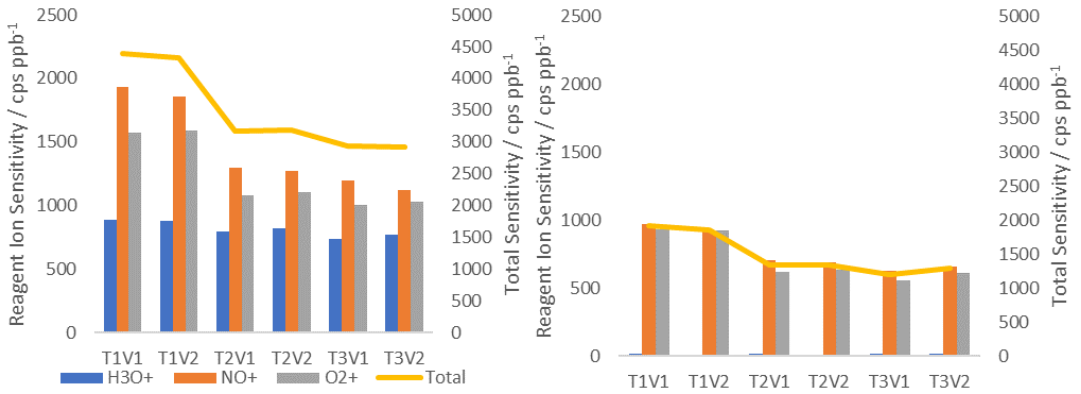

Figure 2.6 – *Sensitivity of the instrument to benzene across all reagent ion channels under dry (left) and humid conditions (right). The temperatures and voltages are denoted by the column labels where T1 = 38 °C, T2 = 120 °C, T3 = 140 °C, V1 = 25 V and V2 = 50 V. The sensitivity reported is a combined sensitivity for all measured product ions.*

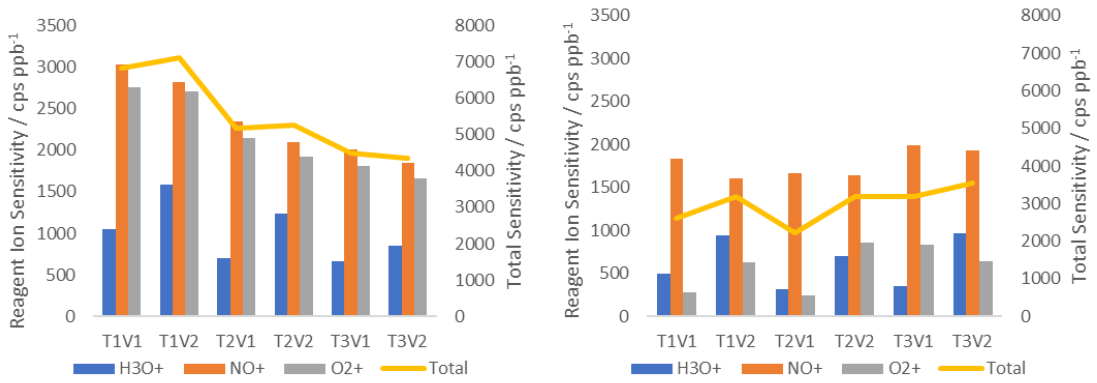

Figure 2.7 – *Sensitivity of the instrument to butanal across all reagent ion channels under dry (left) and humid conditions (right). The temperatures and voltages are denoted by the column labels where T1 = 38 °C, T2 = 120 °C, T3 = 140 °C, V1 = 25 V and V2 = 50 V. The sensitivity reported is a combined sensitivity for all measured product ions.*

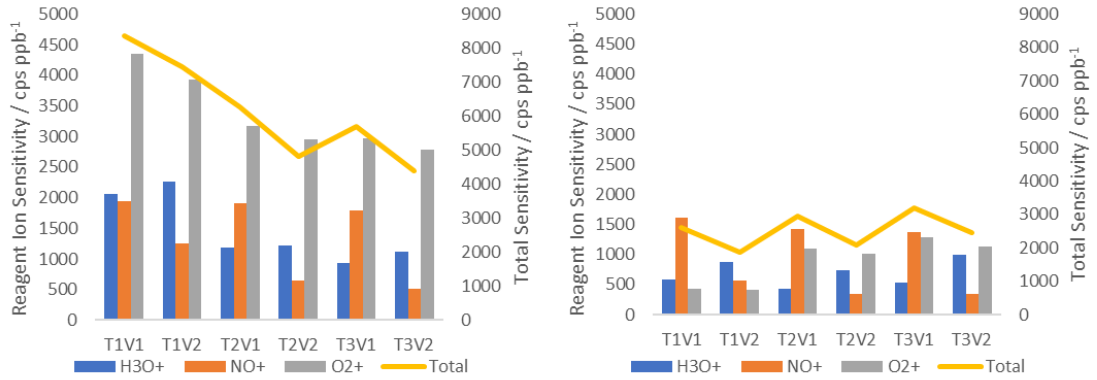

Figure 2.8 – *Sensitivity of the instrument to butanone across all reagent ion channels under dry (left) and humid conditions (right). The temperatures and voltages are denoted by the column labels where T1 = 38 °C, T2 = 120 °C, T3 = 140 °C, V1 = 25 V and V2 = 50 V. The sensitivity reported is a combined sensitivity for all measured product ions.*

For benzene, increasing the temperature reduced the charge transfer product ion under dry conditions in the H_3O^+ channel ***(Figure 2.9)*** by around 1.2 % between 38 °C and 120 °C and around 0.3 % between 120 °C and 140 °C. Increasing the flow tube voltage also reduced the charge transfer product by around 0.4 %. Under humid conditions only the proton transfer product was observed and so there was no impact from the change in temperature or flow tube voltage.

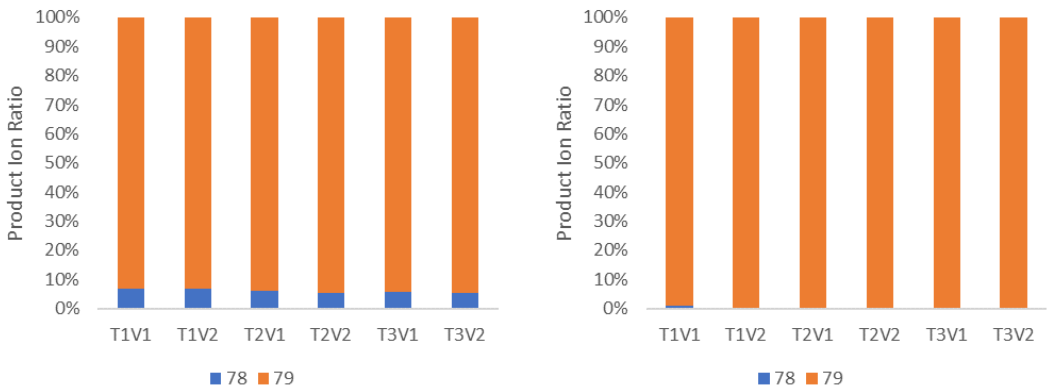

Figure 2.9 – *The product ion ratios of the H_3O^+ reagent ion channel of benzene under dry (left) and humid conditions (right). The temperatures and voltages are denoted by the column labels where T1 = 38 °C, T2 = 120 °C, T3 = 140 °C, V1 = 25 V and V2 = 50 V. The identities of the ions are 78 = $C_6H_6^+$ and 79 = $C_6H_7^+$.*

In the NO^+ channel ***(Figure 2.10)***, increasing the temperature greatly decreased adduct formation, reducing the *m/z* 108 ion by 11.6 % between 38 °C and 120 °C, 13.5 % under humid conditions, and 2.5 % between 120 °C and 140 °C, 2.8 % under humid conditions. Increasing the flow tube voltage also reduced adduct formation by around 22.4 % under dry conditions and 27.8 % under humid conditions. The only O_2^+ product ion measured was the charge transfer product so there were no observed impacts from the change in temperature and flow tube voltage.

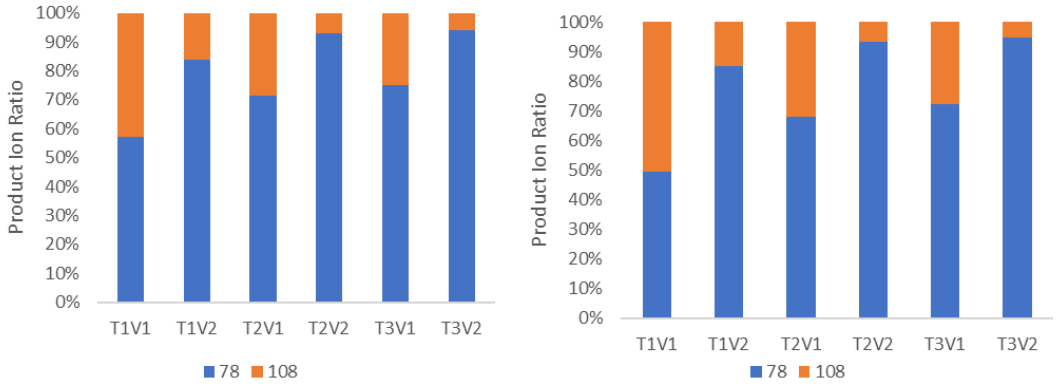

Figure 2.10 – *The product ion ratios of the NO^+ reagent ion channel of benzene under dry (left) and humid conditions (right). The temperatures and voltages are denoted by the column labels where T1 = 38 °C, T2 = 120 °C, T3 = 140 °C, V1 = 25 V and V2 = 50 V. The identities of the ions are 78 = $C_6H_6^+$ and 108 = $C_6H_6.NO^+$.*

For butanal in the H_3O^+ channel ***(Figure 2.11)***, increasing the temperature caused a noticeable increase in water loss and fragmentation, increasing the amounts of *m/z* 43 and *m/z* 55 relative to the measured amount of *m/z* 73, the charge transfer ion, under dry conditions. A humid product ion, *m/z* 91, was also observed at T1V1 but was not present at higher temperatures, but under humid conditions appeared at all 25 V temperatures. The humid product ion disappeared under the 50 V regime. The largest difference, both under dry and humid conditions, was the increase in the water

loss product ion, *m/z* 55, caused by the increased flow tube voltage. The increase of *m/z* 55 was 47.2 % under dry conditions and 70.1 % under humid conditions.

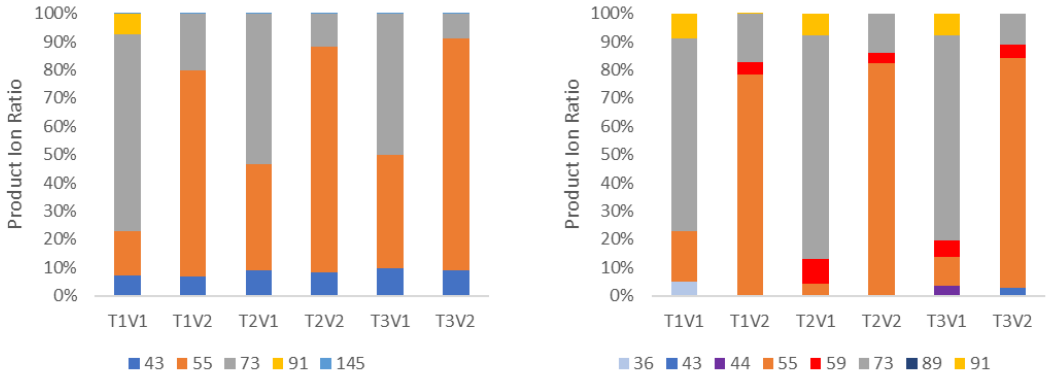

Figure 2.11 – *The product ion ratios of the H_3O^+ reagent ion channel of butanal under dry (left) and humid conditions (right). The temperatures and voltages are denoted by the column labels where T1 = 38 °C, T2 = 120 °C, T3 = 140 °C, V1 = 25 V and V2 = 50 V. The identities of the ions are 36 = C_3^+, 43 = $C_3H_7^+/C_2H_3O^+$, 44 = $C_3H_8^+/C_2H_4O^+$, 55 = $C_4H_7^+$, 73 = $C_4H_9O^+$, 89 = $C_4H_7O^+.H_2O$, 91 = $C_4H_9O^+.H_2O$ and 145 = $C_4H_9O^+.C_4H_8O$.*

In the NO^+ channel ***(Figure 2.12)***, increasing the temperature caused a small increase in the fragmentation ion, *m/z* 43, compared to the hydride abstraction ion, *m/z* 71, at about 6.4 % between 38 °C and 120 °C and 2.3 % between 120 °C and 140 °C under dry conditions. Under humid conditions this increase was 27.0 % between 38 °C and 120 °C and 2.4 % between 120 °C and 140 °C. Under humid conditions a humid product ion is observed, *m/z* 89, at around 43.0 % at 38 °C, this is greatly reduced with increased temperature, down to 7.5 % at 120 °C and 4.8 % at 140 °C, but is not affected by the change in flow tube voltage.

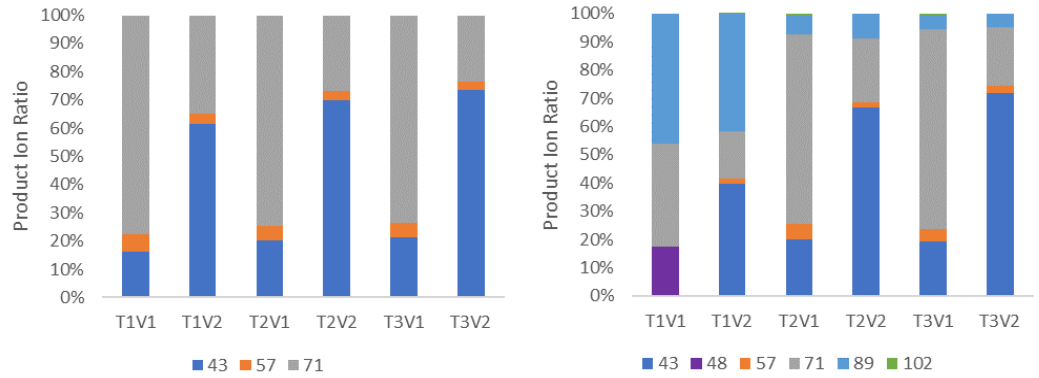

Figure 2.12 – *The product ion ratios of the NO^+ reagent ion channel of butanal under dry (left) and humid conditions (right). The temperatures and voltages are denoted by the column labels where T1 = 38 °C, T2 = 120 °C, T3 = 140 °C, V1 = 25 V and V2 = 50 V. The identities of the ions are 43 = $C_3H_7^+/C_2H_3O^+$, 48 = C_4^+, 57 = $C_3H_5O^+$, 71 = $C_4H_7O^+$, 89 = $C_4H_7O^+.H_2O$ and 102 = $C_4H_8O.NO^+$.*

In the O_2^+ channel ***(Figure 2.13)***, increasing the temperature had little effect on the product ion distribution under dry conditions, though increasing the flow tube voltage increased the amount of fragment ions, *m/z* 43 and *m/z* 57, at the expense of the fragment ion, *m/z* 44, and the charge transfer ion, *m/z* 72. Under humid conditions

the product ion distribution became more complex, increasing the flow tube voltage from 25 V to 50 V produced a new major fragment ion, *m/z* 55, which decreased with increasing temperature. The 25 V product ions were quite sporadic and showed no real trend with increasing temperature, possibly as the sensitivity at lower temperature 25 V settings was so low that some fragment ions were below the quantitation limit.

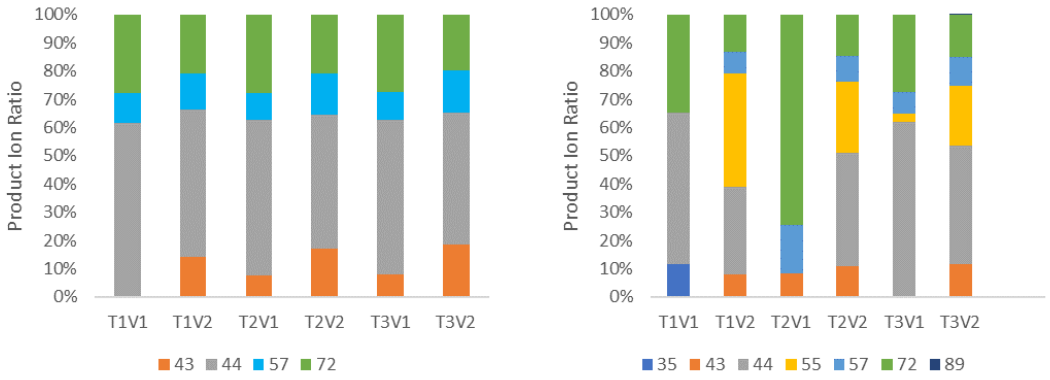

Figure 2.13 – *The product ion ratios of the O_2^+ reagent ion channel of butanal under dry (left) and humid conditions (right). The temperatures and voltages are denoted by the column labels where T1 = 38 °C, T2 = 120 °C, T3 = 140 °C, V1 = 25 V and V2 = 50 V. The identities of the ions are 35 = Unknown, 43 = $C_3H_7^+/C_2H_3O^+$, 44 = $C_3H_8^+/C_2H_4O^+$, 55 = $C_4H_7^+$, 57 = $C_3H_5O^+$, 72 = $C_4H_8O^+$ and 89 = $C_4H_7O^+.H_2O$.*

For butanone in the H_3O^+ channel ***(Figure 2.14)*** there was little variation with both increasing temperature and flow tube voltage. Under dry conditions the proton transfer product ion, *m/z* 73, made up at least 90 % of the product ion distribution and under humid conditions made up at least 98 % of the product distribution. A humid product ion, *m/z* 91, was observed at T1V1, both dry and humid, and fragment ions were observed under dry conditions.

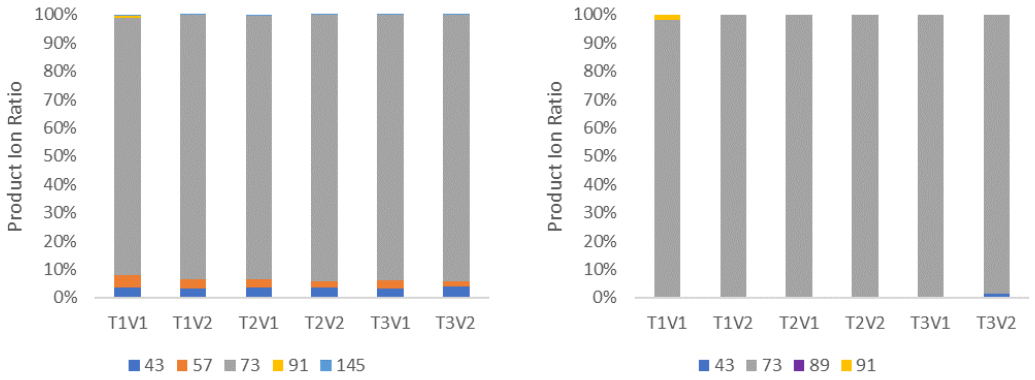

Figure 2.14 – *The product ion ratios of the H_3O^+ reagent ion channel of butanone under dry (left) and humid conditions (right). The temperatures and voltages are denoted by the column labels where T1 = 38 °C, T2 = 120 °C, T3 = 140 °C, V1 = 25 V and V2 = 50 V. The identities of the ions are 43 = $C_3H_7^+/C_2H_3O^+$, 57 = $C_3H_5O^+$, 73 = $C_4H_9O^+$, 89 = $C_4H_7O^+.H_2O$, 91 = $C_4H_9O^+.H_2O$ and 145 = $C_4H_9O^+.C_4H_8O$.*

In the NO^+ channel ***(Figure 2.15)*** the increase in temperature caused little change in the product ion distribution at 25 V but decreased the NO^+ adduct product, *m/z* 102, with increasing temperature at 50 V. Under humid conditions the only product observed was the NO^+ adduct product.

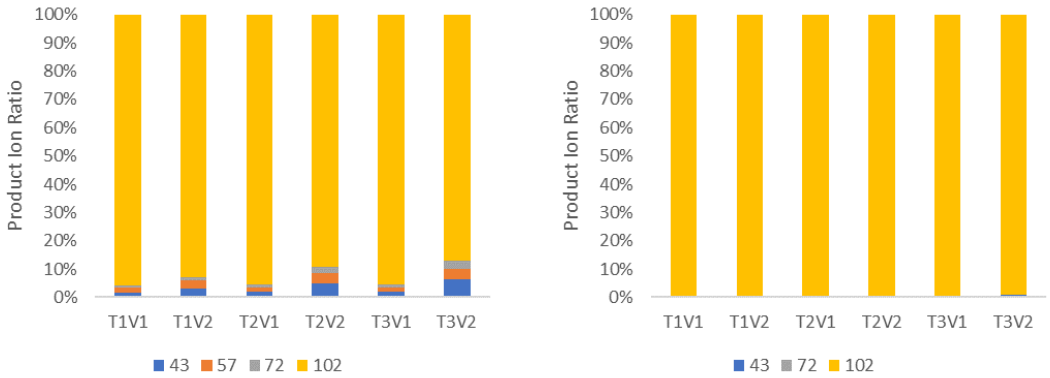

Figure 2.15 – *The product ion ratios of the NO^+ reagent ion channel of butanone under dry (left) and humid conditions (right). The temperatures and voltages are denoted by the column labels where T1 = 38 °C, T2 = 120 °C, T3 = 140 °C, V1 = 25 V and V2 = 50 V. The identities of the ions are 43 = $C_3H_7^+/C_2H_3O^+$, 57 = $C_3H_5O^+$, 72 = $C_4H_8O^+$ and 102 = $C_4H_8O.NO^+$.*

In the O_2^+ channel ***(Figure 2.16)*** the increase in temperature caused little change in the product ion distribution at either 25 V or 50 V under dry or humid conditions. Increasing the flow tube voltage increased the proportion of the fragment ion, *m/z* 29, largely at the expense of another fragment ion, *m/z* 57.

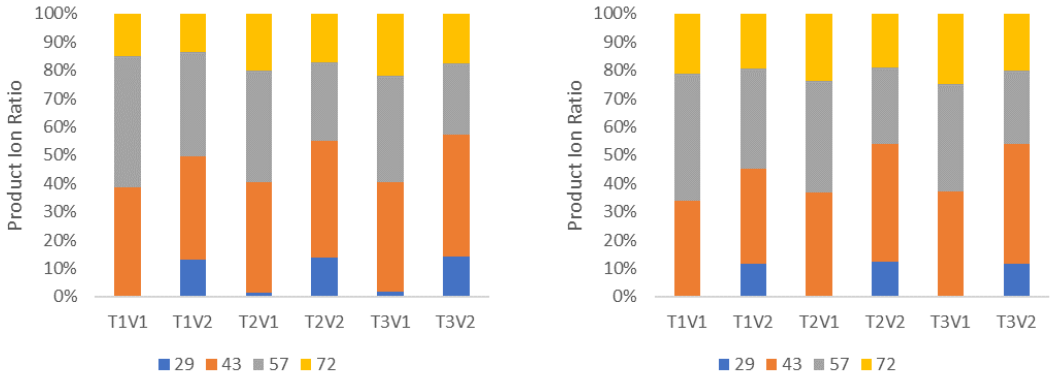

Figure 2.16 – *The product ion ratios of the O_2^+ reagent ion channel of butanone under dry (left) and humid conditions (right). The temperatures and voltages are denoted by the column labels where T1 = 38 °C, T2 = 120 °C, T3 = 140 °C, V1 = 25 V and V2 = 50 V. The identities of the ions are 29 = $CHO^+/C_2H_5^+$, 43 = $C_3H_7^+/C_2H_3O^+$, 57 = $C_3H_5O^+$ and 72 = $C_4H_8O^+$.*

From this it was determined that running the instrument at the highest flow tube voltage and temperature was optimal for the application intended, to measure emissions in a humid sample. Under humid conditions the higher temperature and flow tube voltage generally increased the sensitivity

2.2.3 Determination of Product Ions

Full mass scans were performed on each compound to determine the product ions to be measured in selected ion monitoring (SIM) mode, with an ion dwell limit per *m/z* of 100 ms, count limit per *m/z* of 10,000 counts and repeats over a range of 18 – 400 *m/z* in steps of 1 *m/z*. The flow tube temperature of the SIFT-MS was held at 140 °C with a flow tube pressure of 460 mTorr. Blanks were measured by flowing 0.025 slpm (standard litres per minute) of N_2 diluent gas past the SIFT-MS which sampled at 25 sccm. The main run was performed with a lower diluent flow of 0.01 slpm, but with the permeation oven outflow on. The average of the last five blank measurements at each *m/z*, for each reagent ion, was subtracted from the corresponding value for the non-blank signal to give a blank corrected spectrum from which the product ions were determined. The scans were run at 0.01 slpm diluent flow to introduce as large a possible concentration into the SIFT-MS, allowing all product ions to be easily identifiable as well as any ions arising from secondary chemistry. The blank requires a larger diluent flow to ensure that the minimum SIFT-MS inlet flow of 0.025 slpm is met, the main run combines a 0.01 slpm diluent flow with a 0.10 slpm sample flow thus exceeding the required inlet flow for the SIFT-MS.

2.2.4 Determination of Rate Constants and Branching Ratios

For determination of rate constants, a number of SIM mode scans were run per compound. This used a method identical to that of the full scan method, except with 401 repeats, at a measurement time limit per *m/z* of 100 ms and an ion dwell limit per *m/z* of 10,000 counts, of the H_3O^+ (*m/z* 19, 37 and 55), NO^+ (*m/z* 30) and O_2^+ (*m/z* 32) reagent ions and the required *m/z* values of the relevant product ions. These scans were run over a range of diluent flows to allow the rate constant to be calculated over a range of concentrations. From these runs the last 400 repeats were averaged for each ion in both the blank and non-blank mass spectra. After the removal of outliers, the blank average was subtracted from the non-blank average to give a final run ion count for each measured ion. The branching ratio for each product ion was calculated from this data by dividing the individual product ion count at each *m/z* by the total product ion count.

Properties like the carrier flow rate, flow tube temperature and flow tube pressure were averaged over the two runs, which varied by a maximum of 0.05 %. The rate

constant, k_i, for each reagent ion, i, reacting with a compound can be calculated as; (Huey, 2007)

$$k_i = \frac{\left(\frac{-dN_i}{dt}\right)}{N_i C_j} \quad (Eq. 2.1)$$

where $-dN_i$ is the reduction in reagent counts (essentially the sum of the product ion counts) in counts per second (cps), dt is the reaction time (recorded by the instrument) in s, N_i is the total reagent ion count (taken from the blank) in cps and C_j is the concentration of the compound, taking into account its dilution by the diluent and SIFT-MS carrier gas flow, in molecules cm^{-3}. The rate constant was determined by plotting $-dN_i/dt$ vs. N_iC_j.

The branching ratio was calculated as;

$$BR_x = \frac{N_x}{N_p} \times 100 \quad (Eq. 2.2)$$

Where BR_x is the branching ratio of product ion x (as a percentage), N_x is the product ion count of x and N_p is the total product ion count for all product ion in the reagent ion channel the branching ratio is being calculated for. These branching ratios are useful for both individual compound quantitation, alongside the rate constant, and for method development. It is important to know all product ions that occur for compounds expected in a mixture to ensure no overlapping peaks are used as this ensures reliable quantitation of concentration. Isotopologues are not measured in this work due to their low abundance relative to the major product ions. The contributions of isotopologues to the product ions are much smaller than other uncertainties such as those associated with calibration, which are described below.

2.2.5 Rate Constant Error Calculations

The error of the measured rate constants was calculated as follows. Err_{Cperm}, the error in the concentration of an analyte emitted from the permeation tube, is calculated in ppb as;

$$Err_{C_{perm}} = C_{perm}\sqrt{\left(\frac{Err_T}{T}\right)^2 + \left(\frac{Err_m}{m}\right)^2 + \left(\frac{Err_V}{V}\right)^2} \quad (Eq. 2.3)$$

$$Err_{C_{perm}} = C_{perm}\sqrt{\left(\frac{0.5}{T}\right)^2 + \left(\frac{Err_m}{m}\right)^2 + \left(\frac{0.008V}{V}\right)^2} \quad (Eq. 2.4)$$

The error of the mass loss from the permeation tube, Err_m, is calculated from the slope error determined by the linest function in excel and assumed to be independent of the error in temperature and volume. The error in the temperature, Err_T, is the measurement accuracy of the temperature controller (0.5 K) and assuming that the emission rate of the permeation tube is linearly related to small changes in temperature. The volume, V, is 100 cm^3 (a 100 sccm flow for 1 minute) and its error, Err_V, is the 0.8 % accuracy reported by Alicat flow meters (calculated as (0.008 x V). C_{perm} is the concentration from the permeation tube, T is the temperature at which the permeation oven is held, m is the gradient of the mass loss of the tube over time used to calculate the concentration and V is the volume of air.

$$Err_{C_{SIFT}} = C_{SIFT}\sqrt{\left(\frac{Err_{C_{perm}}}{C_{perm}}\right)^2 + \left(\frac{Err_{Q_{carrier}}}{Q_{carrier}}\right)^2 + \left(\frac{Err_{Q_{sample}}}{Q_{sample}}\right)^2 + x\left(\frac{Err_{Q_{perm}}}{Q_{perm}}\right)^2} \quad (Eq.\,2.5)$$

C_{SIFT} is the concentration of analyte in the SIFT after all dilution steps, in ppb. The error in the carrier gas flow, $Err_{Qcarrier}$, is calculated by taking the standard deviation of all 800 measurements of the carrier flow in the blank and analyte runs divided by sqrt(800) and $Q_{carrier}$ is the flowrate of the instruments internal carrier gas. The error in the sample inlet flow, $Err_{Qsample}$, is calculated as the error of the Alicat (0.8 %), where Q_{sample} is the sample flowrate into the instrument. Err_{Qperm} is the error in the flow rate through a single permeation oven, calculated as the error of the Alicat (0.8 %), and x is the number of permeation oven flows used.

The error in the volume of gas the C_{SIFT} concentration of gas exists in, Err_{V1}, is calculated as;

$$Err_{V1} = V1\sqrt{\left(\frac{Err_T}{T}\right)^2 + \left(\frac{Err_P}{P}\right)^2} \quad (Eq.\,2.6)$$

Where the error in the flow tube temperature, Err_T, and the error in the flow tube pressure, Err_P, are calculated as the relative standard deviations of the respective 800 measurements in the blank and analyte runs. T is the flow tube temperature and P is the flow tube pressure.

The errors previously calculated are used to determine the error in C_{SIFT}, Err_{Csift}, measured in molecules cm^{-3};

$$Err_{C_{SIFT}\,(molecules\,cm^{-3})} = C_{SIFT\,(molecules\,cm^{-3})}\sqrt{\left(\frac{Err_{C_{SIFT}\,(ppb)}}{C_{SIFT}\,(ppb)}\right)^2 + \left(\frac{Err_{V1}}{V1}\right)^2} \quad (Eq.2.7)$$

The error in the total product ion count, Err_{dNi}, is the root sum square of the errors in each individual product ion count, Err_i, which is calculated as;

$$Err_{dNi} = \sqrt{\sum_i (Err)_i^2} \quad (Eq.2.8)$$

$$Err_i = \sqrt{(Err_{blank\,i})^2 + (Err_{run\,i})^2} \quad (Eq.2.9)$$

where the error in the product ion, *i*, in the blank, $Err_{blank\,i}$, is the standard deviation of all measurements of product ion *i* in the blank divided by the square root of the total number of measurements and the error in the product ion, i, in the run, $Err_{run\,i}$, is the same, but for the run.

The final error in the measured rate constant, Err_k, is calculated as;

$$Err_k = k\sqrt{\left(\frac{Err_{C_{SIFT}}}{C_{SIFT}}\right)^2 + \left(\frac{Err_{dN_i}}{dN_i}\right)^2 + \left(\frac{Err_{N_i}}{N_i}\right)^2} \quad (Eq.2.10)$$

where the error in the reagent ion count, Err_{Ni}, is calculated as the standard deviation of all measurements of the reagent ion in the blank divided by the number of measurements in the blank.

2.3 Results and Discussion

2.3.1 Permeation Data

Calculated mixing ratios of all analytes supplied from the permeation tube calibration system are shown in ***Table 2.1***. The error in the mixing ratio emitted from the permeation tube, Err_{Cperm}, is calculated as shown in ***Eq. 2.3***. In ***Table 2.1*** the R^2 value represents the variance in the linear relationship between mass loss and time and is therefore a measure of the precision of the calculated mixing ratios.

Table 2.1 – Calculated mixing ratios for all permeation tubes used in this study.

Compound		Mixing Ratio / ppb		Repeats	Temp. / °C	R^2
Name	Formula	Value	% Error			
Benzene	C_6H_6	2759	0.91	25	40	1.000
1-Propanol	C_3H_8O	284.8	3.77	12	40	0.987
Butanal	C_4H_8O	5035	2.52	10	40	0.996
2-Butanone	C_4H_8O	2641	1.03	10	40	1.000
2-Butenal	C_4H_6O	5006	1.61	8	40	0.999
2-Pentanone	$C_5H_{10}O$	1023	1.06	14	40	1.000
Hexanal	$C_6H_{12}O$	764.5	8.09	15	50	0.926
2-Hexenal	$C_6H_{10}O$	970.0	5.40	14	50	0.968
2-Octanone	$C_8H_{16}O$	230.4	3.46	12	50	0.989
Nonanal	$C_9H_{18}O$	371.0	3.43	8	70	0.994

The permeation tube systems provided stable concentrations of all the compounds, with an average calculated mixing ratio uncertainty of 3.1 %.

2.3.2 SIFT-MS Rate Data

The measured rate constants are shown in ***Table 2.2*** and are compared to previously published rate constants in ***Figure 2.17***. The error in the measured rate constants, Err_k, reported in ***Table 2.2*** and shown in ***Figure 2.17*** was calculated as shown in ***Eq. 2.10***.

2.3.2.1 Benzene

For benzene, the nitrogen H_3O^+ rate constant measured here was within 3.6 % of that measured by Spanel and Smith (1998) (herein referred to as SP01) and within 8.6 % of that measured by Spanel et. al. (1995) (herein referred to as SP02), both measured in helium. The measured H_3O^+ rate constant was also comparable to a PTR-MS rate constant measured by Lindinger et. al. (1998) (herein referred to as LI01) and a theoretical rate constant as calculated by Sekimoto et. al. (2017) (herein referred to as SE01). The nitrogen NO^+ and O_2^+ rate constants measured were also comparable with those measured by SP01 (within 8.7 % and 7.4 % respectively).

2.3.2.2 1-propanol

The measured propanol rate constants in nitrogen are similar to previous data reported by Spanel and Smith (1997) (herein referred to as SP03) for both H_3O^+ (within 15.9 %) and O_2^+ (within 7.7 %) in helium, but the NO^+ rate constant is 35.7 % lower than that reported by SP03 in helium. This pattern is also seen for other compounds in this study where the NO^+ rate constant measured is smaller than those reported in the literature, but the H_3O^+ or O_2^+ rate constants remain similar. The H_3O^+ rate constant also compares well to a PTR-MS rate constant reported by LI01 and a calculated rate constant via SE01.

2.3.2.3 Butenal

The Butenal rate constants for H_3O^+, NO^+ and O_2^+ are all within error of those measured by Spanel et. al. (2002) (herein referred to as SP04) in helium. The NO^+ rate constant measured here is only just within the error of the measurement by SP04, at 3.1 $x10^{-9}$ cm^3 s^{-1} compared to 4.1 $x10^{-9}$ cm^3 s^{-1}.

2.3.2.4 Hexenal

The hexenal rate constants for all reagent ions are all within error of those measured by Spanel et. al. (1997) (herein referred to as SP05) in helium. Both unsaturated aldehydes produced similar results with an H_3O^+:NO^+ rate constant ratio of 1.44:1.00 for butenal and 1.48:1.00 for hexenal. These similar ratios are an indication that unsaturated aldehydes have a similar rate constant ratio trend.

2.3.2.5 2-butanone

The butanone rate constants for H_3O^+ and O_2^+ were comparable to those measured in SP05 in helium. The NO^+ rate constant measured was much lower than that measured by SP05, 0.6 $x10^{-9}$ cm^3 s^{-1} compared to 2.8 $x10^{-9}$ cm^3 s^{-1}, a reduction of almost 80 %. The calibration gas cylinder containing benzene and 2-butanone was also measured to confirm the lower NO^+ rate constant was not an artefact of the permeation tube source. The benzene rate constants determined from the calibration gas cylinder were close (within 21.5 %) to the measured permeation tube rate constants and the literature for all three reagent ions. The measured H_3O^+ rate constants between the permeation tube and cylinder were 0.05 cm^3 s^{-1} within error but the NO^+ and O_2^+ rate constants were 0.07 cm^3 s^{-1} outside of the calculated error. This was used to confirm that the cylinder measurement NO^+ rate constant of 1.0

$x10^{-9}$ cm^3 s^{-1} for 2-butanone was valid, though the real value may be smaller if the apparent error in the benzene measurements holds true for the butanone measurements. The calibration cylinder measurement is much closer to the permeation tube measurement of 0.6 $x10^{-9}$ cm^3 s^{-1} than the value measured in SP05. The theoretical rate constant calculated in SE01 for the H_3O^+ rate constant was lower than that measured in this study.

2.3.2.6 Pentanone

As with butanone, the pentanone rate constants were comparable to those measured in SP05 in helium and the NO^+ rate constant measured was much lower than that measured in SP05. The NO^+ rate constant measured was 1.1 $x10^{-9}$ cm^3 s^{-1} compared to 3.1 $x10^{-9}$ cm^3 s^{-1} in SP05, a reduction of around 65 %. The theoretical rate constant calculated in SE01 for the H_3O^+ rate constant was lower than that measured in this study.

2.3.2.7 Octanone

For octanone, the NO^+ value measured in nitrogen in this study was closer than the other two compounds to the value measured by Smith et. al. (2003) (herein referred to as SM01) in helium, 2.3 $x10^{-9}$ cm^3 s^{-1} compared to 3.3 $x10^{-9}$ cm^3 s^{-1}, a reduction of around 30 % and just outside the error range. The H_3O^+ and O_2^+ rate constants measured were both close to the values reported in SM01. The theoretical rate constant calculated in SE01 for the H_3O^+ rate constant was lower than that measured in this study.

2.3.2.8 Butanal

The butanal rate constants measured in nitrogen were all higher than those reported in SP04 and SP05 in helium, though the NO^+ and SP04 O_2^+ rate constants were within the error of the measured values of this study. The H_3O^+ rate constant measured was especially high, 5.2 $x10^{-9}$ cm^3 s^{-1} compared to 3.8 $x10^{-9}$ cm^3 s^{-1} reported in both SP04 and SP05. This was also higher than the calculated SE01 theoretical rate constant.

2.3.2.9 Hexanal

The nitrogen measured hexanal rate constants for NO^+ and O_2^+ compared well with SP05 helium-based rate constants. The H_3O^+ rate constant was lower, although just within the error of the SP05 value, 2.8 $x10^{-9}$ cm^3 s^{-1} compared to 3.7 $x10^{-9}$ cm^3 s^{-1}, and was similar to the SE01 derived rate constant.

2.3.2.10 Nonanal

There is no literature comparison for nonanal, except for a theoretical SE01 value at 2.4 $x10^{-9}$ cm^3 s^{-1} which is 30 % higher than the value measured in this study of 1.8 $x10^{-9}$ cm^3 s^{-1}.

2.3.2.11 Overview of Rate Constant Data

The most significant differences between the measurements in this study and previous studies all occur for compounds with only a single adduct product, namely the NO^+ ketone rate constants. This likely suggests that the collision complex is being formed but is not effectively stabilised in the higher energy system in this study compared to standard usage of the instrument. Alternatively, the NO^+ adducts could be undergoing collisions that, in the higher energy system employed by the instrument used in this study compared to previous iterations, would be more likely to fragment the adduct complex. This was also seen in the temperature and voltage experiments in ***Section 2.2.2*** which confirmed that both increasing the flow tube temperature and flow tube voltage decrease the sensitivity of NO^+ adduct formation which would reduce the rate constant as is seen in the results. All rate constants reported were measured under dry conditions, no measurements of rate constants under humid conditions were made.

An analysis of the error in this study suggests that most of the error is attributable to noise. The largest of which is in the concentration value determined from the permeation tube whose error tended to decrease gradually with successive measurement. This is evident by the longest running permeation tubes, like benzene, having the lowest error as shown in ***Table 2.1***. Benzene is also the species that was run the most on the SIFT-MS which further reduced the measured error, this further suggests that the bulk of the error exhibited by the permeation tube measurements due to concentration and flow rates is due to noise. If an assumption is made that the measured H_3O^+ rate constants are generally in line with the literature rates, which from the results of this study seems appropriate for most compounds, the results from the gas cylinder are starkly different compared to those measured from the permeation tubes. As they are measured in the same way none of the error between the values can be attributable to noise within the measurements. The benzene results give measurements that are only just within error, 1.97 ± 0.11 $x10^{-9}$ cm^3 s^{-1} from the permeation tube compared to 2.23 ± 0.20 $x10^{-9}$ cm^3 s^{-1}. This raises the possibility

that the difference between the permeation tube and the gas cylinder could be due to bias in the measurement. The measurements are shown in ***Figure 2.17*** and show that the cylinder measurement is towards the high end of the literature error range and the average value is offset 0.38 $x10^{-9}$ cm^3 s^{-1} higher than the literature average and 0.26 $x10^{-9}$ cm^3 s^{-1} higher than the permeation tube average. This offset could be defined as a bias and may also explain why the other gas cylinder measurement used, butanone, is higher than both the literature and permeation tube measurement. The reason for this biased result may be due to the storage method for the compound. The gas cylinder used was calibrated in October 2017 and the measurements were performed in November 2021. The calibration certificate for this cylinder was given as two years which means the measurement was performed more than two years after the validity of the concentrations in the cylinder had expired. This does not guarantee that the concentrations in the cylinder were lower than reported. However, if the concentrations were lower than reported, due to drift and degradation within the cylinder, this would explain the greater rate constant measured for the cylinder relative to the permeation tube. The concentration and rate constant have an inverse relationship and so any decrease in concentration will cause an increase in the measured rate constant.

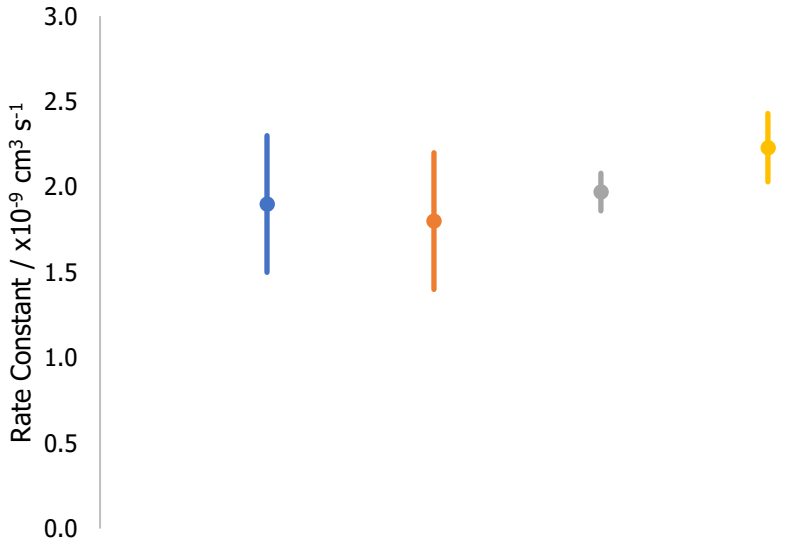

Figure 2.17 *– The literature and measured H_3O^+ rate constants for benzene, where the average is represented by the point and the 2σ error range is represented by the coloured line. Blue = SP01, Orange = SP02, Grey = Permeation tube and Yellow = Gas Cylinder.*

Table 2.2a – Measured and literature rate constants and branching ratios. Branching ratio percentages <10 % have been removed for clarity. Rate is measured in $x10^{-9}$ cm^3 s^{-1}.

Compound	Work	Temperature / °C	Carrier Gas	Source	H_3O^+			NO^+			O_2^+		
					Rate	Ion / *m/z*	Ratio / %	Rate	Ion / *m/z*	Ratio / %	Rate	Ion / *m/z*	Ratio / %
Benzene	This work	140	N_2	Perm. Tube	1.97 ± 0.11	79	100	1.38 ± 0.08	78	93	1.49 ± 0.08	78	100
	This Work	140	N_2	Cylinder	2.23 ± 0.20	79	100	1.69 ± 0.16	78	93	1.82 ± 0.18	78	100
	SP01	Room Temperature	He	Plastic Bag	1.9 ± 0.4	79	100	1.5 ± 0.3	78 108	85 15	1.6 ± 0.3	78	100
	SP02	Room Temperature	He	Plastic Bag	1.8 ± 0.4	79	100	N/A	N/A	N/A	N/A	N/A	N/A
1-propanol	This work	140	N_2	Perm. Tube	2.27 ± 0.25	43	100	1.48 ± 0.14	59	100	2.03 ± 0.20	31 42 59	67 13 20
	SP03	Room Temperature	He	Plastic Bag	2.7 ± 0.5	43 61	90 10	2.3 ± 0.4	59	100	2.2 ± 0.4	42 55	10 90
Butanal	This work	140	N_2	Perm. Tube	5.17 ± 0.64	55 73	89 11	3.66 ± 0.48	43 71	75 25	4.37 ± 0.57	43 44 57 72	17 48 13 23
	SP04	Room Temperature	He	Plastic Bag	3.8 ± 0.8	73	95	3.3 ± 0.7	71	100	3.2 ± 0.6	44 72	50 50
	SP05	Room Temperature	He	Plastic Bag	3.8 ± 0.8	73	95	3.5 ± 0.7	71	100	3.5 ± 0.7	44 72	65 35

Table 2.2b – Measured and literature rate constants and branching ratios. Branching ratio percentages <10 % have been removed for clarity. Rate is measured in $x10^{-9}$ cm^3 s^{-1}.

Compound	Work	Temperature / °C	Carrier Gas	Source	H_3O^+			NO^+			O_2^+		
					Rate	Ion / *m/z*	Ratio / %	Rate	Ion / *m/z*	Ratio / %	Rate	Ion / *m/z*	Ratio / %
Butanone	This work	140	N_2	Perm. Tube	3.67 ± 0.27	73	100	0.56 ± 0.04	102	97	3.69 ± 0.28	29 43 57 72	12 43 26 18
	This work	140	N_2	Cylinder	4.35 ± 0.52	73	100	0.97 ± 0.13	102	92	N/A	N/A	N/A
	SP05	Room Temperature	He	Plastic Bag	3.9 ± 0.8	73	100	2.8 ± 0.5	102	100	3.3 ± 0.6	43 57 72	40 25 35
Butenal	This work	140	N_2	Perm. Tube	4.48 ± 0.36	71	100	3.11 ± 0.22	69	95	3.73 ± 0.29	42 69 70	18 52 20
	SP04	Room Temperature	He	Plastic Bag	4.8 ± 0.9	71	100	4.1 ± 0.8	69	100	4.3 ± 0.9	69 70	65 30
Pentanone	This work	140	N_2	Perm. Tube	4.21 ± 0.25	45 87	27 73	1.05 ± 0.89	116	100	3.71 ± 0.30	43 58 71 86	47 27 13 13
	SP05	Room Temperature	He	Plastic Bag	3.9 ± 0.8	87	100	3.1 ± 0.6	116	100	3.0 ± 0.6	43 58 71 86	50 20 15 15

Table 2.2c – Measured and literature rate constants and branching ratios. Branching ratio percentages <10 % have been removed for clarity. Rate is measured in $x10^{-9}$ cm^3 s^{-1}.

Compound	Work	Temperature / °C	Carrier Gas	Source	H_3O^+			NO^+			O_2^+		
					Rate	Ion / *m/z*	Ratio / %	Rate	Ion / *m/z*	Ratio / %	Rate	Ion / *m/z*	Ratio / %
Hexanal	This work	140	N_2	Perm. Tube	2.78 ± 0.58	55 83 101	22 59 15	2.40 ± 0.50	43 71 99	26 37 32	2.02 ± 0.40	44 56 57 82	32 35 14 10
	SP05	Room Temperature	He	Plastic Bag	3.7 ± 0.7	83 101	50 50	2.5 ± 0.5	99	100	2.0 ± 0.4	44 56	30 50
Hexenal	This work	140	N_2	Perm. Tube	4.12 ± 0.53	57 99	56 36	2.78 ± 0.38	55 97	33 64	3.09 ± 0.43	43 69 83 98	15 10 11 24
	SP05	Room Temperature	He	Plastic Bag	4.6 ± 0.9	99	100	3.8 ± 0.8	71 97	15 85	3.7 ± 0.7	43 69 70 98	30 30 20 20
Octanone	This work	140	N_2	Perm. Tube	3.48 ± 0.34	129	100	2.28 ± 0.23	158	100	2.81 ± 0.31	58 59 128	51 18 12
	SM01	Room Temperature	He	Plastic Bag	4.1 ± 0.8	129	100	3.3 ± 0.6	158	100	3.1 ± 0.6	58 59 128	50 15 30

Table 2.2d – Measured and literature rate constants and branching ratios. Branching ratio percentages <10 % have been removed for clarity. Rate is measured in $x10^{-9}$ cm^3 s^{-1}.

Compound	Work	Temperature / °C	Carrier Gas	Source	H_3O^+			NO^+			O_2^+		
					Rate	Ion / *m/z*	Ratio / %	Rate	Ion / *m/z*	Ratio / %	Rate	Ion / *m/z*	Ratio / %
Nonanal	This work	140	N_2	Perm. Tube	1.77 ± 0.26	57 69 83 143	18 34 11 28	1.10 ± 0.14	57 71 141	29 16 54	N/A	N/A	N/A

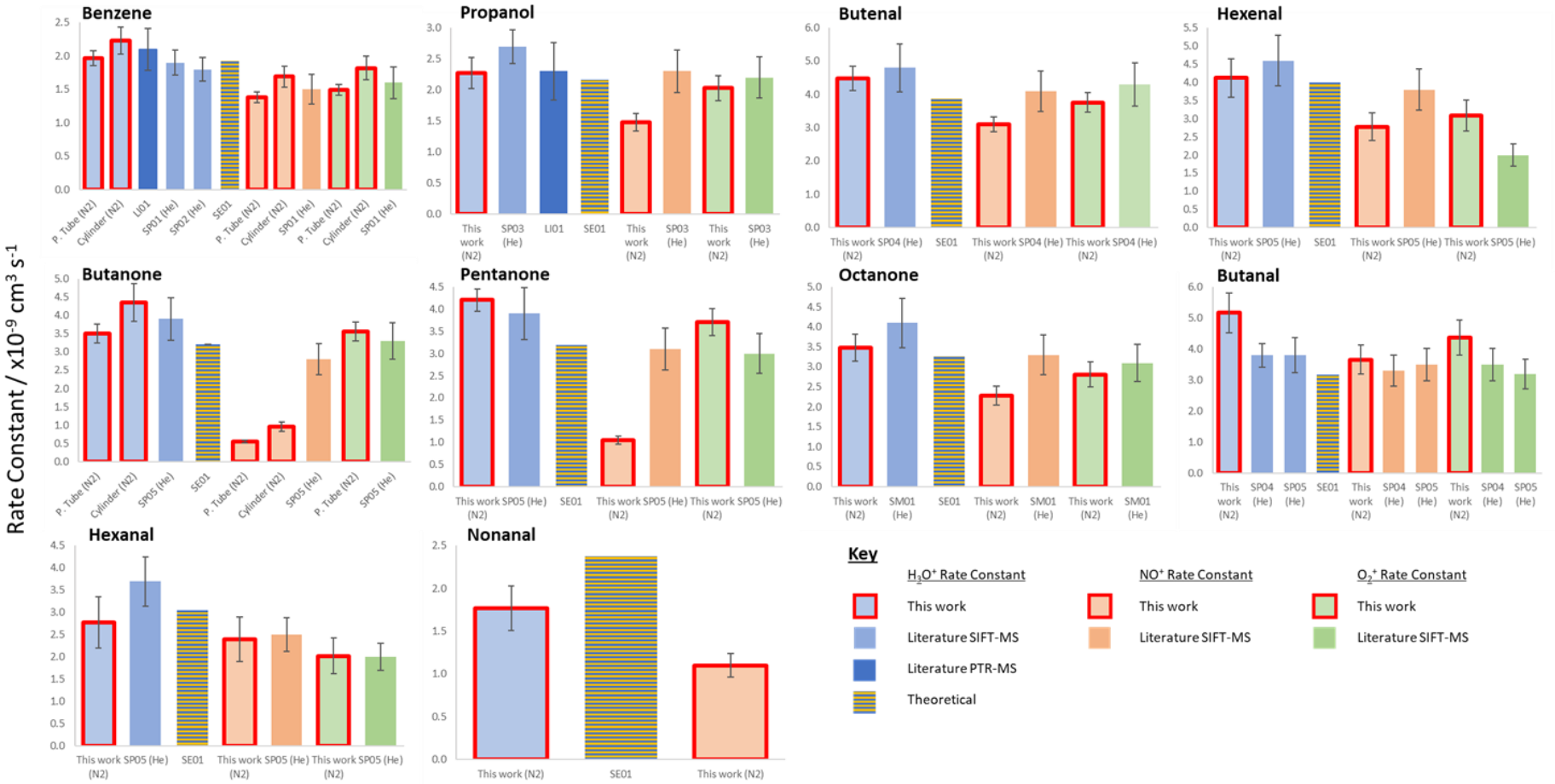

Figure 2.18 *– Comparison of rate constants measured in this study with those of Lindinger et. al. (1998) (LI01), Spanel and Smith (1998) (SP01), Spanel et. al. (1995) (SP02), Sekimoto et. al. (2017) (SE01), Spanel and Smith (1997) (SP03), Spanel et. al. (2002) (SP04), Spanel et. al. (1997) (SP05) and Smith et. al. (2003) (SM01). For benzene and butanone P. Tube represents the permeation tube measurement and Cylinder represents the calibration cylinder measurement.*

2.3.3 SIFT-MS Product Ions and Branching Ratios

2.3.3.1 Benzene (C_6H_6)

The product ions for benzene match those observed in SP01. The only H_3O^+ product appears at *m/z* 79 which is the proton transfer product of benzene as shown in ***Eq. 2.11***.

$$C_6H_6 + H_3O^+ \rightarrow C_6H_6H^+ + H_2O \quad (Eq. 2.11)$$

There are two NO^+ products that form which are the same in this study and that of SP01. These are a charge transfer product appearing at *m/z* 78 ***(Eq. 2.12)*** and an NO adduct at *m/z* 108 ***(Eq. 2.13)***. In the SP01 study, the charge transfer product to NO adduct branching ratio was 85:15 $C_6H_6^+$:$C_6H_6.NO^+$, but a branching ratio of 93:7 $C_6H_6^+$:$C_6H_6.NO^+$ was observed in this study. The higher charge transfer product found in this work is due to a combination of the higher flow tube temperature and increased flow tube voltage used in these measurements that increase the total energy in the system. At higher energy the adduct decomposes at a greater rate leading to a decreased percentage of the adduct.

$$C_6H_6 + NO^+ \rightarrow {C_6H_6}^+ + NO \quad (Eq. 2.12)$$

$$C_6H_6 + NO^+ \rightarrow C_6H_6.NO^+ \quad (Eq. 2.13)$$

The O_2^+ product ion at *m/z* 78, formed by a charge transfer reaction ***(Eq. 2.14)***, is the same in both this work and the Smith and Smith (1998) work. This is the only product formed.

$$C_6H_6 + {O_2}^+ \rightarrow {C_6H_6}^+ + O_2 \quad (Eq. 2.14)$$

2.3.3.2 1-propanol (C_3H_8O)

For the reaction of propanol with H_3O^+ only the *m/z* 43 product ion ($C_3H_7^+$) was detected, derived from the loss of water following proton transfer ***(Eq. 2.15)***, a common mechanism in alcohols and aldehydes.

$$C_3H_7OH + H_3O^+ \rightarrow C_3H_7OHH^+ + H_2O \rightarrow {C_3H_7}^+ + 2H_2O \quad (Eq. 2.15)$$

SP03 observed an additional product ion for this reaction at *m/z* 61, although the *m/z* 43 product ion was favoured with a branching ratio of 90:10. It is possible that the higher energy in the SIFT-MS in this study caused the loss of water to become even more favourable than found in the SP03. The NO^+ product ion at *m/z* 59 appears as

the only NO^+ product ion of propanol in both this study and SP03. The *m/z* 59 ion is formed via hydride transfer as shown in ***(Eq. 2.16)***.

$$C_3H_7OH + NO^+ \rightarrow C_3H_7O^+ + HNO \quad (Eq. 2.16)$$

The O_2^+ product ions in this study are the same as those observed in SP03 but also a product ion at *m/z* 59, equivalent to the loss of a hydrogen atom was also observed. The other two product ions are *m/z* 31 and *m/z* 42, both breakdown products after charge transfer and formed from the loss of an ethyl group and a water molecule, respectively. While the *m/z* 31 ion remains the major product ion in these measurements, the ratios, with the addition of the *m/z* 59 ion, are quite different from those observed by SP03. A branching ratio of 67:13:20 (*m/z* 31:42:59 – CH_3O^+:$C_3H_6^+$/$C_2H_2O^+$:$C_3H_yO^+$) was measured in this study compared to the SP03 branching ratio of 90:10 (*m/z* 31:42 – CH_3O^+:$C_3H_6^+$/$C_2H_2O^+$).

2.3.3.3 Butenal (C_4H_6O)

The observed butenal product ions matched those reported in SP04 closely. The major H_3O^+ product is the proton transfer product at *m/z* 71 ($C_4H_7O^+$). An extra product ion at *m/z* 43 was observed, though at an extremely low ion count of 0.2 %, which could be treated as insignificant.

The major NO^+ product ion is that resulting from hydride transfer at *m/z* 69. Another product ion appears at *m/z* 41 that was not shown by SP04. This ion is formed from fragmentation after the hydride transfer forming either C_2HO^+ or $C_3H_5^+$ at a branching ratio of 5.4 %.

All of the product ion SP04 measured were detected in this study; *m/z* 70 ($C_4H_6O^+$), the charge transfer product, *m/z* 69 ($C_4H_5O^+$), a hydride transfer product, and *m/z* 42 ($C_3H_6^+$/$C_2H_2O^+$), a fragment ion. Two more minor fragment ions were measured at *m/z* 55 ($C_3H_3O^+$) and *m/z* 41 (C_2HO^+/$C_3H_5^+$) and a higher proportion of butenal fragment ions were observed, with only 72 % of the product ion resulting from charge transfer or hydride transfer, compared to 95 % in SP04.

2.3.3.4 Hexenal ($C_6H_{10}O$)

The hexenal product ions detected were quite different to those observed in SP05. The proton transfer product, *m/z* 99 ($C_6H_{11}O^+$), which was the only product ion reported by SP05, only accounted for 35 % of the observed product ion count in this

study. Instead, the major product ion was a fragmentation product at *m/z* 57 ($C_4H_9^+$ - 53 %) with a minor water loss product ion at *m/z* 81 ($C_6H_9^+$ 8 %).

The NO^+ hydride transfer product at *m/z* 99 ($C_6H_9O^+$) was detected in both this work and SP05. In SP05 a fragment ion at *m/z* 71 ($C_4H_7O^+$ - 15 %) was observed which was not detected in this study, though fragment ions at *m/z* 55 ($C_2H_2O^+$ - 31 %) and *m/z* 69 ($C_4H_5O^+/C_5H_9^+$ - 2.8 %) were detected.

More numerous O_2^+ product ions were detected than those observed by SP05, who observed the charge transfer product, *m/z* 98 ($C_6H_{10}O^+$ - 20 %), and three fragment ions, *m/z* 70 ($C_4H_6O^+$ - 20 %), *m/z* 69 ($C_5H_9^+/C_4H_5O^+$ - 30 %) and *m/z* 43 ($C_2H_3O^+/C_3H_7^+$ - 30 %). These product ions only make up 53.2 % of the product ion count in this study, with eight more product ions accounting for the remaining 46.8 %. The charge transfer ion is the only product ion that increases in branching ratio, from 20 % to 24 %, whereas the remaining fragment ions have a range of 2.8% to 14.5 %. This difference is possibly due to the increased energy in this system causing much greater fragmentation compared to SP05. The SP05 data for hexenal was observed using a He carrier gas, whereas the measurements in this study use N_2, which may also influence the product ions formed.

2.3.3.5 2-butanone (C_4H_8O)

The butanone product ions observed here are similar to those observed in SP05. The only H_3O^+ product ion observed in both this work and SP05 is the proton transfer product, *m/z* 73 ($C_4H_9O^+$).

The NO^+ product ions are also similar. The major product ion observed in this study was the NO adduct at *m/z* 102 ($C_4H_8O.NO^+$ - 97 %), which was the only one observed in SP05, but a minor charge transfer product at *m/z* 72 ($C_4H_8O^+$ - 3 %) was also observed in this study.

The O_2^+ product ions were also similar, with only one more fragment ion observed in this work compared to SP05. A lower fraction of the charge transfer product at *m/z* 72 ($C_4H_8O^+$ - 18 %) was measured in this study than in SP05 and similar amounts of the fragment ions at *m/z* 57 ($C_3H_5O^+$ - 26 %) and *m/z* 43 ($C_2H_3O^+$ - 43 %) were observed as well as an additional fragment ion at *m/z* 29 ($C_2H_5^+/CHO^+$ - 12 %).

2.3.3.6 Pentanone ($C_5H_{10}O$)

In agreement with SP05, the major pentanone H_3O^+ product ion observed was the proton transfer product at *m/z* 87 ($C_5H_{10}OH^+$ - 73 %). However, a fragment ion at *m/z* 43 ($C_2H_3O^+/C_3H_7^+$ - 27 %) was also observed.

The NO^+ product ion observed, in both this study and SP05, is the NO adduct at *m/z* 116 ($C_5H_{10}O.NO^+$ - 100 %).

All observed O_2^+ product ions are the same as those in SP05, at similar branching ratios, the charge transfer ion at *m/z* 86 ($C_5H_{10}O^+$ - 13 %) and the fragment ions at *m/z* 71 ($C_4H_7O^+$ - 13 %), *m/z* 58 ($C_3H_6O^+$ - 27 %) and *m/z* 43 ($C_2H_3O^+/C_3H_7^+$ - 47 %).

2.3.3.7 Octanone ($C_8H_{16}O$)

The octanone H_3O^+ and NO^+ product ions observed match those observed by SM01 with the H_3O^+ proton transfer ion at *m/z* 129 ($C_8H_{16}OH^+$ - 100 %) and the NO^+ NO adduct at *m/z* 158 ($C_8H_{16}O.NO^+$ - 100%).

The O_2^+ product ions mostly match SM01, with similar branching ratios. The charge transfer product at *m/z* 128 ($C_8H_{16}O^+$ - 12 %) and fragment ions at *m/z* 113 ($C_7H_{13}O^+$ - 5 %), *m/z* 85 ($C_6H_{13}^+$ - 7 %), *m/z* 71 ($C_5H_{11}^+$ - 7 %), *m/z* 59 ($C_3H_7O^+$ - 18 %), *m/z* 58 ($C_3H_6O^+$ - 51 %). The fragment ion at *m/z* 113 is not observed by SM01 and they measure a fragment at *m/z* 43 ($C_2H_3O^+/C_3H_7^+$), that is not observed in this study, as 5 % of their branching ratio. The major difference being that SM01 measure a greater proportion of the charge transfer ion, *m/z* 128 ($C_8H_{16}O^+$), at 30 % compared to the 12 % measured in this work which is replaced by the increased proportion of fragmentation product ions.

2.3.3.8 Butanal (C_4H_8O)

The butanal H_3O^+ product ions observed by SP05 match those observed in this study, though more of the proton transfer product was observed, at *m/z* 73 ($C_4H_8OH^+$ - 11 %) compared to 5 % for SP05, and less of the proton transfer water loss product, at *m/z* 55 ($C_4H_7^+$ - 89 %) compared to 95 % for SP05.

For NO^+, a different major product ion at *m/z* 43 ($C_2H_3O^+/C_3H_7^+$ - 75 %) was observed in addition to the hydride transfer product at *m/z* 71 ($C_4H_7O^+$ - 25 %) reported by SP05.

For the O_2^+ reagent ion the same major fragment ion as SP04 and SP05 was detected at *m/z* 44 ($C_2H_4O^+$ - 46 %). In this study the charge transfer product, at *m/z* 72 ($C_4H_8O^+$ - 22 %), was reduced significantly compared to SP04, who measured it at 50 %, and lower than in SP05, at 35 %. This is largely due to the measurement of two additional fragment ions at *m/z* 57 ($C_3H_5O^+$ - 13 %) and at *m/z* 43 ($C_2H_3O^+/C_3H_7^+$ - 17 %)

2.3.3.9 Hexanal ($C_6H_{12}O$)

The hexanal H_3O^+ product ions measured were similar to those measured for pentanal but with an extra CH_2 group. The proton transfer product, at *m/z* 101 ($C_6H_{12}O^+$ - 15 %), and the proton transfer water-loss product, at *m/z* 83 ($C_6H_{11}^+$ - 59 %), were observed as well as two extra fragment ions at *m/z* 69 ($C_4H_5O^+/C_5H_9^+$ - 4.7 %) and *m/z* 55 ($C_4H_7^+/C_3H_3O^+$ - 22 %).

The NO^+ product ions consisted of the hydride transfer ion observed by SP05, at *m/z* 99 ($C_6H_{11}O^+$ - 32 %), and multiple fragment ions, that SP05 didn't measure, at *m/z* 85 ($C_5H_9O^+$ - 2 %), *m/z* 71 ($C_4H_7O^+$ - 37 %), *m/z* 57 ($C_3H_5O^+$ - 4 %) and *m/z* 43 ($C_2H_3O^+$ - 26 %).

The O_2^+ product ions were mostly similar to SP05, with one fragment ion missing, *m/z* 97. An additional fragment at *m/z* 82 ($C_5H_6O^+/C_6H_{10}^+$ - 10 %) was observed in addition to fragments at *m/z* 72 ($C_5H_{12}^+$ - 9 %), *m/z* 57 ($C_3H_5O^+$ - 14 %), *m/z* 56 ($C_3H_4O^+$ - 35 %) and at *m/z* 44 ($C_2H_4O^+$ - 32 %) that were also observed in SP05.

2.3.3.10 Nonanal ($C_9H_{18}O$)

The proton transfer product for nonanal at *m/z* 143 ($C_9H_{19}O^+$ - 28 %) and the water loss product at *m/z* 125 ($C_9H_{17}^+$ - 9 %) were observed for the H_3O^+ reagent ion. Three fragment ions at *m/z* 83 ($C_6H_{11}^+$ - 11 %), *m/z* 69 ($C_4H_5O^+$/ $C_5H_9^+$ - 34 %) and *m/z* 57 ($C_4H_9^+$ - 18 %) were also observed in the H_3O^+ channel.

With the NO^+ reagent ion, nonanal formed the hydride transfer product at *m/z* 141 ($C_9H_{15}O^+$ - 54 %) and two fragment ions at *m/z* 71 ($C_4H_7O^+$ - 16 %) and *m/z* 57 ($C_3H_5O^+$ - 29 %). There were no literature references to compare these measurements to.

2.3.3.11 Overview of Product Ions and Branching Ratios

A major feature of many of the results in this study compared to those reported in the literature was the greater proportion of fragmentation in these measurements, especially in larger compounds. This was likely due to a combination of the increased flow tube temperature of 140 °C and the increased flow tube voltage increasing the overall energy in the system, leading to greater fragmentation. The temperature of the flow tube in this study was close to the standard operating temperature (120 °C) of the Voice200*ultra*. The measurements referenced above (SP01-05 and SM01) were performed at 'room temperature'. The flow tube temperature was increased to limit the impact of humidity on the product ions, especially when measuring at humid conditions as the presence of humid product ions would complicate both assignment and quantitation of results. The flow tube voltage change from 25 V to 50 V also increases the energy in the reagent ions by increasing the energy gradient through the flow tube. This will accelerate the reagent ions in the instrument faster relative to the reagent ions in a standard Voice200*ultra*, increasing the amount of fragmentation. The fragmentation was so great in the larger chain aldehydes that the O_2^+ spectra were not observed as the spectra produced were so complex.

2.3.4 Secondary Product Ions Formed Under Humid Conditions

The 'humid product ions' were defined as any product ion that is formed in the humid full scan that is not shown in the dry full scan. These 'humid product ions' consist of single, double and triple water adducts of the dry product ion. An example of the formation of a water adduct in the reaction of propanol with H_3O^+ in humid air is shown below in ***Eq. 2.17*** (where $C_3H_7OHH^+$ is formed in ***Eq. 2.15***) and ***Eq. 2.18***, where M is a third body like N_2;

$$C_3H_7OHH^+ + H_2O + M \rightarrow C_3H_7OHH^+.H_2O + M \quad (Eq.\,2.17)$$

$$C_3H_7OH + H_3O^+.H_2O \rightarrow C_3H_7OHH^+.H_2O + H_2O \quad (Eq.\,2.18)$$

It is important to measure the impacts of humidity as many environmental samples will have varying humidity levels. Being able to accurately identify and quantify compounds over a range of environmental conditions is important for the widespread use of the SIFT-MS technique. Measurements of humid product ions have been made before. Spanel et. al. (2017) observed a mixture of primary alcohols (C_2 – C_6) over a sample gas absolute humidity range 1 – 5.5 %. In their study they find the ratio of the H_3O^+ reagent ion to its water adducts, $H_3O^+(H_2O)_{1,2,3}$, to be 70:18:9:4

(H_3O^+:H_3O^+.H_2O:H_3O^+.$(H_2O)_2$:H_3O^+.$(H_2O)_3$) at 1.6 % absolute humidity and 29:14:19:38 (H_3O^+:H_3O^+.H_2O:H_3O^+.$(H_2O)_2$:H_3O^+.$(H_2O)_3$) at 5.5 % absolute humidity. In this study it was observed that H_3O^+ and its water adducts were present at a ratio of 40:60:0:0 at relative humidities ranging from 38-83 %. This suggests that the ion energies are sufficiently high at the higher flow tube temperature used here (the SIFT-MS isrun at 140 ^oC in nitrogen compared to 27 ^oC in helium by Spanel et. al.) that water clusters greater than one water molecule are readily fragmented, if formed at all. Spanel et. al. also observed NO^+ and its primary and secondary water clusters to be 98.4:1.5:0.1 (NO^+:NO^+.H_2O:NO^+.$(H_2O)_2$) at 1.6 % absolute humidity and 94.6:4.3:1.1 (NO^+:NO^+.H_2O:NO^+.$(H_2O)_2$) at 5.5 % absolute humidity whereas only the dry NO^+ reagent ion at 100 % were measured in this study across all observed humidities.

For a limited number of compounds it was possible to measure additional product ions formed under conditions of high humidity. The method required humidifying the diluent line and so to achieve the higher relative humidities (e.g. 80 %) a high diluent flow was required. This meant that ion counts for the low mixing ratio compounds (1-propanol, octanal, 2-octanone, nonanal and decanal) were too low for any meaningful measurement. For benzene, 2-butenal, 2-hexenal, 2-butanone, 2-pentanone, butanal, pentanal and hexanal, ion counts were sufficiently high to determine ions formed from the introduction of humidity.

Table 2.3 – The humid product ions of all compounds measured in this study reported as a percentage of the entire product ion count for each reagent ion. Relative humidities ranged from 37.5 – 83.3 %.

Compound	NO^+			O_2^+		
	Ion	Formula	% Ion Count	Ion	Formula	% Ion Count
Benzene	-	-	-	-	-	-
2-Butenal	87	$C_4H_5O^+(H_2O)$	0.5 – 1.8	87	$C_4H_5O^+(H_2O)$	1.2 – 2.9
	88	$C_4H_6O^+(H_2O)$	0.0 – 0.1	88	$C_4H_6O^+(H_2O)$	13.4 – 19.2
2-Hexenal	115	$C_6H_9O^+(H_2O)$	0.1 -0.4	-	-	-
2-Butanone	-	-	-	61	$C_2H_3O^+(H_2O)$	0.0 – 8.0
				62	$C_2H_4O^+(H_2O)$	0.0 – 0.2
2-Pentanone	-	-	-	87	??	11.0 -15.2
				89	$C_4H_7O^+(H_2O)$	0.4
Butanal	89	$C_4H_7O^+(H_2O)$	3.7	75	$C_3H_5O^+(H_2O)$	0.2
Pentanal	103	$C_5H_9O^+(H_2O)$	25.9	-	-	-
Hexanal	-	-	-	-	-	-

No 'humid product ions' were detected for any compounds in the H_3O^+ channel, this could be due to the high tube temperature (140 °C). This is unusual as studies like those of Spanel et. al. and Smith et. al. have shown the prevalence of humid product ions for reactions of OVOCs with the H_3O^+ reagent ion under wet conditions. This further supports the theory that the energy in the system may be responsible for adduct breaking. Spanel et. al. (2017) found the maximum percentage for the dry product ions for methanol, at an absolute humidity of 1.6 %, to be 43 %, with the remaining 57 % to be made up of the primary and secondary water clusters. They even found that for their largest alcohol, hexanol, at the lowest absolute humidity, 1.6 %, only 90 % of the product was attributable to dry product ions, the remaining 10 % due to the primary and secondary water clusters. Smith et. al. (2014) found similar results for aldehydes. The highest proportion of dry product ions was observed for ethanal, at 2 % absolute humidity, with only 53 % of the product ion resulting from the dry product ion.

Benzene formed no humid product ions at all in this study. Warneke et. al. (2001) also found no humid product ions when measuring benzene over a range of humidities by PTR-MS, as expected as at normal *E/N* values there would be enough energy to fragment them.

Except for butenal and pentanone, the proportion of humid product ions as a percentage of the total product ion count was relatively low, which was attributed to the higher temperature of the flow tube, resulting in only a small impact of humidity on the final ion distribution. Most of the humid product ions increased as a proportion of the total ion count with increasing humidity but there were a couple that did not, these being the butanal and pentanal humid product ions as well as the pentanone *m/z* 89 humid product ion.

For butenal, humid product ions accounted for 0.5 – 1.8 % of the NO^+ product ions and 14.0 – 20.5 % of the O_2^+ product ions over a range of relative humidities from 37.5 – 83.3 %. The humid product ions here are primary water clusters of each of the product ions, e.g. the NO^+ hydride transfer product at *m/z* 69 forms a water cluster ion at *m/z* 87 $C_4H_5O^+.H_2O$.

For pentanone a humid product ion appeared at *m/z* 87 which cannot be assigned to a water cluster of a dry product ion. It is uncertain what this product ion is, but it appears in all humid spectra of the pentanone permeation tube and the proportion of the product ion increases with increasing humidity.

Due to measurements being performed under either dry conditions or near 100 % relative humidity further work would need to be performed to judge whether these responses are linearly related to humidity.

2.4 Conclusions

Rate constants and branching ratios for a range of OVOCs measured by SIFT-MS were presented here under conditions designed to maximise the sensitivity and decrease the formation of water clusters when measuring humid samples, namely a flow tube temperature of 140 ^oC and alterations to the lens voltages compared to standard operating conditions. Nitrogen carrier gas rather than helium carrier gas was used; this is becoming an increasingly common practice in many analytical techniques due to the dwindling supply of helium and associated rising costs. Using nitrogen carrier gas coupled with changed flow tube conditions to better control humidity dependence

and increase sensitivity had a noticeable impact on some rate constants, especially reactions with the NO^+ reagent ion where an adduct is formed. This is particularly noticeable for ketones where NO^+ rate constants in nitrogen carrier gas were up to a factor of 5 lower than those previously measured in helium. This is potentially due to the increased flow tube temperature and voltage as demonstrated by the data presented in ***Section 2.2.2***.

The branching ratios measured in this study were markedly different to those measured previously. Ion energies in the SIFT-MS, and therefore fragmentation and branching ratios, are very dependent upon the operating conditions of the instrument. The higher energy of the reagent ions in the system, from alterations to the flow tube voltage and an increase in the flow tube temperature, led to an increase in fragmentation compared to previous studies. Accurate branching ratios are important as, without external calibration, they are used in SIFT-MS measurements in the quantitation of target compounds. Thus, ensuring the correct branching ratios and product ions is vital for accurate concentration calculations.

The high tube temperature and ion energies in the system also has a large impact on the humidity dependence of the product ions. No secondary product ions with the H_3O^+ reagent ion under humid conditions were observed. However, primary water clusters were observed with the NO^+ and O_2^+ reagent ions but no secondary or tertiary water clusters. In general, the secondary product ions accounted for little of the overall product ion count, with the largest secondary product ion count still only accounting for 26 % of the overall product ion count. The work focusing on varying the conditions described in ***Section 2.2.2*** further shows the large impact of both flow tube temperature and the flow tube voltage on the production and destruction of humid product ions.

Overall, this study shows that adjusting the SIFT-MS for extra sensitivity has a demonstrable impact on ionisation, which may require reassessment of library records for target compounds. Particularly, the application of a flow tube voltage in the Voice200*ultra* compared to instruments used in previous literature has been shown to cause an increase in fragmentation and an impact on the sensitivity of adduct formation product ions. This study shows the impact of varying the flow tube temperature and flow tube voltage on both the branching ratios and sensitivity of benzene, butanone and butanal. It highlights the importance of ensuring that rate

constants and branching ratios used for calibration in SIFT-MS are measured under the same operating conditions as the analyses.

3. Oceanic Methyl Iodide Emissions

3.1 Introduction

Some previous studies have shown that the oceanic photoproduction of methyl iodide has a dependence on ocean iodide concentrations (Y. Chen et al., 2020; Moore and Zafiriou, 1994), but the parameterisation used to calculate global oceanic CH_3I emissions (Bell et al., 2002; Ordóñez et al., 2012) does not include any iodide dependence. This study aimed to re-examine the iodide dependence of methyl iodide production and emissions under both photochemical and non-photochemical regimes. All experiments were carried out under environmentally relevant conditions, including iodide concentrations and ozone concentrations. The measurements of emissions from Plymouth and Bridlington samples were performed by me and the Bermuda measurements were performed by Lewis Marden. Sample collection in Plymouth was performed by the Plymouth Marine Laboratory (PML), in Bridlington by 4 members of my research group (including myself) and the Bermuda sample by Lucy Brown and members of the Bermuda campaign. Measurements of the iodine speciation were performed by me and Matthew Jones. Measurements of total organic carbon (TOC) were performed by Katherine Weddell. Measurements of biological activity were performed by me.

3.2 Experimental

3.2.1 Methyl Iodide Emissions Measurements

A bespoke photochemical cell was created for the work performed. The cell itself consists of an inner chamber lined with PTFE with two ¼" Swagelok inlets for carrier gas flows. This is encased in a stainless-steel shell in two pieces, which can be sealed with clasps, with an open window in the top to allow light into the central chamber as shown in ***Figure 3.1***.

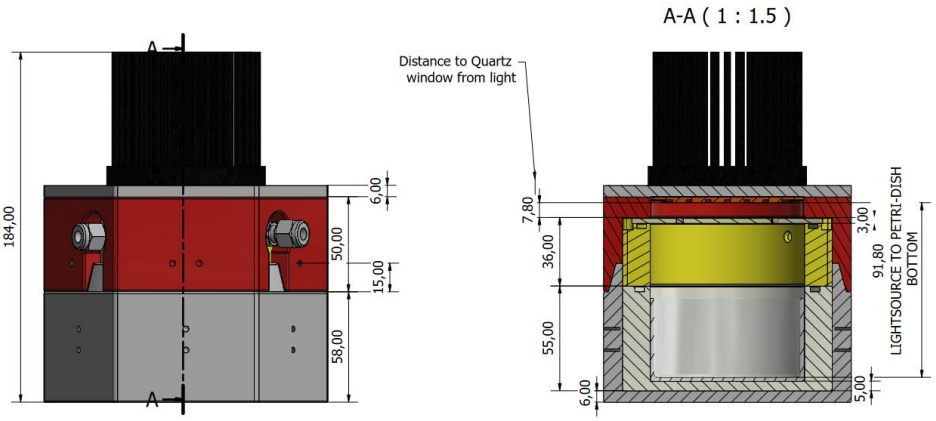

Figure 3.1 – *Schematic of the gas tight photochemical cell. The light grey and yellow hashed sections represent the internal PTFE chamber and the darker grey and red hashed sections represent the external steel casing. Also shown are the two inlet ports (left). The black lines above indicate the location of the IR water filter and the solar simulator lamp. The measurements are in mm.*

A quartz glass window is placed in the top of the chamber to allow UV light to pass through into the reaction chamber and onto the sample that is held in a glass dish inside. The flow diagram shown in ***Figure 3.2*** shows the overall construction of the setup.

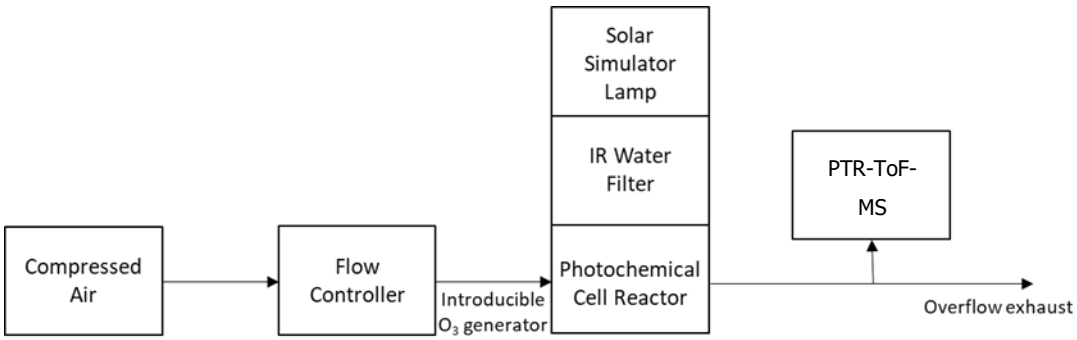

Figure 3.2 – *Flow diagram for the photochemical cell setup.*

Compressed air supplied by a lab generator (Spiralair SPR 5T, Oil Free Compressors, Turin, Italy) was controlled by a mass flow controller (MC-10SLPM-D, Alicat Scientific, Tucson, AZ, USA) and was optionally passed through a Xe-lamp based ozone generator, which when measuring samples exposed to ozone was on for the duration of sample measurement, both dark and light exposure. The compressed air flows though the photochemical cell reactor, which is described above, which was illuminated by a solar simulator lamp (Oriel LCS-100 Small Area Sol1A, Newport Corporation – Oriel Instruments, Bozeman, MT, USA) and filtered by an inhouse built water bath style IR filter to limit heating experienced by the water sample. This flow was then directed to the exhaust and a sample was extracted by a PTR-Tof-MS (Vocus, Tofwerk, Thun, Switzerland). The methyl iodide concentration was then

measured by the instrument and recorded. The instrument can perform a zero check, cutting off the inlet flow by flowing zero air at higher pressure than the sample flow, to allow for results to be zero corrected for internal variation. This zero check is used to account for instrument variations between and during measurements. The PTR-ToF-MS and data processing, including normalisation, are described in S***ection 3.2.6***.

A flow rate of 150 sccm of compressed air was used for this study. This resulted in a headspace displacement rate of 0.75 complete displacements a minute, or that the headspace of the cell was completely removed every 80 seconds. No adjustment was made for losses to the cell in this study.

3.2.2 Solar Lamp Spectrum

The solar simulator lamp used in this study contained an optional filter to adjust the for atmospheric interference. To assess the similarity of the spectrum of light provided by the lamp, both with and without the filter, to that expected to be experienced by samples in the tropics the spectra were compared to a model generated spectrum. The generated spectrum was measured at 15.83842 N 24.64059 W, a point near Cape Verde, to represent a typical tropics region, at midday local time. The spectra were measured using the NCAR Quick TUV Calculator (NCAR, 2016) and two were calculated, one during the Summer Solstice and another during the Winter Solstice, to represent maximum and minimum midday solar exposures. The results are shown in ***Figure 3.3***.

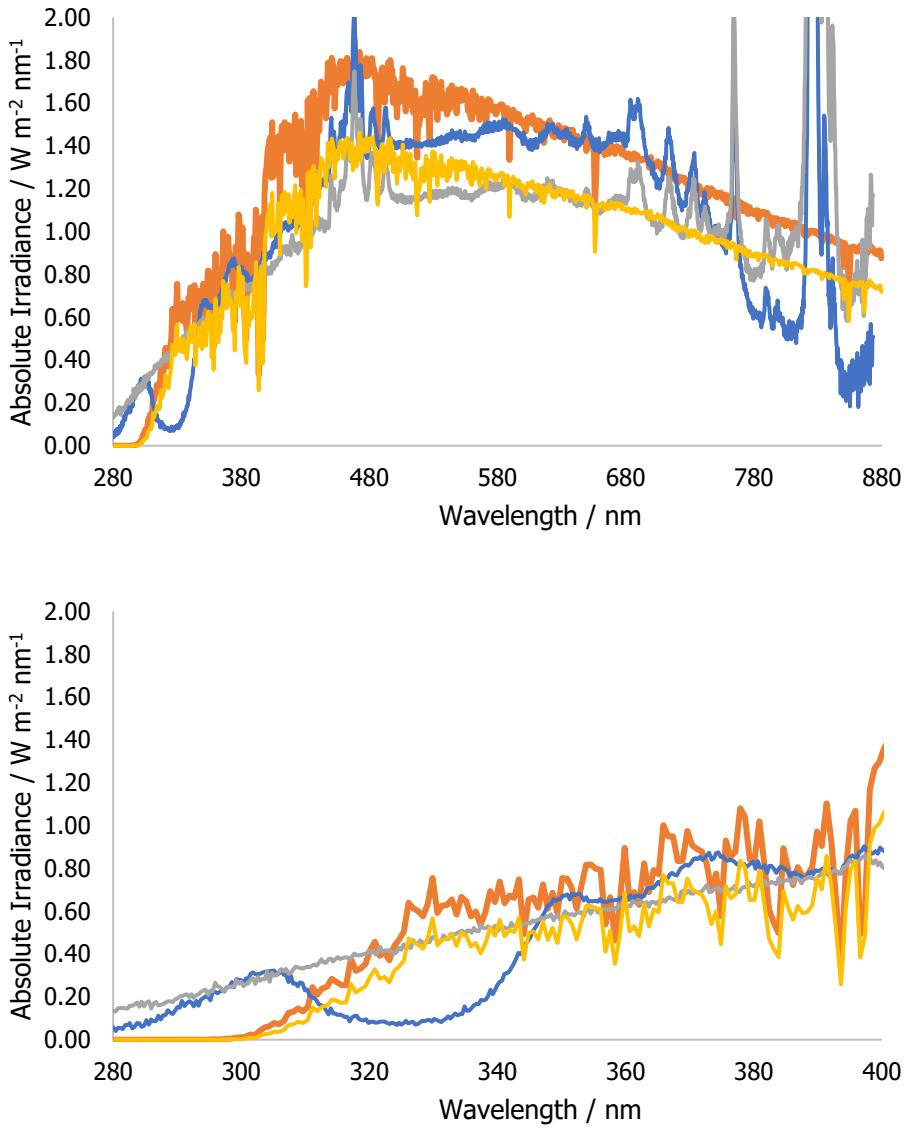

Figure 3.3 *– The absolute irradiance spectra of the solar simulator lamp with filter (Blue) and without filter (Gray) compared to NCAR TUV generated spectra (15.83842, -24.64059) during Summer (Orange) and Winter (Yellow). The full spectrum (top) is shown as well as a zoom in to the UV region (bottom).*

Comparing the two solar lamp spectra the main differences were a large trough in the filter measurement between 307 – 350 nm that does not appear in the unfiltered lamp spectrum. As this trough occurs in the UV region, the primary region in which photochemistry is expected to occur, the decision was made to remove the lamp filter. The spectrum of the lamp without a filter closely matches both the summer and winter TUV spectra in the range 320 – 400 nm. The only major difference is that the lamp produced a higher irradiance in the far UV range of 280 – 320 nm. To ascertain the suitability of the solar lamp as a mimic of the solar spectrum at the ocean surface the average absolute irradiance values in the 320 – 400 nm ranges were compared. The

summer generated spectrum measured an average absolute irradiance of 0.74 ± 0.02 W m^{-2} nm^{-1} and the winter generated spectrum measured 0.56 ± 0.02 W m^{-2} nm^{-1}. This compared to the lamp spectrum average of 0.62 ± 0.01 W m^{-2} nm^{-1} which measured between the two values. Due to the similarities of the shape of the spectrum and the closeness of the measured absolute irradiance value to the generated spectra it was decided no correction factor for the received solar irradiation was required.

3.2.3 Methyl Iodide Measurement Technique

During measurements approximately 160 mL of sample was spiked with between 0 – 1.1 mL of approximately 40 µM (exact value not required due to subsequent iodine speciation) potassium iodide (Sigma-Aldrich). An aliquot of 10 mL was taken, for performing pre-run ancillary measurements, and the remaining 150 mL of sample was placed in a glass dish in the photochemical reactor. The instrument zero was ended and the mass spectrum was measured for 10 minutes with the lamp shield on which blocks all light from the solar simulator lamp. Another instrument zero was performed for 2 minutes and the lamp shield was removed. Another measurement was made for 20 minutes, followed by a 2 minute instrument zero while the lamp shield was turned back on. A final 10 minute measurement with the lamp shield on was performed. The instrument was then set to zero until the next sample was measured. The zero before and after a measurement is averaged and subtracted from the corresponding measurement, e.g. for the 11:34 – 11:44 measurement shown in ***Figure 3.4*** the zero immediately before and after were averaged and subtracted from the result to zero correct. An aliquot of 10 mL was again taken to perform post-run ancillary measurements. A blank measurement was performed in an identical manner using non-spiked HPLC water.

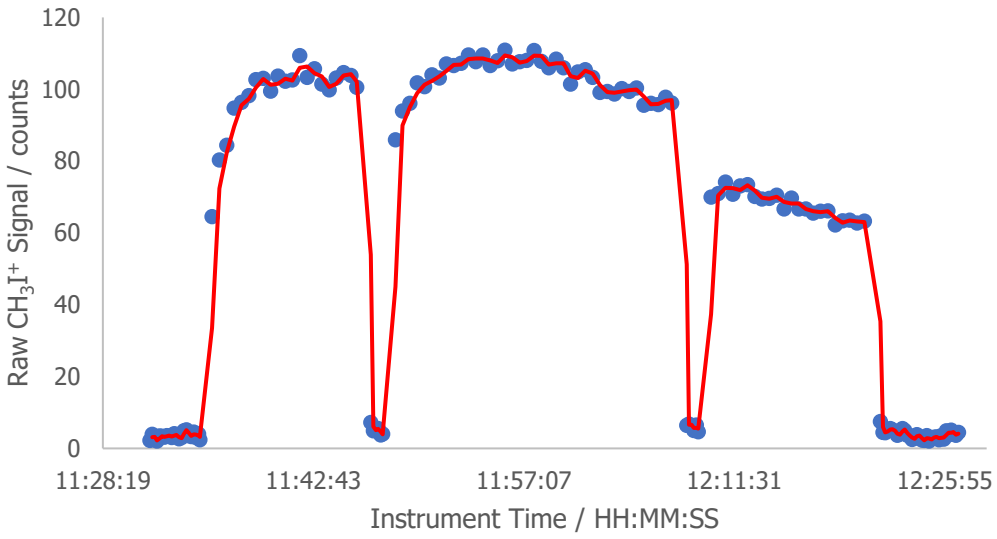

Figure 3.4 – *An example of the results of the experiment for a typical sample, the large dips showing the instrument zero. The results are 10 s averaged.*

As shown in ***Figure 3.4*** when switching from to CH_3I sampling from a zero, the signal takes time to equilibrate and can also begin to decrease over the course of the measurement. The initial dark reaction has the longest equilibration time followed by a stable signal, the light reaction takes a minute or two to build to peak production and then remains stable for around 5 minutes before beginning to decay, indicating a depletion of readily available precursors for methyl iodide production. Consequently, the second dark signal shows a reduction in methyl iodide production as well as a similar decay pattern to that seen at the end of the light regime. To obtain more precise and stable results, the data were filtered by removing all measurements which were 2 standard deviations above or below the average. This included the removal of equilibration data points and the removal of the points at which methyl iodide production begins to decay as the analysis is focused on peak methyl iodide production.

3.2.4 Methyl Iodide Calibration

To calibrate the instrument a permeation tube setup similar to that described in Chapter 2 was used. The methyl iodide permeation tube (385 ± 22 ppb) was measured on the instrument across multiple dilutions and the methyl iodide mixing ratio was plotted against the signal ***(Figure 3.5)***. To eliminate the impact of source fluctuations the raw CH_3I^+ product ion signal was reagent ion corrected using the sum of the NO^+ and O_2^+ reagent ions during zero measurements, both of which undergo charge transfer reactions with methyl iodide to form the CH_3I^+ product ion. The

gradient of ***Figure 3.5*** is equal to the sensitivity of the instrument to methyl iodide in ncps ppb^{-1}. All but the three Bermuda samples were calibrated using this method. Four calibrations were performed over the course of the measurements with no clear trend in sensitivity, therefore it was decided to take the average of the four sensitivities, giving a sensitivity of 0.579 ± 0.075 ncps ppb^{-1} (an error of 13.0 %). The error here is calculated from the propagation of the error in the concentration from permeation tube and the error of each individual calibration line.

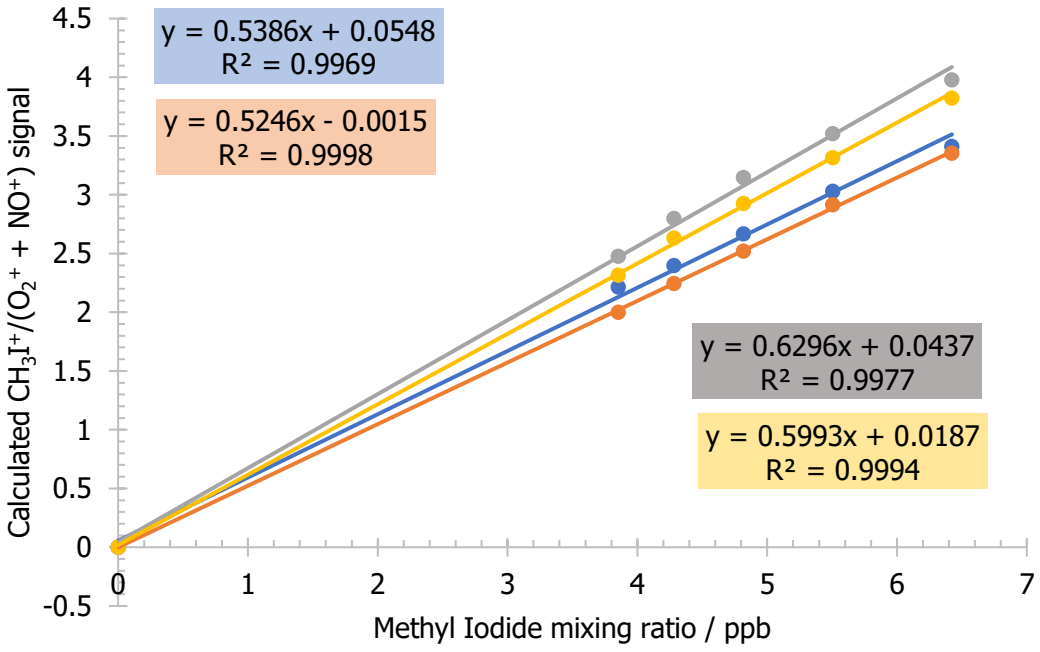

Figure 3.5 – *Methyl iodide permeation tube calibrations performed on the Vocus PTR-ToF-MS for the Plymouth and Bridlington samples. Colours indicate calibrations run on different days, Blue = 1st March 2022, Orange = 2nd March 2022, Gray = 3rd March 2022, Yellow = 4th March 2022.*

For the measurements performed in Bermuda a new calibration was performed with a new methyl iodide permeation tube ***(Figure 3.6)***. Only a single calibration was performed due to the smaller number of samples measured. The calculated sensitivity was 0.055 ± 0.001 ncps ppb^{-1}, an order of magnitude lower than measured previously. It is uncertain what caused this difference, but it may be due to numerous compounding factors including the shipping of the instrument to Bermuda and alterations to the instrument before it was shipped to modify it for field measurements. One major factor between the two measurements is the differing source gases. The measurements performed in York were done when the group was learning how to effectively use the instrument. It was unknown at the time but the reduction of the H_3O^+ flow within the instrument to increase sensitivity led to air being drawn into the plasma, this is what led to the generation of O_2^+ and NO^+ ions that

were used as reagent ions. Exposure to air is damaging for the instrument and so the source for the Bermuda samples was switched to a pure O_2 cylinder. This may be why the calibrations look different to each other but give similar results.

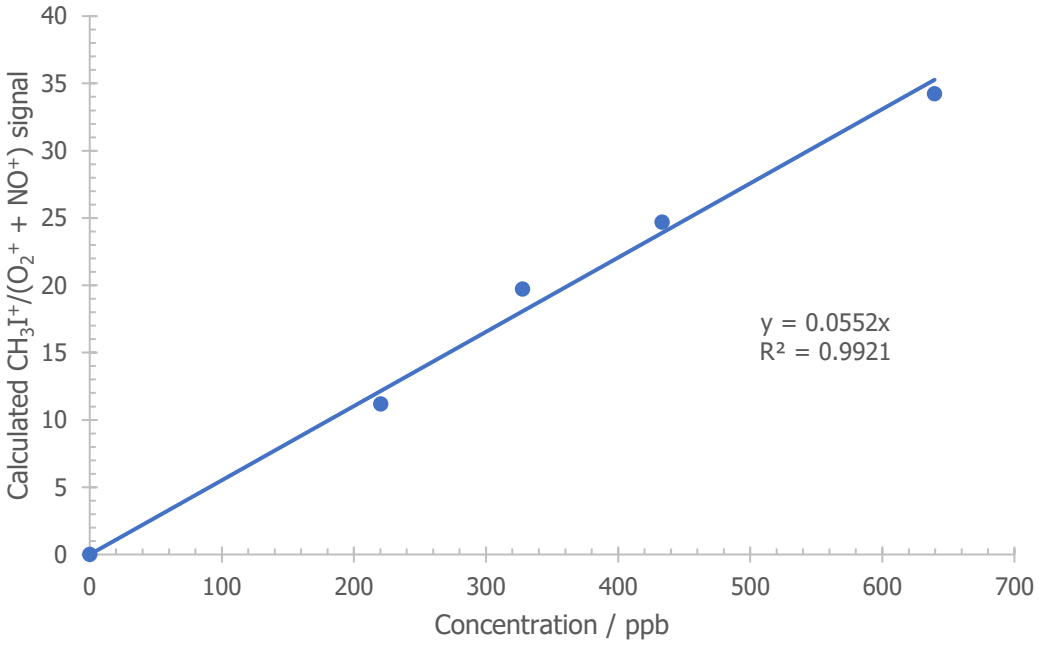

Figure 3.6 – *Methyl iodide permeation tube calibrations performed on the Vocus PTR-ToF-MS for the Bermuda samples.*

3.2.5 Methyl Iodide Emissions Calculations

To convert from the reagent corrected methyl iodide signal to a methyl iodide mixing ratio the value was divided by the sensitivity (S) as shown in ***Eq. 3.1***.

$$C_{MI}\ (ppt) = \frac{N_{CH_3I^+/(NO^+ + O_2^+)}\ (cps)}{S\ (cps\ ppb^{-1})} \times 1000 \quad (Eq. 3.1)$$

Where C_{MI} is the mixing ratio of methyl iodide in ppt, N, is the signal in counts per second and S is the sensitivity in normalised counts per second ppb^{-1}. The error in the mixing ratio, Err_{CMI}, was calculated as shown in ***Eq. 3.2***,

$$Err_{C_{MI}} = C_{MI}\sqrt{\left(\frac{Err_{N_{CH_3I^+/(NO^+ + O_2^+)}}}{N_{CH_3I^+/(NO^+ + O_2^+)}}\right)^2 + \left(\frac{Err_S}{S}\right)^2} \quad (Eq. 3.2)$$

where the error in the methyl iodide signal, Err_N, was calculated by propagating the errors of the ncps of methyl iodide and the ncps of the reagent ions, NO^+ and O_2^+, and the error in the sensitivity, Err_S, was calculated from the slope error of the calibration and the error in the methyl iodide mixing ratio from the permeation tube.

The value, C_{MI}, can be used to calculate the emissions from either a surface area or from a volume. This allowed comparison between previous measurements performed in literature and this work. The equations to calculate the emissions by surface area ***(Eq. 3.3)*** and by volume ***(Eq. 3.15)*** are shown below.

$$E_{SA} = \frac{C_{MI} N_{air} F_{air} N_A}{A_l} \quad (Eq. 3.3)$$

Where E_{SA} is the emissions from the surface in nmol m^{-2} day^{-1}, C_{MI} has been converted from ppt to mol, N_{air} is the number of molecules of air in mol m^{-3}, F_{air} is the flowrate of the air in m^3 day^{-1}, N_A is Avogadro's number in mol^{-1} and A_l is the liquid surface area of the sample. These emissions are calculated as peak emissions values assuming a constant source of iodide and methyl radicals and so the rate of change of concentration with time has been assumed to be zero.

The error in surface area based emissions is calculated based on a propagation of the errors of the constituent parts ***(Eq. 3.4)***.

$$Err_{E_{SA}} = E_{SA} \sqrt{\left(\frac{Err_{C_{MI}}}{C_{MI}}\right)^2 + \left(\frac{Err_{N_{air}}}{N_{air}}\right)^2 + \left(\frac{Err_{F_{air}}}{F_{air}}\right)^2 + \left(\frac{Err_{A_l}}{A_l}\right)^2} \quad (Eq. 3.4)$$

Where Err_{CMI} is calculated in ***Eq. 3.2***, Err_{Nair} is calculated by propagating the errors of the $pV=nRT$ equation it is calculated from, Err_{Fair} is the error in the flowrate determined as the flow accuracy (0.8 %) reported by Alicat and Err_{Al} is the error in the surface area calculated from the measurement error of the radius of the glass dish.

The alternative emissions calculation based on sample volume is shown below, with the only difference being the replacement of the surface area, A_l, with the volume, V_l. These calculations were performed to compare to similar measurements performed by similar studies (Richter, 2004; Zafiriou, 1974b).

$$E_V = \frac{C_{MI} N_{air} F_{air} N_A}{V_l} \quad (Eq. 3.5)$$

The error calculation for E_V is hence the same as that calculate in ***Eq. 3.4*** but with the surface area terms replaced with those for the volume instead.

3.2.6 Vocus PTR-ToF-MS and Reagent Ion Normalisation

All samples were run on a Vocus PTR-Tof-MS (TOFWERK, Thun, Switzerland) running using the PTR mode of the instrument.

For the experiments performed in York the instrument sampled 150 sccm from the sample flow. The focussing ion-molecule reactor (FIMR) was operated at a front and back voltage of 700 V and 20 V, a pressure of 1.5 mbar and a temperature of 150 ^{o}C. The flow rate of H_3O^+ was set to 1 sccm. These parameters were used as they produced the highest sensitivity for measuring methyl iodide. This resulted in a system in which NO^+ and O_2^+ were produced at far greater amounts than H_3O^+. During the pre-measurement zero blank the H_3O^+ reagent ion measured 0.514 cps whereas the NO^+ reagent ion measured 112 cps and the O_2^+ reagent ion measured 475 cps.

For the experiments performed in Bermuda the instrument sampled 150 sccm from the sample flow. The focussing ion-molecule reactor (FIMR) was operated at a front and back voltage of 700 V and 30 V, a pressure of 1.5 mbar and a temperature of 150 ^{o}C. The experiments used a 10 sccm flow of O_2 as the reagent flow, meaning O_2^+ and limited amounts of generated NO^+ were the reagent ions.

Due to small variations occurring within the instrument overtime throughout the experiments all the measurements were normalised to standard reagent ions. Under the conditions of the York experiments the H_3O^+ reagent ion and its water adducts were below the detection limit of the instrument. Instead, the NO^+ and O_2^+ reagent ions were used as stable normalisation ions as it is expected that these were the ions generating the CH_3I^+ product ion. Over a 5 hour period of measurement the zero values of the NO^+ reagent ion were 116 ± 0.38 cps (a range of 95.7 – 131 cps) and O_2^+ reagent ion were 505 ± 1.49 cps (a range of 421 – 562 cps). To calculate the normalised ion count the sum of the averages of each of the ions were taken from the zero performed before and after a measurement. These two totals were then averaged together to give an estimated value over the measurement. To normalise the measured value it is then divided by this estimated total reagent ion. The actual value of the NO^+ and O_2^+ ions during measurements cannot be used as it was partially depleted due to reacting with compounds in the sample flow.

3.2.7 Sample Collection and Preparation

Water samples were collected at three separate locations, Plymouth (UK), Bridlington (UK) and Hog Bay (Bermuda). The Plymouth samples were split into two groups, water from the footprint of the Penlee Point Atmospheric Observatory (PPAO) were labelled PF and water from the Plymouth estuary were labelled PY. Samples were also split into surface microlayer (SML) and underlying water (ULW) fractions. These samples were treated in various ways (with both SML and ULW being treated the same), PY1 samples were unfiltered, PY1 O3 samples were unfiltered and exposed to 60 ppb O_3, PY2 samples were amalgamated and 0.2 µm filtered, PF3 samples were 0.7 µm filtered, PF4 samples were 0.2 µm filtered and PF5 samples were 0.2 µm filtered and deoxygenated by bubbling through N_2 before being measured. The PY samples were collected on 29th September 2021 and the PF samples were collected on 21st May (PF3), 19th April (PF4) and 8th May (PF5) all in 2018. The sample locations are shown in ***Figure 3.7***.

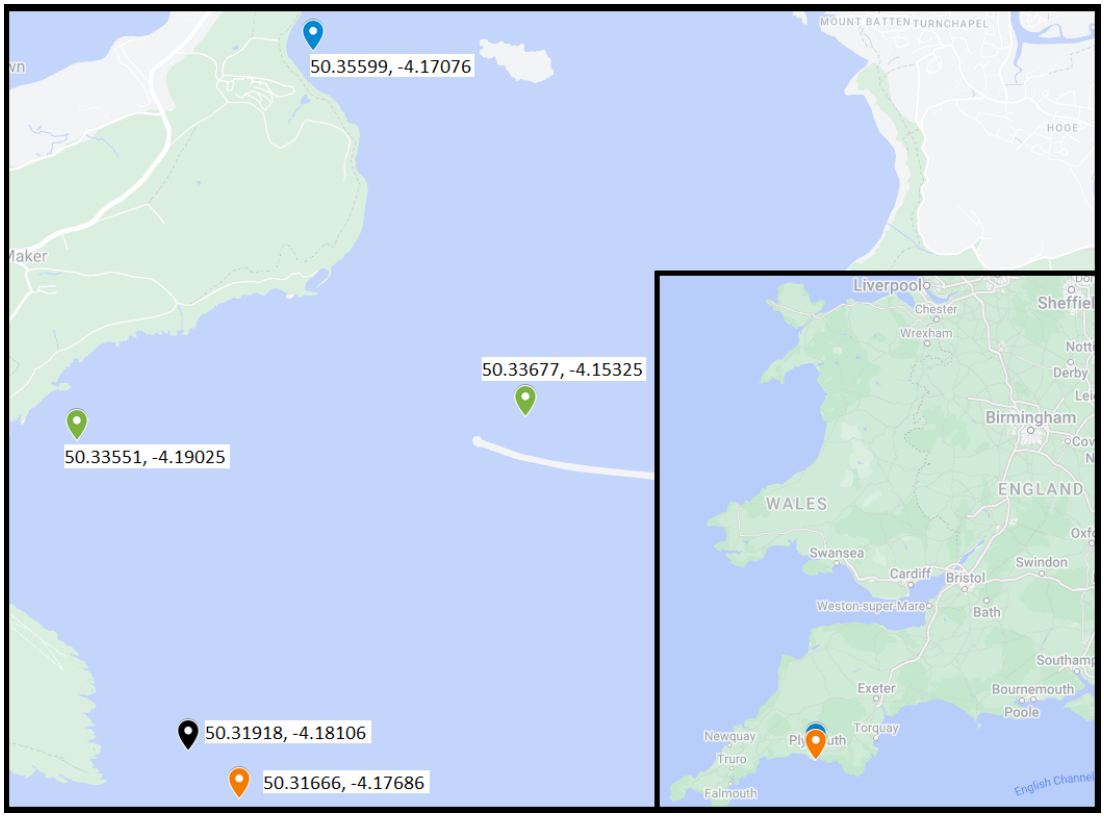

Figure 3.7 – *A map showing the locations of the various Plymouth samples where blue is PY1, green are both PY2, black is PF3 and PF5 and orange is PF4. The inset shows the location of Plymouth Sound in relation to the geography of the United Kingdom.*

The Bridlington sample (54.09562, 0.03952) was collected on the 15th August 2018 from a point about 8 km off the coast of Flamborough Head and 23 km off the coast of Bridlington. This sample was split into B1, which was 0.7 µm filtered, and B2 which was 0.2 µm filtered.

The Bermuda samples were collected off the southwest coast of Hog Bay, Bermuda, about 300 m from the shoreline. Sample S1 was collected on the 4th July 2022, which was left unfiltered, and sample S2 was collected 27th June 2022 and was filtered. The sample locations are shown in ***Figure 3.8***.

Figure 3.8 – *A map showing the locations of the Bermuda sample sites with blue being the site of S1 and red being the site of S2. The inset shows the locations in relation to the archipelago of Bermuda.*

SML samples were collected using custom built steel-frame Garrett screens and ULW samples were collected using a plastic niskin bottles able to be opened remotely underwater.

3.2.8 Iodine Speciation

Measurements were performed as described in Jones et. al. (2023). All standards and reagents were made up in 18.1 MΩ deionised water (Di-H_2O). For ion chromatography (IC), the isocratic mobile phase was 0.4 M sodium chloride (NaCl, Sigma-Aldrich BioXtra ≥99.5%; 2 M stock solution). Potassium iodide (KI, Fisher ≥99 %) standards

were produced through serial dilutions of a gravimetrically prepared ~0.1 M solution. The following reagent stock solutions were used; 10% w/v hydroxylamine hydrochloride (NH_2OH-HCl; Sigma-Aldrich Reagent Plus, 99 %), 70 mM calcium hypochlorite ($Ca(ClO)_2$, Sigma-Aldrich Technical Grade) and 500 mM sodium sulphite (Na_2SO_3, Sigma-Aldrich, min. 98%), the Na_2SO_3 was refreshed bi-monthly.

Iodide samples were prepared by adding 800 µL of sample to 832 µL of Di-H_2O (as a diluent). Inorganic iodine samples were prepared by adding 32 µL of NH_2OH-HCl to 800 µL of sample and 800 µL of Di-H_2O. Total iodine were prepared by adding 12 µL of 24 mM $Ca(ClO)_2$ to 800 µL of sample and 800 µL of Di-H_2O, after waiting for an hour 20 µL of 220 mM Na_2SO_3 and 571 mM NH_2OH.HCl were added. All samples were then shaken to ensure thorough mixing before measurement.

To measure iodide, a chromatographic separation of the sample was performed on a 400 µL analytical replicate using an Agilent 1100 HPLC with a 1260 series detector monitoring absorbance at 226 nm over a 60 mm path length. The isocratic mobile phase was 0.4 M NaCl at 0.64 mL min^{-1}. The guard and analytical columns were Dionex IonPac AS-23 4x50 mm and 4x250 mm, respectively. Once injected, the chromatogram was collected for 16.1 minutes; iodide eluted at c.11 minutes.

Iodate and dissolved organic iodine were quantified as iodide following chemical amendments described above which selectively converted iodine fractions to iodide. A chemical reduction of the sample enabled the measurement of the inorganic iodine fraction (Iinorg = iodide + iodate) allowing for the quantification, by difference, of iodate. A second chemical manipulation enabled measurement of the total dissolved iodine fraction (dIT = Iinorg + DOI) and hence quantification, by difference, of dissolved organic iodine (DOI). All standards, blanks, samples and chemical amendments were added to acid-washed class 1 hydrolytic glass vials; the caps contained a polytetrafluoroethylene (PTFE) septum.

3.2.9 TOC Measurements

Total organic carbon (TOC) measurements were run on an Elementar Various TOC cube. Approximately 9 mL of seawater sample, blank or standard was added to a 12 mL vial covered in foil. All samples, blanks and standards (a range of 0.5 – 3.5 mg L^{-1}, 50 mg L^{-1} standard, Sigma Aldrich) were then loaded into the instrument along with a vial containing 10 % HCl. Vials were acidified prior to measurement and each vial was measured in triplicate.

3.2.10 Bacterial Measurements

Bacterial count, both live and dead, was measured using a LIVE/DEAD *Bac*Light Bacterial Viability Kit (ThermoFisher Scientific, Waltham, MA, USA) and a Beckman Coulter CytoFLEX S flow cytometer (Beckman Coulter Life Sciences, Indianapolis, IN, USA) ("LIVE/DEAD BacLight Bacterial Viability Kits," 2004). An equal volume of SYTO 9 and propidium iodide dyes were mixed to form a dye mixture, 15 µL of which was added to 5 mL of each measured sample. These combined mixtures of dye and sample were then individually mixed using a vortex mixer (Cole-Parmer, St Neots, UK) at 500 rpm to ensure homogenisation. The samples were then incubated in the dark at room temperature for 15 minutes before 5 µL of sample was added to individual wells for measurement by flow cytometry.

3.3 Results and Discussion

3.3.1 Iodide Dependence of Methyl Iodide Emissions

The results of the methyl iodide experiments are performed on the Plymouth, Bridlington and Bermuda waters as described in ***Section 3.2.1*** are summarised in ***Table 3.1***, ***Table 3.2*** and ***Table 3.3***. Of particular interest in these results is the presence of an iodide dependence of methyl iodide production in dark and light conditions, but only for certain samples ***(Figure 3.8)***. These samples were PYSML1 and PFSML3. The main similarities between these two samples were that they were the least filtered of the Plymouth SML samples, with PYSML1 being unfiltered and PFSML3 being 0.7 µm filtered. All other samples, as well as the samples from Bridlington or from Bermuda, exhibited iodide-independent methyl iodide emissions.

Table 3.1 – CH_3I mixing ratios measured from all emissions experiments.

Sample	Date	Filtered	O_3	Light	Methyl Iodide Mixing Ratio / ppt			
					Minimum	Maximum	Average	Error
PYSML1	29/09/21	N/A	N	Off	92.3	448	282	117
				On	77.6	312	209	86.1
PYSML1 O_3	29/09/21	N/A	Y	Off	-8.94	-0.61	-5.63	8.27
				On	7.10	55.6	25.3	33.3
PYULW1	29/09/21	N/A	N	Off	43.6	262	132	72.3
				On	27.7	242	106	63.2
PYULW1 O_3	29/09/21	N/A	Y	Off	-1.21	51.9	22.4	20.6
				On	16.0	41.3	30.3	27.3
PYSML2	29/09/21	0.2 µm	N	Off	50.5	63.4	56.4	48.9
				On	15.8	48.9	27.4	58.1
PYULW2	29/09/21	0.2 µm	N	Off	-0.73	36.6	20.1	16.1
				On	8.94	94.1	30.0	34.0
PFSML3	21/05/18	0.7 µm	N	Off	39.2	364	175	91.5
				On	72.3	258	146	69.5
PFULW3	21/05/18	0.7 µm	N	Off	-2.22	27.2	17.8	14.6
				On	-1.39	44.7	23.4	28.2
PFSML4	19/04/18	0.2 µm	N	Off	29.7	33.8	37.4	12.1
				On	50.2	78.2	62.2	29.2
PFULW4	19/04/18	0.2 µm	N	Off	-13.5	40.4	14.4	19.9
				On	19.6	49.1	28.7	24.6
PFSML5	08/05/18	0.2 µm	N	Off	17.4	29.6	24.5	13.3
				On	19.9	45.0	30.3	26.0
PFULW5	08/05/18	0.2 µm	N	Off	31.3	45.6	37.6	43.7
				On	-2.35	34.0	11.3	48.9
BSML1	15/08/18	0.7 µm	N	Off	22.0	69.8	50.8	23.0
				On	42.6	62.7	48.6	26.6
BULW1	15/08/18	0.7 µm	N	Off	16.8	19.9	18.3	10.8
				On	4.90	28.1	16.5	25.2
BSML2	15/08/18	0.2 µm	N	Off	26.5	49.2	33.9	16.1
				On	36.5	71.2	54.8	30.9
S1U	04/07/22	0.7 µm	N	Off	10.3	17.3	14.9	3.40
				On	110	135	129	28.0
S1F	04/07/22	0.2 µm	N	Off	11.2	17.3	14.8	2.42
				On	84.4	96.8	90.3	19.3
S2U	27/06/22	0.7 µm	N	Off	50.0	67.6	57.8	14.8
				On	59.2	78.7	71.7	21.9

Table 3.2 – Iodine speciation of measured samples before the run.

Sample	$[I^-]$ / nM		$[IO_3^-]$ / nM		[Org I] / nM		[I] / nM	
	Value	Error	Value	Error	Value	Error	Value	Error
PYSML1	107	11.7	219	8.58	45.8	9.43	371	20.7
PYSML1 O_3	195	37.2	217	9.06	63.9	11.8	476	49.8
PYULW1	172	45.1	222	16.8	37.6	12.5	431	48.8
PYULW1 O_3	189	41.1	209	8.11	46.7	7.95	445	48.6
PYSML2	263	45.9	301	6.76	41.4	14.2	606	53.8
PYULW2	211	46.8	292	18.2	29.8	7.54	532	52.3
PFSML3	61.8	10.8	210	7.65	26.0	7.04	297	15.3
PFULW3	155	49.0	172	30.1	7.22	8.66	334	81.9
PFSML4	182	37.2	245	7.61	18.0	8.33	445	43.4
PFULW4	171	35.4	256	7.61	13.6	8.00	441	43.1
PFSML5	144	53.1	207	15.8	27.9	10.4	379	74.1
PFULW5	220	50.7	272	4.88	4.68	4.28	496	50.7
BSML1	252	48.0	310	7.49	23.4	5.21	585	50.7
BULW1	174	38.0	283	12.6	12.8	14.5	470	52.8
BSML2	181	45.8	295	24.5	28.0	21.0	504	56.2
S1U	-	-	-	-	-	-	-	-
S1F	-	-	-	-	-	-	-	-
S2U	-	-	-	-	-	-	-	-

Table 3.3 – Biological activity and total organic carbon data for measured samples before and after the runs.

Sample	Syto9+ve Events / μL^{-1}		[TOC] mg L^{-1}		
	Before	After	Before	After	Loss
PYSML1	321	320	1.01	0.99	0.02
PYSML1 O_3	-	-	1.57	1.67	-0.11
PYULW1	247	232	1.89	1.15	0.74
PYULW1 O_3	-	-	1.89	0.96	0.93
PYSML2	67.5	78.1	0.85	0.85	0.00
PYULW2	70.2	92.6	0.91	1.11	-0.20
PFSML3	105	74	0.96	1.07	-0.12
PFULW3	84.4	87.3	0.81	1.09	-0.29
PFSML4	60.2	81.1	1.84	1.79	0.05
PFULW4	43.4	76.0	1.27	1.42	-0.15
PFSML5	217	120	1.58	1.78	-0.20
PFULW5	117	66.3	1.09	0.93	0.16
BSML1	169	140	1.39	1.13	0.27
BULW1	198	231	1.50	0.91	0.59
BSML2	198	175	1.33	0.97	0.36
S1U	-	-	1.21	-	-
S1F	-	-	-	-	-
S2U	-	-	1.69	-	-

CH_3I emissions were also found to be significantly suppressed in the presence of ozone (red lines in ***Figure 3.9***), a reduction of 288 ± 117 ppt for the SML sample exposed to ozone and 110 ± 75.2 ppt for the ULW sample. To the best of my knowledge this has not been measured before. This may have significant implications for the production of methyl iodide in the marine atmosphere and requires further work to ascertain the full impacts. The exposure to light often increased the production of methyl iodide, though this was usually within error of the dark run. The samples for which exposure to light decreases the methyl iodide production relative to the dark exposure tend to be the reactions in which iodide dependence of methyl iodide production was observed (PYSML1 and PFSML3). The only increases that occur that are not within error are those of the Bermuda S1U and S1F samples which see much greater methyl iodide production under exposure to light.

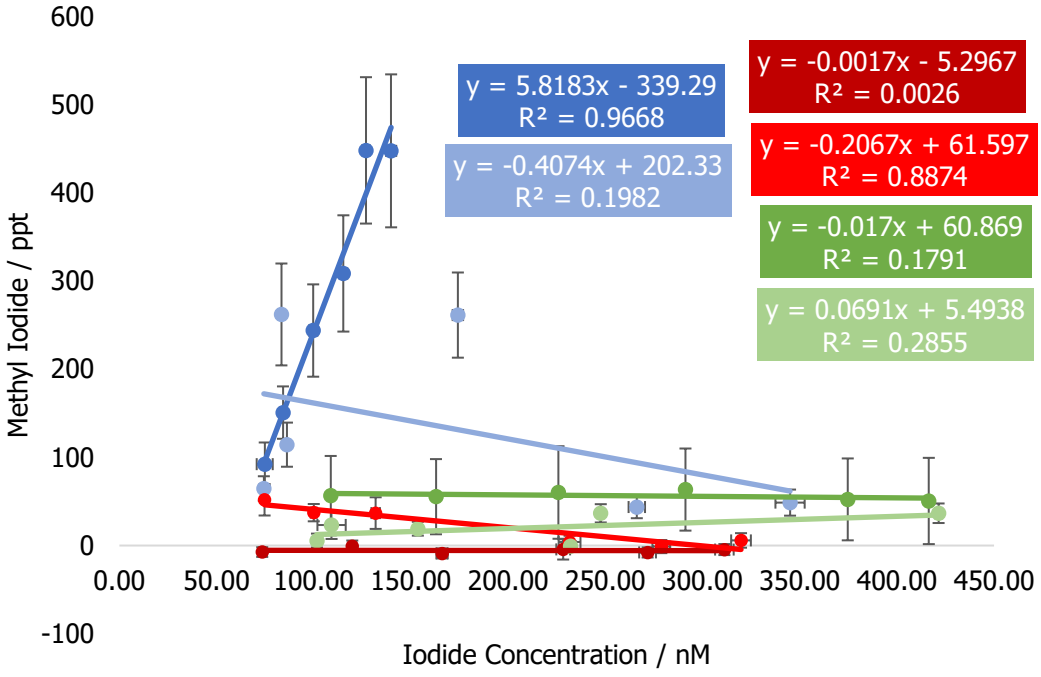

Figure 3.9 – *Methyl iodide mixing ratios of the dark experiments using PY samples, with dark colours representing SML samples and light colours representing ULW samples. Blue is sample PY1 (unfiltered), red is sample PY1 O3 (unfiltered, 60 ppb O_3) and green is sample PY2 (0.2 µm filtered).*

The data in ***Figure 3.9*** shows that a strong positive correlation was found between CH_3I mixing ratios and iodide in the PYSML1 samples with an R^2 value of 0.9668. The remaining results from PY suggested no iodide dependence at all. The SML was found to emit higher amounts of CH_3I than the corresponding ULW samples, except for when the samples were exposed to ozone. It is possible that the ozone in the system outcompetes the methyl iodide release mechanism. The O_3 in the PY1 O3 sample may

be reacting with the DOC, which is commonly assumed to be the rate limiting precursor of CH_3I (Bell et al., 2002), or that the O_3 is preferentially reacting with the iodide to form IO and iodine.

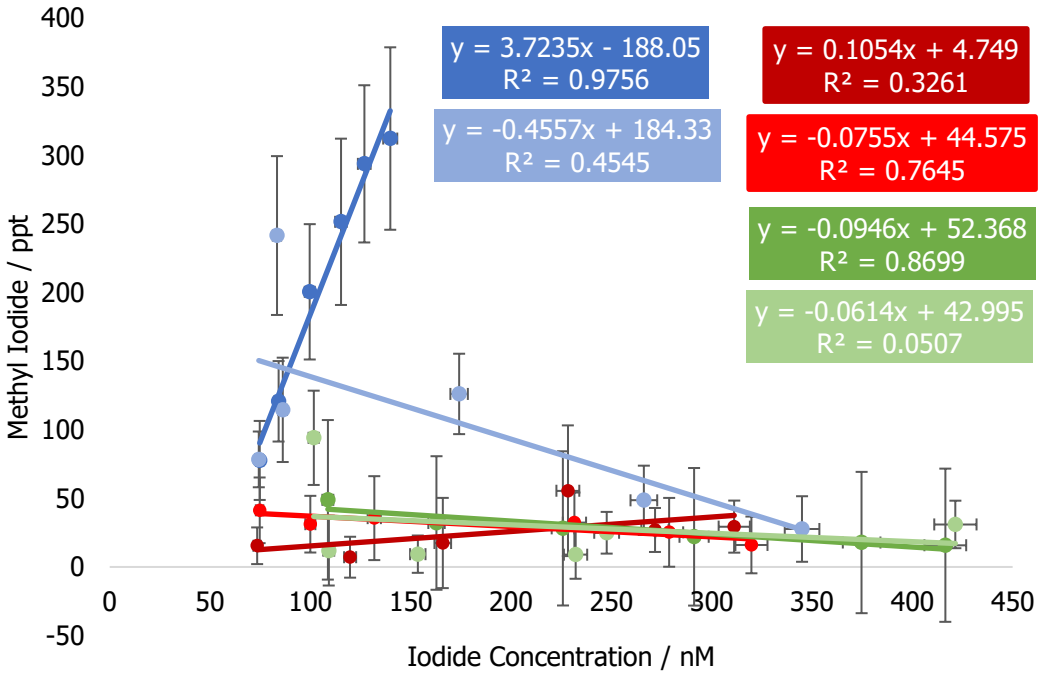

Figure 3.10 - *Methyl iodide mixing ratios of the light experiments using PY samples, with dark colours representing SML samples and light colours representing ULW samples. Blue is sample PY1 (unfiltered), red is sample PY1 O3 (unfiltered, 60 ppb O_3) and green is sample PY2 (0.2 µm filtered).*

Figure 3.10 shows the results of the illuminated experiments. Similar trends to the dark experiments were seen. The only sample which showed an iodide dependant reaction was again PYSML1, though the gradient of the reaction was lower than in the dark reaction. This suggests that the introduction of light suppresses the process by which iodide enhances CH_3I production in these estuarine samples. In other samples the amount of methyl iodide released generally increased in the light compared to the dark. This is consistent with the expected light production method shown in ***Eq. 1.9***.

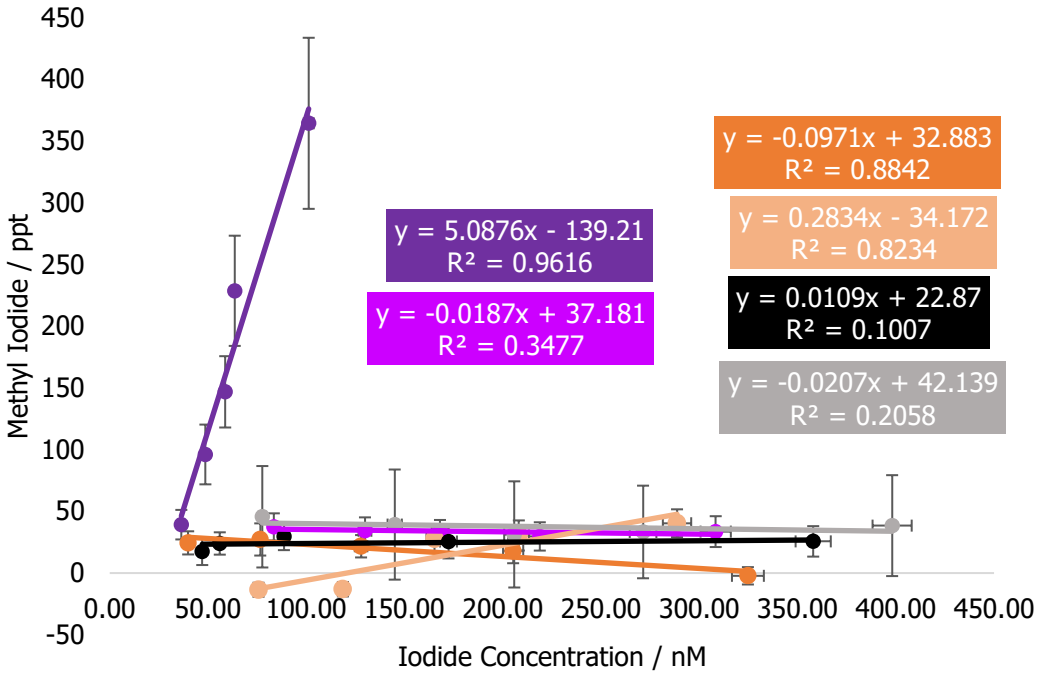

Figure 3.11 - *Methyl iodide mixing ratios of the dark experiments using PF samples, with dark colours representing SML samples and light colours representing ULW samples. Purple is sample PF3 (0.7 µm filtered), orange is sample PF4 (0.2 µm filtered) and black/grey is sample PF5 (0.2 µm filtered + deoxygenated).*

Figure 3.11 compares the CH_3I measured from different PF samples (all filtered to 0.2 µm except PF3 which were filtered to 0.7 µm) in the dark. PFSML3 (dark purple) shows an iodide dependant reaction like that observed in the PY samples. Similar to the PY samples, the remaining samples are all iodide independent. Other than PFSML3, the CH_3I emitted across all samples, for all concentrations of iodide, were very similar implying that once filtered to 0.2 µm there is little extra variation in CH_3I emission, possibly due to low precursor availability.

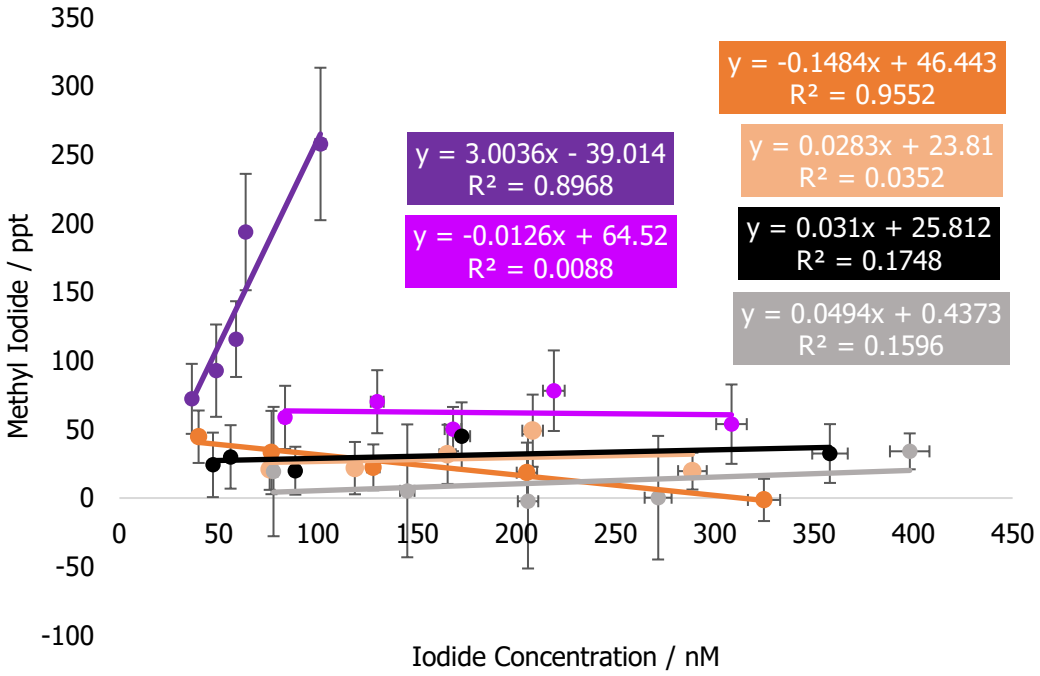

Figure 3.12 - *Methyl iodide mixing ratios of the light experiments using PF samples, with dark colours representing SML samples and light colours representing ULW samples. Purple is sample PF3 (0.7 µm filtered), orange is sample PF4 (0.2 µm filtered) and black/grey is sample PF5 (0.2 µm filtered + deoxygenated.*

Figure 3.12 compares the CH_3I measured from different PF samples (all filtered to 0.2 µm except PF3 which was filtered to 0.7 µm), both SML and ULW, under illumination. The CH_3I measured from the PFSML3 sample under light conditions (dark purple) was lower in magnitude than detected under dark conditions ***(Figure 3.11)***, similar to that of PYSML1. In the other samples however, higher CH_3I amounts were detected in the light experiments compared to the dark experiments. The largest increase (from dark to light) seems to appear for the PFULW3 sample, though all of these reactions appear generally within the same error range at 100 ppt or below.

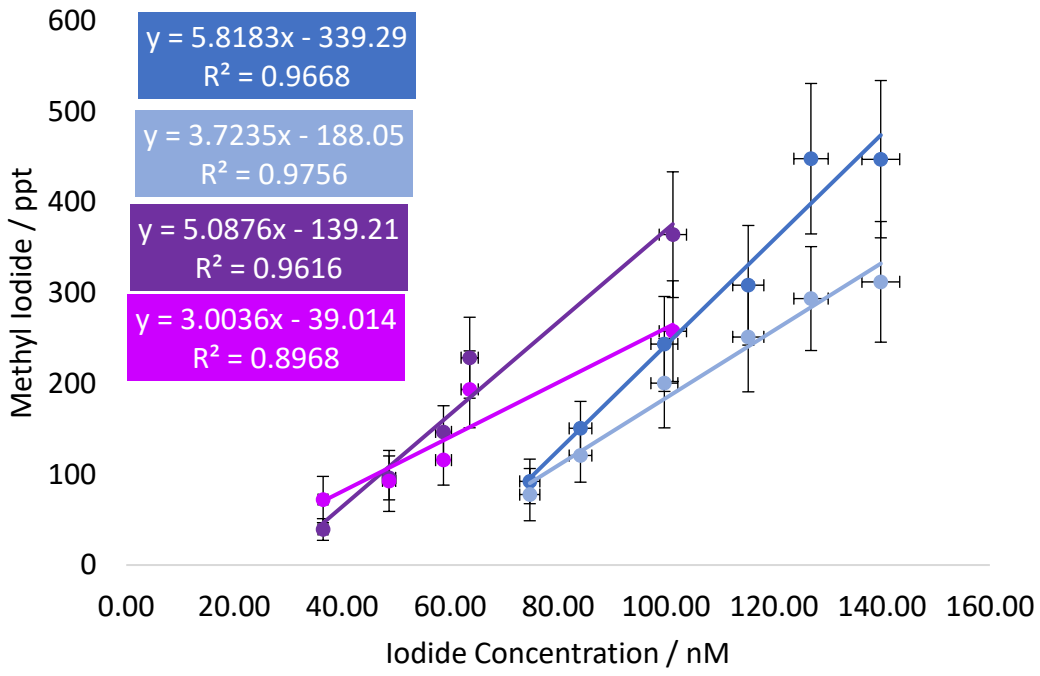

Figure 3.13 – *Methyl iodide mixing ratios of the dark and light experiments using the PYSML1 (blue - unfiltered) and PFSML3 (purple – 0.7 µm filtered) samples. The darker colour represents the dark reaction and the lighter reaction represents the light reaction.*

Figure 3.13 compares the results of the dark and light experiments where CH_3I was found to increase with $[I^-]$, namely from samples PYSML1 (unfiltered) and PFSML3 (0.7 µm filtered). The gradients of the dark reactions (5.82 ppt nM^{-1} and 5.09 ppt nM^{-1}) are quite similar, as are those of the light reactions (3.72 ppt nM^{-1} and 3.00 ppt nM^{-1}). The differences in the gradients between PYSML1 and PFSML3 are also consistent, the difference between the light reaction gradients being 0.72 ppt nM^{-1} and the dark reaction gradient being 0.73 ppt nM^{-1}. This suggests that the reactions occurring here are similar.

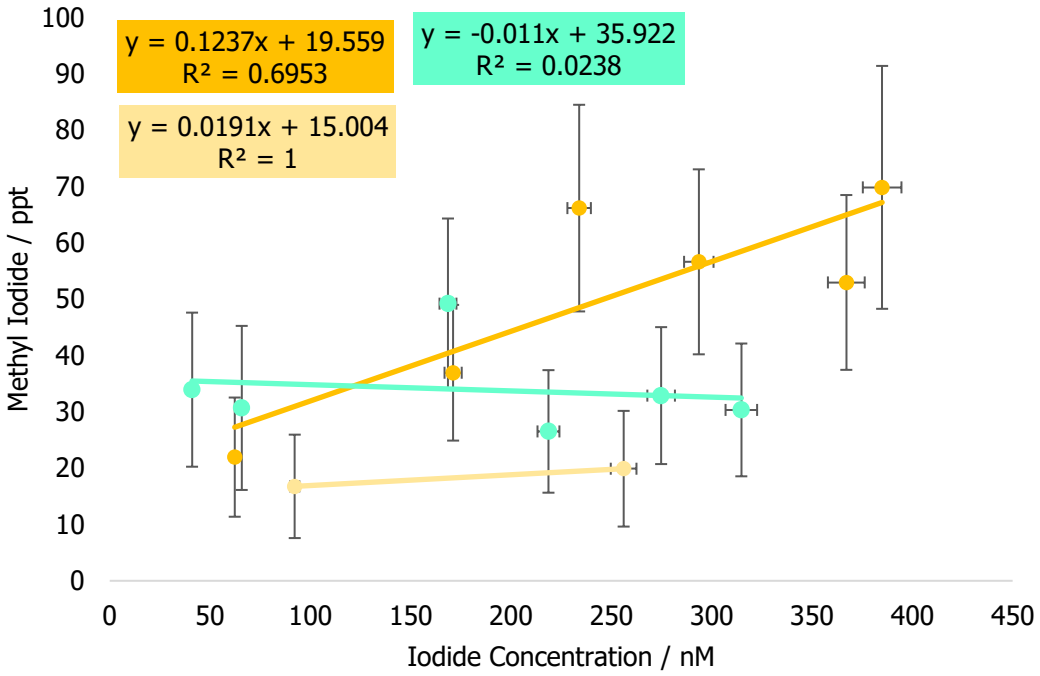

Figure 3.14 - *Methyl iodide mixing ratios of the dark experiments using B samples, with dark colours representing SML samples and light colours representing ULW samples. Yellow is sample B1 (0.7 µm filtered) and turquoise is sample B2 (0.7 µm filtered).*

Figure 3.14 shows the results of the dark experiments using Bridlington seawater samples. A slight positive gradient between CH_3I and I^- is apparent from sample BSML1 (0.7 µm filtered), though the CH_3I mixing ratios were a full order of magnitude smaller than those observed in the Plymouth samples for a given amount of iodide. The methyl iodide released was generally higher for SML samples under both dark and light conditions than for the equivalent ULW samples. For B1 the dark SML average of 50.8 ± 23.0 ppt is higher than the 18.3 ± 10.8 ppt measured for the B1 ULW. T-tests were performed to ascertain the significance of any relationships seen, where a probability of p=0.05 or smaller is equivalent to statistically significant result. It was found that the change in iodide dependence was statistically significant between the dark and illuminated regimes for 5/10 of the SML samples and only 1/7 of the ULW samples. However, this statistical significance only resulted in any large changes for PYSML1, 2.09 ppt nM^{-1} increase in the dark over the illuminated regime, and PFSML3, 2.08 ppt nM^{-1} increase in the dark over the illuminated regime, the remaining statistically significant changes are small differences between -0.13 to 0.15 ppt nM^{-1}.

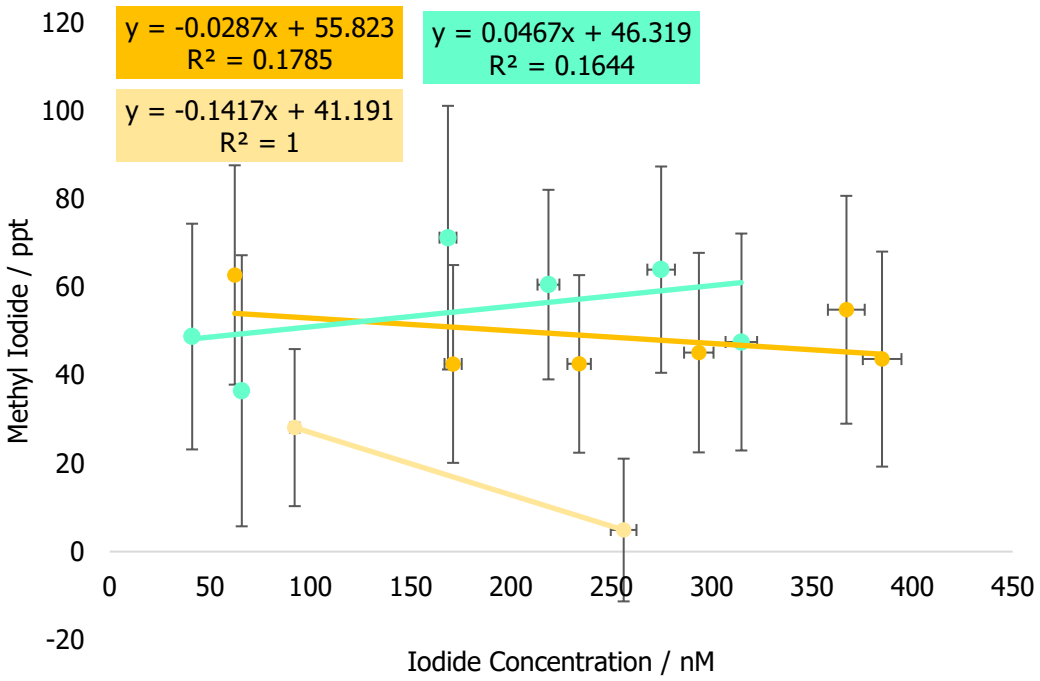

Figure 3.15 - *Methyl iodide mixing ratios of the light experiments using B samples, with dark colours representing SML samples and light colours representing ULW samples. Yellow is sample B1 (0.7 µm filtered) and turquoise is sample B2 (0.2 µm filtered).*

Figure 3.15 shows the results of the light experiments using Bridlington samples. The exposure to light causes no statistically significant change to the iodide dependence of the methyl iodide emissions for B1ULW (p-value = 0.389). The weak iodide dependence observed in the dark reaction B1SML was statistically distinct from when the light was switched on (p-value = 0.018). Though this does not fit with the same pattern as samples PYSML1 and PFSML3 which saw large positive iodide dependencies in both light and dark exposures. This suggests that either the cause of the iodide dependent reaction was much weaker in the Bridlington sample or that the statistical variation has caused a falsely significant result. As only 2 samples were run for the B2SML sample it was not possible to perform a t-test.

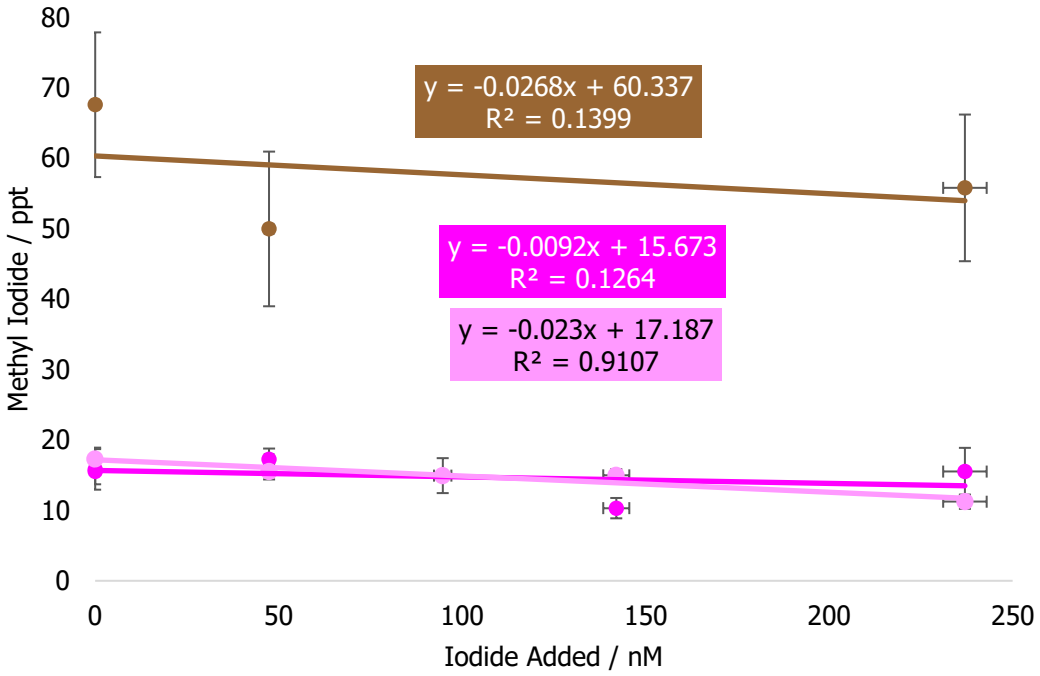

Figure 3.16 - *Methyl iodide mixing ratios of the dark experiments using S samples, with dark colours representing unfiltered samples and light colours representing 0.2 µm filtered samples. Pink is sample S1 (unfiltered and 0.2 µm filtered) and brown is sample S2 (unfiltered).*

Figure 3.16 compares the CH_3I measured from the Bermuda samples (unfiltered except for S1F which was 0.2 µm filtered) in the dark. Timing of the thesis deadline meant that returning samples for pre/post run measurements (including iodine speciation) could not be completed. Therefore, the data reported for the Bermuda samples uses the moles of iodide added as a proxy for the iodide concentration in the sample. No iodide dependent methyl iodide production was measured in any of the samples and no difference between the same sample with different degrees of filtration. The only difference between the samples was the larger production in sample S2U (57.8 ± 14.8 ppt) compared to S1U (14.9 ± 3.40 ppt).

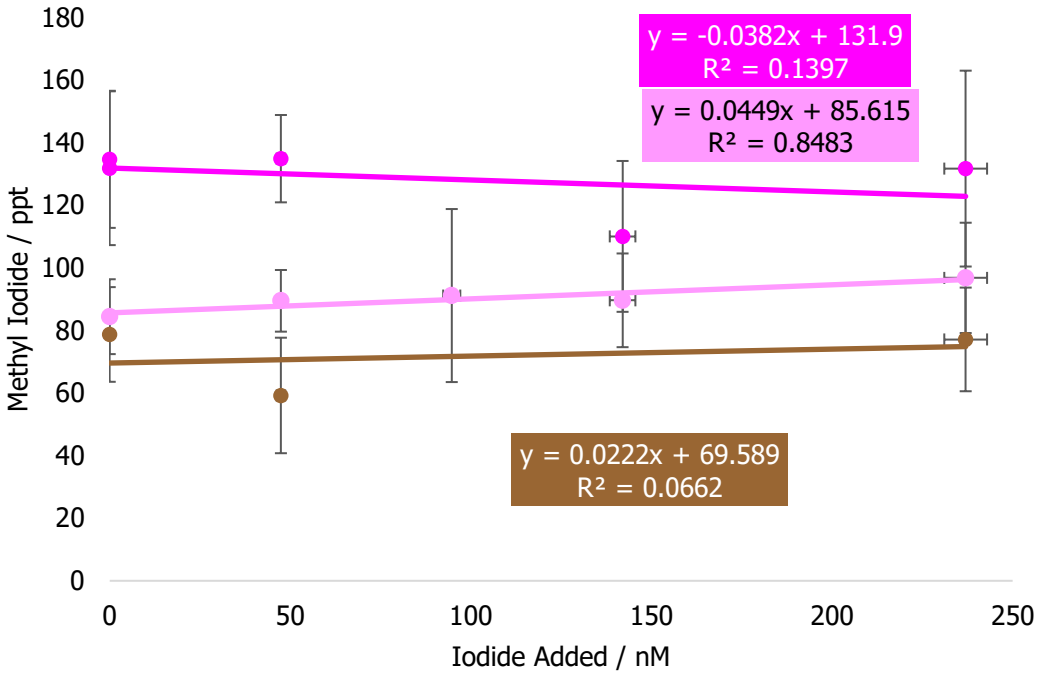

Figure 3.17 - *Methyl iodide mixing ratios of the light experiments using S samples, with dark colours representing unfiltered samples and light colours representing 0.2 µm filtered samples. Pink is sample S1 (unfiltered and 0.2 µm filtered) and brown is sample S2 (unfiltered).*

Figure 3.17 compares the CH_3I measured from the Bermuda samples (unfiltered except for S1F which was 0.2 µm filtered) when illuminated. There was again no apparent iodide dependence on the methyl iodide production in any of the samples. There was little difference between the methyl iodide produced in the dark (57.8 ± 14.8 ppt) and the illuminated (71.7 ± 21.9 ppt) regimes. However, large increases in both the S1U and S1F methyl iodide emissions were observed when illuminated compared to the dark regime. These differences, 114 ± 28.2 ppt for S1U and 75.5 ± 19.5 ppt for S1F, suggest that there was a photolytic source of methyl iodide that was present in sample S1 but not in sample S2. As these samples were collected a week apart there are a number of possibilities that could explain this, it could likely be a combination of multiple factors including different biological components of the water samples and different quantities of photochemically active substances in the water sample. This would require further testing to verify what the cause of this greater non-iodide dependent methyl iodide production was.

Table 3.4 – Calculated probabilities from the t-test determining the significance of the difference between the light and dark measurements of individual samples and ULW and SML (both light and dark) samples. A statistically significant probability is highlighted in bold.

Sample	p-values for the difference between the two samples			
	Between Light/Dark		Between SML/ULW	
	SML	ULW	Dark	Light
PY1	**0.009**	0.922	**<0.001**	**<0.001**
PY1 O3	0.205	**0.015**	**0.001**	0.050
PY2	**0.017**	0.390	**0.003**	0.811
PF3	**0.046**	0.111	**<0.001**	**0.002**
PF4	0.941	0.067	**0.001**	0.733
PF5	0.659	0.352	**0.005**	0.817
B1	**0.018**	0.389	**0.037**	0.251
B2	N/A	-	-	-
S1U	0.626	-	-	-
S1F	**0.001**	-	-	-
S2U	0.691	-	-	-

The results of t-test between the light and dark samples of each pair of SML and ULW sample (columns 2 and 3) or between the SML and ULW samples of dark or light measurements (columns 4 and 5) of each individual sample set are shown in ***Table 3.4***. These results indicate that the differences between the gradients of dark SML and dark ULW are all statistically significant as well as the differences between the gradients of the light and dark measurements of all the SML samples that exhibited iodide dependant methyl iodide production, samples PY1 and PF3, as well as samples PY2, B1 and S1F. While the difference between the dark SML and ULW results is statistically significant, there are two different types of result. For all the samples other than PY1 O3 and PF4 the methyl iodide production is greater in the SML than in the ULW.

Moore and Zafiriou (1994) reported that iodide concentration did have an impact on methyl iodide production. Using Labrador Sea water and coastal water they showed that methyl iodide production was greater in coastal water, though they state that this alone is not enough evidence of iodide concentration impacting methyl iodide production as coastal water will generally be higher in DOC, providing a greater source of methyl radicals, and light-absorbing organic compounds further increasing the photochemical production rate. They then report that increasing the iodide

concentration in the samples to 2.3 μM increased methyl iodide production fourfold. Unfortunately, no data was reported between the natural iodide levels of 250 nM (coastal) and 92 nM (offshore) and this 2.3 μM level and so the iodide dependence of this methyl iodide increase is unclear. The iodide concentrations Moore and Zafiriou used were 1-2 orders of magnitude higher than naturally observed iodide levels of 28 to 140 nM and the impact on real world studies is unclear. There could be a threshold concentration at which methyl iodide emissions increase with iodide concentrations which is worth further study. The iodide concentrations measured in this study peaked at 425 nM and there is no indication of a threshold concentration at which methyl iodide dependence would occur so for this to be true the iodide concentration threshold would need to be between the top concentration of this study and the 2.3 μM used by Moore and Zafiriou.

Chen et. al. (2020) also performed experiments to measure the iodide dependence of methyl iodide emissions. They used artificial seawater spiked with 2 mg L^{-1} humic acid and with potassium iodide, with iodide concentration ranging from 420 nM to 4.23 mM. Again, these levels are higher than observed naturally, with even their lowest point being at the higher end of observed iodide measurements. Similar to Moore and Zafiriou, Chen et. al. (2020) also detected a trend of increasing methyl iodide production with increasing iodide concentration in a pseudo-logarithmic relationship. They suggested that this was proof for the photochemical production of methyl iodide via the combination of methyl radicals and iodide radicals ***(Eq. 1.9)***. For this to be the case would require the production of iodide radicals to be the rate limiting step, i.e. for methyl radicals to be far in excess of iodine radicals, assuming the same production mechanism as in ***Eq. 1.10***. It is possible that under these conditions that methyl radical was not the rate limiting factor due to the high humic acid concentration and/or there could be some unknown chemistry occurring that is iodide dependent.

To test whether the iodide dependent production of methyl iodide was occurring in samples with excess methyl radicals the total organic carbon (TOC) measurements were used as a proxy for the abundance of methyl radicals ***(Figure 3.18)***. This was done by plotting the gradients of the methyl iodide production across individual samples against the initial TOC measurements in that sample. The result showed absolutely no correlation between the two samples that observed the iodide dependent reaction and their TOC concentration. While this doesn't confirm the iodide

dependent reaction is due to TOC concentration, it cannot rule out possibility of an organic element to it. The required organic molecules for the iodide dependent methyl iodide production could be dependent on a small portion of the TOC fraction, meaning that the organic molecules necessary could have no relation to the TOC concentration.

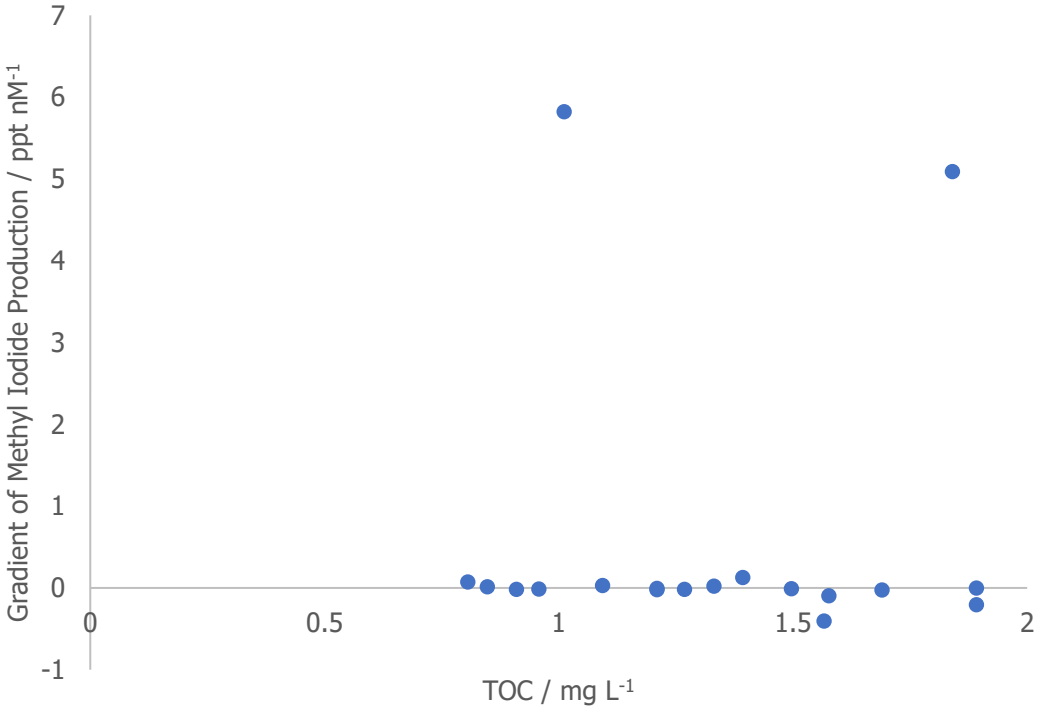

Figure 3.18 – *Relationship between methyl iodide production gradients for all samples and their measured TOC values.*

The relationship between biological activity and the iodide dependence of CH_3I production was examined. Syto 9 stain is a green-fluorescent permanent counterstain of nuclear and chromosome content of prokaryotic and eukaryotic cells. Propidium iodide is a red-fluorescent nuclear and chromosome counterstain that is unable to permeate live cells and so can be used to detect specifically dead cells. A mixture of these two counterstains was used to measure the number of living and dead prokaryotic and eukaryotic cells in a given sample, which was then used as a proxy for biological activity. This was then used to determine whether the iodide dependent emission of methyl iodide in PYSML1 and PFSML3 was due to biological factors. Plotting the data in ***Figure 3.19*** showed no clear relationship between the number of Syto 9+ve events and the gradient of methyl iodide production. The two high gradient responses, PYSML1 and PFSML3, are those that saw the iodide dependent methyl iodide production. This suggests that biological influence is not causing this reaction, though it cannot rule be ruled out as the reaction could be occurring due to

substances from degraded biological material that is no longer viable for staining. It is also possible that there are different mixtures of biological matter that don't all contribute the same amount to methyl iodide production, but contribute the same amount to the overall cell count.

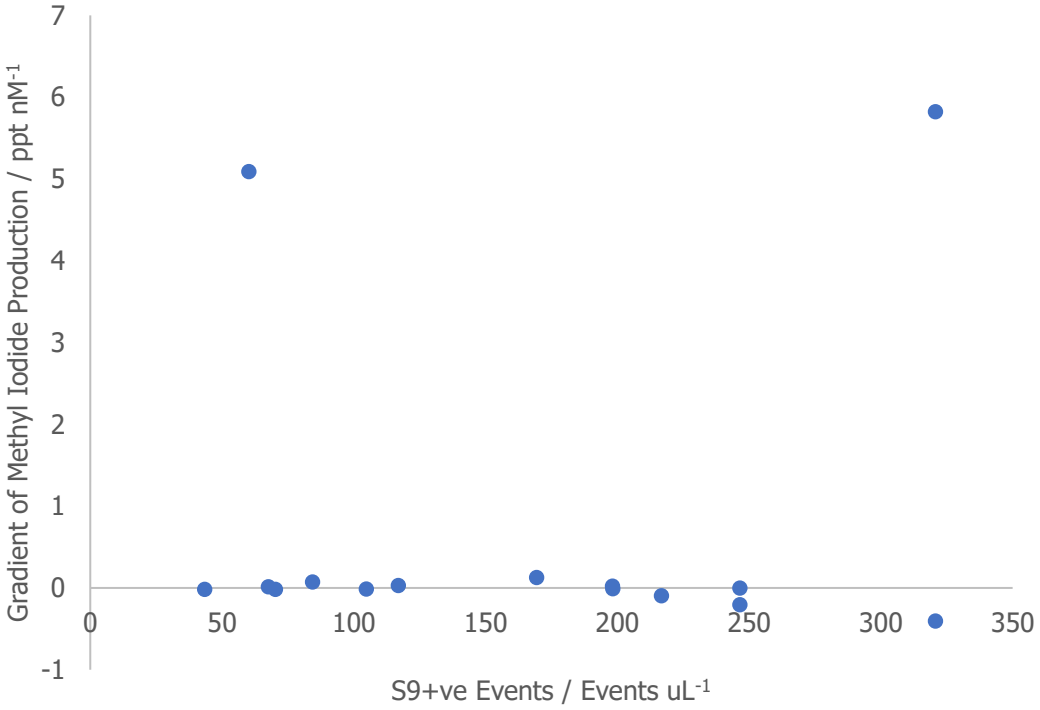

Figure 3.19 – *Relationship between methyl iodide production gradients for all samples and their measured Syto 9+ve events.*

It was also examined whether there was any relationship between iodide dependence of CH_3I production and organic iodine content. ***Figure 3.20*** shows that the gradient of methyl iodide production has no relation to the organic iodine concentration of the sample.

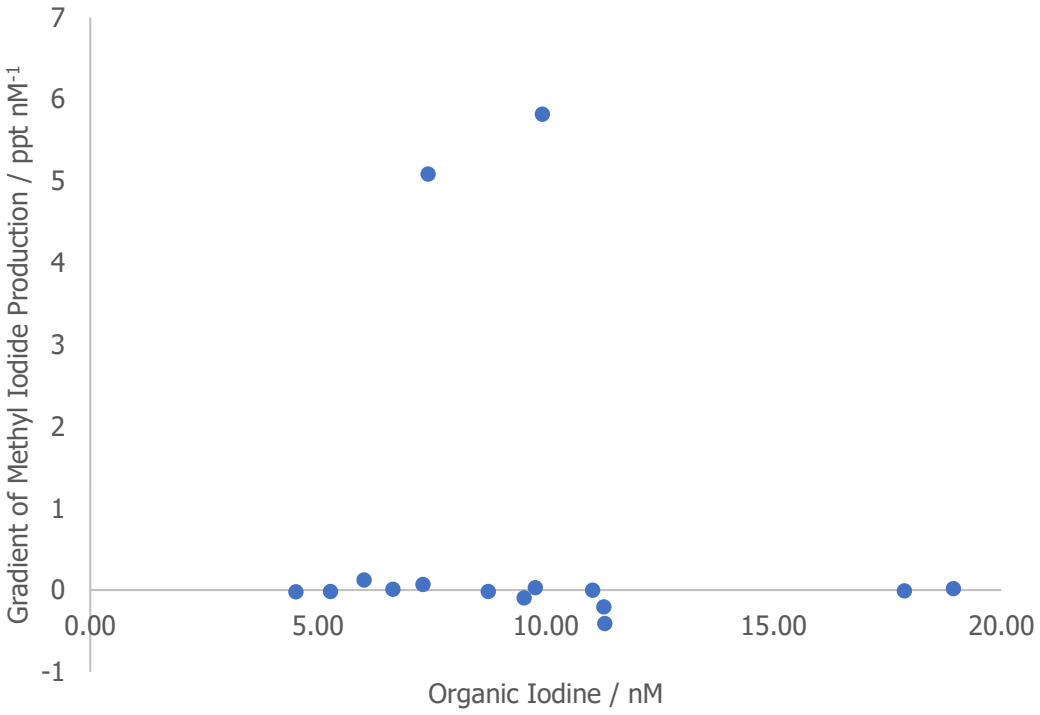

Figure 3.20 – *Relationship between methyl iodide production gradients for all samples and their measured total dissolved organic iodine concentrations.*

Currently it is not known what the cause(s) of the iodide dependent methyl iodide production in PYSML1 and PFSML3 are. Future work could be performed to explore more possibilities. One such possibility is that the reaction is mediated by MnO_2 present in silts through the oxidation of iodide to iodate, which can go on to produce methyl iodide directly or via the production of iodine, or through acting as a catalyst for the direct mono-iodination of a terminal methyl group in DOC (Allard et al., 2010). A study from Allard et. al. (2010) demonstrated the production of methyl iodide from waters spiked with iodide, Mn sand and DOC. ***Eq 3.7*** and ***Eq. 3.8*** show the proposed mechanisms for formation of iodate and iodine for the Mn oxidation of iodide;

$$I^- + 3MnO_2 + 6H^+ \rightarrow 3Mn^{2+} + IO_3^- + 3H_2O \quad (Eq. 3.7)$$

$$2I^- + MnO_2 + 4H^+ \rightarrow Mn^{2+} + I_2 + 2H_2O \quad (Eq. 3.8)$$

Some iodide reacts to form iodine ***(Eq. 3.8)*** which could react further to produce iodine radicals. The iodate formed in ***Eq. 3.7*** could also react to form iodine radicals through reaction with photosensitized DOC (Saunders et al., 2012). Methyl iodide may also be formed through the mono-iodination of a terminal methyl group that could be catalysed by manganese dioxide through activation of the iodine molecule (Allard et al., 2010; Gallard et al., 2009). In the present study, the samples where iodide

dependence was evident were estuarine samples from Plymouth with minimal filtering. It is possible that MnO_2 particulates were suspended in the sample and that they were filtered out of remaining samples at the site due to being between 0.7 and 0.2 µm. The other sites may not have shown this iodide dependent reaction due to a potential lack of silts. This could be tested by testing the Mn content of the samples and determining any correlation between the Mn content and the gradient of methyl iodide production. However, this may be unlikely as the iodide dependence is only detected in SML samples which are likely to have lower concentrations of the heavier MnO_2 particulates than their corresponding ULW samples.

The presence of the iodide dependent reaction only within SML samples suggests that whatever is causing the reaction to occur must be preferentially partitioned into the SML or is produced/deposited into the SML itself. This raises the possibility of the samples being contaminated by paint from the vessel as MnO_2 is a common ingredient in paint. The cause of this reaction could either be due to the presence of some compound(s) that are preferentially produced in the SML or that are introduced into the SML through runoff or enrichment heavily favouring the SML from the ULW. There are a number of different possibilities that fit into the categories and so to ascertain the cause of the reaction would require further work on samples across a range of sample locations and time periods to attempt to narrow down the possible causes of the reaction.

3.3.2 Literature Comparison of Methyl Iodide Surface Area Emissions

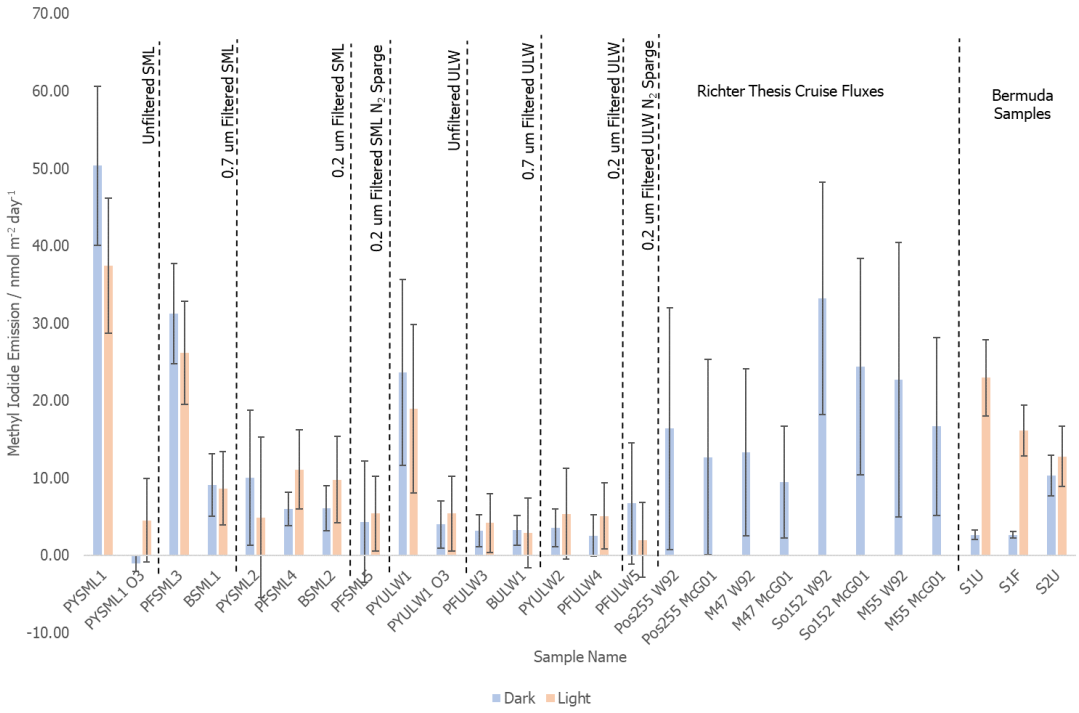

Figure 3.21 – *Surface area based emissions calculations of measurements in this study and measurements by Richter* (Richter, 2004)*. For measurements from this study blue is dark reactions and orange are light reactions.*

Surface area based CH_3I emissions were calculated from the experiments described above and are displayed in ***Figure 3.21*** in comparison to cruise based flux measurements by Richter (Richter, 2004). Richter calculated the fluxes by multiplying the transfer velocity by the concentration difference between seawater and air. The author calculated two fluxes for each cruise, one based on a quadratic relationship between transfer velocity and wind speed (Wanninkhof, 1992) (W92) and another with an additional term which causes a flux to occur even at zero wind speed (McGillis et al., 2001) (McG01). Overall, the McG01 parameterisation resulted in a slightly lower flux than that calculated by the W92 method. It is important to note that the measurements made in this study occur in a confined gas cell in which the only perturbation of the surface come from the gas flow across the cell and the stirring of the solution. These perturbations are much less than would be experienced in a natural sample which is subject to wind, wave breaking and bubbles rising through the water column. With less perturbations there is less mixing in this study compared to the measurements by Richter which would likely lessen the emissions measured in this study. Future measurements could use the measurement of methyl iodide

concentration in the surface water before and after the measurement to attempt to calculate an alternative flux value.

The iodide dependent reactions (PYSML1 and PFSML3) measured appear above or at the top-end of the averages of fluxes measured by Richter. Also, the maximum emissions measured during PYSML1 (80.0 ± 15.0 nmol m^{-2} d^{-1}) and PFSML3 (65.1 ± 12.5 nmol m^{-2} d^{-1}) were lower than those measured on the So152 cruise (110 (W92) or 120 (McG01) nmol m^{-2} d^{-1}) and the M55 cruise (93.5 (W92) or 81.0 (McG01) nmol m^{-2} d^{-1}).

The Richter flux averages agree quite well with the remainder of samples. The emissions from the illuminated untreated S1U Bermuda samples (23.0 ± 4.94 nmol m^{-2} d^{-1}) were around the average of the Richter fluxes (18.6 ± 15.6 nmol m^{-2} d^{-1}). The remaining SML samples, other than those purged with nitrogen or ozone, also fall close to the fluxes measured by Richter though they are generally towards the lower end of the flux measurements reported.

3.3.3 Literature Comparison of Methyl Iodide Volume Emissions

The volume based emissions measurements are calculated and shown in ***Figure 3.22***. The only comparisons available are incubation experiments (Moore and Zafiriou, 1994; Richter, 2004). The light induced CH_3I emissions measurements by Moore and Zafiriou (1994) far exceed any measurements performed in this study and any results reported by Richter (2004).

The samples which showed iodide-dependent CH_3I production (PYSML1 = 16.6 ± 3.38 nmol m^{-3} d^{-1}, PFSML3 = 10.3 ± 2.12 nmol m^{-3} d^{-1} both in the dark) have a much higher emissions rate than other ambient seawater samples and are incomparable to any measurements by Richter. The Richter incubations all showed very small dark emissions (0.66 ± 0.47 nmol m^{-3} d^{-1}), similar to many of the iodide independent measurements detected in this study. The reason PYSML1 and PFSML3 are higher in this study than the literature comparisons was due to an absence of any mechanism for methyl iodide production detected in the dark by Richter or by Moore and Zafiriou, possibly due to the iodide dependent dark reaction only occurring in estuarine samples and their samples both being oceanic.

Incubation emissions by Richter found higher emissions due to light than in the dark, with incubations exposed to light often causing a 400 – 600 % increase in the

emissions rate compared to those in the dark. While this was not observed for the Plymouth and Bridlington samples, with often the opposite being true, it was observed in the Bermuda samples. The S1U sample showed a light based increase of 764 % over the dark measurements and S1F showed an increase of 511 % in the light based measurements over the dark measurement. This may indicate that the Bermuda samples were more 'open ocean' in character compared to the more 'estuarine' nature of the Plymouth samples. If so, that may also explain the difference in the surface area based emissions between the Plymouth/Bridlington samples and the Bermuda samples where there was a large increase in light based methyl iodide production.

The light based emissions by Moore and Zafiriou (Moore and Zafiriou, 1994) are much lower than any light based emissions measured either in this work or in work by Richter. It is possible that their results are much lower as they oxygenated their samples which Moore and Zafiriou said decreased the rate of methyl iodide production compared to deoxygenated samples.

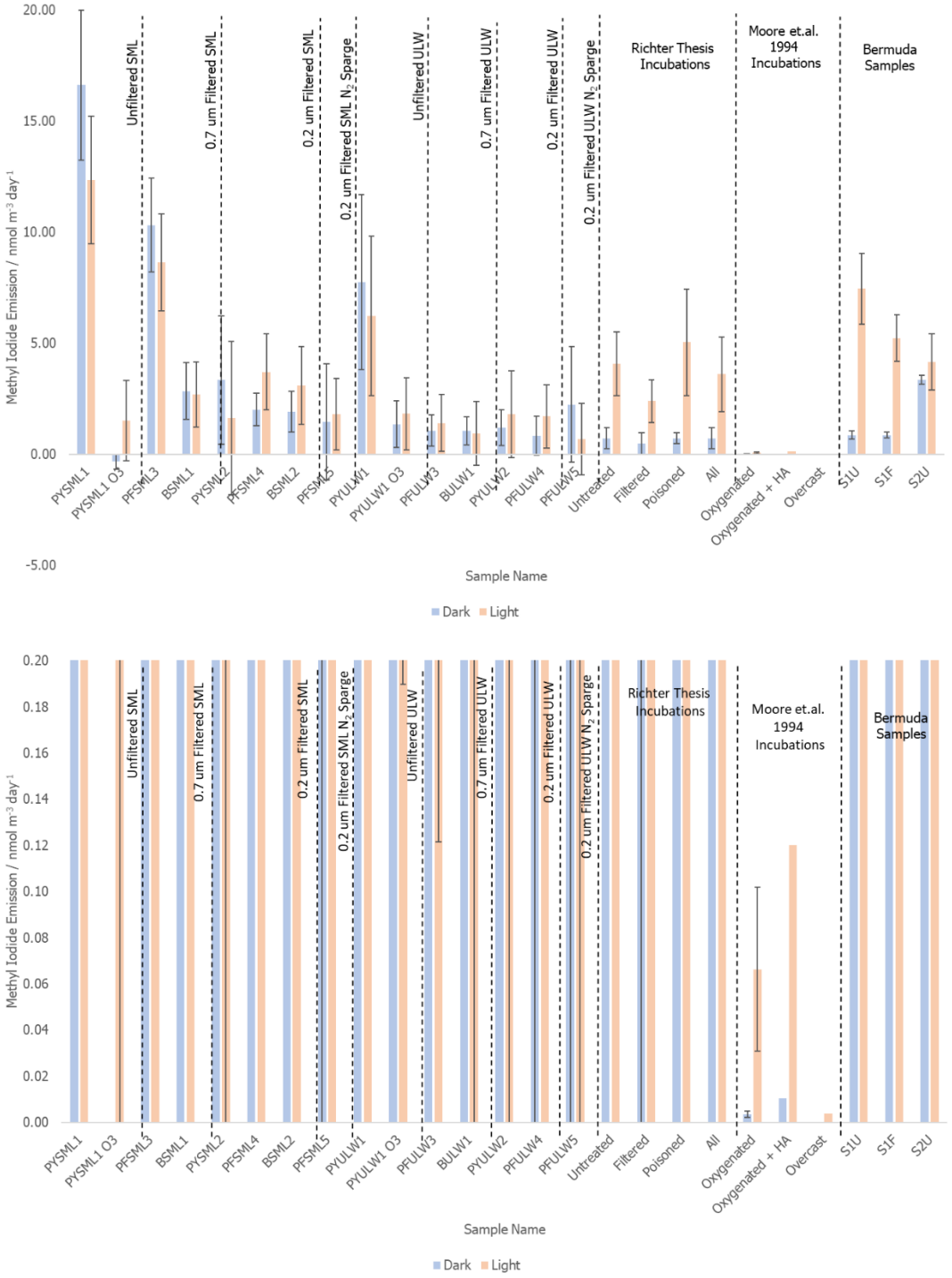

Figure 3.22 – *Volume based emissions calculations of measurements in this study and measurements by Richter* (Richter, 2004) *and Moore and Zafiriou* (Moore and Zafiriou, 1994)*. Blue is dark reactions and orange are light reactions. Bottom shows zoomed in view of lower range to highlight Moore and Zafiriou measurements.*

3.4 Conclusions

Photochemical cell based measurements of methyl iodide production from a range of seawater types with varying iodide concentration were performed to ascertain the iodide dependence of methyl iodide production.

Measurements determined that two samples exhibited iodide dependent methyl iodide production. These two samples, PYSML1 and PFSML3, were both SML samples from the waters around Plymouth. Measurement of the total organic carbon determined that this quantity was not a determining factor in CH_3I production, although the influence of specific organic compounds cannot be determined from these measurements. Measurement of the Syto9+ve events, a proxy for the biological activity of the sample indicated that methyl iodide production was not due to the presence or the absence of biological activity. We also demonstrated that CH_3I production was not related to the abundance of total dissolved organic iodine in the samples. In future work it may be prudent to test other features of the water samples, like the surfactant activity.

No time was left to perform more measurements, though a hypothesis on the cause of the iodide dependent reaction remains to be tested in future work. It is possible that the presence of an oxidant such as MnO_2, a common component of silts, could cause the reaction to occur. This reaction could proceed either via the oxidation of iodide to iodate, facilitated by the MnO_2 particles, or through the direct mono-iodination of labile methyl groups in organic matter, catalysed by MnO_2.

It is possible that the silt concentration is high enough in the estuarine Plymouth samples to cause the reaction to occur, but too low in the Bridlington or Bermuda samples. The lack of the reaction occurring in any other Plymouth samples may be explained by the MnO_2 particles being too large to pass through the smaller 0.2 µm filters. If this is the case then this may prove to be an important route of production of methyl iodide in coastal waters, though will have little to no impact on open ocean waters. However, this may not occur because of silts in the sample as it would then be expected that the reaction would occur in the corresponding ULW sample as the silt should be distributed through the water column and be enriched in the ULW relative to the SML due to its density. An alternative source of MnO_2 may be through contamination of the sample from the paint of the boat used for sampling.

Measurements of the emissions rate of methyl iodide were generally in good agreement with previous work by Richter (Richter, 2004), but were much higher than the measurements reported by Moore and Zafiriou (Moore and Zafiriou, 1994). It is possible that the oxygenation of all of the Moore and Zafiriou samples may be the cause for the reduction in methyl iodide production compared to these measurements and those of Richter. The measurements from Bermuda in particular were quite close to those measured by Richter. If these samples are representative of open ocean emissions like the Richter cruise flux measurements it provides another indication that photochemical production of methyl iodide is the most important production pathway for CH_3I in open ocean regions. The measurements in this study suggest that there is little difference between the production of methyl iodide in the SML and the ULW when exposed to light, with SML measurements not subject to the iodide dependent reaction producing 41.4 ± 59.8 ppt of methyl iodide whereas ULW measurements not subject to the iodide dependent reaction produced 35.2 ± 102 ppt of methyl iodide. This suggests that photochemical production is occurring throughout the water column.

4. Measuring VOC and OVOC Emissions from Seawater

4.1 Introduction

In this chapter the emissions of a suite of VOC compounds were assigned and measured from a sample of Bermuda seawater, filtered and unfiltered. These measurements were performed under zero ozone and natural ozone (60 ppb) conditions and were performed under dark and light conditions at each ozone level. The sample was collected by Lucy Brown and measured by Lewis Marden. I performed the data analysis on the collected data and guided the experiment remotely from York during the Bermuda campaign.

4.1.1 The Vocus PTR-ToF-MS

The Vocus proton transfer reaction-time of flight-mass spectrometer (PTR-Tof-MS) utilises a new design of reagent ion source and focusing ion-molecule reactor (FIMR) developed by TOFWERK (Krechmer et al., 2018). Using a quadrupole radiofrequency field in the reactor the FIMR forms a tight beam of reagent and product ions, improving detection efficiency while also maintaining similar collision conditions to previous instruments. ***Figure 4.1*** shows the design of the ion source and FIMR regions of the Vocus.

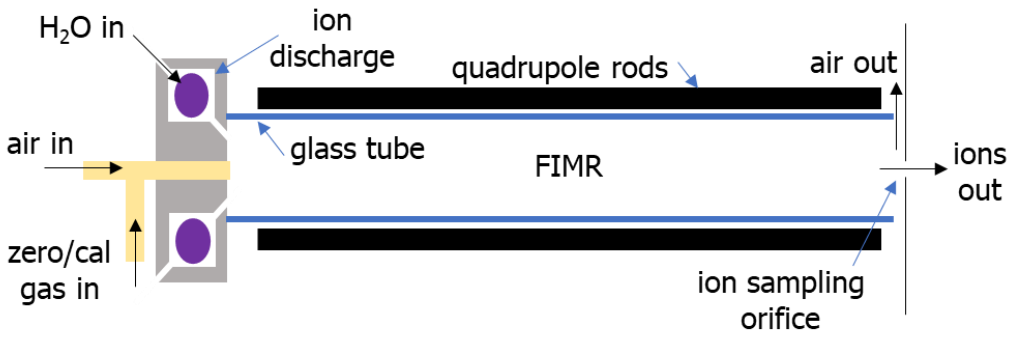

Figure 4.1 – *A schematic view of the Vocus discharge reagent-ion source and the focusing ion-molecule reactor (FIMR) adapted from (Krechmer et al., 2018)*

The reagent source creates a plasma between two conical surfaces compared to the original hollow-cathode ion sources used in standard PTR-MS instruments. A flow of 20 – 30 sccm of water vapour (HPLC/18 MΩ milli-Q water) passes between these conical surfaces into the FIMR. This flow is exposed to a voltage of about 450 V which discharges at a regulated current of 1.5 – 2.0 mA. The discharge occurs in a ring around the sample inlet and the reagent ions enter the FIMR offset from the central axis (Krechmer et al., 2018).

Analyte travels via a 10 mm PEEK tube (id = 0.18 mm) to enter the FIMR which is operated at 1.0 – 1.5 mbar. About 100 sccm of flow is sampled into the FIMR through the sample port which has a valve allowing for switching between the sample line and a calibrant line or a VOC-free air line. This allows for frequent in run calibrations and zero measurements to be performed without impacting the conditioning of the sample line (Krechmer et al., 2018).

The FIMR is comprised of a 10 cm glass tube of diameter 13 mm (glass thickness 1.5 mm). The inner surface of the tube has a resistive coating which forms a more homogeneous electric field than the stacked ring electrode approach (Kaplan et al., 2010). A direct current (DC) voltage of around 500 V applied across the ends of the glass tube establishes an electric field in the FIMR. While resistive glass tubes have been used as reactors in PTR-MS before (Mikoviny et al., 2010; Thornberry et al., 2009) the Vocus uses four 6 mm diameter rods radially mounted on the outside of the glass tube. These rods are used to establish a quadrupole radiofrequency field inside the glass tube to focus the ions into a narrow beam (Krechmer et al., 2018).

Krechmer et. al. (2018) tested the instrument and determined that the Vocus' use of radiofrequency fields improved the detection efficiency of H_3O^+ and VOC product ions by an order of magnitude and that the instrument had no sensitivity dependence on ambient humidity. The Vocus also has a mass resolving power of 12,000 which is ideal for measuring complex systems like the VOC components of the atmosphere.

4.2 Experimental

4.2.1 Sample Collection and Measurement

A sample of SML water from 0.4 km off the coast of Hog Bay, Bermuda, (32.264944 N, 64.883028 W) was collected on 29th June 2022. Only the SML sample was collected as it was expected that it would produce greater emissions due to increased concentrations of surfactant compounds in the SML that would be reactive with ozone. The sample was split in two and half was frozen at -20 ^{o}C until measurement and the other half was filtered to 0.2 µm and then frozen at -20 ^{o}C. Prior to measurement samples were defrosted by being left on the lab bench to thaw slowly to room temperature. An unfiltered and filtered sample were both measured to compare the impact of biological activity as a large portion of the biologically active substances are removed when filtered at 0.2 µm (Abushaban et al., 2019). The freezing of the samples will decrease the biological content of the samples through the breaking of

cell walls. This occurs due to the slow expansion of the water within cells on freezing which ruptures the cell wall (Scouten and Cunningham, 2006). Due to this it is likely any biological production was reduced in the results, though it is possible that increased concentrations of chemicals present in the biological cells will result in higher emissions of these specific species and those produced by their physical and chemical processing.

An identical setup to that used in ***Section 3.2.1*** was used. To perform a measurement 160 mL of sample was poured into a glass dish and placed within the photochemical cell. This was then connected to the instrument. Depending on the measurement performed, the UV lamp could be switched on and/or the O_3 generator could be turned on. The diluent gas was UHP (ultra-high purity) nitrogen (99.999 %, Airgas, Radnor, PN, USA). For both the filtered and unfiltered samples four measurements were performed, each lasting an hour. The first was with no illumination and no O_3, the second was with no illumination and 60 ppb O_3, the third was illuminated with no O_3 and the fourth was illuminated with 60 ppb O_3. All these measurements used a fresh aliquot of the sample and were measured in sequence. The sample was stirred with a stirrer bar throughout each run to ensure mixing of the sample.

For the experiments the instrument sampled 150 sccm from the sample flow. The focussing ion-molecule reactor (FIMR) was operated at a front and back voltage of 600 V and 20 V, a pressure of 2.25 mbar and a temperature of 150 ^oC. A H_3O^+ flowrate of 18 sccm was used making H_3O^+ and its water adducts the reagent ion in these measurements.

The initial dark measurement without ozone for each sample was used as the blank measurement. Emissions were calculated by subtracting this blank measurement from the values measured during the corresponding runs giving three emissions value, one due to ozone, one due to photochemistry and one due to combined ozone and photochemistry. Instrument zeroes were performed in between each of these runs under the varying conditions. The zero before and the zero after a single run condition (i.e. before and after the illuminated no ozone run etc.) were averaged and used as an additional blank measurement for the run, these largely had a small impact compared to the larger magnitude dark no ozone sample measurement blank.

A description of the solar simulator lamp is made in ***Section 3.2.2*** and is used in the same manner as described in this work.

4.2.2 Vocus PTR-ToF-MS Settings

All samples were run on a Vocus PTR-Tof-MS (TOFWERK, Thun, Switzerland) running using the PTR mode of the instrument. The instrument sampled 150 sccm of the sample flow into the FIMR. The FIMR was operated at a front and back voltage of 600 V and 20 V, a pressure of 2.25 mbar and a temperature of 150 ^{o}C. The flow rate of H_3O^+ through the chamber was set to 18 sccm making H_3O^+ and its water adducts the reagent ion in these measurements.

As with the data in ***Chapter 3*** the data was normalised to the reagent ion count, though in this case that was the sum of the $H_3O(H_2O)_{0\text{-}3}{}^+$ ions. This should account for any drift in the instrument through the course of the measurements and an inter-day irregularity in the reagent ion count.

The instrument was run in full scan mode and post processing was used to pick out peaks with a range carbon and oxygen atoms, specifically a carbon range of C_2 – C_9 and an oxygen range of O_0 – O_3. Any remaining major peaks were then included in the final output and the data was minute averaged to give 60 data points per product ion. For many of these product ions the first 15 – 20 minutes were unrepresentative of the final counts of the species due to the equilibration of the photochemical cell system.

Therefore, the first half of the data was discounted when taking the average of the counts. The headspace displacement, the rate at which the entire volume of the headspace was swept from the vessel by the carrier flow, was 0.75 displacements a minute. Most species equilibrate within the hour time period, but a few species were still slowly climbing in the light exposed measurements as seen in ***Figure 4.2*** and ***Figure 4.3***.

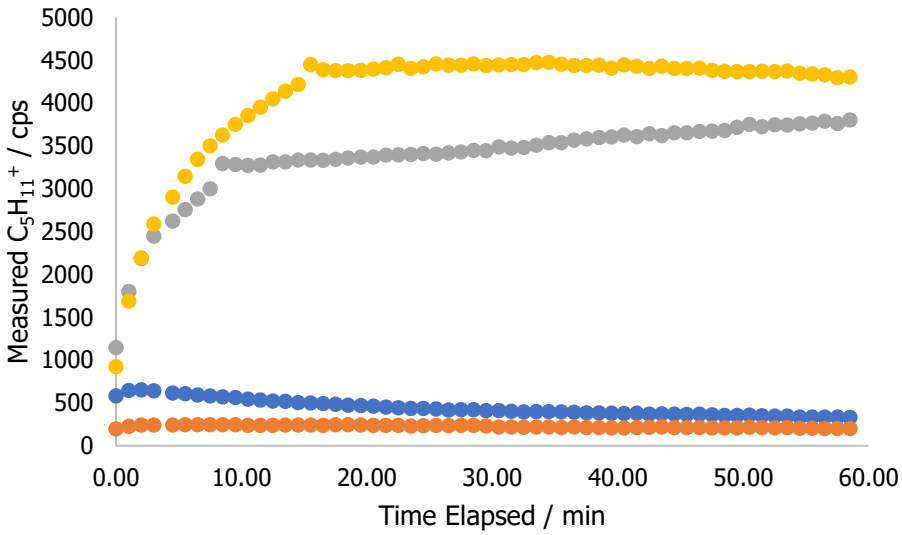

Figure 4.2 – *Measured counts of the $C_5H_{11}^+$ product ion across the full exposure time all the filtered Bermuda water sample. Where Blue = No O_3 and light off, Orange = 60 ppb O_3 and light off, Gray = No O_3 and light on, Yellow = 60 ppb O_3 and light on.*

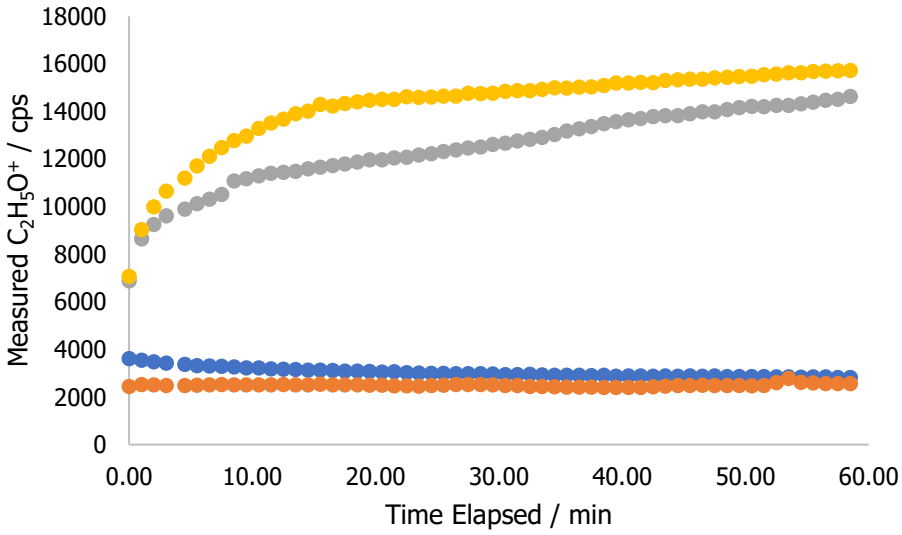

Figure 4.3 – *Measured counts of the $C_2H_5O^+$ product ion across the full exposure time all the filtered Bermuda water sample. Where Blue = No O_3 and light off, Orange = 60 ppb O_3 and light off, Gray = No O_3 and light on, Yellow = 60 ppb O_3 and light on.*

For each ion up to three species were identified as likely candidates. For a full view of all detected ions and the assumed compounds see ***Table 6.1*** in the ***Appendix***.

4.2.3 Calibration for VOC and OVOC Species

If the proton transfer rate constant, k_{PTR}, and instrument sensitivity to a compound at the operating conditions are known then the relationship of known compounds can be used to parameterise the sensitivity of unknown compounds. The instrument was calibrated using a cylinder containing known concentrations of several VOCs. This

cylinder was an NPL (2013) standard containing isoprene (3.98 ± 0.08 ppb), benzene (4.01 ±0.08 ppb), toluene (4.00 ± 0.10 ppb), *m*-xylene (4.05 ± 0.10 ppb), *p*-xylene (3.99 ± 0.10 ppb), *o*-xylene (4.00 ± 0.10 ppb), 1,3,5-trimethylbenzene (4.23 ± 0.11 ppb), 1,2,4-trimethylbenzene (4.13 ± 0.10 ppb), 1,2,3-trimethylbenzene (3.82 ± 0.10 ppb) and others. ***Figure 4.4*** shows the measured reagent corrected sensitivities of butene, isoprene, pentene, benzene, toluene, xylene, ethylbenzene and trimethylbenzene against their experimentally determined rate constants for all compounds but trimethylbenzene which used calculated values all determined by Zhao and Zhang (2004). All of the xylene compounds share a product ion as do the trimethylbenzene compounds and so each of these compound groups are represented by a single point with their rate constants averaged together.

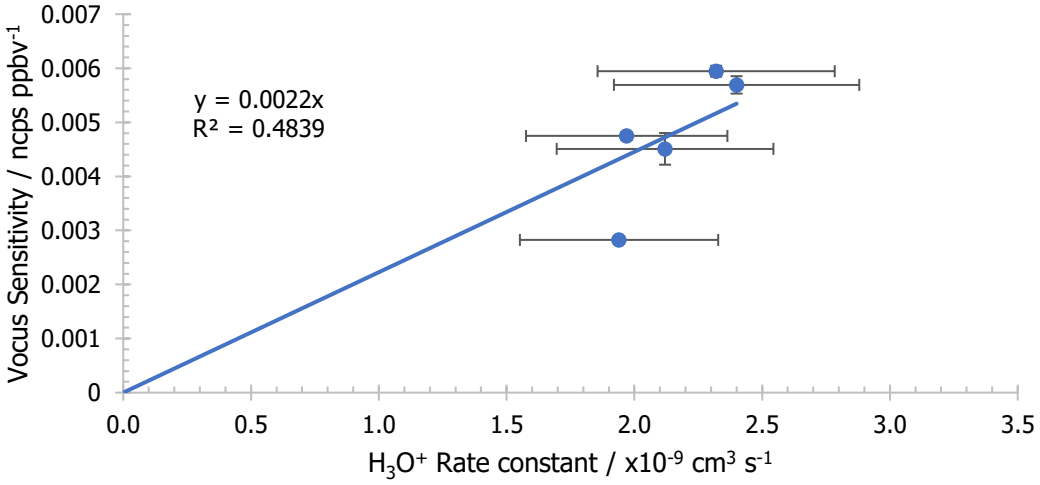

Figure 4.4 – *Sensitivity of the Vocus PTR-Tof as a function of the analyte rate constant. The graph is forced through zero as at a reaction rate of zero there is no reaction occurring and so no zero sensitivity would be measured.*

The relationship in ***Figure 4.4*** is fairly strong, with a gradient error of only 8.24 %. To convert this sensitivity into a concentration requires the use of ***Eq. 4.1.***

$$[VOC]\ (ppb) = \frac{Signal_{VOC}\ (cps)}{Sens[f(k_{PTR})]\ (cps\ ppb^{-1}) \times Trans[m/z]} \qquad (Eq.\ 4.1)$$

Where [VOC] is the mixing ratio of the VOC in ppb, $Signal_{VOC}$ is the instrument measured signal of the aforementioned VOC in cps, $Sens[f(k_{PTR})]$ is the sensitivity of Vocus to measuring that particular VOC as determined by the equation in ***Figure 4.4***, using the H_3O^+ rate constants reported in ***Table 6.1***, in cps ppb^{-1} and Trans[m/z] is the transmission efficiency of the mass to charge ratio of the VOC being calculated. The transmission efficiency for m/z values of 80 and over is 1 but the values for m/z

numbers under 80 can be determined from the function displayed in ***Figure 4.5***. The mass transmission curve is stable under the standard conditions that the Vocus is used at (Lopez-Hilfiker et al., 2019)

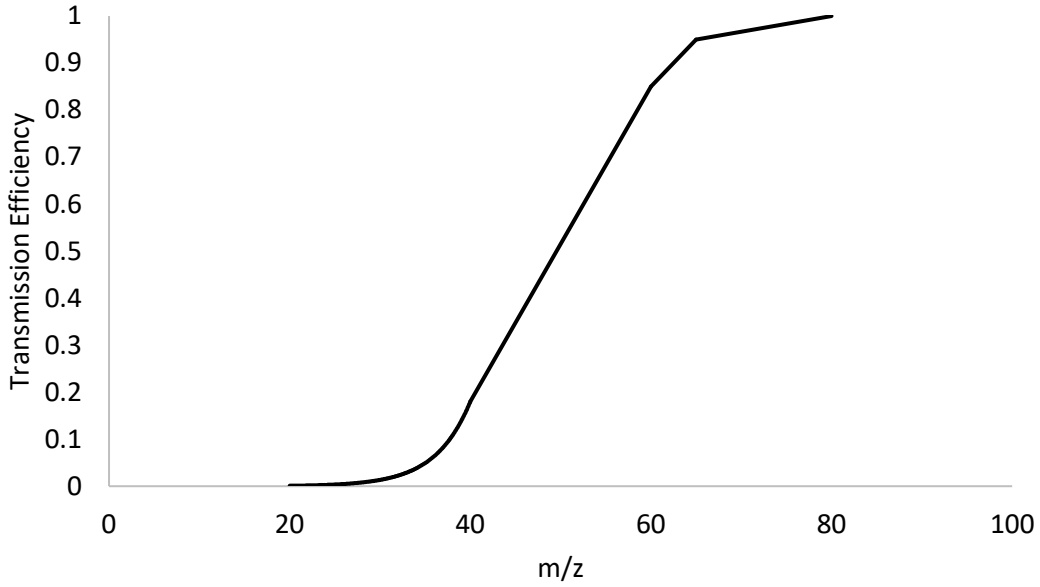

Figure 4.5 – *The mass transmission curve of a Vocus PTR-ToF. Graph derived from TOFWERK document on company website (Lopez-Hilfiker et al., 2019).*

Only literature H_3O^+ rate constants for 83 of the 219 potential compounds identified in the emissions measurements could be found in the literature (Diskin et al., 2002; Francis et al., 2007; "LabSyft," 2016; Smith et al., 2011, 2003; Španěl et al., 2002; Španěl et al., 2002, 1997; Španěl and Smith, 1997; Ŝpaněl and Smith, 1998; Španěl and Smith, 1998; Wang et al., 2004a, 2004b; Zhao and Zhang, 2004). Without having performed external calibrations like those performed in the previous chapters it is impossible to say whether the literature rate constants are truly accurate for these measurements. However, there is often very little variation in the observed rate constants, as seen in Chapter 2, when instruments are used at factory settings and so the likelihood of the rate constants being outside of the given errors is unlikely. To calculate the remaining rate constants two methods were employed.

- For compounds that belonged to a compound class with multiple other literature rate constants a correlation was produced between rate constant and molar mass and new rate constants were calculated. (an example graph for alcohols is shown in ***Figure 4.6***) To see all of the graphs see the **Appendix *(Fig. 6.1 – 6.16)***.

- For compounds not belonging to a compound class or whose compound class had no literature rates an estimated rate was produced. This estimation is possible due to PTR reaction rates being almost collision limited (de Gouw and Warneke, 2007). This estimation is 2.75 x 10^{-9} cm^3 s^{-1} with an error of 2.20 x10^{-9} cm^3 s^{-1}. The error was estimated by assuming that the range in the literature rate constants, including their errors, represented the error of the unknown rate constants. The range in literature rate constants was 1.30 – 4.80 x10^{-9} cm^3 s^{-1}. The propagation of errors led to an error of 80 % (Eq. 4.4).

$$Err_{k\ est} = \sqrt{\left(\frac{Max_{k\ lit} - Avg_{k\ lit}}{Avg_{k\ lit}}\right) + \left(\frac{Err_{k\ lit}}{Avg_{k\ lit}}\right)} \quad (Eq.\ 4.2)$$

Where $Err_{k\ est}$ is the error in the estimated rate constant, $Max_{k\ lit}$ is the maximum literature rate constant, $Avg_{k\ lit}$ is the average literature rate constant and $Err_{k\ lit}$ is the error in the literature rate constant, all values in cm^3 s^{-1}.

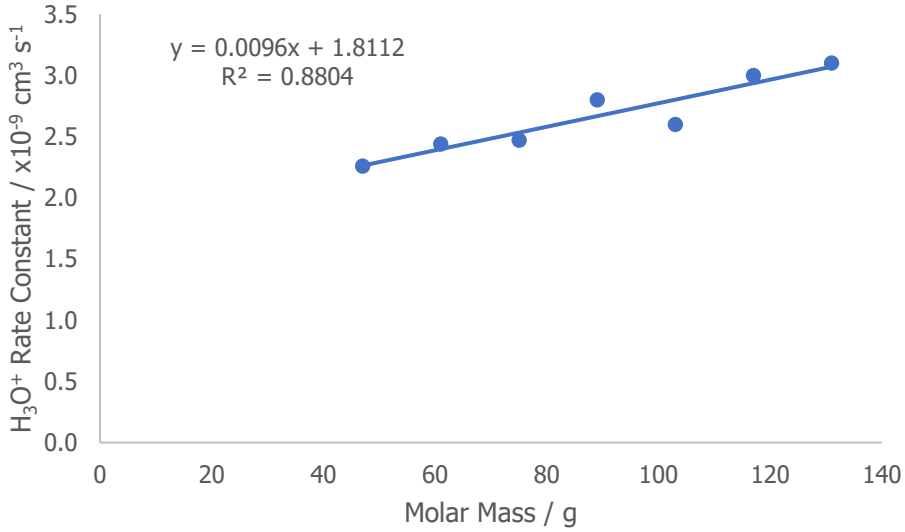

Figure 4.6 – *Correlation of alcohol molar mass with H_3O^+ rate constant used to calculate unknown alcohol rate constants.*

For ions where more than one compound has been assigned it was not possible to determine which of the compounds may be more prevalent. As such the counts for each ion were evenly divided between the number of compounds that have been assigned to that ion. For example, both propanal and propanone are detected as $C_3H_7O^+$. It was not possible without a secondary system to determine the distribution of propanal to propanone and so the total ion counts of $C_3H_7O^+$ were divided 50:50

between propanal and propanone to provide an estimation of concentration. Such compounds are distinguished clearly in the results and discussion.

4.2.4 Emissions Calculations

To convert the concentration of a specific VOC into an emission the following calculation was used ***(Eq. 4.3)***.

$$E_{VOC} = \frac{[VOC]N_{air}F_{air}N_A}{A_l} \quad (Eq. 4.3)$$

Where E_{VOC} is the emissions from the surface in μmol m^{-2} day^{-1}, *[VOC]* is the concentration of VOC and has been converted from ppb to mol, N_{air} is the number of molecules of air in mol m^{-3}, F_{air} is the flowrate of the air in m^3 day^{-1}, N_A is Avogadro's number in mol^{-1} and A_l is the liquid surface area of the sample. The error in surface area based emissions is calculated based on a propagation of the errors of the constituent parts ***(Eq. 4.4)***.

$$Err_{E_{[VOC]}} = E_{VOC}\sqrt{\left(\frac{Err_{[VOC]}}{C_{[VOC]}}\right)^2 + \left(\frac{Err_{N_{air}}}{N_{air}}\right)^2 + \left(\frac{Err_{F_{air}}}{F_{air}}\right)^2 + \left(\frac{Err_{A_l}}{A_l}\right)^2} \quad (Eq. 4.4)$$

Where $Err_{[VOC]}$ is calculated from the error in the sensitivity (dominated by rate error) and error in the instrumental counts, Err_{Nair} is calculated by propagating the errors of the pv=nRT equation it is calculated from, Err_{Fair} is the error in the flowrate determined as the flow accuracy (0.8 %) reported by Alicat, the flowmeter manufactors, and Err_{Al} is the error in the surface area calculated from the measurement error of the radius of the glass dish.

For the measurements, the no illumination and no ozone run was treated as a blank measurement for the other three measurements. The final emission measurement is the calculated by subtracting the calculated emission of the dark measurement from the corresponding measurement the emission is being calculated for. The result was also then divided by two to adjust the emission for a diurnal cycle. As the emission is calculated as a daily value it would only be exposed to light for roughly half the day. This is a simplistic correction factor to roughly account for this and results in a final correction factor of 0.5.

Calculations were also performed to determine the total carbon emissions of the measurements. The global ocean surface area was estimated to be 3.61 $x10^{14}$ m^2 (Webb, 2021) and the total carbon emissions per VOC were calculated as ***(Eq. 4.5)***.

$$E_{C(VOC)} = \frac{N_C \times M_C \times A_O \times E_{VOC} \times 365}{10^{12}} \quad (Eq.\ 4.5)$$

Where $E_{C(VOC)}$ is the carbon emission of a specific VOC in TgC yr^{-1}, N_C is the number of carbons in that VOC, M_C is the molar mass of carbon in g mol^{-1}, A_O is the surface area of the ocean in m^2 and E_{VOC} is the emissions of that VOC in mol m^{-2} d^{-1}. The multiplication by 365 converts the emission from d^{-1} to yr^{-1} and the division by 10^{12} converts the emission from g to Tg.

Like for the emissions of each VOC, the total carbon emissions are also corrected for the diurnal cycle by multiplying the final number by 0.5. The emissions are not corrected for geographic distribution of solar radiation as they are taken as point values measured in the tropics. The total carbon emissions, however, are scaled up to a global measurement and so need to be corrected for the global solar radiation distribution. To perform this the globe was split into three regions: polar (± 66.57 – 90.00 ^{O}), mid-latitude (± 23.43 – 66.57 ^{O}) and tropic (- 23.43 – (+)23.43). The percentage of ocean surface in each region was then calculated to be: polar (5.32 %), mid-latitude (52.3 %) and tropic (42.4 %). The average absolute irradiance was then calculated for each reason by taking a mid-point in each region and calculating the average of the absolute irradiance between 320 – 400 nm as determined by the NCAR TUV model (NCAR, 2016) measuring at the local solar noon in mid-September to represent an average yearly value. These were calculated to be: polar (0.103 W m^{-2} nm^{-1}), mid-latitude (0.433 W m^{-2} nm^{-1}) and tropic (0.739 W m^{-2} nm^{-1}). The individual absolute irradiances for each region were then multiplied by their percentage ocean coverages and added together to give a total average global absolute irradiance of 0.545 W m^{-2} nm^{-1}. This was then compared to the absolute irradiance in the same range, as determined in ***Section 3.2.2***, of the solar simulator lamp of 0.624 W m^{-2} nm^{-1}. To calculate a correction factor the global value was divided by the lamp value to give a correction factor of 0.874. This is then combined with the correction factor of 0.5 given by the diurnal cycle to give an overall correction factor for the total carbon emission values of 0.437.

4.3 Results and Discussion

All of the emissions results are compiled into tables in the **Appendix**, in which ***Table 6.2*** shows the emissions measurements of the filtered samples and ***Table 6.3*** shows the emissions of the unfiltered samples.

4.3.1 Emissions Under Standard Conditions

The major emissions from the unfiltered and filtered standard reaction with no O_3 and no illumination are shown in ***Table 4.1*** and ***Table 4.2*** respectively. For these reactions no blank was used as these values were used as the blank to calculate the future emissions measurements.

Table 4.1 – Ten highest emissions from the unfiltered SML sample under standard conditions, where 'dist.' indicates correction factor due to the number of compounds assigned at that specific *m/z* value. This is used as the unfiltered blank.

Name	Formula	Dist.	Emissions / μmol m^{-2} d^{-1}		% Σ_{Ion}	
			Value	Error	Value	Error
Ketene	$C_2H_3O^+$	1.00	0.575	0.100	17.5	2.99
Acetaldehyde	$C_2H_5O^+$	0.50	0.525	0.092	16.0	2.74
Ethanoic Acid	$C_2H_5O_2^+$	1.00	0.277	0.048	8.41	1.44
Butene	$C_4H_9^+$	1.00	0.172	0.029	5.07	0.87
Propanone	$C_3H_7O^+$	0.50	0.106	0.019	3.21	0.55
Propanal	$C_3H_7O^+$	0.50	0.092	0.016	2.80	0.48
Propanoic Acid	$C_3H_7O_2^+$	1.00	0.079	0.017	2.38	0.52
Propene	$C_3H_7^+$	1.00	0.065	0.010	1.96	0.34
Benzoquinone	$C_6H_5O_2^+$	1.00	0.060	0.011	1.83	0.31
Oxobutenoic Acid	$C_4H_5O_3^+$	1.00	0.058	0.047	1.76	1.42

Table 4.2 – Ten highest emissions from the filtered SML sample under standard conditions, where 'dist.' indicates correction factor due to the number of compounds assigned at that specific *m/z* value. This is used as the filtered blank.

Name	Formula	Dist.	Emissions / μmol m^{-2} d^{-1}		% Σ_{Ion}	
			Value	Error	Value	Error
Ketene	$C_2H_3O^+$	1.00	0.626	0.109	19.6	3.35
Acetaldehyde	$C_2H_5O^+$	1.00	0.521	0.90	16.2	2.77
Ethanoic Acid	$C_2H_5O_2^+$	1.00	0.257	0.045	8.00	1.37
Butene	$C_4H_9^+$	1.00	0.123	0.022	3.98	0.68
Propene	$C_3H_7^+$	1.00	0.122	0.021	3.73	0.64
Propanoic Acid	$C_3H_7O_2^+$	1.00	0.113	0.025	3.58	0.77
Propanone	$C_3H_7O^+$	0.50	0.107	0.018	3.22	0.55
Propanal	$C_3H_7O^+$	0.50	0.088	0.016	2.81	0.48
Benzoquinone	$C_6H_5O_2^+$	1.00	0.061	0.011	1.85	0.32
Oxobutenoic Acid	$C_4H_5O_3^+$	1.00	0.057	0.043	1.65	1.33

The 10 top compounds account for 61.0 ± 4.72 % of the unfiltered emissions (μmol m^{-2} d^{-1}) and 64.6 ± 4.96 % of the filtered emissions (μmol m^{-2} d^{-1}). The total mixing ratios in the headspace of the unfiltered sample total 18.5 ± 1.00 ppb and 18.0 ± 0.92 ppb in the filtered sample. There was no statistically significant difference between the total abundance of OVOCs emitted from the filtered and unfiltered samples in the standard measurement. This indicates that *in situ* biological activity is not an important factor in causing these emissions and more likely they arise from the aqueous reservoir of these compounds.

4.3.2 Emissions Under Exposure to Light

The major emissions from the unfiltered and filtered standard reaction with no O_3 and with sample illumination are shown in ***Table 4.3*** and ***Table 4.4*** respectively. These emissions were calculated in the normal manner and then blank corrected by subtracting the no light no ozone emissions from them.

Table 4.3 – Ten highest emissions from the blank corrected unfiltered SML sample under illumination with no ozone (hv), where 'dist.' indicates correction factor due to the number of compounds assigned at that specific *m/z* value.

Name	Formula	Dist.	Emissions / μmol m^{-2} d^{-1}		% Σ_{Ion}	
			Value	Error	Value	Error
Acetaldehyde	$C_2H_5O^+$	1.00	1.536	0.266	23.6	4.04
Butene	$C_4H_9^+$	1.00	0.886	0.154	13.6	2.33
Pentene	$C_5H_{11}^+$	1.00	0.429	0.075	6.60	1.13
Propene	$C_3H_7^+$	1.00	0.325	0.056	4.99	0.85
Propanone	$C_3H_7O^+$	0.50	0.293	0.051	4.50	0.77
Pentadiene	$C_5H_9^+$	0.50	0.271	0.047	4.16	0.71
Propanal	$C_3H_7O^+$	0.50	0.256	0.044	3.93	0.67
Pentyne	$C_5H_9^+$	0.50	0.254	0.044	3.90	0.67
Hexadiene	$C_6H_{11}^+$	0.50	0.218	0.048	3.35	0.72
Ketene	$C_2H_3O^+$	1.00	0.214	0.037	3.29	0.56

Table 4.4 – Ten highest emissions from the blank corrected filtered SML sample under illumination with no ozone (hv), where 'dist.' indicates correction factor due to the number of compounds assigned at that specific *m/z* value.

Name	Formula	Dist.	Emissions / μmol m^{-2} d^{-1}		% Σ_{Ion}	
			Value	Error	Value	Error
Acetaldehyde	$C_2H_5O^+$	1.00	1.982	0.343	27.5	4.71
Butene	$C_4H_9^+$	1.00	0.827	0.143	11.5	1.96
Pentene	$C_5H_{11}^+$	1.00	0.385	0.067	5.35	0.91
Propanone	$C_3H_7O^+$	0.50	0.362	0.063	5.02	0.86
Propene	$C_3H_7^+$	1.00	0.319	0.055	4.43	0.76
Propanal	$C_3H_7O^+$	0.50	0.316	0.055	4.38	0.75
Ketene	$C_2H_3O^+$	1.00	0.278	0.043	3.85	0.66
Pentadiene	$C_5H_9^+$	0.50	0.249	0.041	3.46	0.59
Pentyne	$C_5H_9^+$	0.50	0.234	0.047	3.24	0.56
Hexadiene	$C_6H_{11}^+$	0.50	0.215	0.017	2.98	0.64

The 10 top compounds account for 72.0 ± 5.16 % of the unfiltered emissions and 71.7 ± 5.50 % of the filtered emissions. The total emissions in the unfiltered sample total 36.4 ± 1.97 ppb and 40.3 ± 2.28 ppb in the filtered sample. Again, no statistically significant difference between the filtered and unfiltered samples was seen in these measurements. The impact of photochemistry on the emissions rates is evident, with large increases occurring for all the top ten compounds compared to that without photochemistry. The emission rate of acetaldehyde increased by between a factor of 3 – 4.

4.3.3 Emissions Under Exposure to Ozone

The major emissions from the unfiltered and filtered standard reaction with O_3 and no illumination are shown in ***Table 4.5*** and ***Table 4.6*** respectively. These emissions were calculated in the normal manner and then blank corrected by subtracting the no light no ozone emissions from them.

Table 4.5 – Ten highest emissions from the blank corrected unfiltered SML sample under ozone and no illumination (60 ppb O_3), where 'dist.' indicates correction factor due to the number of compounds assigned at that specific *m/z* value.

Name	Formula	Dist.	Emissions / µmol m^{-2} d^{-1}		% Σ_{Ion}	
			Value	Error	Value	Error
Ketene	$C_2H_3O^+$	1.00	0.146	0.026	23.8	4.07
Propanoic Acid	$C_3H_7O_2^+$	1.00	0.107	0.023	17.4	3.77
Propanone	$C_3H_7O^+$	0.50	0.096	0.017	15.7	2.68
Propanal	$C_3H_7O^+$	0.50	0.084	0.015	13.7	2.34
Ethanoic Acid	$C_2H_5O_2^+$	1.00	0.030	0.005	4.85	0.83
Ethanol	$C_2H_7O^+$	0.50	0.029	0.005	4.68	0.80
Dimethyl Ether	$C_2H_7O^+$	0.50	0.024	0.019	3.85	3.09
Acetaldehyde	$C_2H_5O^+$	1.00	0.023	0.004	3.72	0.64
Toluene	$C_7H_9^+$	1.00	0.022	0.004	3.53	0.60
Benzoquinone	$C_6H_5O_2^+$	1.00	0.006	0.001	0.92	0.16

Table 4.6 – Ten highest emissions from the blank corrected filtered SML sample under ozone and no illumination (60 ppb O_3), where 'dist.' indicates correction factor due to the number of compounds assigned at that specific *m/z* value.

Name	Formula	Dist.	Emissions / µmol m^{-2} d^{-1}		% Σ_{Ion}	
			Value	Error	Value	Error
Ethanol	$C_2H_7O^+$	0.50	0.023	0.004	18.7	3.19
Dimethyl Ether	$C_2H_7O^+$	0.50	0.019	0.015	15.3	12.3
Toluene	$C_7H_9^+$	1.00	0.012	0.002	9.38	1.61
Propanone	$C_3H_7O^+$	0.50	0.007	0.001	5.36	0.92
Propanal	$C_3H_7O^+$	0.50	0.006	0.001	4.67	0.80
Propene	$C_3H_7^+$	1.00	0.006	0.001	4.40	0.75
??	$C_8H_{13}^+$	1.00	0.006	0.005	4.37	3.52
Hexadiene	$C_6H_{11}^+$	0.50	0.005	0.001	3.86	0.83
Hexyne	$C_6H_{11}^+$	0.50	0.005	0.001	3.57	0.61
Urea	$CH_5N_2O^+$	1.00	0.004	0.004	3.31	2.66

The 10 top compounds account for 92.1 ± 7.43 % of the unfiltered emissions and 72.9 ± 13.7 % of the filtered emissions. The total abundance of VOCs in the headspace of the unfiltered sample totalled 3.43 ± 0.25 ppb and 0.69 ± 0.10 ppb in the filtered sample. Especially for the filtered sample, the increase in emissions from ozone deposition compared to the blank measurement was small. The emissions of ethanol and dimethyl ether from the filtered sample make up just over a third of the total increase over the standard blank. Of note was the appearance of two *m/z*'s in the filtered sample that do not appear in the unfiltered sample, which could be due

to much lower emissions in the filtered sample. These two *m/z*'s were assigned as the $C_8H_{13}^+$ product ion, which could not be identified as a specific compound, and $CH_5N_2O^+$, which was identified as urea ($CO(NH_2)_2$). Urea is estimated to comprise 3.31 % of the ozonolysis yield. It is important to note that this measurement of urea has not been verified with a secondary technique so assignment as urea was not certain. The detected peak assigned to urea appeared at 61.0467 *m/z*, a protonated urea molecule should appear at 61.0402 *m/z*. Alternative possible compounds are acetic acid ($C_2H_4O_2$), which should appear at 61.0289 *m/z*, and propanol (C_3H_8O), which should appear at 61.0653 *m/z*. Acetic acid is assigned to another peak but the preassigned peak for propanol detects no ions under any of the reaction regimes, either filtered or unfiltered. It is possible that this apparent peak for urea is a small amount of propanol being formed but this would require further testing to confirm. This could be tested by either attempting to directly measure the presence of urea in the water sample or gaseous emissions or by attempting to quantify the emissions of propanol through alternative mass spectrometry measurements (i.e. NO^+ reagent ion mass spectrometry) or gas chromatography and rechecking against the observed peak in the H_3O^+ spectrum.

4.3.4 Emissions Under Exposure to Light and Ozone

The major emissions from the unfiltered and filtered standard reaction with O_3 and illumination are shown in ***Table 4.7*** and ***Table 4.8*** respectively. These emissions were calculated in the normal manner and then blank corrected by subtracting the no light no ozone emissions from them.

Table 4.7 – Ten highest emissions from the blank corrected unfiltered SML sample under ozone and illumination (60 ppb O_3+hv), where 'dist.' indicates correction factor due to the number of compounds assigned at that specific *m/z* value.

Name	Formula	Dist.	Emissions / µmol m^{-2} d^{-1}		% Σ_{Ion}	
			Value	Error	Value	Error
Acetaldehyde	$C_2H_5O^+$	1.00	0.615	0.106	19.7	3.37
Butene	$C_4H_9^+$	1.00	0.505	0.088	16.2	2.77
Pentene	$C_5H_{11}^+$	1.00	0.263	0.046	8.46	1.45
Propene	$C_3H_7^+$	1.00	0.182	0.032	5.86	1.00
Pentadiene	$C_5H_9^+$	0.50	0.163	0.028	5.23	0.90
Pentyne	$C_5H_9^+$	0.50	0.153	0.027	4.91	0.84
Hexadiene	$C_6H_{11}^+$	0.50	0.145	0.032	4.65	1.01
Hexyne	$C_6H_{11}^+$	0.50	0.134	0.027	4.30	0.74
Propanone	$C_3H_7O^+$	0.50	0.094	0.016	3.00	0.51
Propanal	$C_3H_7O^+$	0.50	0.082	0.014	2.62	0.45

Table 4.8 – Ten highest emissions from the blank corrected filtered SML sample under ozone and illumination (60 ppb O_3+hv), where 'dist.' indicates correction factor due to the number of compounds assigned at that specific *m/z* value.

Name	Formula	Dist.	Emissions / µmol m^{-2} d^{-1}		% Σ_{Ion}	
			Value	Error	Value	Error
Acetaldehyde	$C_2H_5O^+$	1.00	2.289	0.397	27.8	4.75
Butene	$C_4H_9^+$	1.00	1.002	0.173	12.1	2.08
Pentene	$C_5H_{11}^+$	1.00	0.479	0.083	5.81	0.99
Propene	$C_3H_7^+$	1.00	0.388	0.067	4.70	0.80
Propanone	$C_3H_7O^+$	0.50	0.373	0.065	4.52	0.77
Propanal	$C_3H_7O^+$	0.50	0.325	0.057	3.94	0.67
Pentadiene	$C_5H_9^+$	0.50	0.293	0.051	3.55	0.61
Ketene	$C_2H_3O^+$	1.00	0.289	0.050	3.51	0.60
Pentyne	$C_5H_9^+$	0.50	0.225	0.042	3.33	0.57
Hexadiene	$C_6H_{11}^+$	0.50	0.258	0.057	3.13	0.68

The 10 top compounds account for 75.0 ± 5.07 % of the unfiltered emissions and 72.4 ± 5.58 % of the filtered emissions. The total emissions in the unfiltered sample total 17.4 ± 0.93 ppb and 46.2 ± 2.65 ppb in the filtered sample. Unlike previous samples that have shown no change between sample treatment or a reduction in the filtered fraction, the reaction with ozone and light seems to produce 2.7 times greater emissions from the filtered fraction.

4.3.5 Comparison of Emissions to Literature Measurements

The emission of acetaldehyde from the filtered O_3+hv of 2.289 µmol m^{-2} d^{-1} compares well with those measured in literature. Field measurements of acetaldehyde calculated fluxes using the comparison of atmospheric and seawater concentrations have measured flux values of 2.85 µmol m^{-2} d^{-1} over the Atlantic Ocean (Beale et al., 2013) and 6.89 µmol m^{-2} d^{-1} 100 km east of the Bahamas (Zhou and Mopper, 1997). An eddy covariance calculation of the acetaldehyde flux over the open Atlantic of 2.87 µmol m^{-2} d^{-1} (Yang et al., 2014) has also been measured. These numbers are of the same magnitude of those observed in the hv measurements or greater.

Average isoprene fluxes ranging between 0.005 - 0.156 µmol m^{-2} d^{-1} measured in a range of studies covering equatorial to polar waters (Baker et al., 2000; Broadgate et al., 1997; Hackenberg et al., 2017; Meskhidze and Nenes, 2006; Milne et al., 1995; Tran et al., 2013; Zhang and Gu, 2022). Maximum isoprene emissions of 0.430 µmol m^{-2} d^{-1} over the open ocean and 0.559 µmol m^{-2} d^{-1} over the coastal ocean were measured by Zhang and Gu (Zhang and Gu, 2022) and a maximum of 1.23 µmol m^{-2} d^{-1} was recorded over a phytoplankton bloom by Meskhidze and Nenes (Meskhidze and Nenes, 2006). The C_5H_8 flux values of 0.163 – 0.293 µmol m^{-2} d^{-1} in this study are above the top end of the literature averages, but are lower than the peak emissions values reported by Zhang and Gu (Zhang and Gu, 2022). It is important to note though that the C_5H_8 is here assumed to be pentadiene, an isomer of isoprene, and the peak measured is assumed to be equivalent to the pentyne peak. This means that there may be a much larger range in the isoprene emissions measured in this study which could make up any proportion of the measured $C_5H_9^+$ product ion. Using authentic SML samples from Bergen Ciuraru et. al. (2015a) measured emissions of 0.100 – 16.5 µmol m^{-2} d^{-1} using a sample with an enrichment factor of humic acid of 1, with the average emissions being 1.15 µmol m^{-2} d^{-1}. The lower range of these values are close to those that were measured for C_5H_8 in this study but the larger values are around thirty times larger than the maximum range which could be due to the greater organic content used in their study compared to the natural SML samples in this study.

There is no indication from the data in this study to be able to draw the conclusion of whether the photochemistry in this cell is completely realistic to photochemistry in the surface ocean which would require further testing. This could include the measurement of physical properties of the water sample, like DOC and surfactant

activity, as well as measurements of the contents of the water sample before and after exposure by solid phase extraction dissolved organic matter (SPE-DOM) followed by measurement by mass spectrometry.

It is important to note that these emissions are not a new or unknown source of VOCs to the atmosphere. However, the emissions measured in this study and potential subsequent studies could provide more granularity to the distribution of compound classes and specific compounds within the suite of VOCs measured in the study. These compounds will be represented in measurements of overall VOC emissions but may not be included in specific measurements analysing properties like aerosol generation.

4.3.6 Global Scaling of Emissions

The calculated carbon emissions, as described in ***Section 4.2.4***, for the blank corrected light, ozone and O_3+hv regimes are listed in ***Table 4.9***.

Table 4.9 – Total carbon emissions from the blank corrected light, ozone and O_3+hv regimes (60 ppb O_3).

Sample	Total Carbon Emissions / TgC yr^{-1}		
	Light	Ozone	O_3+hv
Filtered	40.3 ± 2.20	0.73 ± 0.19	46.3 ± 2.52
Unfiltered	37.7 ± 2.11	2.48 ± 0.30	19.6 ± 1.28

The carbon emissions between both the unfiltered and filtered sample for the light regime were similar but in the ozone regime the unfiltered sample measured about three times greater total carbon emissions than from the filtered sample and in the O_3+hv regime twice the carbon emissions were measured from the filtered sample than were measured from the unfiltered sample. It is uncertain what might be causing this variation. The reduction of total carbon emissions in the ozone+light regime could potentially be explained through the removal of a large quantity of potentially reactive compounds through filtration. However, this is counter to the trend seen in the ozone regime and the light emissions see a very small reduction that is within error so not statistically significant.

For the light emissions there were little differences in the speciation with acetaldehyde, butene and pentene being the largest three contributors to the total carbon emissions, 31.6 % of the filtered emissions and 32.1 % of the unfiltered emissions. For the ozone emissions there was a large difference in speciation between the major carbon emissions between the filtered and unfiltered samples. For the

filtered sample the top 3 emissions were toluene, the unknown $C_8H_{13}^+$ ion and hexadiene (not detected in the unfiltered sample) and accounted for about 28.9 % of the total emissions. The top 3 emissions from the unfiltered sample were propanoic acid, acetaldehyde and propanone which account for 50.1 % of all the carbon emissions. The acetaldehyde and propanoic acid emissions are completely missing in the filtered measurement. This suggests that the filtering may remove ozone reactive substances explaining both the reduced overall production and the lower and missing individual emissions. While the speciations for the O_3+hv regime are similar between the unfiltered and filtered samples, most emissions drop roughly 50 % from the filtered to unfiltered samples like the overall emissions, the aldehyde and ketone emissions appear to drop to 25 % of their filtered values in the unfiltered run.

Travis et. al. (2020) included a range of biogenic ocean emissions and sinks of VOCs in their model of OH reactivity. All of these emissions and sinks are relatively small compared to the large acetone sink of 75.7 TgC yr^{-1} leading to a total biogenic VOC emission of -74.8 TgC yr^{-1}. Travis et. al. (2020) do not include any abiotic VOC production in their main model, though they do propose that surface ocean photochemistry may provide a source of VOC emissions. They used the methodology of Brüggemann et. al. (2017) to derive species specific emission factors to calculate photochemical VOC emissions. Travis et. al. (2020) calculated a photochemical emission source of 28 TgC yr^{-1} of VOCs which is approximately 1.4 times smaller than the photochemical carbon emissions measured in this study of 37.7 – 40.3 TgC yr^{-1}. Gantt et. al. (2009) estimated, through remote sensing, a marine VOC source of 22.3 TgC yr^{-1}, similarly lower than the values measured in this study by a factor of 1.75. A possible explanation for this is that the calculation of the global scaling of the carbon emissions in this study assumes that the only factor impacting variation of emissions by location (latitude) are changes in solar irradiance. Realistically, there will be large variations in the oceanic conditions. For instance, there will be variations in the organic content of the water, both in terms of overall concentration of DOC and in terms of the distribution between the precursors of various compounds measured in this study. A study by Hansell and Orellana (2021) modelled the distribution of DOC in the surface ocean and showed that greater concentrations existed in the tropics than the mid-latitudes with very low concentrations modelled in the Southern Ocean. Further studies could perform measurements over a range of water samples with varying organic contents to assess how large of an impact this has on the emissions

measurements. The inability in this study to account for factors such as the variation in global DOC concentration could account for the higher total carbon emissions measured.

In comparison to the global carbon emissions of methane (CH_4) the total carbon emissions of VOCs from this study represent a small fraction of the overall global carbon fraction. The global carbon emissions of CH_4 have been modelled to be 703 TgC yr^{-1} (bottom-up) or 547 TgC yr^{-1} (top-down) which are an order of magnitude greater than the 37.7 – 40.3 TgC yr^{-1} VOC emissions calculated in this study (Saunois et al., 2020).

Studies (Luo and Yu, 2010; Wohl et al., 2020) of isoprene emissions show total carbon emissions ranging from 0.27 – 11.6 TgC yr^{-1} with an average of 3.47 ± 2.36 TgC yr^{-1}. An emissions range of 0.00 – 3.93 TgC yr^{-1} of the isoprene equivalent, C_5H_8, was measured with an average emission of 2.18 ± 1.16 TgC yr^{-1}. These results agree closely with the results of Luo and Yu and those of Wohl. If these large values of VOC carbon emissions are repeated in nature, then the abiotic photochemical production of VOCs could prove an important source of carbon to the atmosphere, especially in the remote open ocean far from other sources other than biological marine production.

4.3.7 Compound Class Distribution of Emissions

The 213 compounds chosen were sorted into a total of 22 different compound classes. Compounds that fit multiple compound classes were sorted into other instead. The distributions of the compound classes found in the emissions of the blank corrected light, ozone and O_3+hv regimes are listed in ***Table 4.10***.

Table 4.10 – Compound class distribution of VOC emissions from the blank corrected light, ozone and O_3+hv regimes. (60 ppb O_3)

Name	Unfiltered Distribution / %			Filtered Distribution / %		
	Light	Ozone	Both	Light	Ozone	Both
Aldehyde	31.9	17.7	27.2	35.3	7.93	35.1
Enone	4.24	23.8	0.75	4.79	1.00	4.41
Carboxylic Acid	0.63	23.4	0.26	1.02	1.07	0.73
Alkene	27.3	0.00	32.7	23.3	4.40	24.6
Aromatic	0.42	7.46	0.19	0.59	15.4	0.56
Ketone	8.50	15.7	7.54	9.01	7.77	8.47
Diketone	0.38	0.03	0.08	0.50	0.00	0.46
Diene	10.4	0.00	13.2	8.94	4.86	9.17
Alkyne	9.60	0.00	12.3	8.28	4.51	8.49
Enal	2.20	0.00	1.84	2.09	0.62	1.96
Oxoacid	0.12	0.57	0.08	0.21	1.09	0.20
Dialdehyde	0.30	0.13	0.14	0.38	0.08	0.36
Di-enoic Acid	0.11	0.11	0.01	0.16	0.59	0.14
Enoic Acid	0.22	0.00	0.08	0.27	0.00	0.26
Diacid	0.06	0.04	0.02	0.07	0.16	0.06
Diol	2.16	0.53	2.42	2.39	0.84	2.44
Hydroxy Acid	0.12	0.05	0.10	0.19	0.71	0.20
Oxo-enoic Acid	0.03	0.11	0.01	0.06	2.24	0.06
Hydroxy Aldehyde	0.12	0.05	0.11	0.18	0.71	0.19
Alcohol	0.01	4.68	0.02	0.03	18.7	0.04
Alkane	0.04	0.00	0.04	0.04	0.03	0.04
Others	1.18	5.62	0.87	2.21	27.3	2.07

Aldehydes and alkenes were the major products formed in both the light and O_3+hv regime, accounting for around 60 % of the total emissions for both filtered and unfiltered samples. Minor products of these two regimes are ketones, dienes and alkynes. The similarity between the light and O_3+hv suggests that emissions stimulated by the O_3+hv regime are largely dominated by photochemistry, especially when compared to the distribution seen in the O_3 regime. The unfiltered O_3 regime is dominated primarily by enones and carboxylic acids, which comprise about 50 % of the total emissions, and also aldehydes and ketones, a further 30 %. Alkenes, as well as dienes and alkynes, completely disappear under exposure of the SML sample to ozone, which is likely due to their high reactivity with this gas.

Brüggemann et. al. (2017) measured a range of compounds emitted from the photochemical processing of biofilm samples and samples that had been autoclaved to kill all biological material. The compound class distribution is shown in ***Table 4.11***.

The distributions determined by Brüggemann et. al. (2017) are quite different to those that were measured in this study for samples exposed to light. Similar proportions of carbonyls were detected, 36.4 ± 9.87 % for Brüggemann et. al. versus 40.8 ± 1.89 % in this study, as were aromatics, 0.54 ± 0.09 % versus 0.44 ± 0.08 % in this study, dicarbonyls, 0.30 ± 0.07 % versus 0.65 ± 0.13 % in this study, and dienoic acids, 0.01 ± 0.00 % versus 0.11 ± 0.03 % in this study. Much lower emissions of alcohols, 22.5 ± 4.28 % versus 0.03 ± 0.01 % in this study, and much larger emissions of dienes/alkynes, 4.69 ± 0.76 % versus 20.1 ± 1.65 % in this study, and alkenes, 4.29 ± 0.62 % versus 27.0 ± 1.80 % in this study, are measured in this study. Potentially these differences are due to the highly biological nature of Brüggemann et. al.'s (2017) sample compared to the sample measured in this study. The difference between these results may suggest that there was little biological activity occurring in this study's samples and/or they did not contain large amounts of biological components when the samples were collected.

Table 4.11 – Compound class distribution of VOC emissions rates from the photochemical exposure of biofilms and an autoclaved sample (Brüggemann et al., 2017).

Compound Class	Distribution in different regimes / %		
	Biofilm (5 day)	Biofilm (6 day)	Autoclaved
Carbonyl	26.6	60.5	22.3
Alcohol	18.1	16.5	32.9
Enal/Enone	3.54	6.64	17.6
Diene/Alkyne	2.83	5.73	5.51
Alkene	2.78	5.13	4.97
Aromatic	0.35	0.71	0.58
Diol	0.32	0.36	0.52
Dicarbonyl	0.28	0.46	0.15
Dienoic Acid	0.02	0.02	0.00
Other	45.2	4.02	15.5

4.4 Conclusions

Photochemical cell based measurements of VOC emissions of SML samples were performed under a range of conditions including illumination and ozone exposure. In these experiments it is likely that photochemistry is occurring throughout the entire volume of the cell. This would mean that these measurements are unlikely to represent an unknown source of VOCs not currently measured in other studies of

oceanic emissions. They may however provide a useful method for the bulk measurement of VOC emissions and lead to research into currently less well researched compounds if their emissions are found to be higher than currently expected or modelled.

Under exposure to light, both with and without ozone, acetaldehyde was always the highest emission, accounting for between 19.7 and 27.8 % of the total overall carbon mass yield. Acetaldehyde accounts for approximately two thirds of the entire aldehyde emissions budget. It is important to note that, while the instrument does detect some formaldehyde (0.001 – 0.007 μmol m^{-2} d^{-1}) the measured value is low and could be underestimated by the instrument due to being below the instruments optimal range of detection which begins at *m/z* 40 (formaldehyde *m/z* 31). For this reason, it cannot be certain that there was not a significant fraction of the aldehyde emissions being missed by the potential absence of formaldehyde.

Literature measurements of acetaldehyde fluxes over the open Atlantic of 2.87 μmol m^{-2} d^{-1} (Yang et al., 2014) and 6.89 μmol m^{-2} d^{-1} east of the Bahamas (Zhou and Mopper, 1997) compared well with this studies results of 2.29 ± 0.397 μmol m^{-2} d^{-1} measured from the O_3+hv filtered regime.

The isoprene emissions measured in this study were higher than those reported in the literature (Baker et al., 2000; Broadgate et al., 1997; Hackenberg et al., 2017; Meskhidze and Nenes, 2006; Milne et al., 1995; Tran et al., 2013; Zhang and Gu, 2022). Average flux values of isoprene measured in these studies was 0.005 – 0.156 μmol m^{-2} d^{-1} which compare to emissions flux values of 0.163 – 0.293 μmol m^{-2} d^{-1} measured in this study. . The values measured in the study were greater than the literature averages but were also lower than the maximum emissions values measured by Zhang and Gu (Zhang and Gu, 2022) of 0.430 μmol m^{-2} d^{-1} in the open ocean and 0.559 μmol m^{-2} d^{-1} in coastal waters. There is also a possibility that some of the $C_5H_9^+$ ion is being produced by fragment ions of larger carbon chains. This is unlikely due to the low energy system employed in this study, but it could be tested by using the NO^+ reagent ion to attempt to separate overlapping products apart. It is also important to note that, without secondary information on the water samples like DOC, it is impossible to completely accurately compare the emissions measured in this study to those of the literature as the water samples measured in these studies may have a higher concentration of DOC than the literature studies or different compositions.

A drawback to the short time period of this study is that only one sample was able to be measured, this increases the uncertainties surrounding the work as secondary measurements could not be taken to confirm the data. For example, the presence of urea cannot be confirmed or the potential presence of urea in the emissions as a common feature due to the lack of repeat measurements and lack of secondary techniques.

Measurements by Mao et. al. (2009) demonstrated that there was missing OH reactivity in the remote atmosphere. They linked this to being due to an over prediction of OH mixing ratios, which they then suggested were due to an unidentified source of VOCs that oxidise to from formaldehyde. Travis et. al. (2020) tested this hypothesis by modelling how much the emissions of greater than C_4 alkanes have to increase to account for the missing OH mixing ratio. They determined an incredibly large 340 TgC yr^{-1} source of greater than C_4 alkanes was required which is implausible as the remaining VOC source in their model only totalled 28.3 TgC yr^{-1}. However, it is possible that a portion of the missing VOC reactivity could be formed from a large range of compounds that are not currently modelled, especially OVOCs and alkenes that were generated in the photochemical experiments.

Various modelling studies indicate that there is a missing source of organic aerosols in the troposphere (Gantt et al., 2009; Heald et al., 2006, 2005; Roelofs, 2008; Spracklen et al., 2008). While it has been suggested that isoprene may account for this missing organic aerosol (Meskhidze and Nenes, 2006; Roelofs, 2008) observations of isoprene, as described above, do not contribute enough to account for the increase in organic aerosols. Like with OH reactivity it is possible that the observed photochemical, and to a lesser extent heterogeneous chemistry, source of VOCs and OVOCs may play a significant role in accounting for the missing organic aerosol source. While these compounds don't represent an unknown source of VOC to the atmosphere, they may represent before unknown specific compounds that may contribute to organic aerosol production. Future work could look at the potential of some of the major products detected from these measurements to produce organic aerosol.

The work presented shows that Vocus PTR-ToF-MS is a suitable method for measuring a suite of marine VOC emissions, allowing basic quantification of emissions to be performed with relative ease. The mass sensitivity of the instrument allows for more compounds to be directly measured and, in conjunction with a GC or SIFT-MS, it

would be possible to disentangle important co-eluting species like aldehydes and ketones.

The emissions of VOCs this study implies are produced from photolysis of the ocean surface could potentially have a large impact on SOA formation and modelling as well as oxidative capacity. Future work is required to provide quantification and identification of the species produced. This would allow for better modelling of SOA formation, OH reactivity and concentration of measured VOCs in the marine atmosphere that are all currently underestimated (Bates et al., 2021; Gantt et al., 2009; Heald et al., 2006, 2005; Luo and Yu, 2010; Mao et al., 2009; Roelofs, 2008; Travis et al., 2020).

5. Conclusions

5.1 Successes of this Study

The second chapter in this thesis attempted to determine whether SIFT-MS would be a viable method of measuring OVOCs of importance to oceanic emissions and what the impact of adjusting the parameters of the instrument to maximise instrument sensitivity and limit water cluster formation. The experimental work performed in this study provided measurements of rate constants based in nitrogen which, due to ongoing problems with helium supply (Bettenhausen and Jansen, 2022; Kramer, 2022), will likely begin to replace helium as a cheaper and more sustainable carrier gas in mass spectrometry measurements. These rate constants were broadly similar to those measured in literature studies except for in the measurements where adduct formation was the major product. This largely impacted the NO^+ rate constants of ketones, for which the major product ion was the NO adduct. In the study this was attributed to the increased energy within the flow tube from increasing the voltage and temperature.

The branching ratios were also greatly changed from those in relevant literature studies, which again was likely as a consequence of increased energy within the flow tube from the alterations made to the operating conditions. The increased energy also caused much less humid ion production. It is clear from these measurements that increasing the energy in the flow tube, through either temperature or voltage, can be an effective way of reducing the impact of humidity on the measurement of OVOCs. In the chapter the development of a cheap in-house method for constructing semi-recyclable permeation tubes was of great help and was used to create the calibration standards in the subsequent chapter.

The third chapter attempted to measure the iodide dependence of methyl iodide production. This measurement was done due to studies detecting an iodide dependence (Y. Chen et al., 2020; Moore and Zafiriou, 1994) but models not including this iodide dependence (Bell et al., 2002; Ordóñez et al., 2012). The measurements in this study were performed under ambient conditions and largely failed to find an iodide dependence in the methyl iodide production. Iodide dependence was only detected in two samples, PYSML1 and PFSML3, the cause of which is still currently not understood. There was no correlation of iodide dependence with an increase in TOC, the biological activity or the organic iodine content of the sample. The presence of the iodide dependence was removed both by filtering the sample to 0.2 µm and through the exposure to a 60 ppb O_3 flow. The reaction was also only detected in the

SML samples and was absent from the corresponding ULW samples suggesting that the cause of the iodide dependence is either preferably partitioned into the SML from the ULW or is generated or introduced directly into the SML with a clear partitioning preference for the SML.

The measurements of methyl iodide emissions were also compared to those measured by Richter (2004) and Moore and Zafiriou (1994). It was found that the measurements made were of a similar magnitude of the measurements made by Richter but both these measurements and those by Richter were much larger than those measured by Moore and Zafiriou. If the measurements in this study are of the same magnitude as those by Richter it suggests that strictly photochemical production of methyl iodide is a more dominant source than biogenic production.

In chapter four the emissions from the exposure of a sample, filtered and un-filtered, to a flow of ozone and/or a solar simulator lamp were measured. The measurements performed were largely exploratory in nature and confirmed the Vocus PTR-ToF-MS was a suitable instrument for quantifying and identifying a large quantity of VOCs in real time allowing for comprehensive analysis of emissions. While the study likely did not measure an unknown source of VOC emissions, these emissions are likely accounted for in studies of sea-air fluxes, the study did provide a useful method for future studies.

Comparisons to the literature measurements (Baker et al., 2000; Broadgate et al., 1997; Hackenberg et al., 2017; Meskhidze and Nenes, 2006; Milne et al., 1995; Tran et al., 2013; Yang et al., 2014; Zhang and Gu, 2022; Zhou and Mopper, 1997) of specific compounds showed similar magnitude emissions of acetaldehyde and isoprene. Comparisons of the total carbon emissions of the VOCs in this study ranged from 37.7 – 40.3 TgC yr^{-1} much lower than the global carbon emissions of methane, 547 -703 TgC yr^{-1} (Saunois et al., 2020). However, the value measured in this study is slightly greater than the 22.3 TgC yr^{-1} measured by Gantt et. al. (2009) or the 28 TgC yr^{-1} modelled by Travis et. al. (2020).

5.2 Complications and the Lessons Learnt

The thesis suffered from a number of complications, the major complication being the Covid lockdowns and the impact on work delays that was caused by this. I only suffered a temporary absence due to covid as the WACL labs remained open for select staff and students through lockdown. The major delay due to covid came from the

workshop team who were developing the photochemical cell utilised in ***Chapter 3*** and ***Chapter 4*** being absent for around six months. This significantly delayed the time taken to construct the photochemical cell, delaying the point at which we could start the experiments for these chapters. Knowing this now I would likely have adjusted the experimental plans to attempt to perform some preliminary measurements on methyl iodide emissions from lake water samples testing various alternative photochemical cell equipment to lessen the time required to fully assess the methyl iodide emissions work.

Another major issue towards the start of the PhD was severe technical issues with the SIFT-MS. This technical issue had caused the instrument to accumulate dirt inside the workings through an intake during start-up. While this caused severe delays due to it taking a long time to identify the problem and then fix it the problem also allowed me to develop an extensive knowledge in the operation and maintenance of the instrument far beyond what I would have learnt had the instrument worked.

For both ***Chapter 3*** and ***Chapter 4*** a major lesson would be to have measured many more samples. Unfortunately, in the project I suffered from a lack of samples and time as these experiments were started relatively late into the PhD and this was to the detriment of the conclusions. The findings in the methyl iodide chapter are very interesting and a greater number of samples across a wider range and of greater volumes would allow for a greater range of tests to be performed. The measurement of only a single sample in the VOC emissions chapter greatly diminished the ability to effectively interpret the data with confidence, both in that it is not possible to confirm that the measurements are representative of real emissions and that data used couldn't be used to develop calibration techniques for newer measurements. I would have begun measuring VOC emissions from seawater samples earlier if I were to repeat the PhD.

5.3 Future Work

Future work from **Chapter 2** would entail the continued calibration of the SIFT-MS for a range of (O)VOC compounds. The conditions in which the SIFT-MS in this study is run require new calibrations for each compound measured to ensure the correct rate constant and branching ratios to give accurate quantitation. This would allow for the SIFT-MS to be run in conjunction with the Vocus PTR-ToF-MS to provide greater

separation of certain compounds, mainly ketones and aldehydes which are currently unable to be separated in the H_3O^+ technique used on the Vocus.

Future work from **Chapter 3** would entail the measurement of a wider range of water samples to attempt to ascertain the cause of the iodide dependent methyl iodide emissions. A wider range of secondary measurements could be performed to narrow down the cause of the reaction, including measurements to rule out the current potential MnO_2 hypothesis. Further measurements across a wider area would also be able to further confirm whether the methyl iodide emissions are truly iodide independent or not.

Future work from **Chapter 4** would entail first the measurement of many more samples across a wide range of locations and times to analyse how the changing composition of the water sample impacts the emissions. Introduction of a secondary reagent flow, like NO^+, would also potentially be a great aid to both identifying co-eluting compounds and aid in the quantification of all the compounds in the analysis. Measurements of rate constants utilising a similar technique to that used in **Chapter 2** would also greatly reduce uncertainties in these measurements. Measurements of the water samples both before and after the measurements would also greatly aid in the understanding of the processes occurring and would allow for alternative emissions calculations based on water-air concentration gradients to be determined.

Overall, there is a great deal of further work that could be undertaken to further the findings developed within this thesis.

6. Appendix

Table 6.1 – The rate constants and of all compounds with estimated concentrations from both the unfiltered and filtered samples. The mass is the mass of the ion in m/z. For references; *Graph* indicates a rate calculated using the graph technique, *Est.* indicates the use of the estimated rate constant (2.75 x 10^{-9} cm^2 s^{-1}), *SYFT* indicates a rate measured by Syft[Ltd.], other references are numbered and listed below.

Name	Ion	Ratio	Mass	Rate / x10^{-9} cm^2 s^{-1}		
				Val.	Err.	Ref.
Formaldehyde	CH_3O^+	1.00	31	2.92	0.44	1
Propene	$C_3H_7^+$	1.00	43	1.71	0.26	1
Ethenone	$C_2H_3O^+$	1.00	43	2.21	0.33	1
Isocyanic Acid	CH_2NO^+	1.00	44	2.75	2.20	*Est.*
Acetaldehyde	$C_2H_5O^+$	1.00	45	3.36	0.50	1
Propane	$C_3H_9^+$	1.00	45	1.68	0.84	*Graph*
Formic Acid	$CH_3O_2^+$	1.00	47	2.02	0.30	1
Ethanol	$C_2H_7O^+$	0.50	47	2.26	0.34	1
Dimethyl Ether		0.50	47	2.75	2.00	*Est.*
Butene	$C_4H_9^+$	1.00	57	1.73	0.26	1
Unknown (?)	$C_3H_6O^+$	1.00	58	2.75	2.20	*Est.*
Propanal	$C_3H_7O^+$	0.50	59	3.44	0.52	1
Propanone		0.50	59	3.00	0.45	1
Glyoxal	$C_2H_3O_2^+$	1.00	59	1.34	0.20	1
Butane	$C_4H_{11}^+$	1.00	59	1.80	0.36	2
Ethanoic Acid	$C_2H_5O_2^+$	1.00	61	2.27	0.34	1
Urea (?)	*61.0467*	1.00	61	2.75	2.20	*Est.*
Propanol	$C_3H_9O^+$	1.00	61	2.44	0.37	1
Ethylene Glycol	$C_2H_7O_2^+$	0.50	63	3.30	1.65	*Graph*
Methoxymethanol		0.50	63	2.75	2.20	*Est.*
Pentadiene	$C_5H_9^+$	0.50	69	1.83	0.27	1
Pentyne		0.50	69	1.95	0.29	1
Pentene	$C_5H_{11}^+$	1.00	71	1.87	0.28	1
Butenone	$C_4H_7O^+$	0.50	71	3.83	0.77	1
Butenal		0.50	71	3.55	0.53	1
Propiolic Acid	$C_3H_3O_2^+$	1.00	71	2.75	2.20	*Est.*
Butanal	$C_4H_9O^+$	0.50	73	3.49	0.52	1
Butanone		0.50	73	3.38	0.68	1
Malondialdehyde	$C_3H_5O_2^+$	0.33	73	2.75	2.20	*Est.*
Methyl Glyoxal		0.33	73	0.91	0.45	*Graph*
Acrylic Acid		0.33	73	2.70	0.54	3
Pentane	$C_5H_{13}^+$	1.00	73	1.90	0.38	2
Propanoic Acid	$C_3H_7O_2^+$	1.00	75	2.70	0.54	3
Glyoxylic Acid	$C_2H_3O_3^+$	1.00	75	2.00	0.40	1
Butanol	$C_4H_{11}O^+$	1.00	75	2.47	0.37	1
Propanediol	$C_3H_9O_2^+$	1.00	77	3.50	0.70	4

Name	Ion	Ratio	Mass	Rate / x10^{-9} cm^2 s^{-1}		
				Val.	Err.	Ref.
Hydroxyacetaldehyde	$C_2H_5O_3^+$	0.50	77	2.75	2.20	*Est.*
Glycolic Acid		0.50	77	2.75	2.20	*Est.*
Benzene	$C_6H_7^+$	1.00	79	1.97	0.30	1
Hexadiene	$C_6H_{11}^+$	0.50	83	2.00	0.40	2
Hexyne		0.50	83	2.16	0.32	1
Hexene	$C_6H_{13}^+$	1.00	85	2.02	0.30	1
Pentenone	$C_5H_9O^+$	0.50	85	3.00	0.6	*SYFT*
Pentenal		0.50	85	4.60	0.92	5
Butadienoic Acid	$C_4H_5O_2^+$	0.50	85	2.75	2.20	*Est.*
Furanone		0.50	85	2.75	2.20	*Est.*
Pentanal	$C_5H_{11}O^+$	0.50	87	3.34	0.67	1
Pentanone		0.50	87	3.38	0.68	1
Succindialdehyde	$C_4H_7O_2^+$	0.33	87	2.75	2.20	*Est.*
Butanedione		0.33	87	1.71	0.34	1
Butenoic Acid		0.33	87	3.00	0.45	*SYFT*
Malonic Anhydride	$C_3H_3O_3^+$	0.50	87	2.75	2.20	*Est.*
Oxopropenoic Acid		0.50	87	2.75	2.20	*Est.*
Hexane	$C_6H_{15}^+$	1.00	87	2.00	0.40	2
Butanoic Acid	$C_4H_9O_2^+$	1.00	89	3.00	0.60	6
Pyruvic Acid	$C_3H_5O_3^+$	1.00	89	3.20	0.64	6
Unkonwn (?)	*89.0345*	1.00	89	2.75	2.20	*Est.*
Pentanol	$C_5H_{13}O^+$	1.00	89	2.80	0.56	7
Butanediol	$C_4H_{11}O_2^+$	1.00	91	3.70	0.74	4
Unknown (?)	$C_7H_7^+$	1.00	91	2.75	2.20	*Est.*
Glyceraldhyde	$C_3H_7O_3^+$	0.50	91	2.75	2.20	*Est.*
Lactic Acid		0.50	91	3.00	0.60	3
Toluene	$C_7H_9^+$	1.00	93	2.12	0.32	1
Heptadiene	$C_7H_{13}^+$	0.50	97	2.17	1.08	*Graph*
Heptyne		0.50	97	2.37	1.19	*Graph*
Hydroxyquinol	$C_6H_7O_3^+$	1.00	98	2.75	2.20	*Est.*
Heptene	$C_7H_{15}^+$	1.00	99	2.14	0.32	1
Hexenone	$C_6H_{11}O^+$	0.50	99	3.11	2.49	*Graph*
Hexenal		0.50	99	4.40	0.88	8
Pentadienoic Acid	$C_5H_7O_2^+$	0.50	99	2.75	2.20	*Est.*
Cyclopentadione		0.50	99	2.39	1.20	*Graph*
Maleic Anhydride	$C_4H_3O_3^+$	1.00	99	2.75	2.20	*Est.*
Hexanal	$C_6H_{13}O^+$	0.50	101	3.74	0.75	1
Hexanone		0.50	101	3.63	1.81	*Graph*
Tetronic Acid	$C_4H_5O_3^+$	1.00	101	2.75	2.20	*Est.*
Glutaraldehyde	$C_5H_9O_2^+$	0.33	101	4.14	0.62	1
Pentanedione		0.33	101	2.51	0.50	1
Pentenoic Acid		0.33	101	3.30	1.65	*Graph*
Heptane	$C_7H_{17}^+$	1.00	101	2.13	1.07	*Graph*

Name	Ion	Ratio	Mass	Rate / x10^{-9} cm^2 s^{-1}		
				Val.	Err.	Ref.
Pentanoic Acid	$C_5H_{11}O_2^+$	1.00	103	2.90	0.58	*SYFT*
Oxobutanoic Acid	$C_4H_7O_3^+$	0.50	103	2.75	2.20	*Est.*
Acetic Anhydride		0.50	103	3.00	0.60	*SYFT*
Hexanol	$C_6H_{15}O^+$	1.00	103	2.60	0.52	1
Pentanediol	$C_5H_{13}O_2^+$	1.00	105	3.90	0.78	4
Unknown (?)	$C_7H_5O^+$	1.00	105	2.75	2.20	*Est.*
Dihydroxybutanal	$C_4H_9O_3^+$	0.50	105	2.75	2.20	*Est.*
Hydroxybutyric Acid		0.50	105	2.75	2.20	*Est.*
Malonic Acid	$C_3H_5O_4^+$	1.00	105	2.75	2.20	*Est.*
Styrene	$C_8H_9^+$	1.00	105	2.33	0.47	1
Ethylbenzene	$C_8H_{11}^+$	0.50	106	2.25	0.34	1
Xylene		0.50	106	2.28	0.34	1
Benzaldehyde	$C_7H_7O^+$	1.00	107	4.12	0.82	1
Unknown (?)	$C_8H_{13}^+$	1.00	109	2.75	2.20	*Est.*
Benzoquinone	$C_6H_5O_2^+$	1.00	109	2.15	0.32	1
Cresol/Benzyl Alcohol	$C_7H_9O^+$	1.00	109	2.59	0.52	1
Unknown (?)	$C_8H_{14}^+$	1.00	110	2.75	2.20	*Est.*
Octadiene	$C_8H_{15}^+$	0.50	111	2.34	1.17	*Graph*
Octyne		0.50	111	2.58	1.29	*Graph*
Benzenediol	$C_6H_7O_2^+$	1.00	111	2.70	0.54	9
Methylcyclohexenone	$C_7H_{11}O^+$	0.50	111	3.18	2.55	*Graph*
Heptadienal		0.50	111	3.00	0.60	*SYFT*
Octene	$C_8H_{17}^+$	1.00	113	2.26	0.34	1
Heptenone	$C_7H_{13}O^+$	0.50	113	3.20	2.56	*Graph*
Heptenal		0.50	113	4.70	0.94	5
Sorbic Acid	$C_6H_9O_2^+$	0.50	113	2.75	2.20	*Est.*
Cyclohexadione		0.50	113	3.19	1.60	*Graph*
Succinic Anhydride	$C_5H_5O_3^+$	1.00	113	2.75	2.20	*Est.*
Heptanal	$C_7H_{15}O^+$	0.50	115	3.34	0.50	1
Heptanone		0.50	115	3.82	1.91	*Graph*
Hexadial	$C_6H_{11}O_2^+$	0.33	115	2.75	2.20	*Est.*
Hexadione		0.33	115	3.31	1.65	*Graph*
Hexenoic Acid		0.33	115	3.60	1.80	*Graph*
Glutaric Anhydride	$C_5H_7O_3^+$	0.50	115	2.75	2.20	*Est.*
Oxopentenoic Acid		0.50	115	2.75	2.20	*Est.*
Octane	$C_8H_{19}^+$	1.00	115	2.25	0.34	1
Hexanoic Acid	$C_6H_{13}O_2^+$	1.00	117	3.00	0.60	*SYFT*
Oxopentanoic Acid	$C_5H_9O_3^+$	1.00	117	2.75	2.20	*Est.*
Heptanol	$C_7H_{17}O^+$	1.00	117	3.00	0.60	10
Hexanediol	$C_6H_{15}O_2^+$	1.00	119	4.10	2.05	*Graph*
Succinic Acid	$C_4H_7O_4^+$	1.00	119	2.75	2.20	*Est.*
Dihydroxypentanal	$C_5H_{11}O_3^+$	0.50	119	2.75	2.20	*Est.*
Hydroxypentanoic Acid		0.50	119	2.75	2.20	*Est.*

Name	Ion	Ratio	Mass	Rate / x10^{-9} cm^2 s^{-1} Val.	Err.	Ref.
Acetophenone	$C_8H_9O^+$	0.50	121	3.91	0.78	1
Phenylacetaldehyde		0.50	121	2.75	2.20	*Est.*
C3 Benzene	$C_9H_{13}^+$	1.00	121	2.42	0.36	1
Pentanetriol	$C_5H_{13}O_3^+$	1.00	121	2.97	1.49	*Graph*
Unknown (?)	$C_9H_{15}^+$	1.00	123	2.75	2.20	*Est.*
Benzoic Acid	$C_7H_7O_2^+$	0.50	123	3.02	0.60	1
Salicylaldehyde		0.50	123	3.00	0.60	*SYFT*
Erythritol	$C_4H_{11}O_4^+$	1.00	123	2.75	2.20	*Est.*
Ethylphenol/Xylenol	$C_8H_{11}O^+$	1.00	123	2.90	0.58	9
Nonadiene	$C_9H_{17}^+$	0.50	125	2.50	1.25	*Graph*
Nonyne		0.50	125	2.79	1.40	*Graph*
Methoxyphenol	$C_7H_9O_2^+$	1.00	125	3.00	0.60	*SYFT*
Acetyl Cyclohexenone	$C_8H_{13}O^+$	0.50	125	3.27	2.61	*Graph*
Cyclohexenacetaldehyde		0.50	125	4.52	2.26	*Graph*
Hydroxybenzoquinone	$C_6H_5O_3^+$	1.00	125	2.75	2.20	*Est.*
Unknown (?)	$C_5H_{17}O_3^+$	1.00	125	2.75	2.20	*Est.*
Octenone	$C_8H_{15}O^+$	0.50	127	3.00	0.60	*Graph*
Octenal		0.50	127	4.80	0.96	5
Nonene	$C_9H_{19}^+$	1.00	127	2.45	0.49	11
Heptadienoic Acid	$C_7H_{11}O_2^+$	1.00	127	2.75	2.20	*Est.*
Octanal	$C_8H_{17}O_2^+$	0.50	129	3.53	0.53	1
Octanone		0.50	129	4.01	2.00	*Graph*
Nonane	$C_9H_{21}^+$	1.00	129	1.30	0.26	12
Heptanedial	$C_7H_{13}O_2^+$	0.33	129	2.75	2.20	*Est.*
Heptanedione		0.33	129	4.10	2.05	*Graph*
Heptenoic Acid		0.33	129	3.90	1.95	*Graph*
Sotolon	$C_6H_9O_3^+$	0.33	129	3.00	0.60	*SYFT*
Furaneol		0.33	129	3.00	0.60	*SYFT*
Oxohexenoic Acid		0.33	129	2.75	2.20	*Est.*
Heptanoic Acid	$C_7H_{15}O_2^+$	1.00	131	3.00	1.50	*Graph*
Oxohexanoic Acid	$C_6H_{11}O_3^+$	1.00	131	2.75	2.20	*Est.*
Citraconic Acid	$C_5H_7O_4^+$	0.50	131	2.75	2.20	*Est.*
Heptenedioic Acid		0.50	131	2.75	2.20	*Est.*
Octanol	$C_8H_{19}O^+$	1.00	131	3.10	0.62	7
Heptanediol	$C_7H_{17}O^+$	1.00	133	4.30	2.15	*Graph*
Dihydroxyhexanal	$C_6H_{13}O_3^+$	0.50	133	2.75	2.20	*Est.*
Hydroxyhexanoic Acid		0.50	133	2.75	2.20	*Est.*
Glutaric Acid	$C_5H_9O_4^+$	1.00	133	2.75	2.20	*Est.*
Oxobutanedioic Acid	$C_4H_5O_5^+$	1.00	133	2.75	2.20	*Est.*
Unknown (?)	$C_8H_5O_2^+$	1.00	133	2.75	2.20	*Est.*
Nonenone	$C_9H_{17}O^+$	0.50	141	3.36	2.69	*Graph*
Nonenal		0.50	141	4.80	0.96	5
Decene	$C_{10}H_{21}^+$	1.00	141	2.60	0.52	11

Name	Ion	Ratio	Mass	Rate / x10^{-9} cm^2 s^{-1}		
				Val.	Err.	Ref.
Octadienoic Acid	$C_8H_{13}O_2^+$	1.00	141	2.75	2.20	*Est.*
Methoxycatechol	$C_7H_9O_3^+$	1.00	141	2.75	2.20	*Est.*
Dihydroxybenzoquinone	$C_6H_5O_4^+$	1.00	141	2.75	2.20	*Est.*
Nonanal	$C_9H_{19}O^+$	0.50	143	3.84	0.77	1
Nonanone		0.50	143	4.20	0.84	13
Octanedial	$C_8H_{15}O_2^+$	0.33	143	2.75	2.20	*Est.*
Octanedione		0.33	143	4.90	2.45	*Graph*
Octenoic Acid		0.33	143	4.20	2.10	*Graph*
Octanoic Acid	$C_8H_{17}O_2^+$	1.00	145	3.00	0.60	*SYFT*
Oxoheptanoic Acid	$C_7H_{13}O_3^+$	1.00	145	2.75	2.20	*Est.*
Dimethyl Maleate	$C_6H_9O_4^+$	0.50	145	3.00	0.60	*SYFT*
Hexenedioic Acid		0.50	145	2.75	2.20	*Est.*
Nonanol	$C_9H_{21}O^+$	1.00	145	3.20	1.60	*Graph*
Octanediol	$C_8H_{19}O_2^+$	1.00	147	4.50	2.25	*Graph*
Adipic Acid	$C_6H_{11}O_4^+$	1.00	147	2.75	2.20	*Est.*
Dihydroxyheptanal	$C_7H_{15}O_3^+$	0.50	147	2.75	2.20	*Est.*
Hydroxyheptanoic Acid		0.50	147	2.75	2.20	*Est.*
Oxopentanedioic Acid	$C_5H_7O_5^+$	1.00	147	2.75	2.20	*Est.*
Decanal	$C_{10}H_{21}O^+$	0.50	157	3.67	0.55	1
Decanone		0.50	157	4.39	2.19	*Graph*
Nonanedial	$C_9H_{17}O_2^+$	0.33	157	2.75	2.20	*Est.*
Nonadione		0.33	157	5.70	2.85	*Graph*
Nonenoic Acid		0.33	157	4.50	2.25	*Graph*
Oxooctenoic Acid	$C_8H_{13}O_3^+$	1.00	157	2.75	2.20	*Est.*
Unknown (?)	$C_7H_9O_4^+$	1.00	157	2.75	2.20	*Est.*
Nonanoic Acid	$C_9H_{19}O_2^+$	1.00	159	3.00	0.60	*SYFT*
Oxooctanoic Acid	$C_8H_{15}O_3^+$	1.00	159	2.75	2.20	*Est.*
Dioxoheptanoic Acid	$C_7H_{11}O_4^+$	1.00	159	2.75	2.20	*Est.*
Oxohexendioic Acid	$C_6H_7O_5^+$	0.50	159	2.75	2.20	*Est.*
Pentahydroxybenzene		0.50	159	2.75	2.20	*Est.*
Nonanediol	$C_9H_{21}O_2^+$	1.00	161	4.70	2.35	*Graph*
Dihydroxyoctanal	$C_8H_{17}O_3^+$	0.50	161	2.75	2.20	*Est.*
Hydroxyoctanoic Acid		0.50	161	2.75	2.20	*Est.*
Undecanal	$C_{11}H_{23}O^+$	0.50	171	3.81	1.90	*Graph*
Undecanone		0.50	171	4.30	0.86	13
Decanedial	$C_{10}H_{19}O_2^+$	0.33	171	2.75	2.20	*Est.*
Decanedione		0.33	171	6.50	3.25	*Graph*
Decenoic Acid		0.33	171	4.80	2.40	*Graph*
Oxononenoic Acid	$C_9H_{15}O_3^+$	1.00	171	2.75	2.20	*Est.*
Oxononanoic Acid	$C_9H_{17}O_3^+$	1.00	173	2.75	2.20	*Est.*
Dihydroxynonanal	$C_9H_{19}O_3^+$	0.50	175	2.75	2.20	*Est.*
Hydroxynonanoic Acid		0.50	175	2.75	2.20	*Est.*
Cladinose	$C_8H_{17}O_4^+$	1.00	177	2.75	2.20	*Est.*

Name	Ion	Ratio	Mass	Rate / x10^{-9} cm^2 s^{-1}		
				Val.	Err.	Ref.
Oxodecanoic Acid	$C_{10}H_{19}O_3^+$	1.00	187	2.75	2.20	*Est.*
Dioxononanoic Acid	$C_9H_{15}O_4^+$	1.00	187	2.75	2.20	*Est.*
Azelaic Acid	$C_9H_{17}O_4^+$	1.00	189	2.75	2.20	*Est.*
Dihydroxynonanoic Acid	$C_9H_{19}O_4^+$	1.00	191	2.75	2.20	*Est.*
Oxoundecanoic Acid	$C_{11}H_{21}O_3^+$	1.00	201	2.75	2.20	*Est.*
Oxodecenoic Acid	$C_{12}H_{21}O_3^+$	1.00	213	2.75	2.20	*Est.*
Heptadecanal	$C_{17}H_{35}O^+$	0.50	255	4.19	2.09	*Graph*
Heptadecanone		0.50	255	5.71	2.85	*Graph*
Heptadecanoic Acid	$C_{17}H_{35}O_2^+$	1.00	271	3.00	1.50	*Graph*
Thapsic Acid	$C_{16}H_{31}O_4^+$	1.00	287	2.75	2.20	*Est.*
Oxooctadecanoic Acid	$C_{18}H_{35}O_3^+$	0.50	299	2.75	2.20	*Est.*
Ricinelaidic Acid		0.50	299	2.75	2.20	*Est.*
Octadecanedioic Acid	$C_{18}H_{35}O_4^+$	1.00	315	2.75	2.20	*Est.*
Viniferin	$C_{28}H_{23}O_6^+$	1.00	455	2.75	2.20	*Est.*

References – 1 = (Zhao and Zhang, 2004), 2 = (Španěl and Smith, 1998), 3 = (Ŝpaněl and Smith, 1998), 4 = (Španěl et al., 2002), 5 = (Španěl et al., 2002), 6 = (Smith et al., 2011), 7 = (Španěl and Smith, 1997), 8 = (Španěl et al., 1997), 9 = (Wang et al., 2004b), 10 = (Wang et al., 2004a), 11 = (Diskin et al., 2002), 12 = (Francis et al., 2007), 13 = (Smith et al., 2003)

Table 6.2 – The daily emission rates for each compound under the three regimes, ozone (60 ppb), light and light plus ozone (60 ppb), from the unfiltered Bermuda sample. Values are background corrected using the no light, no ozone measurement.

Name	Ratio	Mass	Emissions / μmol m^{-2} day^{-1}					
			Ozone (O_3)		Light (hv)		O_3 + hv	
			Val.	Err.	Val.	Err.	Val.	Err.
Formaldehyde	1.00	31	0.002	0.001	0.004	0.001	0.001	0.000
Propene	1.00	43	N/A	N/A	0.325	0.056	0.182	0.032
Ethenone	1.00	43	0.146	0.025	0.214	0.037	N/A	N/A
Isocyanic Acid	1.00	44	0.002	0.002	0.003	0.003	N/A	N/A
Acetaldehyde	1.00	45	0.023	0.004	1.536	0.266	0.613	0.106
Propane	1.00	45	N/A	N/A	N/A	N/A	N/A	N/A
Formic Acid	1.00	47	0.006	0.001	N/A	N/A	N/A	N/A
Ethanol	0.50	47	0.029	0.005	0.000	0.000	N/A	N/A
Dimethyl Ether	0.50	47	0.024	0.019	0.000	0.000	N/A	N/A
Butene	1.00	57	N/A	N/A	0.886	0.154	0.504	0.087
Unknown (?)	1.00	58	N/A	N/A	0.011	0.009	0.004	0.003
Propanal	0.50	59	0.084	0.015	0.256	0.044	0.082	0.014
Propanone	0.50	59	0.096	0.017	0.293	0.051	0.094	0.016
Glyoxal	1.00	59	0.001	0.000	0.003	0.001	0.001	0.000
Butane	1.00	59	N/A	N/A	N/A	N/A	N/A	N/A
Ethanoic Acid	1.00	61	0.030	0.005	0.021	0.004	N/A	N/A
Urea (?)	1.00	61	N/A	N/A	N/A	N/A	N/A	N/A
Propanol	1.00	61	N/A	N/A	N/A	N/A	N/A	N/A
Ethylene Glycol	0.50	63	N/A	N/A	0.013	0.007	0.005	0.003
Methoxymethanol	0.50	63	N/A	N/A	0.015	0.012	0.006	0.005
Pentadiene	0.50	69	N/A	N/A	0.271	0.047	0.163	0.028
Pentyne	0.50	69	N/A	N/A	0.254	0.044	0.153	0.027
Pentene	1.00	71	N/A	N/A	0.429	0.075	0.263	0.046
Butenone	0.50	71	N/A	N/A	0.015	0.004	0.004	0.001
Butenal	0.50	71	N/A	N/A	0.017	0.003	0.005	0.001
Propiolic Acid	1.00	71	0.001	0.001	0.004	0.003	N/A	N/A
Butanal	0.50	73	N/A	N/A	0.058	0.010	0.025	0.005
Butanone	0.50	73	N/A	N/A	0.060	0.013	0.026	0.005
Malondialdehyde	0.33	73	N/A	N/A	0.002	0.002	N/A	N/A
Methyl Glyoxal	0.33	73	N/A	N/A	0.050	0.003	N/A	N/A
Acrylic Acid	0.33	73	N/A	N/A	0.002	0.001	N/A	N/A
Pentane	1.00	73	N/A	N/A	N/A	N/A	N/A	N/A
Propanoic Acid	1.00	75	0.107	0.023	N/A	N/A	N/A	N/A
Glyoxylic Acid	1.00	75	0.000	0.000	0.000	0.000	N/A	N/A
Butanol	1.00	75	N/A	N/A	N/A	N/A	N/A	N/A
Propanediol	1.00	77	0.003	0.001	0.019	0.004	0.007	0.002
Hydroxyacetaldehyde	0.50	77	0.000	0.000	0.002	0.002	0.001	0.001
Glycolic Acid	0.50	77	0.000	0.000	0.002	0.002	0.001	0.001
Benzene	1.00	79	0.002	0.001	0.008	0.002	N/A	N/A
Hexadiene	0.50	83	N/A	N/A	0.218	0.048	0.145	0.032
Hexyne	0.50	83	N/A	N/A	0.202	0.035	0.134	0.023
Hexene	1.00	85	N/A	N/A	0.081	0.014	0.039	0.007

Name	Ratio	Mass	Emissions / µmol m^{-2} day^{-1}					
			Ozone (O_3)		Light (hv)		O_3 + hv	
			Val.	Err.	Val.	Err.	Val.	Err.
Pentenone	0.50	85	N/A	N/A	0.010	0.002	0.003	0.001
Pentenal	0.50	85	N/A	N/A	0.007	0.002	0.002	0.001
Butadienoic Acid	0.50	85	0.000	0.000	0.002	0.002	N/A	N/A
Furanone	0.50	85	0.000	0.000	0.002	0.002	N/A	N/A
Pentanal	0.50	87	N/A	N/A	0.034	0.008	0.016	0.004
Pentanone	0.50	87	N/A	N/A	0.034	0.008	0.015	0.004
Succindialdehyde	0.33	87	N/A	N/A	0.005	0.004	N/A	N/A
Butanedione	0.33	87	N/A	N/A	0.007	0.002	N/A	N/A
Butenoic Acid	0.33	87	N/A	N/A	0.004	0.001	N/A	N/A
Malonic Anhydride	0.50	87	0.000	0.000	0.000	0.000	N/A	N/A
Oxopropenoic Acid	0.50	87	0.000	0.000	0.000	0.000	N/A	N/A
Hexane	1.00	87	N/A	N/A	N/A	N/A	N/A	N/A
Butanoic Acid	1.00	89	0.002	0.001	0.003	0.001	N/A	N/A
Pyruvic Acid	1.00	89	N/A	N/A	0.001	0.000	N/A	N/A
Unkonwn (?)	1.00	89	N/A	N/A	N/A	N/A	N/A	N/A
Pentanol	1.00	89	N/A	N/A	N/A	N/A	N/A	N/A
Butanediol	1.00	91	N/A	N/A	0.013	0.003	0.006	0.001
Unknown (?)	1.00	91	0.004	0.003	0.002	0.002	N/A	N/A
Glyceraldhyde	0.50	91	N/A	N/A	0.001	0.001	N/A	N/A
Lactic Acid	0.50	91	N/A	N/A	0.001	0.000	N/A	N/A
Toluene	1.00	93	0.022	0.004	N/A	N/A	N/A	N/A
Heptadiene	0.50	97	N/A	N/A	0.079	0.040	0.041	0.021
Heptyne	0.50	97	N/A	N/A	0.072	0.037	0.038	0.019
Hydroxyquinol	1.00	98	0.002	0.002	0.000	0.000	N/A	N/A
Heptene	1.00	99	N/A	N/A	0.013	0.002	0.006	0.001
Hexenone	0.50	99	N/A	N/A	0.010	0.008	0.003	0.002
Hexenal	0.50	99	N/A	N/A	0.007	0.002	0.002	0.001
Pentadienoic Acid	0.50	99	0.000	0.000	0.003	0.002	N/A	N/A
Cyclopentadione	0.50	99	0.000	0.000	0.003	0.002	N/A	N/A
Maleic Anhydride	1.00	99	0.001	0.001	0.000	0.000	N/A	N/A
Hexanal	0.50	101	N/A	N/A	0.027	0.006	0.015	0.004
Hexanone	0.50	101	N/A	N/A	0.028	0.014	0.016	0.008
Tetronic Acid	1.00	101	N/A	N/A	0.004	0.004	N/A	N/A
Glutaraldehyde	0.33	101	0.000	0.000	0.002	0.001	N/A	N/A
Pentanedione	0.33	101	0.000	0.000	0.003	0.001	N/A	N/A
Pentenoic Acid	0.33	101	0.000	0.000	0.003	0.001	N/A	N/A
Heptane	1.00	101	N/A	N/A	0.000	0.000	N/A	N/A
Pentanoic Acid	1.00	103	N/A	N/A	0.003	0.001	0.001	0.000
Oxobutanoic Acid	0.50	103	0.000	0.000	0.000	0.000	N/A	N/A
Acetic Anhydride	0.50	103	0.000	0.000	0.000	0.000	N/A	N/A
Hexanol	1.00	103	0.000	0.000	0.000	0.000	0.000	0.000
Pentanediol	1.00	105	N/A	N/A	0.017	0.004	0.009	0.002
Unknown (?)	1.00	105	N/A	N/A	0.003	0.002	0.001	0.001
Dihydroxybutanal	0.50	105	N/A	N/A	0.001	0.001	N/A	N/A
Hydroxybutyric Acid	0.50	105	N/A	N/A	0.001	0.001	N/A	N/A
Malonic Acid	1.00	105	0.000	0.000	0.000	0.000	N/A	N/A

Name	Ratio	Mass	Emissions / µmol m^{-2} day^{-1}					
			Ozone (O_3)		Light (hv)		O_3 + hv	
			Val.	Err.	Val.	Err.	Val.	Err.
Styrene	1.00	105	0.003	0.001	N/A	N/A	N/A	N/A
Ethylbenzene	0.50	106	0.003	0.001	N/A	N/A	N/A	N/A
Xylene	0.50	106	0.003	0.001	N/A	N/A	N/A	N/A
Benzaldehyde	1.00	107	0.000	0.000	0.085	0.002	0.004	0.001
Unknown (?)	1.00	109	0.003	0.002	0.018	0.014	0.008	0.007
Benzoquinone	1.00	109	0.006	0.001	0.002	0.001	N/A	N/A
Cresol/Benzyl Alcohol	1.00	109	0.000	0.000	0.001	0.000	N/A	N/A
Unknown (?)	1.00	110	N/A	N/A	0.002	0.002	0.001	0.001
Octadiene	0.50	111	N/A	N/A	0.086	0.044	0.047	0.024
Octyne	0.50	111	N/A	N/A	0.077	0.039	0.043	0.022
Benzenediol	1.00	111	0.005	0.001	0.000	0.000	N/A	N/A
Methylcyclohexenone	0.50	111	N/A	N/A	0.000	0.000	N/A	N/A
Heptadienal	0.50	111	N/A	N/A	0.000	0.000	N/A	N/A
Octene	1.00	113	N/A	N/A	0.034	0.006	0.020	0.004
Heptenone	0.50	113	N/A	N/A	0.007	0.006	0.004	0.003
Heptenal	0.50	113	N/A	N/A	0.005	0.001	0.003	0.001
Sorbic Acid	0.50	113	N/A	N/A	0.001	0.001	N/A	N/A
Cyclohexadione	0.50	113	N/A	N/A	0.001	0.001	N/A	N/A
Succinic Anhydride	1.00	113	0.001	0.001	0.001	0.001	N/A	N/A
Heptanal	0.50	115	N/A	N/A	0.052	0.009	0.029	0.005
Heptanone	0.50	115	N/A	N/A	0.044	0.023	0.025	0.013
Hexadial	0.33	115	N/A	N/A	0.004	0.003	0.002	0.001
Hexadione	0.33	115	N/A	N/A	0.003	0.002	0.001	0.001
Hexenoic Acid	0.33	115	N/A	N/A	0.003	0.002	0.001	0.001
Glutaric Anhydride	0.50	115	0.001	0.001	0.001	0.001	N/A	N/A
Oxopentenoic Acid	0.50	115	0.001	0.001	0.001	0.001	N/A	N/A
Octane	1.00	115	0.000	0.000	0.001	0.000	0.000	0.000
Hexanoic Acid	1.00	117	N/A	N/A	0.004	0.001	0.001	0.001
Oxopentanoic Acid	1.00	117	0.000	0.000	0.001	0.001	N/A	N/A
Heptanol	1.00	117	0.000	0.000	0.000	0.000	0.000	0.000
Hexanediol	1.00	119	N/A	N/A	0.018	0.009	0.011	0.006
Succinic Acid	1.00	119	N/A	N/A	0.002	0.001	N/A	N/A
Dihydroxypentanal	0.50	119	0.000	0.000	0.001	0.001	0.000	0.000
Hydroxypentanoic Acid	0.50	119	0.000	0.000	0.001	0.001	0.000	0.000
Acetophenone	0.50	121	0.000	0.000	0.002	0.001	0.001	0.000
Phenylacetaldehyde	0.50	121	0.000	0.000	0.002	0.002	0.001	0.001
C3 Benzene	1.00	121	0.002	0.001	0.001	0.000	N/A	N/A
Pentanetriol	1.00	121	N/A	N/A	0.000	0.000	0.000	0.000
Unknown (?)	1.00	123	N/A	N/A	0.012	0.010	0.008	0.007
Benzoic Acid	0.50	123	N/A	N/A	0.001	0.000	N/A	N/A
Salicylaldehyde	0.50	123	N/A	N/A	0.001	0.000	N/A	N/A
Erythritol	1.00	123	N/A	N/A	0.001	0.000	0.001	0.000
Ethylphenol/Xylenol	1.00	123	N/A	N/A	N/A	N/A	N/A	N/A
Nonadiene	0.50	125	N/A	N/A	0.023	0.012	0.016	0.008
Nonyne	0.50	125	N/A	N/A	0.020	0.010	0.015	0.008
Methoxyphenol	1.00	125	N/A	N/A	0.002	0.001	0.001	0.000

Name	Ratio	Mass	Emissions / µmol m^{-2} day^{-1}					
			Ozone (O_3)		Light (hv)		O_3 + hv	
			Val.	Err.	Val.	Err.	Val.	Err.
Acetyl Cyclohexenone	0.50	125	N/A	N/A	0.001	0.001	0.001	0.000
Cyclohexenacetaldehyde	0.50	125	N/A	N/A	0.001	0.001	0.000	0.000
Hydroxybenzoquinone	1.00	125	0.001	0.001	0.000	0.000	N/A	N/A
Unknown (?)	1.00	125	N/A	N/A	N/A	N/A	N/A	N/A
Octenone	0.50	127	N/A	N/A	0.012	0.003	0.006	0.002
Octenal	0.50	127	N/A	N/A	0.008	0.002	0.004	0.001
Nonene	1.00	127	N/A	N/A	0.006	0.002	0.003	0.001
Heptadienoic Acid	1.00	127	N/A	N/A	0.001	0.001	N/A	N/A
Octanal	0.50	129	N/A	N/A	0.052	0.009	0.028	0.005
Octanone	0.50	129	N/A	N/A	0.046	0.024	0.025	0.013
Nonane	1.00	129	N/A	N/A	0.003	0.001	0.001	0.001
Heptanedial	0.33	129	N/A	N/A	0.002	0.002	0.001	0.001
Heptanedione	0.33	129	N/A	N/A	0.001	0.001	0.001	0.001
Heptenoic Acid	0.33	129	N/A	N/A	0.001	0.001	0.001	0.001
Sotolon	0.33	129	0.000	0.000	0.000	0.000	N/A	N/A
Furaneol	0.33	129	0.000	0.000	0.000	0.000	N/A	N/A
Oxohexenoic Acid	0.33	129	0.000	0.000	0.000	0.000	N/A	N/A
Heptanoic Acid	1.00	131	N/A	N/A	0.004	0.002	0.002	0.001
Oxohexanoic Acid	1.00	131	0.003	0.002	0.000	0.000	N/A	N/A
Citraconic Acid	0.50	131	0.000	0.000	0.000	0.000	N/A	N/A
Heptenedioic Acid	0.50	131	N/A	N/A	N/A	N/A	N/A	N/A
Octanol	1.00	131	0.000	0.000	0.000	0.000	0.000	0.000
Heptanediol	1.00	133	N/A	N/A	0.018	0.009	0.010	0.005
Dihydroxyhexanal	0.50	133	0.000	0.000	0.001	0.001	0.000	0.000
Hydroxyhexanoic Acid	0.50	133	0.000	0.000	0.001	0.001	0.000	0.000
Glutaric Acid	1.00	133	N/A	N/A	0.001	0.001	N/A	N/A
Oxobutanedioic Acid	1.00	133	0.000	0.000	0.000	0.000	N/A	N/A
Unknown (?)	1.00	133	0.001	0.001	N/A	N/A	N/A	N/A
Nonenone	0.50	141	N/A	N/A	0.007	0.005	0.004	0.003
Nonenal	0.50	141	N/A	N/A	0.005	0.001	0.003	0.001
Decene	1.00	141	N/A	N/A	0.005	0.001	0.002	0.001
Octadienoic Acid	1.00	141	N/A	N/A	0.001	0.001	0.000	0.000
Methoxycatechol	1.00	141	N/A	N/A	0.001	0.001	N/A	N/A
Dihydroxybenzoquinone	1.00	141	0.000	0.000	0.000	0.000	N/A	N/A
Nonanal	0.50	143	N/A	N/A	0.037	0.008	0.027	0.006
Nonanone	0.50	143	N/A	N/A	0.034	0.008	0.025	0.006
Octanedial	0.33	143	N/A	N/A	0.002	0.002	0.001	0.001
Octanedione	0.33	143	N/A	N/A	0.001	0.001	0.001	0.000
Octenoic Acid	0.33	143	N/A	N/A	0.001	0.001	0.001	0.000
Octanoic Acid	1.00	145	N/A	N/A	0.005	0.001	0.003	0.001
Oxoheptanoic Acid	1.00	145	0.000	0.000	0.001	0.001	0.000	0.000
Dimethyl Maleate	0.50	145	0.000	0.000	0.000	0.000	N/A	N/A
Hexenedioic Acid	0.50	145	0.000	0.000	0.000	0.000	N/A	N/A
Nonanol	1.00	145	0.000	0.000	0.000	0.000	0.000	0.000
Octanediol	1.00	147	N/A	N/A	0.025	0.013	0.014	0.007
Adipic Acid	1.00	147	0.000	0.000	0.002	0.001	0.001	0.001

Name	Ratio	Mass	Emissions / µmol m^{-2} day^{-1}					
			Ozone (O_3)		Light (hv)		O_3 + hv	
			Val.	Err.	Val.	Err.	Val.	Err.
Dihydroxyheptanal	0.50	147	N/A	N/A	0.000	0.000	N/A	N/A
Hydroxyheptanoic Acid	0.50	147	N/A	N/A	0.000	0.000	N/A	N/A
Oxopentanedioic Acid	1.00	147	0.000	0.000	N/A	N/A	N/A	N/A
Decanal	0.50	157	N/A	N/A	0.018	0.003	0.012	0.002
Decanone	0.50	157	N/A	N/A	0.015	0.008	0.010	0.005
Nonanedial	0.33	157	N/A	N/A	0.001	0.001	0.001	0.001
Nonadione	0.33	157	N/A	N/A	0.001	0.001	0.001	0.000
Nonenoic Acid	0.33	157	N/A	N/A	0.001	0.001	0.001	0.000
Oxooctenoic Acid	1.00	157	N/A	N/A	0.001	0.001	0.000	0.000
Unknown (?)	1.00	157	0.001	0.001	0.000	0.000	N/A	N/A
Nonanoic Acid	1.00	159	N/A	N/A	0.003	0.001	0.001	0.000
Oxooctanoic Acid	1.00	159	0.000	0.000	0.001	0.001	0.001	0.001
Dioxoheptanoic Acid	1.00	159	0.000	0.000	0.000	0.000	N/A	N/A
Oxohexendioic Acid	0.50	159	0.000	0.000	0.000	0.000	N/A	N/A
Pentahydroxybenzene	0.50	159	0.000	0.00	0.000	0.000	N/A	N/A
Nonanediol	1.00	161	N/A	N/A	0.021	0.011	0.15	0.008
Dihydroxyoctanal	0.50	161	0.000	0.000	0.000	0.000	N/A	N/A
Hydroxyoctanoic Acid	0.50	161	0.000	0.000	0.000	0.000	N/A	N/A
Undecanal	0.50	171	N/A	N/A	N/A	N/A	N/A	N/A
Undecanone	0.50	171	N/A	N/A	N/A	N/A	N/A	N/A
Decanedial	0.33	171	N/A	N/A	0.001	0.001	0.001	0.001
Decanedione	0.33	171	N/A	N/A	0.001	0.000	0.000	0.000
Decenoic Acid	0.33	171	N/A	N/A	0.001	0.000	0.000	0.000
Oxononenoic Acid	1.00	171	N/A	N/A	N/A	N/A	N/A	N/A
Oxononanoic Acid	1.00	173	N/A	N/A	0.003	0.002	0.002	0.001
Dihydroxynonanal	0.50	175	N/A	N/A	0.003	0.003	0.002	0.002
Hydroxynonanoic Acid	0.50	175	N/A	N/A	0.003	0.003	0.002	0.002
Cladinose	1.00	177	N/A	N/A	0.001	0.001	0.001	0.000
Oxodecanoic Acid	1.00	187	N/A	N/A	0.001	0.001	0.001	0.001
Dioxononanoic Acid	1.00	187	0.000	0.000	N/A	N/A	N/A	N/A
Azelaic Acid	1.00	189	N/A	N/A	0.001	0.001	0.000	0.000
Dihydroxynonanoic Acid	1.00	191	N/A	N/A	0.001	0.001	0.000	0.000
Oxoundecanoic Acid	1.00	201	N/A	N/A	0.001	0.001	0.000	0.000
Oxodecenoic Acid	1.00	213	N/A	N/A	0.002	0.001	0.000	0.000
Heptadecanal	0.50	255	N/A	N/A	0.000	0.000	N/A	N/A
Heptadecanone	0.50	255	N/A	N/A	0.000	0.000	N/A	N/A
Heptadecanoic Acid	1.00	271	N/A	N/A	0.000	0.000	N/A	N/A
Thapsic Acid	1.00	287	0.000	0.000	0.000	0.000	N/A	N/A
Oxooctadecanoic Acid	0.50	299	0.000	0.000	0.000	0.000	0.000	0.000
Ricinelaidic Acid	0.50	299	0.000	0.000	0.000	0.000	0.000	0.000
Octadecanedioic Acid	1.00	315	0.000	0.000	0.000	0.000	0.000	0.000
Viniferin	1.00	455	0.000	0.000	0.000	0.000	0.000	0.000

Table 6.3 - The daily emission rates for each compound under the three regimes, ozone (60 ppb), light and light plus ozone (60 ppb), from the 0.2 µm filtered Bermuda sample. Values are background corrected using the no light, no ozone measurement.

Name	Ratio	Mass	Emissions / µmol m^{-2} day^{-1}					
			Ozone (O_3)		Light (hv)		O_3 + hv	
			Val.	Err.	Val.	Err.	Val.	Err.
Formaldehyde	1.00	31	0.001	0.000	0.005	0.001	0.05	0.001
Propene	1.00	43	0.006	0.001	0.319	0.055	0.388	0.067
Ethenone	1.00	43	N/A	N/A	0.278	0.048	0.289	0.050
Isocyanic Acid	1.00	44	0.001	0.001	0.003	0.003	0.004	0.003
Acetaldehyde	1.00	45	N/A	N/A	1.982	0.343	2.290	0.397
Propane	1.00	45	0.000	0.000	0.001	0.000	0.001	0.000
Formic Acid	1.00	47	0.002	0.000	0.004	0.001	0.004	0.001
Ethanol	0.50	47	0.023	0.004	0.002	0.001	0.003	0.001
Dimethyl Ether	0.50	47	0.019	0.015	0.002	0.001	0.002	0.002
Butene	1.00	57	N/A	N/A	0.827	0.143	1.000	0.173
Unknown (?)	1.00	58	N/A	N/A	0.012	0.010	0.013	0.011
Propanal	0.50	59	0.006	0.001	0.316	0.055	0.325	0.057
Propanone	0.50	59	0.007	0.001	0.362	0.063	0.373	0.065
Glyoxal	1.00	59	0.000	0.000	0.006	0.001	0.006	0.001
Butane	1.00	59	N/A	N/A	N/A	N/A	N/A	N/A
Ethanoic Acid	1.00	61	N/A	N/A	0.035	0.006	0.029	0.005
Urea (?)	1.00	61	0.004	0.004	0.000	0.000	0.001	0.001
Propanol	1.00	61	N/A	N/A	N/A	N/A	N/A	N/A
Ethylene Glycol	0.50	63	N/A	N/A	0.018	0.009	0.021	0.011
Methoxymethanol	0.50	63	N/A	N/A	0.022	0.018	0.025	0.020
Pentadiene	0.50	69	0.001	0.000	0.249	0.043	0.293	0.052
Pentyne	0.50	69	0.001	0.000	0.234	0.041	0.225	0.048
Pentene	1.00	71	N/A	N/A	0.380	0.067	0.479	0.083
Butenone	0.50	71	N/A	N/A	0.019	0.004	0.021	0.005
Butenal	0.50	71	N/A	N/A	0.020	0.004	0.022	0.004
Propiolic Acid	1.00	71	N/A	N/A	0.004	0.003	0.005	0.004
Butanal	0.50	73	N/A	N/A	0.068	0.012	0.070	0.012
Butanone	0.50	73	N/A	N/A	0.070	0.015	0.073	0.016
Malondialdehyde	0.33	73	N/A	N/A	0.004	0.003	0.004	0.003
Methyl Glyoxal	0.33	73	N/A	N/A	0.010	0.005	0.011	0.006
Acrylic Acid	0.33	73	N/A	N/A	0.004	0.001	0.004	0.001
Pentane	1.00	73	0.000	0.000	0.000	0.000	N/A	N/A
Propanoic Acid	1.00	75	N/A	N/A	0.013	0.003	N/A	N/A
Glyoxylic Acid	1.00	75	0.000	0.000	0.000	0.000	0.000	0.000
Butanol	1.00	75	0.000	0.000	N/A	N/A	N/A	N/A
Propanediol	1.00	77	0.001	0.000	0.026	0.006	0.029	0.006
Hydroxyacetaldehyde	0.50	77	N/A	N/A	0.003	0.003	0.004	0.003
Glycolic Acid	0.50	77	N/A	N/A	0.003	0.003	0.004	0.003
Benzene	1.00	79	0.001	0.000	0.010	0.002	0.012	0.002
Hexadiene	0.50	83	0.005	0.001	0.215	0.047	0.258	0.057
Hexyne	0.50	83	0.005	0.001	0.199	0.035	0.239	0.042
Hexene	1.00	85	N/A	N/A	0.092	0.016	0.095	0.017

Name	Ratio	Mass	Emissions / µmol m^{-2} day^{-1}					
			Ozone (O_3)		Light (hv)		O_3 + hv	
			Val.	Err.	Val.	Err.	Val.	Err.
Pentenone	0.50	85	N/A	N/A	0.012	0.003	0.013	0.003
Pentenal	0.50	85	N/A	N/A	0.008	0.002	0.008	0.002
Butadienoic Acid	0.50	85	N/A	N/A	0.002	0.002	0.002	0.002
Furanone	0.50	85	N/A	N/A	0.002	0.002	0.002	0.002
Pentanal	0.50	87	N/A	N/A	0.039	0.009	0.041	0.009
Pentanone	0.50	87	N/A	N/A	0.038	0.008	0.042	0.009
Succindialdehyde	0.33	87	N/A	N/A	0.005	0.004	0.005	0.004
Butanedione	0.33	87	N/A	N/A	0.008	0.002	0.008	0.002
Butenoic Acid	0.33	87	N/A	N/A	0.005	0.001	0.005	0.001
Malonic Anhydride	0.50	87	0.000	0.000	0.001	0.001	0.001	0.001
Oxopropenoic Acid	0.50	87	0.000	0.000	0.001	0.001	0.001	0.001
Hexane	1.00	87	N/A	N/A	N/A	N/A	N/A	N/A
Butanoic Acid	1.00	89	N/A	N/A	0.005	0.001	0.006	0.001
Pyruvic Acid	1.00	89	N/A	N/A	0.002	0.001	0.002	0.001
Unkonwn (?)	1.00	89	0.000	0.000	N/A	N/A	N/A	N/A
Pentanol	1.00	89	0.000	0.000	N/A	N/A	N/A	N/A
Butanediol	1.00	91	N/A	N/A	0.018	0.004	0.019	0.004
Unknown (?)	1.00	91	0.002	0.002	0.003	0.002	0.003	0.002
Glyceraldhyde	0.50	91	N/A	N/A	0.001	0.001	0.002	0.001
Lactic Acid	0.50	91	N/A	N/A	0.001	0.000	0.001	0.001
Toluene	1.00	93	0.012	0.002	0.003	0.001	0.003	0.001
Heptadiene	0.50	97	N/A	N/A	0.083	0.042	0.094	0.048
Heptyne	0.50	97	N/A	N/A	0.076	0.039	0.086	0.044
Hydroxyquinol	1.00	98	0.001	0.001	0.001	0.001	0.001	0.001
Heptene	1.00	99	N/A	N/A	0.015	0.003	0.015	0.003
Hexenone	0.50	99	N/A	N/A	0.011	0.009	0.012	0.010
Hexenal	0.50	99	N/A	N/A	0.008	0.002	0.009	0.002
Pentadienoic Acid	0.50	99	N/A	N/A	0.003	0.003	0.004	0.003
Cyclopentadione	0.50	99	N/A	N/A	0.004	0.002	0.004	0.002
Maleic Anhydride	1.00	99	N/A	N/A	0.001	0.000	0.000	0.000
Hexanal	0.50	101	N/A	N/A	0.028	0.006	0.031	0.007
Hexanone	0.50	101	N/A	N/A	0.029	0.015	0.032	0.016
Tetronic Acid	1.00	101	N/A	N/A	0.005	0.004	0.003	0.002
Glutaraldehyde	0.33	101	N/A	N/A	0.004	0.001	0.004	0.001
Pentanedione	0.33	101	N/A	N/A	0.006	0.002	0.007	0.002
Pentenoic Acid	0.33	101	N/A	N/A	0.005	0.003	0.005	0.003
Heptane	1.00	101	N/A	N/A	0.000	0.000	N/A	N/A
Pentanoic Acid	1.00	103	N/A	N/A	0.004	0.001	0.004	0.001
Oxobutanoic Acid	0.50	103	N/A	N/A	0.001	0.001	0.001	0.001
Acetic Anhydride	0.50	103	N/A	N/A	0.001	0.000	0.001	0.000
Hexanol	1.00	103	N/A	N/A	N/A	N/A	N/A	N/A
Pentanediol	1.00	105	N/A	N/A	0.021	0.005	0.023	0.005
Unknown (?)	1.00	105	N/A	N/A	0.003	0.002	0.003	0.002
Dihydroxybutanal	0.50	105	N/A	N/A	0.002	0.001	0.002	0.001
Hydroxybutyric Acid	0.50	105	N/A	N/A	0.002	0.001	0.002	0.001
Malonic Acid	1.00	105	N/A	N/A	0.001	0.001	0.001	0.000

Name	Ratio	Mass	Emissions / µmol m^{-2} day^{-1}					
			Ozone (O_3)		Light (hv)		O_3 + hv	
			Val.	Err.	Val.	Err.	Val.	Err.
Styrene	1.00	105	N/A	N/A	N/A	N/A	N/A	N/A
Ethylbenzene	0.50	106	0.002	0.001	N/A	N/A	0.001	0.000
Xylene	0.50	106	0.002	0.001	N/A	N/A	0.001	0.000
Benzaldehyde	1.00	107	N/A	N/A	0.012	0.003	0.013	0.003
Unknown (?)	1.00	109	0.006	0.005	0.020	0.016	0.022	0.018
Benzoquinone	1.00	109	N/A	N/A	0.004	0.001	0.004	0.001
Cresol/Benzyl Alcohol	1.00	109	N/A	N/A	0.001	0.000	0.001	0.000
Unknown (?)	1.00	110	N/A	N/A	0.002	0.003	0.003	0.002
Octadiene	0.50	111	N/A	N/A	0.077	0.039	0.087	0.044
Octyne	0.50	111	N/A	N/A	0.070	0.035	0.079	0.040
Benzenediol	1.00	111	N/A	N/A	0.002	0.001	0.002	0.001
Methylcyclohexenone	0.50	111	N/A	N/A	0.001	0.001	0.001	0.001
Heptadienal	0.50	111	N/A	N/A	0.001	0.000	0.001	0.000
Octene	1.00	113	N/A	N/A	0.031	0.006	0.037	0.007
Heptenone	0.50	113	N/A	N/A	0.007	0.006	0.008	0.007
Heptenal	0.50	113	N/A	N/A	0.005	0.001	0.006	0.001
Sorbic Acid	0.50	113	N/A	N/A	0.002	0.002	0.002	0.002
Cyclohexadione	0.50	113	N/A	N/A	0.002	0.001	0.002	0.001
Succinic Anhydride	1.00	113	0.001	0.001	0.001	0.001	0.001	0.001
Heptanal	0.50	115	N/A	N/A	0.057	0.010	0.076	0.013
Heptanone	0.50	115	N/A	N/A	0.050	0.025	0.066	0.034
Hexadial	0.33	115	N/A	N/A	0.004	0.003	0.004	0.004
Hexadione	0.33	115	N/A	N/A	0.003	0.002	0.004	0.002
Hexenoic Acid	0.33	115	N/A	N/A	0.003	0.002	0.003	0.002
Glutaric Anhydride	0.50	115	0.000	0.000	0.001	0.001	0.001	0.001
Oxopentenoic Acid	0.50	115	0.000	0.000	0.001	0.001	0.001	0.001
Octane	1.00	115	N/A	N/A	0.001	0.000	0.001	0.000
Hexanoic Acid	1.00	117	N/A	N/A	0.004	0.001	0.005	0.001
Oxopentanoic Acid	1.00	117	N/A	N/A	0.002	0.002	0.002	0.002
Heptanol	1.00	117	N/A	N/A	N/A	N/A	N/A	N/A
Hexanediol	1.00	119	0.000	0.000	0.020	0.010	0.024	0.012
Succinic Acid	1.00	119	N/A	N/A	0.002	0.002	0.002	0.001
Dihydroxypentanal	0.50	119	0.000	0.000	0.001	0.001	0.002	0.002
Hydroxypentanoic Acid	0.50	119	0.000	0.000	0.001	0.001	0.002	0.002
Acetophenone	0.50	121	N/A	N/A	0.002	0.001	0.002	0.001
Phenylacetaldehyde	0.50	121	N/A	N/A	0.003	0.002	0.003	0.003
C3 Benzene	1.00	121	0.002	0.001	0.001	0.000	0.001	0.000
Pentanetriol	1.00	121	N/A	N/A	0.000	0.000	0.000	0.000
Unknown (?)	1.00	123	0.001	0.001	0.014	0.011	0.015	0.012
Benzoic Acid	0.50	123	N/A	N/A	0.001	0.000	0.001	0.000
Salicylaldehyde	0.50	123	N/A	N/A	0.001	0.000	0.001	0.000
Erythritol	1.00	123	N/A	N/A	0.001	0.000	0.001	0.001
Ethylphenol/Xylenol	1.00	123	0.000	0.000	0.000	0.000	0.001	0.000
Nonadiene	0.50	125	0.000	0.000	0.021	0.011	0.025	0.013
Nonyne	0.50	125	0.000	0.000	0.029	0.010	0.022	0.011
Methoxyphenol	1.00	125	N/A	N/A	0.003	0.001	0.004	0.001

Name	Ratio	Mass	Emissions / µmol m^{-2} day^{-1}					
			Ozone (O_3)		Light (hv)		O_3 + hv	
			Val.	Err.	Val.	Err.	Val.	Err.
Acetyl Cyclohexenone	0.50	125	N/A	N/A	0.002	0.001	0.002	0.002
Cyclohexenacetaldehyde	0.50	125	N/A	N/A	0.001	0.001	0.001	0.001
Hydroxybenzoquinone	1.00	125	0.000	0.000	0.001	0.001	0.001	0.001
Unknown (?)	1.00	125	N/A	N/A	N/A	N/A	N/A	N/A
Octenone	0.50	127	0.001	0.001	0.011	0.003	0.012	0.003
Octenal	0.50	127	0.001	0.000	0.007	0.002	0.008	0.002
Nonene	1.00	127	N/A	N/A	0.008	0.004	0.008	0.002
Heptadienoic Acid	1.00	127	N/A	N/A	0.002	0.001	0.002	0.001
Octanal	0.50	129	N/A	N/A	0.045	0.008	0.050	0.009
Octanone	0.50	129	N/A	N/A	0.039	0.020	0.044	0.023
Nonane	1.00	129	N/A	N/A	0.003	0.001	0.003	0.001
Heptanedial	0.33	129	N/A	N/A	0.002	0.002	0.003	0.002
Heptanedione	0.33	129	N/A	N/A	0.002	0.001	0.002	0.001
Heptenoic Acid	0.33	129	N/A	N/A	0.002	0.001	0.002	0.001
Sotolon	0.33	129	0.000	0.000	N/A	N/A	0.000	0.000
Furaneol	0.33	129	0.000	0.000	N/A	N/A	0.000	0.000
Oxohexenoic Acid	0.33	129	0.000	0.000	N/A	N/A	0.000	0.000
Heptanoic Acid	1.00	131	N/A	N/A	0.003	0.002	0.004	0.002
Oxohexanoic Acid	1.00	131	0.001	0.001	0.002	0.002	0.003	0.002
Citraconic Acid	0.50	131	0.001	0.001	0.001	0.001	0.001	0.001
Heptenedioic Acid	0.50	131	0.001	0.001	0.001	0.001	0.001	0.001
Octanol	1.00	131	0.000	0.000	0.000	0.000	0.000	0.000
Heptanediol	1.00	133	N/A	N/A	0.023	0.012	0.030	0.015
Dihydroxyhexanal	0.50	133	0.000	0.000	0.001	0.001	0.002	0.001
Hydroxyhexanoic Acid	0.50	133	0.000	0.000	0.001	0.001	0.002	0.001
Glutaric Acid	1.00	133	N/A	N/A	0.001	0.001	0.001	0.001
Oxobutanedioic Acid	1.00	133	0.000	0.000	0.000	0.000	0.000	0.000
Unknown (?)	1.00	133	0.001	0.000	0.000	0.000	0.000	0.000
Nonenone	0.50	141	N/A	N/A	0.007	0.005	0.007	0.006
Nonenal	0.50	141	N/A	N/A	0.005	0.001	0.005	0.001
Decene	1.00	141	N/A	N/A	0.006	0.001	0.006	0.001
Octadienoic Acid	1.00	141	N/A	N/A	0.002	0.002	0.002	0.002
Methoxycatechol	1.00	141	0.000	0.000	0.001	0.001	0.001	0.001
Dihydroxybenzoquinone	1.00	141	0.000	0.000	0.000	0.000	0.000	0.000
Nonanal	0.50	143	0.001	0.000	0.033	0.007	0.039	0.009
Nonanone	0.50	143	0.001	0.000	0.030	0.007	0.036	0.008
Octanedial	0.33	143	N/A	N/A	0.003	0.002	0.003	0.002
Octanedione	0.33	143	N/A	N/A	0.002	0.001	0.002	0.001
Octenoic Acid	0.33	143	N/A	N/A	0.002	0.001	0.002	0.001
Octanoic Acid	1.00	145	N/A	N/A	0.005	0.001	0.006	0.002
Oxoheptanoic Acid	1.00	145	N/A	N/A	0.001	0.001	0.001	0.001
Dimethyl Maleate	0.50	145	0.000	0.000	0.000	0.000	0.000	0.000
Hexenedioic Acid	0.50	145	0.000	0.000	0.000	0.000	0.000	0.000
Nonanol	1.00	145	N/A	N/A	0.000	0.000	0.000	0.000
Octanediol	1.00	147	N/A	N/A	0.026	0.014	0.030	0.015
Adipic Acid	1.00	147	0.000	0.000	0.001	0.001	0.001	0.001

Name	Ratio	Mass	Emissions / µmol m^{-2} day^{-1}					
			Ozone (O_3)		Light (hv)		O_3 + hv	
			Val.	Err.	Val.	Err.	Val.	Err.
Dihydroxyheptanal	0.50	147	N/A	N/A	0.000	0.000	0.000	0.000
Hydroxyheptanoic Acid	0.50	147	N/A	N/A	0.000	0.000	0.000	0.00
Oxopentanedioic Acid	1.00	147	0.000	0.000	0.000	0.000	0.000	0.000
Decanal	0.50	157	0.003	0.001	0.023	0.004	0.027	0.005
Decanone	0.50	157	0.003	0.001	0.020	0.010	0.023	0.012
Nonanedial	0.33	157	N/A	N/A	0.001	0.001	0.002	0.001
Nonadione	0.33	157	N/A	N/A	0.001	0.001	0.001	0.001
Nonenoic Acid	0.33	157	N/A	N/A	0.001	0.001	0.001	0.001
Oxooctenoic Acid	1.00	157	0.000	0.000	0.001	0.001	0.001	0.001
Unknown (?)	1.00	157	0.001	0.001	0.001	0.000	0.001	0.001
Nonanoic Acid	1.00	159	N/A	N/A	0.004	0.001	0.004	0.001
Oxooctanoic Acid	1.00	159	0.000	0.000	0.001	0.001	0.001	0.001
Dioxoheptanoic Acid	1.00	159	0.000	0.000	0.000	0.000	0.000	0.000
Oxohexendioic Acid	0.50	159	N/A	N/A	0.000	0.000	0.000	0.000
Pentahydroxybenzene	0.50	159	N/A	N/A	0.000	0.000	0.000	0.000
Nonanediol	1.00	161	0.001	0.000	0.022	0.012	0.027	0.014
Dihydroxyoctanal	0.50	161	N/A	N/A	0.001	0.001	0.001	0.001
Hydroxyoctanoic Acid	0.50	161	N/A	N/A	0.001	0.001	0.001	0.001
Undecanal	0.50	171	N/A	N/A	0.015	0.008	0.016	0.008
Undecanone	0.50	171	N/A	N/A	0.014	0.003	0.014	0.003
Decanedial	0.33	171	N/A	N/A	0.001	0.001	0.002	0.001
Decanedione	0.33	171	N/A	N/A	0.001	0.000	0.001	0.001
Decenoic Acid	0.33	171	N/A	N/A	0.001	0.001	0.001	0.001
Oxononenoic Acid	1.00	171	0.001	0.000	0.001	0.001	0.001	0.001
Oxononanoic Acid	1.00	173	N/A	N/A	0.003	0.002	0.003	0.003
Dihydroxynonanal	0.50	175	0.001	0.001	0.005	0.004	0.006	0.005
Hydroxynonanoic Acid	0.50	175	0.001	0.001	0.005	0.004	0.006	0.005
Cladinose	1.00	177	0.000	0.000	0.001	0.001	0.001	0.001
Oxodecanoic Acid	1.00	187	0.000	0.000	0.002	0.002	0.002	0.002
Dioxononanoic Acid	1.00	187	0.000	0.000	N/A	N/A	N/A	N/A
Azelaic Acid	1.00	189	N/A	N/A	0.001	0.001	0.001	0.001
Dihydroxynonanoic Acid	1.00	191	N/A	N/A	0.001	0.001	0.001	0.001
Oxoundecanoic Acid	1.00	201	N/A	N/A	0.002	0.001	0.001	0.001
Oxodecenoic Acid	1.00	213	0.002	0.002	0.002	0.002	0.002	0.002
Heptadecanal	0.50	255	N/A	N/A	0.000	0.000	N/A	N/A
Heptadecanone	0.50	255	N/A	N/A	0.000	0.000	0.000	0.000
Heptadecanoic Acid	1.00	271	0.000	0.000	0.000	0.000	0.000	0.000
Thapsic Acid	1.00	287	0.000	0.000	0.000	0.000	0.000	0.000
Oxooctadecanoic Acid	0.50	299	0.000	0.000	0.000	0.000	0.000	0.000
Ricinelaidic Acid	0.50	299	0.000	0.000	0.000	0.000	0.000	0.000
Octadecanedioic Acid	1.00	315	0.000	0.000	0.000	0.000	0.000	0.000
Viniferin	1.00	455	0.000	0.000	0.000	0.000	0.000	0.000

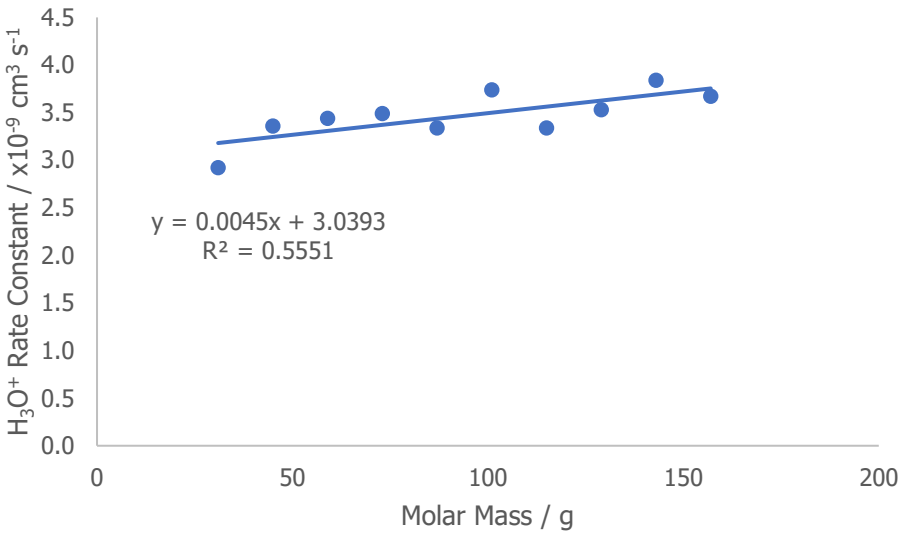

Figure 6.1 - Correlation of aldehyde molar mass with H_3O^+ rate constant used to calculate unknown aldehyde rate constants.

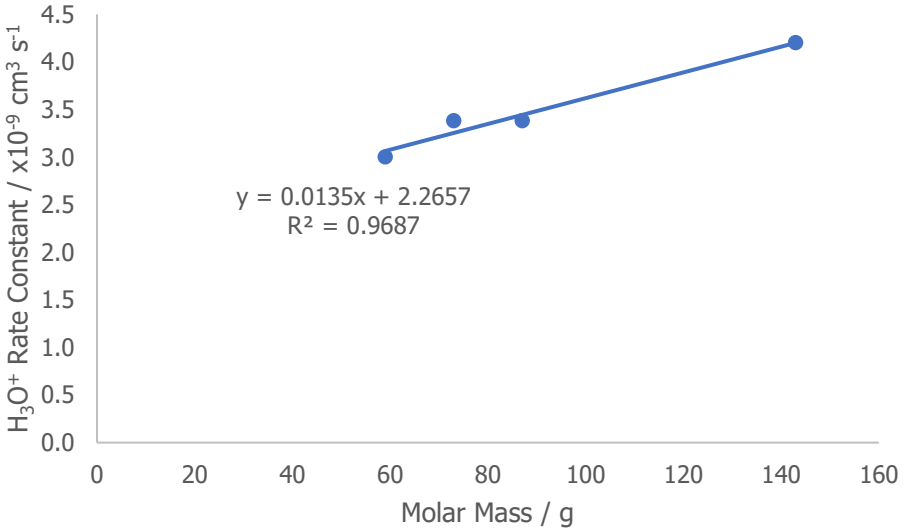

Figure 6.2 - Correlation of ketone molar mass with H_3O^+ rate constant used to calculate unknown ketone rate constants.

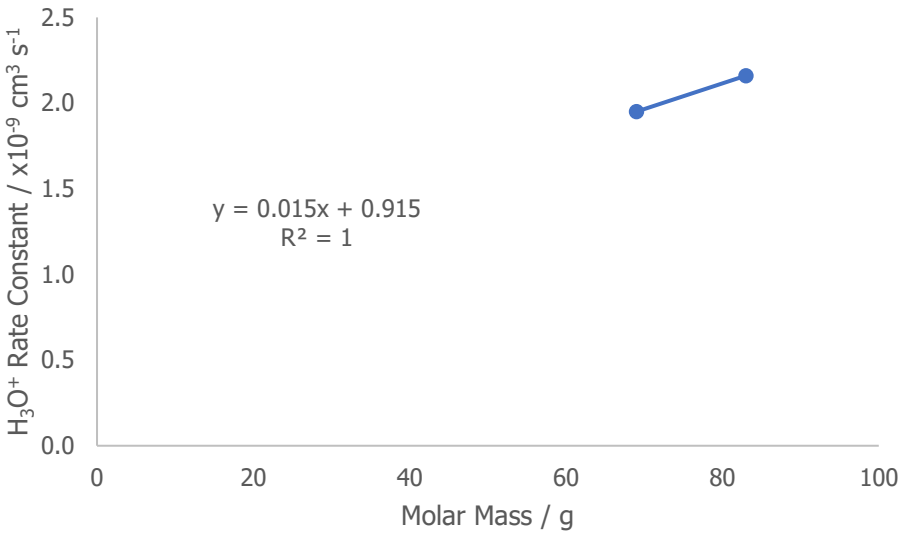

Figure 6.3 - Correlation of alkyne molar mass with H_3O^+ rate constant used to calculate unknown alkyne rate constants.

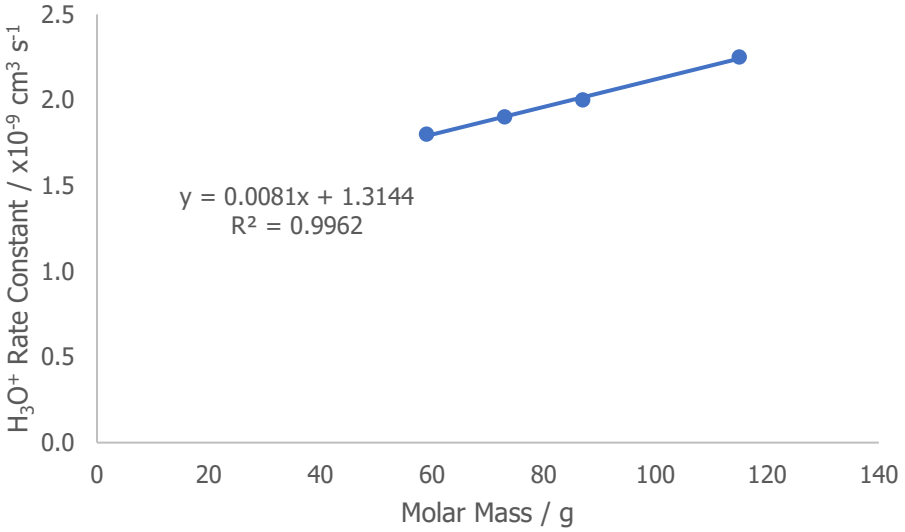

Figure 6.4 - Correlation of alkane molar mass with H_3O^+ rate constant used to calculate unknown alkane rate constants.

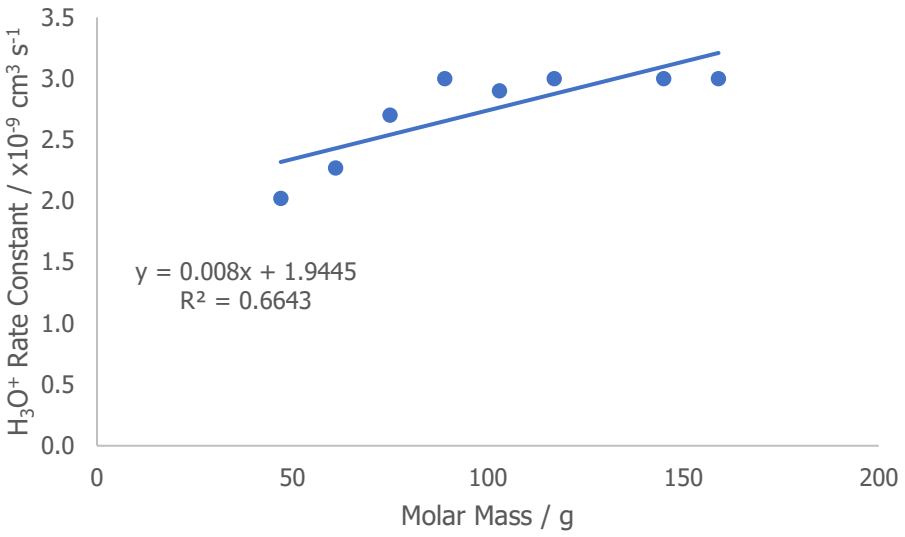

Figure 6.5 - Correlation of carboxylic acid molar mass with H_3O^+ rate constant used to calculate unknown carboxylic acid rate constants.

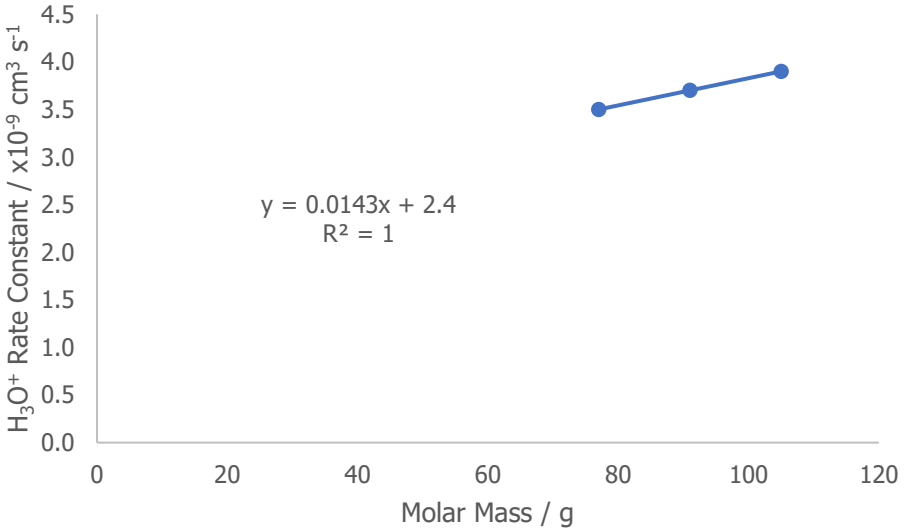

Figure 6.6 - Correlation of diol molar mass with H_3O^+ rate constant used to calculate unknown diol rate constants.

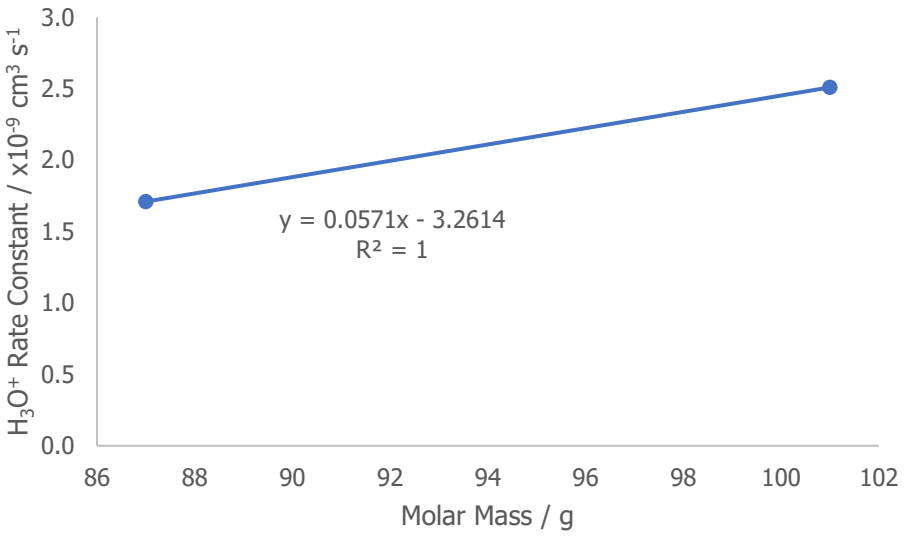

Figure 6.7 - Correlation of diketone molar mass with H_3O^+ rate constant used to calculate unknown diketone rate constants.

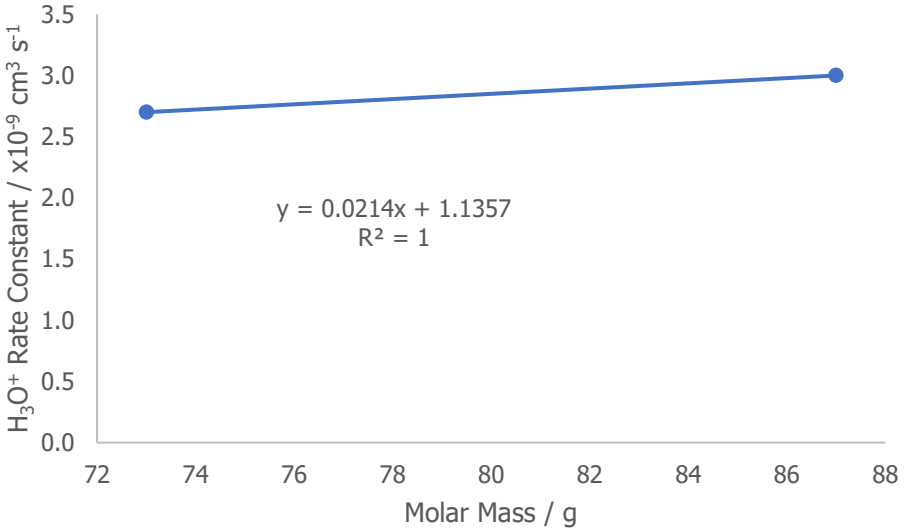

Figure 6.8 - Correlation of enoic acid molar mass with H_3O^+ rate constant used to calculate unknown enoic acid rate constants.

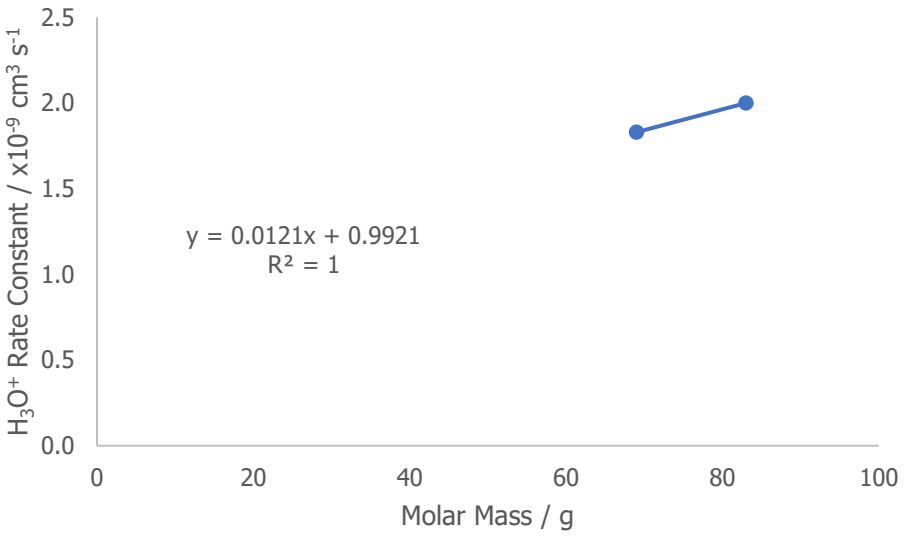

Figure 6.9 - Correlation of diene molar mass with H_3O^+ rate constant used to calculate unknown diene rate constants.

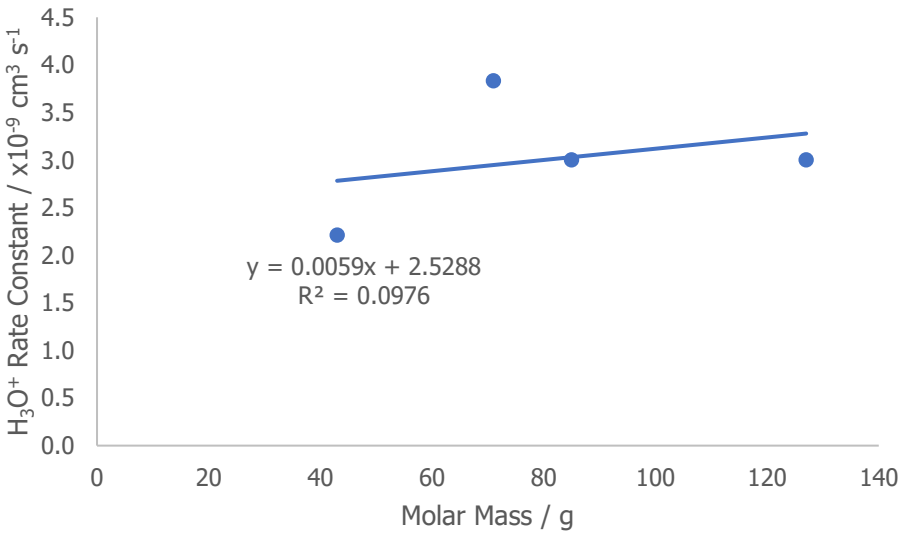

Figure 6.10 - Correlation of enone molar mass with H_3O^+ rate constant used to calculate unknown enone rate constants.

Abbreviations

CCN – Cloud Condensation Nuclei

CH_3I – Methyl Iodide

CIMS – Chemical Ionisation Mass Spectrometry

DC – Direct Current

DOC – Dissolved Organic Carbon

DOI – Dissolved Organic Iodine

DOM – Dissolved Organic Matter

FIMR – Focusing Ion-Molecule Reactor

MSA – Methylsulfonic Acid

NO_3 – Nitrate

O_3 – Ozone

OVOC – Oxygenated Volatile Organic Compound

PA – Proton Affinity

PEEK – Polyether Ether Ketone

PPAO – Penlee Point Atmospheric Observatory

PTFE – Polytetrafluoroethylene

SIFT-MS – Selected Ion Flow Tube – Mass Spectrometry

SML – Surface Microlayer

SO_2 – Sulfur Dioxide

SOA – Secondary Organic Aerosol

SSA – Sea Spray Aerosol

ULW – Underlying Water

VOC – Volatile Organic Compound

Bibliography

Abushaban, A., Salinas-Rodriguez, S.G., Mangal, M.N., Mondal, S., Goueli, S.A., Knezev, A., Vrouwenvelder, J.S., Schippers, J.C., Kennedy, M.D., 2019. ATP measurement in seawater reverse osmosis systems: Eliminating seawater matrix effects using a filtration-based method. Desalination 453, 1–9. https://doi.org/10.1016/j.desal.2018.11.020

Allard, S., Gallard, H., Fontaine, C., Croué, J.-P., 2010. Formation of methyl iodide on a natural manganese oxide. Water Res. 44, 4623–4629. https://doi.org/10.1016/j.watres.2010.06.008

Amachi, S., Kamagata, Y., Kanagawa, T., Muramatsu, Y., 2001. Bacteria Mediate Methylation of Iodine in Marine and Terrestrial Environments. Appl. Environ. Microbiol. 67, 2718–2722. https://doi.org/10.1128/AEM.67.6.2718-2722.2001

Arnold, S.R., Spracklen, D.V., Williams, J., Yassaa, N., Sciare, J., Bonsang, B., Gros, V., Peeken, I., Lewis, A.C., Alvain, S., Moulin, C., 2009. Evaluation of the global oceanic isoprene source and its impacts on marine organic carbon aerosol. Atmospheric Chem. Phys. 9, 1253–1262. https://doi.org/10.5194/acp-9-1253-2009

Baker, A.R., Turner, S.M., Broadgate, W.J., Thompson, A., McFiggans, G.B., Vesperini, O., Nightingale, P.D., Liss, P.S., Jickells, T.D., 2000. Distribution and sea-air fluxes of biogenic trace gases in the eastern Atlantic Ocean. Glob. Biogeochem. Cycles 14, 871–886. https://doi.org/10.1029/1999GB001219

Bates, K.H., Jacob, D.J., Wang, S., Hornbrook, R.S., Apel, E.C., Kim, M.J., Millet, D.B., Wells, K.C., Chen, X., Brewer, J.F., Ray, E.A., Commane, R., Diskin, G.S., Wofsy, S.C., 2021. The Global Budget of Atmospheric Methanol: New Constraints on Secondary, Oceanic, and Terrestrial Sources. J. Geophys. Res. Atmospheres 126, e2020JD033439. https://doi.org/10.1029/2020JD033439

Beale, R., Dixon, J.L., Arnold, S.R., Liss, P.S., Nightingale, P.D., 2013. Methanol, acetaldehyde, and acetone in the surface waters of the Atlantic Ocean. J. Geophys. Res. Oceans 118, 5412–5425. https://doi.org/10.1002/jgrc.20322

Bell, N., Hsu, L., Jacob, D.J., Schultz, M.G., Blake, D.R., Butler, J.H., King, D.B., Lobert, J.M., Maier-Reimer, E., 2002. Methyl iodide: Atmospheric budget and use as a tracer of marine convection in global models. J. Geophys. Res. Atmospheres 107, ACH 8-1. https://doi.org/10.1029/2001JD001151

Bettenhausen, C., Jansen, K., 2022. Podcast: How did we get to helium shortage 4.0? Chem. Eng. News.

Blake, N.J., Blake, D.R., Wingenter, O.W., Sive, B.C., Kang, C.H., Thornton, D.C., Bandy, A.R., Atlas, E., Flocke, F., Harris, J.M., Rowland, F.S., 1999. Aircraft measurements of the latitudinal, vertical, and seasonal variations of NMHCs, methyl nitrate, methyl halides, and DMS during the First Aerosol Characterization Experiment (ACE 1). J. Geophys. Res. Atmospheres 104, 21803–21817. https://doi.org/10.1029/1999JD900238

Booge, D., Marandino, C.A., Schlundt, C., Palmer, P.I., Schlundt, M., Atlas, E.L., Bracher, A., Saltzman, E.S., Wallace, D.W.R., 2016. Can simple models predict large-scale surface ocean isoprene concentrations? Atmospheric Chem. Phys. 16, 11807–11821. https://doi.org/10.5194/acp-16-11807-2016

Boucher, O., Moulin, C., Belviso, S., Aumont, O., Bopp, L., Cosme, E., von Kuhlmann, R., Lawrence, M.G., Pham, M., Reddy, M.S., Sciare, J., Venkataraman, C., 2003. DMS atmospheric concentrations and sulphate aerosol indirect radiative forcing: a sensitivity study to the DMS source representation and oxidation. Atmospheric Chem. Phys. 3, 49–65. https://doi.org/10.5194/acp-3-49-2003

Breider, T.J., Chipperfield, M.P., Richards, N. a. D., Carslaw, K.S., Mann, G.W., Spracklen, D.V., 2010. Impact of BrO on dimethylsulfide in the remote marine boundary layer. Geophys. Res. Lett. 37. https://doi.org/10.1029/2009GL040868

Broadgate, W.J., Liss, P.S., Penkett, S.A., 1997. Seasonal emissions of isoprene and other reactive hydrocarbon gases from the ocean. Geophys. Res. Lett. 24, 2675–2678. https://doi.org/10.1029/97GL02736

Brownell, D.K., Moore, R.M., Cullen, J.J., 2010. Production of methyl halides by Prochlorococcus and Synechococcus. Glob. Biogeochem. Cycles 24. https://doi.org/10.1029/2009GB003671

Brüggemann, M., Hayeck, N., Bonnineau, C., Pesce, S., Alpert, P.A., Perrier, S., Zuth, C., Hoffmann, T., Chen, J., George, C., 2017. Interfacial photochemistry of biogenic surfactants: a major source of abiotic volatile organic compounds. Faraday Discuss. 200, 59–74. https://doi.org/10.1039/C7FD00022G

Burkart, J., Hodshire, A.L., Mungall, E.L., Pierce, J.R., Collins, D.B., Ladino, L.A., Lee, A.K.Y., Irish, V., Wentzell, J.J.B., Liggio, J., Papakyriakou, T., Murphy, J., Abbatt, J., 2017. Organic Condensation and Particle Growth to CCN Sizes in the Summertime Marine Arctic Is Driven by Materials More Semivolatile Than at Continental Sites. Geophys. Res. Lett. 44, 10,725-10,734. https://doi.org/10.1002/2017GL075671

Butler, J.H., King, D.B., Lobert, J.M., Montzka, S.A., Yvon-Lewis, S.A., Hall, B.D., Warwick, N.J., Mondeel, D.J., Aydin, M., Elkins, J.W., 2007. Oceanic distributions and emissions of short-lived halocarbons. Glob. Biogeochem. Cycles 21. https://doi.org/10.1029/2006GB002732

Campos, M.L. a. M., Nightingale, P.D., Jickells, T.D., 1996. A comparison of methyl iodide emissions from seawater and wet depositional fluxes of iodine over the southern North Sea. Tellus B 48, 106–114. https://doi.org/10.1034/j.1600-0889.1996.00010.x

Carpenter, L.J., Archer, S.D., Beale, R., 2012. Ocean-atmosphere trace gas exchange. Chem. Soc. Rev. 41, 6473–6506. https://doi.org/10.1039/C2CS35121H

Carpenter, L.J., MacDonald, S.M., Shaw, M.D., Kumar, R., Saunders, R.W., Parthipan, R., Wilson, J., Plane, J.M.C., 2013. Atmospheric iodine levels influenced by sea surface emissions of inorganic iodine. Nat. Geosci. 6, 108–111. https://doi.org/10.1038/ngeo1687

Carpenter, L.J., Malin, G., Liss, P.S., Küpper, F.C., 2000. Novel biogenic iodine-containing trihalomethanes and other short-lived halocarbons in the coastal east Atlantic. Glob. Biogeochem. Cycles 14, 1191–1204. https://doi.org/10.1029/2000GB001257

Carpenter, L.J., Nightingale, P.D., 2015. Chemistry and Release of Gases from the Surface Ocean. Chem. Rev. 115, 4015–4034. https://doi.org/10.1021/cr5007123

Carpenter, L.J., Sturges, W.T., Penkett, S.A., Liss, P.S., Alicke, B., Hebestreit, K., Platt, U., 1999. Short-lived alkyl iodides and bromides at Mace Head, Ireland: Links to biogenic sources and halogen oxide production. J. Geophys. Res. Atmospheres 104, 1679–1689. https://doi.org/10.1029/98JD02746

Cates, R.D., Bowers, M.T., 1980. Energy transfer in ion-molecule association reactions. Dependence of collisional stabilization efficiency on the collision gas. J. Am. Chem. Soc. 102, 3994–3996. https://doi.org/10.1021/ja00532a002

Chameides, W.L., Davis, D.D., 1980. Iodine: Its possible role in tropospheric photochemistry. J. Geophys. Res. Oceans 85, 7383–7398. https://doi.org/10.1029/JC085iC12p07383

Chance, R., Baker, A.R., Carpenter, L., Jickells, T.D., 2014. The distribution of iodide at the sea surface. Environ. Sci. Process. Impacts 16, 1841–1859. https://doi.org/10.1039/C4EM00139G

Charlson, R.J., Lovelock, J.E., Andreae, M.O., Warren, S.G., 1987. Oceanic phytoplankton, atmospheric sulphur, cloud albedo and climate. Nature 326, 655–661. https://doi.org/10.1038/326655a0

Chen, Y., Liu, S., Yang, G., He, Z., 2020. Influence Factors on Photochemical Production of Methyl Iodide in Seawater. J. Ocean Univ. China 19, 1353–1361. https://doi.org/10.1007/s11802-020-4463-8

Chen, Y.-C., Li, J.-L.F., Lee, W.-L., Diner, D.J., Garay, M.J., Jiang, J.H., Wang, Y.-H., Yu, J.-Y., Kalashnikova, O.V., 2020. Evaluation of sea salt aerosols in climate systems: global climate modeling and observation-based analyses. Environ. Res. Lett. 15, 034047. https://doi.org/10.1088/1748-9326/ab751c*

Chuck, A.L., Turner, S.M., Liss, P.S., 2005. Oceanic distributions and air-sea fluxes of biogenic halocarbons in the open ocean. J. Geophys. Res. Oceans 110. https://doi.org/10.1029/2004JC002741

Ciuraru, R., Fine, L., Pinxteren, M. van, D'Anna, B., Herrmann, H., George, C., 2015a. Unravelling New Processes at Interfaces: Photochemical Isoprene Production at the Sea Surface. Environ. Sci. Technol. 49, 13199–13205. https://doi.org/10.1021/acs.est.5b02388

Ciuraru, R., Fine, L., van Pinxteren, M., D'Anna, B., Herrmann, H., George, C., 2015b. Photosensitized production of functionalized and unsaturated organic compounds at the air-sea interface. Sci. Rep. 5, 12741. https://doi.org/10.1038/srep12741

Claeys, M., Graham, B., Vas, G., Wang, W., Vermeylen, R., Pashynska, V., Cafmeyer, J., Guyon, P., Andreae, M.O., Artaxo, P., Maenhaut, W., 2004. Formation of Secondary Organic Aerosols Through Photooxidation of Isoprene. Science 303, 1173–1176. https://doi.org/10.1126/science.1092805

Clarke, A.D., Varner, J.L., Eisele, F., Mauldin, R.L., Tanner, D., Litchy, M., 1998. Particle production in the remote marine atmosphere: Cloud outflow and subsidence during ACE 1. J. Geophys. Res. Atmospheres 103, 16397–16409. https://doi.org/10.1029/97JD02987

Conte, L., Szopa, S., Aumont, O., Gros, V., Bopp, L., 2020. Sources and Sinks of Isoprene in the Global Open Ocean: Simulated Patterns and Emissions to the Atmosphere. J. Geophys. Res. Oceans 125, e2019JC015946. https://doi.org/10.1029/2019JC015946

Cotter, E.S.N., Canosa-Mas, C.E., Manners, C.R., Wayne, R.P., Shallcross, D.E., 2003. Kinetic study of the reactions of OH with the simple alkyl iodides: CH3I, C2H5I, 1-C3H7I and 2-C3H7I. Atmos. Environ. 37, 1125–1133. https://doi.org/10.1016/S1352-2310(02)00928-7

Cravigan, L.T., Mallet, M.D., Vaattovaara, P., Harvey, M.J., Law, C.S., Modini, R.L., Russell, L.M., Stelcer, E., Cohen, D.D., Olsen, G., Safi, K., Burrell, T.J., Ristovski, Z., 2020. Sea spray aerosol organic enrichment, water uptake and surface tension effects. Atmospheric Chem. Phys. 20, 7955–7977. https://doi.org/10.5194/acp-20-7955-2020

Croft, B., Martin, R.V., Leaitch, W.R., Burkart, J., Chang, R.Y.-W., Collins, D.B., Hayes, P.L., Hodshire, A.L., Huang, L., Kodros, J.K., Moravek, A., Mungall, E.L., Murphy, J.G., Sharma, S., Tremblay, S., Wentworth, G.R., Willis, M.D., Abbatt, J.P.D., Pierce, J.R., 2019. Arctic marine secondary organic aerosol contributes significantly to summertime particle size distributions in the Canadian Arctic Archipelago. Atmospheric Chem. Phys. 19, 2787–2812. https://doi.org/10.5194/acp-19-2787-2019

Croft, B., Martin, R.V., Moore, R.H., Ziemba, L.D., Crosbie, E.C., Liu, H., Russell, L.M., Saliba, G., Wisthaler, A., Müller, M., Schiller, A., Galí, M., Chang, R.Y.-W., McDuffie, E.E., Bilsback, K.R., Pierce, J.R., 2021. Factors controlling marine aerosol size distributions and their climate effects over the northwest Atlantic Ocean region. Atmospheric Chem. Phys. 21, 1889–1916. https://doi.org/10.5194/acp-21-1889-2021

Dahl, E.E., Saltzman, E.S., 2008. Alkyl nitrate photochemical production rates in North Pacific seawater. Mar. Chem. 112, 137–141. https://doi.org/10.1016/j.marchem.2008.10.002

Dahl, E.E., Saltzman, E.S., de Bruyn, W.J., 2003. The aqueous phase yield of alkyl nitrates from ROO + NO: Implications for photochemical production in seawater. Geophys. Res. Lett. 30. https://doi.org/10.1029/2002GL016811

Dani, K.G.S., Loreto, F., 2017. Trade-Off Between Dimethyl Sulfide and Isoprene Emissions from Marine Phytoplankton. Trends Plant Sci. 22, 361–372. https://doi.org/10.1016/j.tplants.2017.01.006

Davie-Martin, C.L., Giovannoni, S.J., Behrenfeld, M.J., Penta, W.B., Halsey, K.H., 2020. Seasonal and Spatial Variability in the Biogenic Production and Consumption of Volatile Organic Compounds (VOCs) by Marine Plankton in the North Atlantic Ocean. Front. Mar. Sci. 7.

Davis, D., Crawford, J., Liu, S., McKeen, S., Bandy, A., Thornton, D., Rowland, F., Blake, D., 1996. Potential impact of iodine on tropospheric levels of ozone and other critical oxidants. J. Geophys. Res. Atmospheres 101, 2135–2147. https://doi.org/10.1029/95JD02727

de Gouw, J., Warneke, C., 2007. Measurements of volatile organic compounds in the earth's atmosphere using proton-transfer-reaction mass spectrometry. Mass Spectrom. Rev. 26, 223–257. https://doi.org/10.1002/mas.20119

De Laurentiis, E., Minella, M., Maurino, V., Minero, C., Mailhot, G., Sarakha, M., Brigante, M., Vione, D., 2012. Assessing the occurrence of the dibromide radical (Br2−) in natural waters: Measures of triplet-sensitised formation, reactivity, and modelling. Sci. Total Environ. 439, 299–306. https://doi.org/10.1016/j.scitotenv.2012.09.037

Diskin, A.M., Wang, T., Smith, D., Španěl, P., 2002. A selected ion flow tube (SIFT), study of the reactions of H3O+, NO+ and O2+ ions with a series of alkenes; in support of SIFT-MS. Int. J. Mass Spectrom. 218, 87–101. https://doi.org/10.1016/S1387-3806(02)00662-0

Dixon, J.L., Beale, R., Nightingale, P.D., 2013. Production of methanol, acetaldehyde, and acetone in the Atlantic Ocean. Geophys. Res. Lett. 40, 4700–4705. https://doi.org/10.1002/grl.50922

Donahue, N.M., Prinn, R.G., 1990. Nonmethane hydrocarbon chemistry in the remote marine boundary layer. J. Geophys. Res. Atmospheres 95, 18387–18411. https://doi.org/10.1029/JD095iD11p18387

Engel, A., Bange, H.W., Cunliffe, M., Burrows, S.M., Friedrichs, G., Galgani, L., Herrmann, H., Hertkorn, N., Johnson, M., Liss, P.S., Quinn, P.K., Schartau, M., Soloviev, A., Stolle, C., Upstill-Goddard, R.C., van Pinxteren, M., Zäncker, B., 2017. The Ocean's Vital Skin: Toward an Integrated Understanding of the Sea Surface Microlayer. Front. Mar. Sci. 4. https://doi.org/10.3389/fmars.2017.00165

Exton, D.A., Suggett, D.J., McGenity, T.J., Steinke, M., 2013. Chlorophyll-normalized isoprene production in laboratory cultures of marine microalgae and implications for global models. Limnol. Oceanogr. 58, 1301–1311. https://doi.org/10.4319/lo.2013.58.4.1301

Fischer, E.V., Jacob, D.J., Millet, D.B., Yantosca, R.M., Mao, J., 2012. The role of the ocean in the global atmospheric budget of acetone. Geophys. Res. Lett. 39. https://doi.org/10.1029/2011GL050086

Fischer, R., Weller, R., Jacobi, H.-W., Ballschmiter, K., 2002. Levels and pattern of volatile organic nitrates and halocarbons in the air at Neumayer Station (70°S), Antarctic. Chemosphere 48, 981–992. https://doi.org/10.1016/S0045-6535(02)00110-8

Fisher, J.A., Atlas, E.L., Barletta, B., Meinardi, S., Blake, D.R., Thompson, C.R., Ryerson, T.B., Peischl, J., Tzompa-Sosa, Z.A., Murray, L.T., 2018. Methyl, Ethyl, and Propyl Nitrates: Global Distribution and Impacts on Reactive Nitrogen in Remote Marine Environments. J. Geophys. Res. Atmospheres 123, 12,429-12,451. https://doi.org/10.1029/2018JD029046

Fogelqvist, E., Tanhua, T., 1995. Iodinated C1-C4 hydrocarbons released from ice algae in Antarctica, in: Grimvall, A., de Leer, E.W.B. (Eds.), Naturally-Produced Organohalogens, Environment & Chemistry. Springer Netherlands, Dordrecht, pp. 295–305. https://doi.org/10.1007/978-94-011-0061-8_27

Francis, G.J., Wilson, P.F., Milligan, D.B., Langford, V.S., McEwan, M.J., 2007. GeoVOC: A SIFT-MS method for the analysis of small linear hydrocarbons of relevance to oil exploration. Int. J. Mass Spectrom. 268, 38–46. https://doi.org/10.1016/j.ijms.2007.08.005

Frew, N.M., 1997. The role of organic films in air–sea gas exchange, in: Liss, P.S., Duce, R.A. (Eds.), The Sea Surface and Global Change. Cambridge University Press, Cambridge, pp. 121–172. https://doi.org/10.1017/CBO9780511525025.006

Frew, N.M., Goldman, J.C., Dennett, M.R., Johnson, A.S., 1990. Impact of phytoplankton-generated surfactants on air-sea gas exchange. J. Geophys. Res. Oceans 95, 3337–3352. https://doi.org/10.1029/JC095iC03p03337

Frew, N.M., Nelson, R.K., Johnson, C.G., 2006. Sea slicks: variability in chemical composition and surface elasticity, in: Gade, M., Hühnerfuss, H., Korenowski, G.M. (Eds.), Marine Surface Films: Chemical Characteristics, Influence on Air-Sea Interactions and Remote Sensing. Springer, Berlin, Heidelberg, pp. 45–56. https://doi.org/10.1007/3-540-33271-5_6

Fujimori, T., Yoneyama, Y., Taniai, G., Kurihara, M., Tamegai, H., Hashimoto, S., 2012. Methyl halide production by cultures of marine proteobacteria Erythrobacter and Pseudomonas and isolated bacteria from brackish water. Limnol. Oceanogr. 57, 154–162. https://doi.org/10.4319/lo.2012.57.1.0154

Fung, K.M., Heald, C.L., Kroll, J.H., Wang, S., Jo, D.S., Gettelman, A., Lu, Z., Liu, X., Zaveri, R.A., Apel, E.C., Blake, D.R., Jimenez, J.-L., Campuzano-Jost, P., Veres, P.R., Bates, T.S., Shilling, J.E., Zawadowicz, M., 2022. Exploring dimethyl sulfide (DMS) oxidation and implications for global aerosol radiative forcing. Atmospheric Chem. Phys. 22, 1549–1573. https://doi.org/10.5194/acp-22-1549-2022

Fuse, H., Inoue, H., Murakami, K., Takimura, O., Yamaoka, Y., 2003. Production of free and organic iodine by Roseovarius spp. FEMS Microbiol. Lett. 229, 189–194. https://doi.org/10.1016/S0378-1097(03)00839-5

Galí, M., Levasseur, M., Devred, E., Simó, R., Babin, M., 2018. Sea-surface dimethylsulfide (DMS) concentration from satellite data at global and regional scales. Biogeosciences 15, 3497–3519. https://doi.org/10.5194/bg-15-3497-2018

Gallard, H., Allard, S., Nicolau, R., von Gunten, U., Croué, J.P., 2009. Formation of Iodinated Organic Compounds by Oxidation of Iodide-Containing Waters with

Manganese Dioxide. Environ. Sci. Technol. 43, 7003–7009. https://doi.org/10.1021/es9010338

Gan, D., 2005. Aqueous Photochemistry of 1,4-benzoquinones and their Possible Role in the Photochemistry of Natural Organic Matter. University of Maryland, Maryland, USA.

Gantt, B., Meskhidze, N., Kamykowski, D., 2009. A new physically-based quantification of marine isoprene and primary organic aerosol emissions. Atmospheric Chem. Phys. 9, 4915–4927. https://doi.org/10.5194/acp-9-4915-2009

Garbe, C.S., Rutgersson, A., Boutin, J., de Leeuw, G., Delille, B., Fairall, C.W., Gruber, N., Hare, J., Ho, D.T., Johnson, M.T., Nightingale, P.D., Pettersson, H., Piskozub, J., Sahlée, E., Tsai, W., Ward, B., Woolf, D.K., Zappa, C.J., 2014. Transfer Across the Air-Sea Interface, in: Liss, P.S., Johnson, M.T. (Eds.), Ocean-Atmosphere Interactions of Gases and Particles, Springer Earth System Sciences. Springer Berlin Heidelberg, Berlin, Heidelberg, pp. 55–112. https://doi.org/10.1007/978-3-642-25643-1_2

Ge, S., Xu, Y., Jia, L., 2017. Effects of inorganic seeds on secondary organic aerosol formation from photochemical oxidation of acetone in a chamber. Atmos. Environ. 170, 205–215. https://doi.org/10.1016/j.atmosenv.2017.09.036

Ghislain, M., Costarramone, N., Sotiropoulos, J.-M., Pigot, T., Berg, R.V.D., Lacombe, S., Bechec, M.L., 2019. Direct analysis of aldehydes and carboxylic acids in the gas phase by negative ionization selected ion flow tube mass spectrometry: Quantification and modelling of ion–molecule reactions. Rapid Commun. Mass Spectrom. 33, 1623–1634. https://doi.org/10.1002/rcm.8504

Giese, B., Laturnus, F., Adams, F.C., Wiencke, C., 1999. Release of Volatile Iodinated C1−C4 Hydrocarbons by Marine Macroalgae from Various Climate Zones. Environ. Sci. Technol. 33, 2432–2439. https://doi.org/10.1021/es980731n

Guenther, A., Karl, T., Harley, P., Wiedinmyer, C., Palmer, P.I., Geron, C., 2006. Estimates of global terrestrial isoprene emissions using MEGAN (Model of Emissions of Gases and Aerosols from Nature). Atmospheric Chem. Phys. 6, 3181–3210. https://doi.org/10.5194/acp-6-3181-2006

Hackenberg, S.C., Andrews, S.J., Airs, R., Arnold, S.R., Bouman, H.A., Brewin, R.J.W., Chance, R.J., Cummings, D., Dall'Olmo, G., Lewis, A.C., Minaeian, J.K., Reifel, K.M., Small, A., Tarran, G.A., Tilstone, G.H., Carpenter, L.J., 2017. Potential controls of isoprene in the surface ocean. Glob. Biogeochem. Cycles 31, 644–662. https://doi.org/10.1002/2016GB005531

Halsey, K.H., Giovannoni, S.J., Graus, M., Zhao, Y., Landry, Z., Thrash, J.C., Vergin, K.L., de Gouw, J., 2017. Biological cycling of volatile organic carbon by phytoplankton and bacterioplankton. Limnol. Oceanogr. 62, 2650–2661. https://doi.org/10.1002/lno.10596

Hansell, D.A., Orellana, M.V., 2021. Dissolved Organic Matter in the Global Ocean: A Primer. Gels 7, 128. https://doi.org/10.3390/gels7030128

Happell, J.D., Wallace, D.W.R., 1996. Methyl iodide in the Greenland/Norwegian Seas and the tropical Atlantic Ocean: Evidence for photochemical production. Geophys. Res. Lett. 23, 2105–2108. https://doi.org/10.1029/96GL01764

H. Bertram, T., E. Cochran, R., H. Grassian, V., A. Stone, E., 2018. Sea spray aerosol chemical composition: elemental and molecular mimics for laboratory studies of heterogeneous and multiphase reactions. Chem. Soc. Rev. 47, 2374–2400. https://doi.org/10.1039/C7CS00008A

Heald, C.L., Jacob, D.J., Park, R.J., Alexander, B., Fairlie, T.D., Yantosca, R.M., Chu, D.A., 2006. Transpacific transport of Asian anthropogenic aerosols and its

impact on surface air quality in the United States. J. Geophys. Res. Atmospheres 111. https://doi.org/10.1029/2005JD006847

Heald, C.L., Jacob, D.J., Park, R.J., Russell, L.M., Huebert, B.J., Seinfeld, J.H., Liao, H., Weber, R.J., 2005. A large organic aerosol source in the free troposphere missing from current models. Geophys. Res. Lett. 32. https://doi.org/10.1029/2005GL023831

Heinze, C., Meyer, S., Goris, N., Anderson, L., Steinfeldt, R., Chang, N., Le Quéré, C., Bakker, D.C.E., 2015. The ocean carbon sink – impacts, vulnerabilities and challenges. Earth Syst. Dyn. 6, 327–358. https://doi.org/10.5194/esd-6-327-2015

Hepach, H., Quack, B., Tegtmeier, S., Engel, A., Bracher, A., Fuhlbrügge, S., Galgani, L., Atlas, E.L., Lampel, J., Frieß, U., Krüger, K., 2016. Biogenic halocarbons from the Peruvian upwelling region as tropospheric halogen source. Atmospheric Chem. Phys. 16, 12219–12237. https://doi.org/10.5194/acp-16-12219-2016

Hien, T.T., Huy, D.H., Dominutti, P.A., Thien Chi, N.D., Hopkins, J.R., Shaw, M., Forster, G., Mills, G., Le, H.A., Oram, D., 2022. Comprehensive volatile organic compound measurements and their implications for ground-level ozone formation in the two main urban areas of Vietnam. Atmos. Environ. 269, 118872. https://doi.org/10.1016/j.atmosenv.2021.118872

Ho, D.T., Wanninkhof, R., Schlosser, P., Ullman, D.S., Hebert, D., Sullivan, K.F., 2011. Toward a universal relationship between wind speed and gas exchange: Gas transfer velocities measured with 3He/SF6 during the Southern Ocean Gas Exchange Experiment. J. Geophys. Res. Oceans 116. https://doi.org/10.1029/2010JC006854

Hu, Q.-H., Xie, Z.-Q., Wang, X.-M., Kang, H., He, Q.-F., Zhang, P., 2013. Secondary organic aerosols over oceans via oxidation of isoprene and monoterpenes from Arctic to Antarctic. Sci. Rep. 3, 2280. https://doi.org/10.1038/srep02280

Huey, L.G., 2007. Measurement of trace atmospheric species by chemical ionization mass spectrometry: Speciation of reactive nitrogen and future directions. Mass Spectrom. Rev. 26, 166–184. https://doi.org/10.1002/mas.20118

Hühnerfuss, H., 2006. Basic physicochemical principles of monomolecular sea slicks and crude oil spills, in: Gade, M., Hühnerfuss, H., Korenowski, G.M. (Eds.), Marine Surface Films: Chemical Characteristics, Influence on Air-Sea Interactions and Remote Sensing. Springer, Berlin, Heidelberg, pp. 21–35. https://doi.org/10.1007/3-540-33271-5_4

Hühnerfuss, H., Alpers, W., Garrett, W.D., Lange, P.A., Stolte, S., 1983. Attenuation of capillary and gravity waves at sea by monomolecular organic surface films. J. Geophys. Res. Oceans 88, 9809–9816. https://doi.org/10.1029/JC088iC14p09809

Hunter, K.A., 1980. Processes affecting particulate trace metals in the sea surface microlayer. Mar. Chem. 9, 49–70. https://doi.org/10.1016/0304-4203(80)90006-7

Jammoul, A., Dumas, S., D'Anna, B., George, C., 2009. Photoinduced oxidation of sea salt halides by aromatic ketones: a source of halogenated radicals. Atmospheric Chem. Phys. 9, 4229–4237. https://doi.org/10.5194/acp-9-4229-2009

Jones, A.E., Weller, R., Minikin, A., Wolff, E.W., Sturges, W.T., McIntyre, H.P., Leonard, S.R., Schrems, O., Bauguitte, S., 1999. Oxidized nitrogen chemistry and speciation in the Antarctic troposphere. J. Geophys. Res. Atmospheres 104, 21355–21366. https://doi.org/10.1029/1999JD900362

Jones, C.E., Hornsby, K.E., Sommariva, R., Dunk, R.M., Glasow, R. von, McFiggans, G., Carpenter, L.J., 2010. Quantifying the contribution of marine organic gases to atmospheric iodine. Geophys. Res. Lett. 37. https://doi.org/10.1029/2010GL043990

Jones, M.R., Chance, R., Dadic, R., Hannula, H.-R., May, R., Ward, M., Carpenter, L.J., 2023. Environmental iodine speciation quantification in seawater and snow using ion exchange chromatography and UV spectrophotometric detection. Anal. Chim. Acta 1239, 340700. https://doi.org/10.1016/j.aca.2022.340700

Kameyama, S., Tanimoto, H., Inomata, S., Suzuki, K., Komatsu, D.D., Hirota, A., Konno, U., Tsunogai, U., 2011. Application of PTR-MS to an incubation experiment of the marine diatom Thalassiosira pseudonana. Geochem. J. 45, 355–363. https://doi.org/10.2343/geochemj.1.0127

Kaplan, K., Graf, S., Tanner, C., Gonin, M., Fuhrer, K., Knochenmuss, R., Dwivedi, P., Hill, H.H.Jr., 2010. Resistive Glass IM-TOFMS. Anal. Chem. 82, 9336–9343. https://doi.org/10.1021/ac1017259

Kaufman, Y.J., Tanré, D., 1994. Effect of variations in super-saturation on the formation of cloud condensation nuclei. Nature 369, 45–48. https://doi.org/10.1038/369045a0

Kazil, J., Lovejoy, E.R., Barth, M.C., O'Brien, K., 2006. Aerosol nucleation over oceans and the role of galactic cosmic rays. Atmospheric Chem. Phys. 6, 4905–4924. https://doi.org/10.5194/acp-6-4905-2006

Kieber, D.J., Blough, N.V., 1990. Determination of carbon-centered radicals in aqueous solution by liquid chromatography with fluorescence detection. Anal. Chem. 62, 2275–2283. https://doi.org/10.1021/ac00220a005

Kieber, R.J., Zhou, X., Mopper, K., 1990. Formation of carbonyl compounds from UV-induced photodegradation of humic substances in natural waters: Fate of riverine carbon in the sea. Limnol. Oceanogr. 35, 1503–1515. https://doi.org/10.4319/lo.1990.35.7.1503

Kim, M.J., Novak, G.A., Zoerb, M.C., Yang, M., Blomquist, B.W., Huebert, B.J., Cappa, C.D., Bertram, T.H., 2017. Air-Sea exchange of biogenic volatile organic compounds and the impact on aerosol particle size distributions. Geophys. Res. Lett. 44, 3887–3896. https://doi.org/10.1002/2017GL072975

Klick, S., Abrahamsson, K., 1992. Biogenic volatile iodated hydrocarbons in the ocean. J. Geophys. Res. Oceans 97, 12683–12687. https://doi.org/10.1029/92JC00948

Kloster, S., Feichter, J., Maier-Reimer, E., Six, K.D., Stier, P., Wetzel, P., 2006. DMS cycle in the marine ocean-atmosphere system – a global model study. Biogeosciences 3, 29–51. https://doi.org/10.5194/bg-3-29-2006

Kramer, D., 2022. Helium is again in short supply. Phys. Today.

Krechmer, J., Lopez-Hilfiker, F., Koss, A., Hutterli, M., Stoermer, C., Deming, B., Kimmel, J., Warneke, C., Holzinger, R., Jayne, J., Worsnop, D., Fuhrer, K., Gonin, M., de Gouw, J., 2018. Evaluation of a New Reagent-Ion Source and Focusing Ion–Molecule Reactor for Use in Proton-Transfer-Reaction Mass Spectrometry. Anal. Chem. 90, 12011–12018. https://doi.org/10.1021/acs.analchem.8b02641

Kulmala, M., Pirjola, L., Mäkelä, J.M., 2000. Stable sulphate clusters as a source of new atmospheric particles. Nature 404, 66–69. https://doi.org/10.1038/35003550

Küpper, F.C., Miller, E.P., Andrews, S.J., Hughes, C., Carpenter, L.J., Meyer-Klaucke, W., Toyama, C., Muramatsu, Y., Feiters, M.C., Carrano, C.J., 2018. Emission of volatile halogenated compounds, speciation and localization of bromine and

iodine in the brown algal genome model Ectocarpus siliculosus. JBIC J. Biol. Inorg. Chem. 23, 1119–1128. https://doi.org/10.1007/s00775-018-1539-7

Kurihara, M.K., Kimura, M., Iwamoto, Y., Narita, Y., Ooki, A., Eum, Y.-J., Tsuda, A., Suzuki, K., Tani, Y., Yokouchi, Y., Uematsu, M., Hashimoto, S., 2010. Distributions of short-lived iodocarbons and biogenic trace gases in the open ocean and atmosphere in the western North Pacific. Mar. Chem. 118, 156–170. https://doi.org/10.1016/j.marchem.2009.12.001

Kuyper, B., Lesch, T., Labuschagne, C., Martin, D., Young, D., Khan, M.A.H., Williams, A.G., O'Doherty, S., Davies-Coleman, M.T., Shallcross, D.E., 2019. Volatile halocarbon measurements in the marine boundary layer at Cape Point, South Africa. Atmos. Environ. 214, 116833. https://doi.org/10.1016/j.atmosenv.2019.116833

LabSyft, 2016.

Lana, A., Bell, T.G., Simó, R., Vallina, S.M., Ballabrera-Poy, J., Kettle, A.J., Dachs, J., Bopp, L., Saltzman, E.S., Stefels, J., Johnson, J.E., Liss, P.S., 2011. An updated climatology of surface dimethlysulfide concentrations and emission fluxes in the global ocean. Glob. Biogeochem. Cycles 25. https://doi.org/10.1029/2010GB003850

Lewis, A.C., Carpenter, L.J., Pilling, M.J., 2001. Nonmethane hydrocarbons in Southern Ocean boundary layer air. J. Geophys. Res. Atmospheres 106, 4987–4994. https://doi.org/10.1029/2000JD900634

Lewis, A.C., Hopkins, J.R., Carpenter, L.J., Stanton, J., Read, K.A., Pilling, M.J., 2005. Sources and sinks of acetone, methanol, and acetaldehyde in North Atlantic marine air. Atmospheric Chem. Phys. 5, 1963–1974. https://doi.org/10.5194/acp-5-1963-2005

Li, J., Wang, Y., Qu, H., 2019. Dependence of Summertime Surface Ozone on NOx and VOC Emissions Over the United States: Peak Time and Value. Geophys. Res. Lett. 46, 3540–3550. https://doi.org/10.1029/2018GL081823

Li, Y., He, Z., Yang, G.-P., Wang, H., Zhuang, G.-C., 2019. Volatile halocarbons in the marine atmosphere and surface seawater: Diurnal and spatial variations and influences of environmental factors. Atmos. Environ. 214, 116820. https://doi.org/10.1016/j.atmosenv.2019.116820

Li, Y., He, Z., Yang, G.-P., Zou, Y., 2021. Spatial distribution and biogeochemical cycling of methyl iodide in the Yellow Sea and the East China Sea during summer. Environ. Pollut. 276, 116749. https://doi.org/10.1016/j.envpol.2021.116749

Liakakou, E., Vrekoussis, M., Bonsang, B., Donousis, Ch., Kanakidou, M., Mihalopoulos, N., 2007. Isoprene above the Eastern Mediterranean: Seasonal variation and contribution to the oxidation capacity of the atmosphere. Atmos. Environ. 41, 1002–1010. https://doi.org/10.1016/j.atmosenv.2006.09.034

Lindinger, W., Hansel, A., Jordan, A., 1998. On-line monitoring of volatile organic compounds at pptv levels by means of proton-transfer-reaction mass spectrometry (PTR-MS) medical applications, food control and environmental research. Int. J. Mass Spectrom. Ion Process. 173, 191–241. https://doi.org/10.1016/S0168-1176(97)00281-4

Liss, P.S., Duce, R.A., 1997. The sea surface and global change. Cambridge University Press, Cambridge.

Liss, P.S., Martinelli, F.N., 1978. Thalassia Jugoslavica, in: Thalassia Jugoslavica. pp. 215–220.

Liss, P.S., Merlivat, L., 1986. Air-Sea Gas Exchange Rates: Introduction and Synthesis, in: Buat-Ménard, P. (Ed.), The Role of Air-Sea Exchange in Geochemical

Cycling, NATO ASI Series. Springer Netherlands, Dordrecht, pp. 113–127. https://doi.org/10.1007/978-94-009-4738-2_5

Liss, P.S., Slater, P.G., 1974. Flux of Gases across the Air-Sea Interface. Nature 247, 181–184. https://doi.org/10.1038/247181a0

Liss, P.S., Slinn, W.G.N. (Eds.), 1983. Air-Sea Exchange of Gases and Particles, 1st ed. Springer Netherlands, Dordrecht. https://doi.org/10.1007/978-94-009-7169-1

Liu, M., Matsui, H., 2022. Secondary Organic Aerosol Formation Regulates Cloud Condensation Nuclei in the Global Remote Troposphere. Geophys. Res. Lett. 49, e2022GL100543. https://doi.org/10.1029/2022GL100543

Liu, S.-S., Yang, G.-P., He, Z., Gao, X.-X., Xu, F., 2021. Oceanic emissions of methyl halides and effect of nutrients concentration on their production: A case of the western Pacific Ocean (2°N to 24°N). Sci. Total Environ. 769, 144488. https://doi.org/10.1016/j.scitotenv.2020.144488

LIVE/DEAD BacLight Bacterial Viability Kits, 2004.

Lopez-Hilfiker, F., Zhu, L., Hutterli, M., Cappellin, L., 2019. Calibrating Vocus PTR-TOF Sensitivity Using a Subset of VOC Standards.

Lovelock, J.E., 1975. Natural halocarbons in the air and in the sea. Nature 256, 193–194. https://doi.org/10.1038/256193a0

Lovelock, J.E., Maggs, R.J., Wade, R.J., 1973. Halogenated Hydrocarbons in and over the Atlantic. Nature 241, 194–196. https://doi.org/10.1038/241194a0

Luo, G., Yu, F., 2010. A numerical evaluation of global oceanic emissions of α-pinene and isoprene. Atmospheric Chem. Phys. 10, 2007–2015. https://doi.org/10.5194/acp-10-2007-2010

Manley, S.L., Dastoor, M.N., 1988. Methyl iodide (CH3I) production by kelp and associated microbes. Mar. Biol. 98, 477–482. https://doi.org/10.1007/BF00391538

Manley, S.L., de la Cuesta, J.L., 1997. Methyl iodide production from marine phytoplankton cultures. Limnol. Oceanogr. 42, 142–147. https://doi.org/10.4319/lo.1997.42.1.0142

Manley, S.L., Goodwin, K., North, W.J., 1992. Laboratory production of bromoform, methylene bromide, and methyl iodide by macroalgae and distribution in nearshore southern California waters. Limnol. Oceanogr. 37, 1652–1659. https://doi.org/10.4319/lo.1992.37.8.1652

Mao, J., Ren, X., Brune, W.H., Olson, J.R., Crawford, J.H., Fried, A., Huey, L.G., Cohen, R.C., Heikes, B., Singh, H.B., Blake, D.R., Sachse, G.W., Diskin, G.S., Hall, S.R., Shetter, R.E., 2009. Airborne measurement of OH reactivity during INTEX-B. Atmospheric Chem. Phys. 9, 163–173. https://doi.org/10.5194/acp-9-163-2009

Matsunaga, S., Mochida, M., Saito, T., Kawamura, K., 2002. In situ measurement of isoprene in the marine air and surface seawater from the western North Pacific. Atmos. Environ. 36, 6051–6057. https://doi.org/10.1016/S1352-2310(02)00657-X

McCoy, D.T., Burrows, S.M., Wood, R., Grosvenor, D.P., Elliott, S.M., Ma, P.-L., Rasch, P.J., Hartmann, D.L., 2015. Natural aerosols explain seasonal and spatial patterns of Southern Ocean cloud albedo. Sci. Adv. 1, e1500157. https://doi.org/10.1126/sciadv.1500157

McFiggans, G., Plane, J.M.C., Allan, B.J., Carpenter, L.J., Coe, H., O'Dowd, C., 2000. A modeling study of iodine chemistry in the marine boundary layer. J. Geophys. Res. Atmospheres 105, 14371–14385. https://doi.org/10.1029/1999JD901187

McGillis, W.R., Edson, J.B., Hare, J.E., Fairall, C.W., 2001. Direct covariance air-sea CO2 fluxes. J. Geophys. Res. Oceans 106, 16729–16745. https://doi.org/10.1029/2000JC000506

McKeen, S.A., Gierczak, T., Burkholder, J.B., Wennberg, P.O., Hanisco, T.F., Keim, E.R., Gao, R.-S., Liu, S.C., Ravishankara, A.R., Fahey, D.W., 1997. The photochemistry of acetone in the upper troposphere: A source of odd-hydrogen radicals. Geophys. Res. Lett. 24, 3177–3180. https://doi.org/10.1029/97GL03349

McKenna, S.P., McGillis, W.R., 2004. The role of free-surface turbulence and surfactants in air–water gas transfer. Int. J. Heat Mass Transf. 47, 539–553. https://doi.org/10.1016/j.ijheatmasstransfer.2003.06.001

Merikanto, J., Spracklen, D.V., Mann, G.W., Pickering, S.J., Carslaw, K.S., 2009. Impact of nucleation on global CCN. Atmospheric Chem. Phys. 9, 8601–8616. https://doi.org/10.5194/acp-9-8601-2009

Meskhidze, N., Nenes, A., 2006. Phytoplankton and Cloudiness in the Southern Ocean. Science 314, 1419–1423. https://doi.org/10.1126/science.1131779

Mikoviny, T., Kaser, L., Wisthaler, A., 2010. Development and characterization of a High-Temperature Proton-Transfer-Reaction Mass Spectrometer (HT-PTR-MS). Atmospheric Meas. Tech. 3, 537–544. https://doi.org/10.5194/amt-3-537-2010

Milne, P.J., Riemer, D.D., Zika, Rod.G., Brand, L.E., 1995. Measurement of vertical distribution of isoprene in surface seawater, its chemical fate, and its emission from several phytoplankton monocultures. Mar. Chem. 48, 237–244. https://doi.org/10.1016/0304-4203(94)00059-M

Mitchell, G.D., 2000. A Review of Permeation Tubes and Permeators. Sep. Purif. Methods 29, 119–128. https://doi.org/10.1081/SPM-100100005

Montzka, S.A., Reimann, S., Engel, A., Krüger, K., O'Doherty, S.J., Sturges, W.T., 2011. Ozone-Depleting Substances (ODSs) and Related Chemicals, in: Scientific Assessment of Ozone Depletion: 2010, Global Ozone Research and Monitoring Project-Report No. 52. World Meteorological Organization, Geneva, Switzerland, pp. 1–112.

Moore, R.M., Groszko, W., 1999. Methyl iodide distribution in the ocean and fluxes to the atmosphere. J. Geophys. Res. Oceans 104, 11163–11171. https://doi.org/10.1029/1998JC900073

Moore, R.M., Oram, D.E., Penkett, S.A., 1994. Production of isoprene by marine phytoplankton cultures. Geophys. Res. Lett. 21, 2507–2510. https://doi.org/10.1029/94GL02363

Moore, R.M., Webb, M., Tokarczyk, R., Wever, R., 1996. Bromoperoxidase and iodoperoxidase enzymes and production of halogenated methanes in marine diatom cultures. J. Geophys. Res. Oceans 101, 20899–20908. https://doi.org/10.1029/96JC01248

Moore, R.M., Zafiriou, O.C., 1994. Photochemical production of methyl iodide in seawater. J. Geophys. Res. Atmospheres 99, 16415–16420. https://doi.org/10.1029/94JD00786

Mopper, K., Zhou, X., 1990. Hydroxyl Radical Photoproduction in the Sea and Its Potential Impact on Marine Processes. Science 250, 661–664. https://doi.org/10.1126/science.250.4981.661

Mungall, E.L., Abbatt, J.P.D., Wentzell, J.J.B., Lee, A.K.Y., Thomas, J.L., Blais, M., Gosselin, M., Miller, L.A., Papakyriakou, T., Willis, M.D., Liggio, J., 2017. Microlayer source of oxygenated volatile organic compounds in the summertime marine Arctic boundary layer. Proc. Natl. Acad. Sci. 114, 6203–6208. https://doi.org/10.1073/pnas.1620571114

Murphy, C.D., Moore, R.M., White, R.L., 2000. An isotopic labeling method for determining production of volatile organohalogens by marine microalgae. Limnol. Oceanogr. 45, 1868–1871. https://doi.org/10.4319/lo.2000.45.8.1868

NCAR, 2016. Quick TUV Calculator.

Neu, J.L., Lawler, M.J., Prather, M.J., Saltzman, E.S., 2008. Oceanic alkyl nitrates as a natural source of tropospheric ozone. Geophys. Res. Lett. 35. https://doi.org/10.1029/2008GL034189

Neumaier, M., Ruhnke, R., Kirner, O., Ziereis, H., Stratmann, G., Brenninkmeijer, C. a. M., Zahn, A., 2014. Impact of acetone (photo)oxidation on HOx production in the UT/LMS based on CARIBIC passenger aircraft observations and EMAC simulations. Geophys. Res. Lett. 41, 3289–3297. https://doi.org/10.1002/2014GL059480

Nightingale, P.D., Malin, G., Law, C.S., Watson, A.J., Liss, P.S., Liddicoat, M.I., Boutin, J., Upstill-Goddard, R.C., 2000. In situ evaluation of air-sea gas exchange parameterizations using novel conservative and volatile tracers. Glob. Biogeochem. Cycles 14, 373–387. https://doi.org/10.1029/1999GB900091

Nightingale, P.D., Malin, G., Liss, P.S., 1995. Production of chloroform and other low molecular-weight halocarbons by some species of macroalgae. Limnol. Oceanogr. 40, 680–689. https://doi.org/10.4319/lo.1995.40.4.0680

Novak, G.A., Bertram, T.H., 2020. Reactive VOC Production from Photochemical and Heterogeneous Reactions Occurring at the Air–Ocean Interface. Acc. Chem. Res. 53, 1014–1023. https://doi.org/10.1021/acs.accounts.0c00095

Ooki, A., Tsuda, A., Kameyama, S., Takeda, S., Itoh, S., Suga, T., Tazoe, H., Okubo, A., Yokouchi, Y., 2010. Methyl halides in surface seawater and marine boundary layer of the northwest Pacific. J. Geophys. Res. Oceans 115. https://doi.org/10.1029/2009JC005703

Ordóñez, C., Lamarque, J.-F., Tilmes, S., Kinnison, D.E., Atlas, E.L., Blake, D.R., Sousa Santos, G., Brasseur, G., Saiz-Lopez, A., 2012. Bromine and iodine chemistry in a global chemistry-climate model: description and evaluation of very short-lived oceanic sources. Atmospheric Chem. Phys. 12, 1423–1447. https://doi.org/10.5194/acp-12-1423-2012

Palmer, P.I., Shaw, S.L., 2005. Quantifying global marine isoprene fluxes using MODIS chlorophyll observations. Geophys. Res. Lett. 32. https://doi.org/10.1029/2005GL022592

Parker, K.M., Mitch, W.A., 2016. Halogen radicals contribute to photooxidation in coastal and estuarine waters. Proc. Natl. Acad. Sci. U. S. A. 113, 5868–5873. https://doi.org/10.1073/pnas.1602595113

Pereira, R., Schneider-Zapp, K., Upstill-Goddard, R.C., 2016. Surfactant control of gas transfer velocity along an offshore coastal transect: results from a laboratory gas exchange tank. Biogeosciences 13, 3981–3989. https://doi.org/10.5194/bg-13-3981-2016

Pierce, J.R., Adams, P.J., 2006. Global evaluation of CCN formation by direct emission of sea salt and growth of ultrafine sea salt. J. Geophys. Res. Atmospheres 111. https://doi.org/10.1029/2005JD006186

Prank, M., Tonttila, J., Ahola, J., Kokkola, H., Kühn, T., Romakkaniemi, S., Raatikainen, T., 2022. Impacts of marine organic emissions on low-level stratiform clouds – a large eddy simulator study. Atmospheric Chem. Phys. 22, 10971–10992. https://doi.org/10.5194/acp-22-10971-2022

Prince, B.J., Milligan, D.B., McEwan, M.J., 2010. Application of selected ion flow tube mass spectrometry to real-time atmospheric monitoring. Rapid Commun. Mass Spectrom. 24, 1763–1769. https://doi.org/10.1002/rcm.4574

Rasmussen, R.A., Khalil, M. a. K., Gunawardena, R., Hoyt, S.D., 1982. Atmospheric methyl iodide (CH3I). J. Geophys. Res. Oceans 87, 3086–3090. https://doi.org/10.1029/JC087iC04p03086

Read, K.A., Carpenter, L.J., Arnold, S.R., Beale, R., Nightingale, P.D., Hopkins, J.R., Lewis, A.C., Lee, J.D., Mendes, L., Pickering, S.J., 2012. Multiannual Observations of Acetone, Methanol, and Acetaldehyde in Remote Tropical Atlantic Air: Implications for Atmospheric OVOC Budgets and Oxidative Capacity. Environ. Sci. Technol. 46, 11028–11039. https://doi.org/10.1021/es302082p

Reeser, D.I., George, C., Donaldson, D.J., 2009. Photooxidation of Halides by Chlorophyll at the Air−Salt Water Interface. J. Phys. Chem. A 113, 8591–8595. https://doi.org/10.1021/jp903657j

Reifenhäuser, W., Heumann, K.G., 1992. Determinations of methyl iodide in the Antarctic atmosphere and the south polar sea. Atmospheric Environ. Part Gen. Top. 26, 2905–2912. https://doi.org/10.1016/0960-1686(92)90282-P

Richter, U., 2004. Factors influencing methyl iodide production in the ocean and its flux to the atmosphere.

Richter, U., Wallace, D.W.R., 2004. Production of methyl iodide in the tropical Atlantic Ocean. Geophys. Res. Lett. 31. https://doi.org/10.1029/2004GL020779

Rindelaub, J.D., McAvey, K.M., Shepson, P.B., 2015. The photochemical production of organic nitrates from α-pinene and loss via acid-dependent particle phase hydrolysis. Atmos. Environ. 100, 193–201. https://doi.org/10.1016/j.atmosenv.2014.11.010

Roehl, C.M., Burkholder, J.B., Moortgat, G.K., Ravishankara, A.R., Crutzen, P.J., 1997. Temperature dependence of UV absorption cross sections and atmospheric implications of several alkyl iodides. J. Geophys. Res. Atmospheres 102, 12819–12829. https://doi.org/10.1029/97JD00530

Roelofs, G.J., 2008. A GCM study of organic matter in marine aerosol and its potential contribution to cloud drop activation. Atmospheric Chem. Phys. 8, 709–719. https://doi.org/10.5194/acp-8-709-2008

Sabbaghzadeh, B., Upstill-Goddard, R.C., Beale, R., Pereira, R., Nightingale, P.D., 2017. The Atlantic Ocean surface microlayer from 50°N to 50°S is ubiquitously enriched in surfactants at wind speeds up to 13 m s−1. Geophys. Res. Lett. 44, 2852–2858. https://doi.org/10.1002/2017GL072988

Saiz-Lopez, A., Glasow, R. von, 2012. Reactive halogen chemistry in the troposphere. Chem. Soc. Rev. 41, 6448–6472. https://doi.org/10.1039/C2CS35208G

Saiz-Lopez, A., Plane, J.M.C., Mahajan, A.S., Anderson, P.S., Bauguitte, S.J.-B., Jones, A.E., Roscoe, H.K., Salmon, R.A., Bloss, W.J., Lee, J.D., Heard, D.E., 2008. On the vertical distribution of boundary layer halogens over coastal Antarctica: implications for O-3, HOx, NOx and the Hg lifetime. Atmospheric Chem. Phys. 8, 887–900. https://doi.org/10.5194/acp-8-887-2008

Saltzman, B.E., Burg, W.R., Ramaswamy, G., 1971. Performance of permeation tubes as standard gas sources. Environ. Sci. Technol. 5, 1121–1128. https://doi.org/10.1021/es60058a004

Sander, S.P., Golden, D.M., Kurylo, M.J., Moortgat, G.K., Wine, P.H., Ravishankara, A.R., Kolb, C.E., Molina, M.J., Finlayson-Pitts, B.J., Huie, R.E., Orkin, V.L., Friedl, R.R., Keller-Rudek, H., 2006. Chemical kinetics and photochemical data for use in atmospheric studies : evaluation number 15 (Technical Report). Pasadena, CA : Jet Propulsion Laboratory, California Institute of Technology.

Saunders, R.W., Kumar, R., MacDonald, S.M., Plane, J.M.C., 2012. Insights into the Photochemical Transformation of Iodine in Aqueous Systems: Humic Acid

Photosensitized Reduction of Iodate. Environ. Sci. Technol. 46, 11854–11861. https://doi.org/10.1021/es3030935

Saunois, M., Stavert, A.R., Poulter, B., Bousquet, P., Canadell, J.G., Jackson, R.B., Raymond, P.A., Dlugokencky, E.J., Houweling, S., Patra, P.K., Ciais, P., Arora, V.K., Bastviken, D., Bergamaschi, P., Blake, D.R., Brailsford, G., Bruhwiler, L., Carlson, K.M., Carrol, M., Castaldi, S., Chandra, N., Crevoisier, C., Crill, P.M., Covey, K., Curry, C.L., Etiope, G., Frankenberg, C., Gedney, N., Hegglin, M.I., Höglund-Isaksson, L., Hugelius, G., Ishizawa, M., Ito, A., Janssens-Maenhout, G., Jensen, K.M., Joos, F., Kleinen, T., Krummel, P.B., Langenfelds, R.L., Laruelle, G.G., Liu, L., Machida, T., Maksyutov, S., McDonald, K.C., McNorton, J., Miller, P.A., Melton, J.R., Morino, I., Müller, J., Murguia-Flores, F., Naik, V., Niwa, Y., Noce, S., O'Doherty, S., Parker, R.J., Peng, C., Peng, S., Peters, G.P., Prigent, C., Prinn, R., Ramonet, M., Regnier, P., Riley, W.J., Rosentreter, J.A., Segers, A., Simpson, I.J., Shi, H., Smith, S.J., Steele, L.P., Thornton, B.F., Tian, H., Tohjima, Y., Tubiello, F.N., Tsuruta, A., Viovy, N., Voulgarakis, A., Weber, T.S., van Weele, M., van der Werf, G.R., Weiss, R.F., Worthy, D., Wunch, D., Yin, Y., Yoshida, Y., Zhang, W., Zhang, Z., Zhao, Y., Zheng, B., Zhu, Qing, Zhu, Qiuan, Zhuang, Q., 2020. The Global Methane Budget 2000–2017. Earth Syst. Sci. Data 12, 1561–1623. https://doi.org/10.5194/essd-12-1561-2020

Schall, C., Heumann, K.G., 1993. GC determination of volatile organoiodine and organobromine compounds in Arctic seawater and air samples. Fresenius J. Anal. Chem. 346, 717–722. https://doi.org/10.1007/BF00321279

Schall, C., Heumann, K.G., Kirst, G.O., 1997. Biogenic volatile organoiodine and organobromine hydrocarbons in the Atlantic Ocean from 42°N to 72°S. Fresenius J. Anal. Chem. 359, 298–305. https://doi.org/10.1007/s002160050577

Schlundt, C., Tegtmeier, S., Lennartz, S.T., Bracher, A., Cheah, W., Krüger, K., Quack, B., Marandino, C.A., 2017. Oxygenated volatile organic carbon in the western Pacific convective center: ocean cycling, air–sea gas exchange and atmospheric transport. Atmospheric Chem. Phys. 17, 10837–10854. https://doi.org/10.5194/acp-17-10837-2017

Schneider, S.R., Collins, D.B., Lim, C.Y., Zhu, L., Abbatt, J.P.D., 2019. Formation of Secondary Organic Aerosol from the Heterogeneous Oxidation by Ozone of a Phytoplankton Culture. Acs Earth Space Chem. 3, 2298–2306. https://doi.org/10.1021/acsearthspacechem.9b00201

Scouten, C.W., Cunningham, M., 2006. Freezing Biological Samples. Microsc. Today 14, 48–48. https://doi.org/10.1017/S1551929500055218

Sekimoto, K., Li, S.-M., Yuan, B., Koss, A., Coggon, M., Warneke, C., de Gouw, J., 2017. Calculation of the sensitivity of proton-transfer-reaction mass spectrometry (PTR-MS) for organic trace gases using molecular properties. Int. J. Mass Spectrom. 421, 71–94. https://doi.org/10.1016/j.ijms.2017.04.006

Shaw, S.L., Gantt, B., Meskhidze, N., 2010. Production and Emissions of Marine Isoprene and Monoterpenes: A Review. Adv. Meteorol. 2010, e408696. https://doi.org/10.1155/2010/408696

Sherwen, T., Evans, M.J., Carpenter, L.J., Andrews, S.J., Lidster, R.T., Dix, B., Koenig, T.K., Sinreich, R., Ortega, I., Volkamer, R., Saiz-Lopez, A., Prados-Roman, C., Mahajan, A.S., Ordóñez, C., 2016. Iodine's impact on tropospheric oxidants: a global model study in GEOS-Chem. Atmospheric Chem. Phys. 16, 1161–1186. https://doi.org/10.5194/acp-16-1161-2016

Singh, H.B., Salas, L.J., Stiles, R.E., 1983. Methyl halides in and over the eastern Pacific (40°N–32°S). J. Geophys. Res. Oceans 88, 3684–3690. https://doi.org/10.1029/JC088iC06p03684

Sinha, V., Williams, J., Meyerhöfer, M., Riebesell, U., Paulino, A.I., Larsen, A., 2007. Air-sea fluxes of methanol, acetone, acetaldehyde, isoprene and DMS from a Norwegian fjord following a phytoplankton bloom in a mesocosm experiment. Atmospheric Chem. Phys. 7, 739–755. https://doi.org/10.5194/acp-7-739-2007

Skeie, R.B., Myhre, G., Hodnebrog, Ø., Cameron-Smith, P.J., Deushi, M., Hegglin, M.I., Horowitz, L.W., Kramer, R.J., Michou, M., Mills, M.J., Olivié, D.J.L., Connor, F.M.O., Paynter, D., Samset, B.H., Sellar, A., Shindell, D., Takemura, T., Tilmes, S., Wu, T., 2020. Historical total ozone radiative forcing derived from CMIP6 simulations. Npj Clim. Atmospheric Sci. 3, 1–10. https://doi.org/10.1038/s41612-020-00131-0

Smith, D., Chippendale, T.W.E., Španěl, P., 2014. Reactions of the selected ion flow tube mass spectrometry reagent ions H3O+ and NO+ with a series of volatile aldehydes of biogenic significance. Rapid Commun. Mass Spectrom. 28, 1917–1928. https://doi.org/10.1002/rcm.6977

Smith, D., Chippendale, T.W.E., Španěl, P., 2011. Selected ion flow tube, SIFT, studies of the reactions of H3O+, NO+ and O2+ with some biologically active isobaric compounds in preparation for SIFT-MS analyses. Int. J. Mass Spectrom. 303, 81–89. https://doi.org/10.1016/j.ijms.2011.01.005

Smith, D., McEwan, M.J., Španěl, P., 2020. Understanding Gas Phase Ion Chemistry Is the Key to Reliable Selected Ion Flow Tube-Mass Spectrometry Analyses. Anal. Chem. 92, 12750–12762. https://doi.org/10.1021/acs.analchem.0c03050

Smith, D., Španěl, P., 2005. Selected ion flow tube mass spectrometry (SIFT-MS) for on-line trace gas analysis. Mass Spectrom. Rev. 24, 661–700. https://doi.org/10.1002/mas.20033

Smith, D., Wang, T., Španěl, P., 2003. Analysis of ketones by selected ion flow tube mass spectrometry. Rapid Commun. Mass Spectrom. 17, 2655–2660. https://doi.org/10.1002/rcm.1244

Smythe-Wright, D., Boswell, S.M., Breithaupt, P., Davidson, R.D., Dimmer, C.H., Eiras Diaz, L.B., 2006. Methyl iodide production in the ocean: implications for climate change. Glob. Biogeochem. Cycles 20, GB3003. https://doi.org/10.1029/2005GB002642

Španěl, P., Doren, J.M.V., Smith, D., 2002. A selected ion flow tube study of the reactions of H3O+, NO+, and O2+ with saturated and unsaturated aldehydes and subsequent hydration of the product ions. Int. J. Mass Spectrom. 213, 163–176. https://doi.org/10.1016/S1387-3806(01)00531-0

Španěl, P., Ji, Y., Smith, D., 1997. SIFT studies of the reactions of H3O+, NO+ and O2+ with a series of aldehydes and ketones. Int. J. Mass Spectrom. Ion Process. 165–166, 25–37. https://doi.org/10.1016/S0168-1176(97)00166-3

Španěl, P., Pavlik, M., Smith, D., 1995. Reactions of H3O+ and OH− ions with some organic molecules; applications to trace gas analysis in air. Int. J. Mass Spectrom. Ion Process. 145, 177–186. https://doi.org/10.1016/0168-1176(95)04164-G

Španěl, P., Smith, D., 1998. Selected ion flow tube studies of the reactions of H3O+, NO+, and O2+ with several aromatic and aliphatic hydrocarbons. Int. J. Mass Spectrom. 181, 1–10. https://doi.org/10.1016/S1387-3806(98)14114-3

Ŝpaněl, P., Smith, D., 1998. SIFT studies of the reactions of H3O+, NO+ and O+2 with a series of volatile carboxylic acids and esters. Int. J. Mass Spectrom. Ion Process. 172, 137–147. https://doi.org/10.1016/S0168-1176(97)00246-2

Španěl, P., Smith, D., 1997. SIFT studies of the reactions of H3O+, NO+ and O2+ with a series of alcohols. Int. J. Mass Spectrom. Ion Process., In Honour of Chava Lifshitz 167–168, 375–388. https://doi.org/10.1016/S0168-1176(97)00085-2

Španěl, P., Wang, T., Smith, D., 2002. A selected ion flow tube, SIFT, study of the reactions of H3O+, NO+ and O2+ ions with a series of diols. Int. J. Mass Spectrom. 218, 227–236. https://doi.org/10.1016/S1387-3806(02)00724-8

Španěl, P., Žabka, J., Zymak, I., Smith, D., 2017. Selected ion flow tube study of the reactions of H3O+ and NO+ with a series of primary alcohols in the presence of water vapour in support of selected ion flow tube mass spectrometry. Rapid Commun. Mass Spectrom. 31, 437–446. https://doi.org/10.1002/rcm.7811

Spracklen, D.V., Arnold, S.R., Sciare, J., Carslaw, K.S., Pio, C., 2008. Globally significant oceanic source of organic carbon aerosol. Geophys. Res. Lett. 35. https://doi.org/10.1029/2008GL033359

Spracklen, D.V., Pringle, K.J., Carslaw, K.S., Mann, G.W., Manktelow, P., Heintzenberg, J., 2007. Evaluation of a global aerosol microphysics model against size-resolved particle statistics in the marine atmosphere. Atmospheric Chem. Phys. 7, 2073–2090. https://doi.org/10.5194/acp-7-2073-2007

Springer, T.G., Pigford, R.L., 1970. Influence of Surface Turbulence and Surfactants on Gas Transport through Liquid Interfaces. Ind. Eng. Chem. Fundam. 9, 458–465. https://doi.org/10.1021/i160035a025

Stemmler, I., Hense, I., Quack, B., Maier-Reimer, E., 2014. Methyl iodide production in the open ocean. Biogeosciences 11, 4459–4476. https://doi.org/10.5194/bg-11-4459-2014

Stocker, T.F., Qin, D., Plattner, G.-K., Tignor, M., Allen, S.K., Boschung, J., Nauels, A., Xia, Y., Bex, V., Midgley, P.M., 2013. Climate Change 2013: The Physical Science Basis. Contribution of WorkingGroup I to the Fifth Assessment Report of the Intergovernmental Panel on Climate Change. Cambridge University Press, Cambridge, UK, and New York, USA.

Stubbins, A., Hubbard, V., Uher, G., Law, C.S., Upstill-Goddard, R.C., Aiken, G.R., Mopper, K., 2008. Relating Carbon Monoxide Photoproduction to Dissolved Organic Matter Functionality. Environ. Sci. Technol. 42, 3271–3276. https://doi.org/10.1021/es703014q

Tai, A.P.K., Sadiq, M., Pang, J.Y.S., Yung, D.H.Y., Feng, Z., 2021. Impacts of Surface Ozone Pollution on Global Crop Yields: Comparing Different Ozone Exposure Metrics and Incorporating Co-effects of CO2. Front. Sustain. Food Syst. 5.

Tanzer, D., Heumann, K.G., 1992. Gas Chromatographic Trace-Level Determination of Volatile Organic Sulfides and Selenides and of Methyl Iodide in Atlantic Surface Water. Int. J. Environ. Anal. Chem. 48, 17–31. https://doi.org/10.1080/03067319208027039

Tessier, E., Amouroux, D., Abril, G., Lemaire, E., Donard, O.F.X., 2002. Formation and Volatilisation of Alkyl-Iodides and -Selenides in Macrotidal Estuaries. Biogeochemistry 59, 183–206.

Thames, A.B., Brune, W.H., Miller, D.O., Allen, H.M., Apel, E.C., Blake, D.R., Bui, T.P., Commane, R., Crounse, J.D., Daube, B.C., Diskin, G.S., DiGangi, J.P., Elkins, J.W., Hall, S.R., Hanisco, T.F., Hannun, R.A., Hintsa, E., Hornbrook, R.S., Kim, M.J., McKain, K., Moore, F.L., Nicely, J.M., Peischl, J., Ryerson, T.B., St. Clair, J.M., Sweeney, C., Teng, A., Thompson, C.R., Ullmann, K., Wennberg, P.O., Wolfe, G.M., 2020. Missing OH reactivity in the global marine boundary layer.

Atmospheric Chem. Phys. 20, 4013–4029. https://doi.org/10.5194/acp-20-4013-2020

Thornberry, T., Murphy, D.M., Thomson, D.S., de Gouw, J., Warneke, C., Bates, T.S., Quinn, P.K., Coffman, D., 2009. Measurement of Aerosol Organic Compounds Using a Novel Collection/Thermal-Desorption PTR-ITMS Instrument. Aerosol Sci. Technol. 43, 486–501. https://doi.org/10.1080/02786820902763132

Toda, H., Itoh, N., 2011. Isolation and characterization of a gene encoding a S-adenosyl-l-methionine-dependent halide/thiol methyltransferase (HTMT) from the marine diatom Phaeodactylum tricornutum: Biogenic mechanism of CH(3)I emissions in oceans. Phytochemistry 72, 337–343. https://doi.org/10.1016/j.phytochem.2010.12.003

Tran, S., Bonsang, B., Gros, V., Peeken, I., Sarda-Esteve, R., Bernhardt, A., Belviso, S., 2013. A survey of carbon monoxide and non-methane hydrocarbons in the Arctic Ocean during summer 2010. Biogeosciences 10, 1909–1935. https://doi.org/10.5194/bg-10-1909-2013

Travis, K.R., Heald, C.L., Allen, H.M., Apel, E.C., Arnold, S.R., Blake, D.R., Brune, W.H., Chen, X., Commane, R., Crounse, J.D., Daube, B.C., Diskin, G.S., Elkins, J.W., Evans, M.J., Hall, S.R., Hintsa, E.J., Hornbrook, R.S., Kasibhatla, P.S., Kim, M.J., Luo, G., McKain, K., Millet, D.B., Moore, F.L., Peischl, J., Ryerson, T.B., Sherwen, T., Thames, A.B., Ullmann, K., Wang, X., Wennberg, P.O., Wolfe, G.M., Yu, F., 2020. Constraining remote oxidation capacity with ATom observations. Atmospheric Chem. Phys. 20, 7753–7781. https://doi.org/10.5194/acp-20-7753-2020

Tsai, W.-T., 1998. A numerical study of the evolution and structure of a turbulent shear layer under a free surface. J. Fluid Mech. 354, 239–276. https://doi.org/10.1017/S0022112097007623

Tsai, W.-T., 1996. Impact of a surfactant on a turbulent shear layer under the air-sea interface. J. Geophys. Res. Oceans 101, 28557–28568. https://doi.org/10.1029/96JC02802

Veres, P.R., Neuman, J.A., Bertram, T.H., Assaf, E., Wolfe, G.M., Williamson, C.J., Weinzierl, B., Tilmes, S., Thompson, C.R., Thames, A.B., Schroder, J.C., Saiz-Lopez, A., Rollins, A.W., Roberts, J.M., Price, D., Peischl, J., Nault, B.A., Møller, K.H., Miller, D.O., Meinardi, S., Li, Q., Lamarque, J.-F., Kupc, A., Kjaergaard, H.G., Kinnison, D., Jimenez, J.L., Jernigan, C.M., Hornbrook, R.S., Hills, A., Dollner, M., Day, D.A., Cuevas, C.A., Campuzano-Jost, P., Burkholder, J., Bui, T.P., Brune, W.H., Brown, S.S., Brock, C.A., Bourgeois, I., Blake, D.R., Apel, E.C., Ryerson, T.B., 2020. Global airborne sampling reveals a previously unobserved dimethyl sulfide oxidation mechanism in the marine atmosphere. Proc. Natl. Acad. Sci. 117, 4505–4510. https://doi.org/10.1073/pnas.1919344117

Vichi, F., Ianniello, A., Frattoni, M., Imperiali, A., Esposito, G., Tomasi Scianò, M.C., Perilli, M., Cecinato, A., 2021. Air Quality Assessment in the Central Mediterranean Sea (Tyrrhenian Sea): Anthropic Impact and Miscellaneous Natural Sources, including Volcanic Contribution, on the Budget of Volatile Organic Compounds (VOCs). Atmosphere 12, 1609. https://doi.org/10.3390/atmos12121609

von Glasow, R., Crutzen, P.J., 2004. Model study of multiphase DMS oxidation with a focus on halogens. Atmospheric Chem. Phys. 4, 589–608. https://doi.org/10.5194/acp-4-589-2004

Wagner, R.L., Farren, N.J., Davison, J., Young, S., Hopkins, J.R., Lewis, A.C., Carslaw, D.C., Shaw, M.D., 2021. Application of a mobile laboratory using a selected-ion flow-tube mass spectrometer (SIFT-MS) for characterisation of volatile

organic compounds and atmospheric trace gases. Atmospheric Meas. Tech. 14, 6083–6100. https://doi.org/10.5194/amt-14-6083-2021

Wang, N., Edtbauer, A., Stönner, C., Pozzer, A., Bourtsoukidis, E., Ernle, L., Dienhart, D., Hottmann, B., Fischer, H., Schuladen, J., Crowley, J.N., Paris, J.-D., Lelieveld, J., Williams, J., 2020. Measurements of carbonyl compounds around the Arabian Peninsula: overview and model comparison. Atmospheric Chem. Phys. 20, 10807–10829. https://doi.org/10.5194/acp-20-10807-2020

Wang, S., Apel, E.C., Schwantes, R.H., Bates, K.H., Jacob, D.J., Fischer, E.V., Hornbrook, R.S., Hills, A.J., Emmons, L.K., Pan, L.L., Honomichl, S., Tilmes, S., Lamarque, J.-F., Yang, M., Marandino, C.A., Saltzman, E.S., de Bruyn, W., Kameyama, S., Tanimoto, H., Omori, Y., Hall, S.R., Ullmann, K., Ryerson, T.B., Thompson, C.R., Peischl, J., Daube, B.C., Commane, R., McKain, K., Sweeney, C., Thames, A.B., Miller, D.O., Brune, W.H., Diskin, G.S., DiGangi, J.P., Wofsy, S.C., 2020. Global Atmospheric Budget of Acetone: Air-Sea Exchange and the Contribution to Hydroxyl Radicals. J. Geophys. Res. Atmospheres 125, e2020JD032553. https://doi.org/10.1029/2020JD032553

Wang, S., Hornbrook, R.S., Hills, A., Emmons, L.K., Tilmes, S., Lamarque, J.-F., Jimenez, J.L., Campuzano-Jost, P., Nault, B.A., Crounse, J.D., Wennberg, P.O., Kim, M., Allen, H., Ryerson, T.B., Thompson, C.R., Peischl, J., Moore, F., Nance, D., Hall, B., Elkins, J., Tanner, D., Huey, L.G., Hall, S.R., Ullmann, K., Orlando, J.J., Tyndall, G.S., Flocke, F.M., Ray, E., Hanisco, T.F., Wolfe, G.M., St. Clair, J., Commane, R., Daube, B., Barletta, B., Blake, D.R., Weinzierl, B., Dollner, M., Conley, A., Vitt, F., Wofsy, S.C., Riemer, D.D., Apel, E.C., 2019. Atmospheric Acetaldehyde: Importance of Air-Sea Exchange and a Missing Source in the Remote Troposphere. Geophys. Res. Lett. 46, 5601–5613. https://doi.org/10.1029/2019GL082034

Wang, T., Smith, D., Španěl, P., 2004a. Selected ion flow tube, SIFT, studies of the reactions of H3O+, NO+ and O2+ with compounds released by Pseudomonas and related bacteria. Int. J. Mass Spectrom., Special Issue: In honour of Tilmann Mark 233, 245–251. https://doi.org/10.1016/j.ijms.2003.12.024

Wang, T., Spanel, P., Smith, D., 2004b. A selected ion flow tube study of the reactions of H3O+, NO+ and O2+- with some phenols, phenyl alcohols and cyclic carbonyl compounds in support of SIFT-MS and PTR-MS. Int. J. Mass Spectrom. 239, 139–146. https://doi.org/10.1016/j.ijms.2004.07.022

Wanninkhof, R., 1992. Relationship between wind speed and gas exchange over the ocean. J. Geophys. Res. Oceans 97, 7373–7382. https://doi.org/10.1029/92JC00188

Warneke, C., van der Veen, C., Luxembourg, S., de Gouw, J.A., Kok, A., 2001. Measurements of benzene and toluene in ambient air using proton-transfer-reaction mass spectrometry: calibration, humidity dependence, and field intercomparison. Int. J. Mass Spectrom. 207, 167–182. https://doi.org/10.1016/S1387-3806(01)00366-9

Webb, P., 2021. 1.1 Overview of the Oceans.

Weber, T., Wiseman, N.A., Kock, A., 2019. Global ocean methane emissions dominated by shallow coastal waters. Nat. Commun. 10, 4584. https://doi.org/10.1038/s41467-019-12541-7

Wohl, C., Brown, I., Kitidis, V., Jones, A.E., Sturges, W.T., Nightingale, P.D., Yang, M., 2020. Underway seawater and atmospheric measurements of volatile organic compounds in the Southern Ocean. Biogeosciences 17, 2593–2619. https://doi.org/10.5194/bg-17-2593-2020

Woodhouse, M.T., Mann, G.W., Carslaw, K.S., Boucher, O., 2013. Sensitivity of cloud condensation nuclei to regional changes in dimethyl-sulphide emissions.

Atmospheric Chem. Phys. 13, 2723–2733. https://doi.org/10.5194/acp-13-2723-2013

Yang, M., Beale, R., Liss, P., Johnson, M., Blomquist, B., Nightingale, P., 2014. Air–sea fluxes of oxygenated volatile organic compounds across the Atlantic Ocean. Atmospheric Chem. Phys. 14, 7499–7517. https://doi.org/10.5194/acp-14-7499-2014

Yu, Z., Li, Y., 2021. Marine volatile organic compounds and their impacts on marine aerosol—A review. Sci. Total Environ. 768, 145054. https://doi.org/10.1016/j.scitotenv.2021.145054

Yuan, D., He, Z., Yang, G.-P., 2019. Spatiotemporal distributions of halocarbons in the marine boundary air and surface seawater of the Changjiang estuary and its adjacent East China Sea. Mar. Pollut. Bull. 140, 227–240. https://doi.org/10.1016/j.marpolbul.2019.01.040

Yvon-Lewis, S.A., Butler, J.H., 2002. Effect of oceanic uptake on atmospheric lifetimes of selected trace gases. J. Geophys. Res. Atmospheres 107, ACH 1-1-ACH 1-9. https://doi.org/10.1029/2001JD001267

Zafiriou, O.C., 1975. Reaction of methyl halides with seawater and marine aerosols. J Mar Res 33, 75–81.

Zafiriou, O.C., 1974a. Sources and reactions of OH and daughter radicals in seawater. J. Geophys. Res. 1896-1977 79, 4491–4497. https://doi.org/10.1029/JC079i030p04491

Zafiriou, O.C., 1974b. Photochemistry of halogens in the marine atmosphere. J. Geophys. Res. 1896-1977 79, 2730–2732. https://doi.org/10.1029/JC079i018p02730

Zafiriou, O.C., McFarland, M., 1981. Nitric oxide from nitrite photolysis in the central equatorial Pacific. J. Geophys. Res. Oceans 86, 3173–3182. https://doi.org/10.1029/JC086iC04p03173

Zafiriou, O.C., True, M.B., 1979. Nitrite photolysis in seawater by sunlight. Mar. Chem. 8, 9–32. https://doi.org/10.1016/0304-4203(79)90029-X

Zeng, Y.-X., Qiao, Z.-Y., Yu, Y., Li, H.-R., Luo, W., 2016. Diversity of bacterial dimethylsulfoniopropionate degradation genes in surface seawater of Arctic Kongsfjorden. Sci. Rep. 6, 33031. https://doi.org/10.1038/srep33031

Zhang, J. (Jim), Wei, Y., Fang, Z., 2019. Ozone Pollution: A Major Health Hazard Worldwide. Front. Immunol. 10.

Zhang, W., Gu, D., 2022. Geostationary satellite reveals increasing marine isoprene emissions in the center of the equatorial Pacific Ocean. Npj Clim. Atmospheric Sci. 5, 1–9. https://doi.org/10.1038/s41612-022-00311-0

Zhao, J., Zhang, R., 2004. Proton transfer reaction rate constants between hydronium ion (H3O+) and volatile organic compounds. Atmos. Environ. 38, 2177–2185. https://doi.org/10.1016/j.atmosenv.2004.01.019

Zheng, P., Chen, T., Dong, C., Liu, Y., Li, H., Han, G., Sun, J., Wu, L., Gao, X., Wang, X., Qi, Y., Zhang, Q., Wang, W., Xue, L., 2019. Characteristics and sources of halogenated hydrocarbons in the Yellow River Delta region, northern China. Atmospheric Res. 225, 70–80. https://doi.org/10.1016/j.atmosres.2019.03.039

Zhou, S., Gonzalez, L., Leithead, A., Finewax, Z., Thalman, R., Vlasenko, A., Vagle, S., Miller, L.A., Li, S.-M., Bureekul, S., Furutani, H., Uematsu, M., Volkamer, R., Abbatt, J., 2014. Formation of gas-phase carbonyls from heterogeneous oxidation of polyunsaturated fatty acids at the air-water interface and of the sea surface microlayer. Atmospheric Chem. Phys. 14, 1371–1384. https://doi.org/10.5194/acp-14-1371-2014

Zhou, X., Mopper, K., 1997. Photochemical production of low-molecular-weight carbonyl compounds in seawater and surface microlayer and their air-sea exchange. Mar. Chem., Modern Chemical and Biological Oceanography: The Influence of Peter J. Wangersky 56, 201–213. https://doi.org/10.1016/S0304-4203(96)00076-X

Zhu, Y., Kieber, D.J., 2018. Wavelength- and Temperature-Dependent Apparent Quantum Yields for Photochemical Production of Carbonyl Compounds in the North Pacific Ocean. Environ. Sci. Technol. 52, 1929–1939. https://doi.org/10.1021/acs.est.7b05462

Zika, R.G., Gidel, L.T., Davis, D.D., 1984. A comparison of photolysis and substitution decomposition rates of methyl iodide in the ocean. Geophys. Res. Lett. 11, 353–356. https://doi.org/10.1029/GL011i004p00353

Ziska, F., Quack, B., Abrahamsson, K., Archer, S.D., Atlas, E., Bell, T., Butler, J.H., Carpenter, L.J., Jones, C.E., Harris, N.R.P., Hepach, H., Heumann, K.G., Hughes, C., Kuss, J., Krüger, K., Liss, P., Moore, R.M., Orlikowska, A., Raimund, S., Reeves, C.E., Reifenhäuser, W., Robinson, A.D., Schall, C., Tanhua, T., Tegtmeier, S., Turner, S., Wang, L., Wallace, D., Williams, J., Yamamoto, H., Yvon-Lewis, S., Yokouchi, Y., 2013. Global sea-to-air flux climatology for bromoform, dibromomethane and methyl iodide. Atmospheric Chem. Phys. 13, 8915–8934. https://doi.org/10.5194/acp-13-8915-2013

Zou, Y., He, Z., Liu, C., Yang, G.-P., 2022. Spatiotemporal distribution and environmental control factors of halocarbons in the Yangtze River Estuary and its adjacent marine area during autumn and spring. Environ. Pollut. 304, 119244. https://doi.org/10.1016/j.envpol.2022.119244